Multi-probe Cosmological Analysis with the Dark Energy Survey

Anna Maria Porredon Diez de Tejada

Multi-probe Cosmological Analysis with the Dark Energy Survey

A thesis submitted for the degree of

Doctor of Philosophy in Physics

by

Anna Maria Porredon Diez de Tejada

Institute of Space Sciences (ICE, IEEC-CSIC)

Advisors:
Dr. Héctor Martín Crocce
and
Dr. Pablo Fosalba Vela

Tutor:
Dr. Àlvar Sánchez Moreno

Departament de Física

Universitat Autònoma de Barcelona

Barcelona, September 2019

Abstract

Ongoing and future photometric surveys will enable detailed measurements of the late-time Universe and powerful tests of the nature of dark energy and General Relativity. These surveys will be able to obtain cosmological constraints from multiple probes, and the combination of these probes can improve their robustness and constraining power.

This thesis is focused on the combination of multiple tracers of large-scale structure (LSS) to obtain tighter cosmological constraints. First, we combine the galaxy clustering from the Dark Energy Survey (DES) Year 1 (Y1) data with CMB lensing from the optimal combination of South Pole Telescope (SPT) and Planck, obtaining constraints on the galaxy bias, the growth function and the cosmological parameters. Our results are consistent with ΛCDM and other measurements of DES Y1. However, their constraining power is limited due to conservative scale cuts. We expect an improved signal-to-noise in future analyses.

We then combine the galaxy clustering of two different galaxy samples (the so-called multi-tracer approach) to explore the constraints on redshift space distortions (RSD) and primordial non-Gaussianities (PNG). For this purpose, we consider a pair of optimistic samples (with large bias differences and number densities) and the DES Year 3 (Y3) lens samples. We find that the constraints on RSD can be improved a factor of five at low redshift with respect to a single tracer, and the constraints on PNG can be improved more than a factor three. We also test the impact of including CMB lensing cross-correlations in our analysis, in which we keep the cosmology fixed, finding it mainly improves the galaxy bias constraints.

Last, we define and optimize a magnitude limited galaxy sample to be used for the galaxy clustering measurements in the DES Y3 analysis, in combination with galaxy-galaxy lensing. We rely on Fisher forecasts, and we test how these change given the variations obtained for the number density and estimated redshift uncertainty for a set of magnitude cuts. We also characterize the impact of redshift binning choices in our cosmological constraints for this sample and the other DES Y3 lens sample: redMaGiC. Finally, our forecasts show that we can potentially obtain 15% tighter constraints with this magnitude limited sample, compared to redMaGiC.

Acknowledgements

En primer lugar, quiero dar las gracias a Martín y a Pablo por haberme introducido a la investigación en Cosmología. He aprendido mucho a vuestro lado y nada de esto hubiese sido posible sin vosotros. Gracias por vuestra confianza en mí, por toda vuestra dedicación y esfuerzo a lo largo de estos años y por todas las oportunidades. Gracias por guiarme tan bien como lo habéis hecho, vuestro consejo es muy preciado. Haig d'agrair també a l'Àlvar que hagi sigut el tutor d'aquesta tesi. Per mi vas ser un mentor durant el grau de Física i els teus consells em van ajudar a introduir-me al món de la investigació.

Gracias también al grupo de Cosmología del ICE, especialmente a Enrique y Francisco, y a todas las personas que han sido parte del grupo: Jorge, Santi, Ricard, Kai, Martin, Linda, Ismael, Andrea, Isaac, Àlex... Arnau i Albert, gràcies per compartir la vostra experiència i ajudar-me durant el doctorat.

I would also like to give special thanks to Elisabeth and Ashley, for all your help and advice, and multiple and useful discussions. I really appreciate it. I am also thankful to the Dark Energy Survey collaboration for supporting my research, for providing me great opportunities and experiences, and allowing me to meet and collaborate with great researchers in the field. I want to mention Joe Zuntz for his invaluable help with the code, as well as Jack and Niall for many discussions.

My acknowledgment goes also to the LACEGAL project, that has allowed me to visit collaborators in Sao Paulo for six months, and to Beatriz and Rogerio for hosting me. Rogerio, you have been an amazing host, thank you for your warm welcome and for making my stay a great experience. It would be great to visit again and collaborate in the future. I would also like to thank Bithika, Antonino, Andrea, Hugo, Felipe, Otávio, Maria Gabriela, and everybody that I met for making me feel comfortable during my stay.

Haig d'agrair a en Josep la seva inestimable ajuda amb problemes informàtics. I tampoc em puc oblidar de la resta de gent que he conegut a l'institut durant aquests anys: Núria, Laura, Carmen, Carles, Padu, Marius, Francesco, Enrique, Juan Pedro, Fran, Nacho... He viscut molt bons moments al vostre costat. No podemos olvidar tampoco las tertúlias de Clara. A la Mariona, Andrea, David i Marina per tot el vostre suport i per fer que cada dia de feina fos molt menys pesat. Us trobaré molt a faltar. Martín, estás muy lejos en Madrid pero te considero también un gran amigo y nunca olvidaré a la polilla.

Per últim, agraeixo als amics i la família pel seu suport i ànims durant aquests anys. Als meus pares, per animar-me a seguir i creure en mi sempre. Oriol, el positró somrient m'ha ajudat, sense dubte. Xènia, ets la millor companya de pis que es pot tenir, gràcies per tots els ànims. A la Berta, per estar sempre allà, des del màster. A l'Axel, per estar sempre allà donant-me suport durant els últims mesos de la tesi i alegrar-me cada dia; el teu power level és molt alt. També haig d'agrair al programa FI de l'AGAUR el suport ecònomic durant aquests anys.

Contents

Introduction

According to the current consensus cosmological model, ΛCDM, dark matter and dark energy make up most of the energy density of the Universe. However, their nature is still unknown and understanding them presents a grand challenge for present-day cosmologists. Ongoing and future photometric surveys will enable detailed measurements of the late-time Universe and powerful tests of the nature of dark energy and General Relativity. The current generation of surveys includes the Kilo-Degree Survey (KiDS) [57], the Hyper Suprime Cam (HSC) [11], and the Dark Energy Survey (DES[1]) [164]. The next generation of surveys, starting in the 2020s, will include the Large Synoptic Survey Telescope (LSST[2]) [104], Euclid[3] [94], the Dark Energy Spectroscopic Instrument (DESI[4]) [95], and the Wide-Field Infrared Survey Telescope (WFIRST[5]) [159].

These surveys will be able to obtain cosmological constraints from multiple probes, such as galaxy clustering, galaxy-galaxy lensing, cosmic shear and Baryon Acoustic Oscillations (BAO). And the combination of these probes can improve the robustness and the constraining power of their cosmological constraints. An example of this is the joint analysis of cosmic shear, galaxy-galaxy lensing and galaxy clustering of DES Year 1 (Y1) data [2], the so-called 3×2pt analysis. We can further extend this multi-probe analysis by combining it with other tracers of large-scale structure (LSS) such as the Cosmic Microwave Background (CMB) (see e.g. [3]).

Photons from the CMB are gravitationally deflected by the large-scale structure, and the distinct pattern of the lensed CMB can be used to probe lensing structures along the line of sight. By cross-correlating the CMB lensing signal with tracers of the matter distribution, such as galaxies, we can measure the growth of structure in the Universe across cosmic time. High signal-to-noise

[1] http://www.darkenergysurvey.org/
[2] https://www.lsst.org/
[3] https://www.euclid-ec.org/
[4] https://www.desi.lbl.gov/
[5] https://wfirst.gsfc.nasa.gov/

measurements of CMB lensing have been obtained by several collaborations, including Planck [129], the Atacama Cosmology Telescope (ACT) [55], POLARBEAR [9], and the South Pole Telescope (SPT) [41].

This thesis is focused on the combination of multiple tracers of LSS to obtain tighter cosmological constraints. In particular, we concentrate on the Dark Energy Survey and its combination with data from the South Pole Telescope (SPT) and Planck collaborations. In this work, we first update the results of G16 by measuring the cross-correlations between galaxy density from the DES Y1 data and a CMB lensing reconstruction using a combination of SPT and Planck data. We use the measured galaxy-CMB lensing cross-correlations to obtain constraints on the galaxy bias, the growth function and the cosmological parameters. In some of these analyses, we perform joint fits to both the galaxy-CMB lensing cross-correlations and galaxy clustering measurements in order to break degeneracies with galaxy bias.

We then combine the galaxy clustering of two different galaxy samples (the so-called multi-tracer approach) to explore the constraints on redshift space distortions (RSD) and primordial non-Gaussianities (PNG). The motivation behind this is that bias-sensitive parameters, such as the redshift space distortions parameter, $\beta(z) = f(z)/b(z)$, and the amplitude of local non-Gaussianities, $f_{\rm NL}$, are different tracers of the same realization of the density field. Therefore, comparing the clustering between different types of LSS enable us to measure these parameters with a precision that is not limited by cosmic variance. In practice, the biases of the two samples may be correlated, which limits the potential gains of the multi-tracer approach. By combining the galaxy clustering from the two samples with CMB lensing correlations, one can mitigate these correlations and break the degeneracies between the biases and the other cosmological parameters of interest.

In this thesis, we extend the idea of a multi-tracer analysis of RSD explored in [14] by including in addition the cross-correlations with CMB lensing in order to break possible degeneracies with the galaxy bias. We also explore the constraints that we could obtain with a multi-tracer analysis of local non-gaussianities, $f_{\rm NL}$, from photometric surveys. In addition, we forecast the constraints on RSD and $f_{\rm NL}$ considering the DES Year 3 (Y3) lens samples: redMaGiC and magnitude limited.

Last, we define the magnitude limited sample from DES Y3 data that, alongside redMaGiC, is going to be used to measure galaxy clustering. These galaxy clustering measurements are then going to be combined with galaxy-galaxy lensing, cosmic shear, and CMB lensing correlations. We optimize the galaxy selection of this sample in terms of its cosmological constraints. For this

purpose we rely on Fisher forecasts, and we test how these change given the variations obtained for the number density and estimated redshift uncertainty given by a set of magnitude cuts. We also characterize the impact of redshift binning choices in our cosmological constraints for both samples.

The outline of the thesis is the following. After a theoretical introduction in Chapter 1, and an overview of the Dark Energy Survey (DES) in Chapter 2, in Chapter 3 we combine the galaxy clustering from DES Y1 data with CMB lensing from SPT and Planck collaborations. Then, in Chapter 4, we combine the galaxy clustering of two different galaxy samples to constrain Redshift Space Distortions and Primordial non-Gaussianities in a multi-tracer approach. Here we also consider the inclusion of galaxy - CMB lensing cross-correlations. Last, in Chapter 5 we define and optimize a magnitude limited lens sample for the combined analysis of galaxy clustering and galaxy-galaxy lensing from DES Y3 data.

Chapter 1

Cosmological Framework

1.1 The Standard Cosmological Model

The fundamental basis of Cosmology is the so-called Cosmological Principle, that states that the Universe is isotropic and homogeneous at large scales. In 1929, Edwin Hubble discovered that the Universe is expanding. In order to describe this effect we introduce the scale factor, a, which is a measure of the expansion rate of the Universe. By the homogeneity property, a is a function of time alone. Since this expansion is uniform, the coordinates of each point remain the same. The distance between coordinates is called the comoving distance ($\mathbf{x}$) and, the physical distance, which is actually the distance we have to travel between two points in the Universe, is defined as

$$\mathbf{d} = a(t)\mathbf{x}. \tag{1.1}$$

We usually normalize the scale factor by setting its present value equal to one ($a(t_0) = 1$) where we use the symbol t_0 to indicate the current age of the Universe. To quantify the change in the scale factor with time we introduce the *Hubble rate*

$$H(t) \equiv \frac{\dot{a}}{a} \tag{1.2}$$

where we denote by $\dot{a}$ the time derivative of the scale factor: da/dt. The value of the Hubble rate today, H_0, is parametrized by the dimensionless Hubble parameter, h, in the following way

$$H_0 = 100\,h\ \ \mathrm{km\,s^{-1}\,Mpc^{-1}}. \tag{1.3}$$

Here Mpc stands for megaparsec units. Due to the expansion of the Universe, galaxies appear to be receding from us, so that the light emitted by those galaxies is redshifted, i.e. the observed wavelength is larger than the emitted one. The relationship between the *redshift* and the scale factor is:

$$1 + z = \frac{1}{a} \tag{1.4}$$

The most general isotropic and homogeneous metric of an expanding, flat Universe is given by the Friedmann-Robertson-Walker (FRW) metric

$$ds^2 = -dt^2 + a(t)^2[dr^2 + r^2 d\Omega^2] \tag{1.5}$$

where we have used spherical coordinates. Therefore, r is the radial comoving distance and $d\Omega^2 = d\theta^2 + sin^2\theta d\phi^2$. Light satisfies $ds^2 = 0$, hence the comoving distance travelled by light moving radially towards us is

$$r(z) = \int_0^z \frac{dz}{H(z)}. \tag{1.6}$$

This can be derived by combining equations (1.5) and (1.4). The evolution of the scale factor is determined by the Friedmann equation, which can be written as

$$H^2(t) = \left(\frac{\dot{a}}{a}\right)^2 = \frac{8\pi G}{3}\left[\rho(t) + \frac{\rho_c(t_0) - \rho_0}{a^2(t)}\right]. \tag{1.7}$$

The parameter $\rho(t)$ is the total energy density of the Universe, so it consists of the sum of the energy densities of each component: baryonic matter, radiation, dark matter and dark energy (or cosmological constant). In the same way, ρ_0 is the energy density of the Universe today. Also, G is Newton's constant and $\rho_c(t_0)$ is the present value of the critical density, i.e. the value of ρ_0 required for the Universe to be spatially flat.

$$\rho_c(t_0) = \frac{3H_0^2}{8\pi G} \tag{1.8}$$

It is more convenient to use the density parameter Ω instead of ρ and it is defined as

$$\Omega(t) = \frac{\rho(t)}{\rho_c(t)}. \tag{1.9}$$

Analogously, the density parameter of each component of the Universe is defined as the ratio of the energy density of the component to the critical density: $\Omega_i = \rho_i/\rho_c$. The Standard Cosmological Model (SCM) is based upon a flat, expanding Universe dominated by dark matter and dark energy (cosmological constant). Therefore, the density parameter today is equal to one:

$\Omega = 1$. Equivalently,

$$\Omega_{r,0} + \Omega_{b,0} + \Omega_{c,0} + \Omega_{\Lambda,0} = 1 \tag{1.10}$$

where the subindices correspond to radiation, baryonic matter, dark matter and the cosmological constant, respectively. According to recent experimental results [128], $\Omega_{\Lambda,0}$ has an approximate value of 0.7 and $\Omega_{m,0}$ of 0.3, as it is just the difference between 1 and $\Omega_{\Lambda,0}$, because $\Omega_r \sim 0$. However, the density parameter corresponding to baryonic matter ($\Omega_{b,0}$) is very small, close to 0.04, so the main contributions come from dark matter and dark energy, in concordance with the SCM. By conservation of the energy-momentum tensor ($T^{\mu}{}_{\nu}$), it can be found that

$$\dot{\rho} = -3H(\rho + P) \tag{1.11}$$

where P is the pressure. This equation gives us the evolution of the energy density. Each one of the components of the Universe satisfies a different equation of state, i.e. has a different value of the parameter w in

$$P = w\rho. \tag{1.12}$$

In particular, we have that: for radiation $w_r = 1/3$, for matter $w_m = 0$ and for the cosmological constant, or dark energy, $w = -1$. Using the equation of state, we can now solve (1.11) and find that the evolution of ρ_i with time is

$$\rho_i = \rho_{i,0} a^{-3(1+w_i)}. \tag{1.13}$$

Thus, for radiation $\rho_r = \rho_{r,0}\, a^{-4}$, for matter $\rho_m = \rho_{m,0}\, a^{-3}$ and, for the cosmological constant $\rho_\Lambda =$ constant. Taking into account that today the Universe is dominated by both matter and dark energy, going back in time (i.e. smaller values of a) we see in Figure 1.1 that, initially the Universe must have been dominated by radiation, followed by a period in which it was dominated by matter.

Since the values of the density parameters are known, it is useful to rewrite the Friedmann equation in the following way:

$$H^2 = H_0^2[\Omega_m\, a^{-3} + \Omega_r\, a^{-4} + \Omega_\Lambda]. \tag{1.14}$$

For more details about the contents included in this section, see Dodelson 2003 [60].

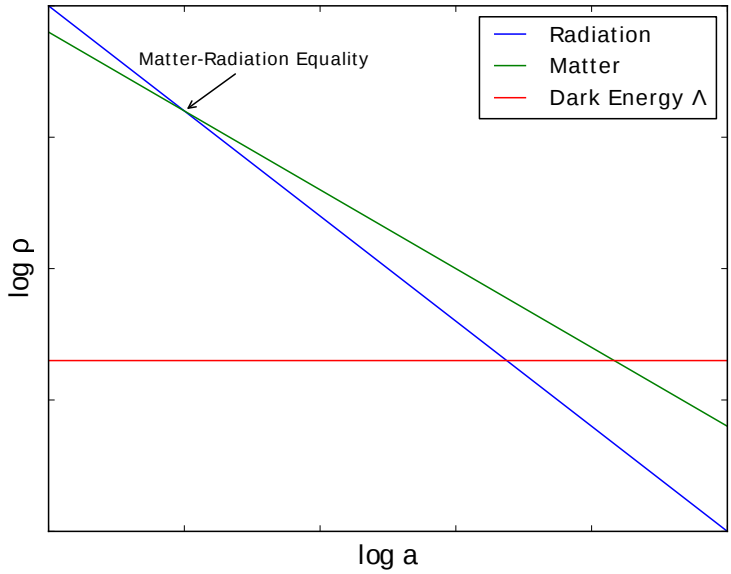

FIGURE 1.1: Energy density with respect to the scale factor for different components of a flat universe.

1.2 Cosmic Inflation

Despite its many successes, such as the Hubble diagram manifesting expansion, light element abundances in agreement with the Big Bang nucleosynthesis and the blackbody radiation of the cosmic microwave background (CMB), the Standard Cosmological Model leaves some questions unanswered. Which is the origin of the perturbations (seeds) that led to structure formation? Why is the Universe so flat today? And why is it, particularly the CMB, so isotropic?

Cosmic Inflation [98] is the most accepted scenario for the evolution of the Universe at early times and it provides an explanation for all these questions. Inflation theorizes that, at very early times, the Universe experienced an exponentially fast expansion.

The initial fluctuations that originated current inhomogeneities are expected to be gaussian. These inhomogeneities would have been produced due to vacuum quantum fluctuations of a scalar field, the *inflaton* (ϕ).

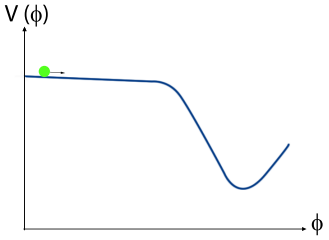

During inflation, the inflaton slowly rolls down the potential until it reaches a minimum, as shown schematically on the right-hand side. As the Universe expands, each wave generated by quantum fluctuations gets stretched out until its wavelength has the size

of the Hubble horizon $\lambda = 1/H$, moment in which it freezes.
Therefore, at every instant of time, the field consists of a superposition of: oscillating waves, that are being stretched out, and frozen waves.

When the inflaton is about to roll over the edge shown in the picture, the expansion is no longer exponential and the energy density dilutes with time. Because of this superposition of frozen waves originated from quantum fluctuations, not all the points in the Universe get to this edge of the potential at the same moment. Those points that cross the edge later will have a higher energy density at the end of inflation than the ones that cross it before. This is the origin of the seeds that later led to structure formation.

1.3 Evolution of Inhomogeneities

In this section we approach the evolution of the inhomogeneities generated during inflation. The inflationary prediction for the primordial power spectrum (i.e. the power spectrum when the waves enter the horizon and freeze) is given by

$$P_0(k) = A_s k^{n_s - 1} \tag{1.15}$$

where n_s is the spectral index and A_s a normalization amplitude. If $n_s = 1$, then the primordial power spectrum is scale invariant. For further details about this, see e.g. [98] or [123].

After inflation, the Universe was radiation dominated, as shown in Figure 1.1, and its expansion was decelerated. It has not been until recently, with the beginning of a period dominated by dark energy, that the expansion has become accelerated.

The deceleration of the expansion provokes that, at some point, the wavelengths re-enter the Hubble horizon. Depending on the scale, the waves will cross the horizon at the radiation dominated epoch or the matter dominated one. Before re-entering the horizon, General Relativity is needed to describe the evolution of inhomogeneities. The general description of the evolution of perturbations is given by Boltzmann-Einstein equations, where the Boltzmann equations govern the evolution of inhomogeneities and the Einstein equations relate perturbations in the metric to perturbations in matter and radiation.

Once the waves have re-entered the horizon, a Newtonian treatment is valid and we can consider matter as an ideal fluid. We will focus on the evolution of matter inhomogeneities in this case,

after they have crossed the horizon.

1.3.1 Equations of motion

The equations of motion for a fluid are the Euler equation, the continuity equation and the Poisson equation:

$$\frac{\partial \mathbf{u}}{\partial t} + (\mathbf{u} \cdot \nabla_d)\,\mathbf{u} = -\frac{1}{\rho}\nabla_d P - \nabla_d \Phi \tag{1.16}$$

$$\frac{\partial \rho}{\partial t} + \nabla_d \cdot \rho \mathbf{u} = 0 \tag{1.17}$$

$$\nabla_r^2 \Phi = 4\pi G \rho. \tag{1.18}$$

Here Φ is the gravitational potential and $\mathbf{u}$ is the physical velocity, i.e. the time derivative of (1.1). These equations are written in physical coordinates.

In order to continue, we will need to convert them into comoving coordinates. First, we derive (1.1) with respect to time:

$$\mathbf{u} = \dot{a}\mathbf{x} + a\dot{\mathbf{x}} = \dot{a}\mathbf{x} + \mathbf{v} \tag{1.19}$$

where $\mathbf{v}$ is the peculiar velocity, which ignores the motion induced by the expansion of the Universe.

Second, we need to transform the derivatives into the comoving system:

$$\left(\frac{\partial}{\partial t}\right)_d = \left(\frac{\partial}{\partial t}\right)_x - H(\mathbf{x} \cdot \nabla_x) \tag{1.20}$$

$$\nabla_d = \frac{1}{a}\nabla_x. \tag{1.21}$$

From now on, we will omit the x subindices that refer to the comoving coordinate system. Since we are only interested in the perturbation with respect to the background, we split the potential Φ in two terms:

$$\Phi(\mathbf{d}, t) = \varphi(\mathbf{x}, t) + \frac{1}{2}a\ddot{a}x^2. \tag{1.22}$$

The first term corresponds to the perturbation component of Φ while the second corresponds to the background potential. Since dark energy is uniformly distributed, it does not contribute anything to the potential perturbation φ. Then, in a Universe consisting of matter and dark energy,

like the current situation, the Poisson equation for the perturbed potential is

$$\nabla^2\varphi = 4\pi G a^2 \bar{\rho}\delta(\mathbf{x}, t) \tag{1.23}$$

where we have transformed the derivatives to comoving coordinates and $\delta(\mathbf{x}, t)$ is the density contrast. If $\bar{\rho}$ is the mean matter energy density, we define the density contrast as

$$\delta(\mathbf{x}) = \frac{\rho(\mathbf{x}) - \bar{\rho}}{\bar{\rho}}. \tag{1.24}$$

If the matter distribution was uniform, δ would vanish. For this reason, the density contrast is a measure of the matter inhomogeneities: underdensities ($\delta < 0$) and overdensities ($\delta > 0$).

The Euler and continuity equations in the comoving system are the following ones, respectively:

$$\frac{\partial \mathbf{v}}{\partial t} + H\mathbf{v} + (\mathbf{v}\cdot\nabla)\,\mathbf{v} = -\frac{1}{a\rho}\nabla P - \frac{1}{a}\nabla\varphi \tag{1.25}$$

$$\frac{\partial \rho}{\partial t} + 3H\rho + \frac{1}{a}\nabla\cdot\rho\mathbf{v} = 0. \tag{1.26}$$

Here, in the continuity equation, we have used (1.11) applied to matter. Also, notice that the last term of the Euler equation ($-a^{-1}\nabla\varphi$) is the peculiar gravitational acceleration, i.e. the extra acceleration with respect to the background. Now, using (1.24), we replace ρ by $\bar{\rho}(\delta + 1)$:

$$\frac{\partial \mathbf{v}}{\partial t} + H\mathbf{v} + (\mathbf{v}\cdot\nabla)\,\mathbf{v} = -\frac{1}{a\bar{\rho}(\delta+1)}\nabla P - \frac{1}{a}\nabla\varphi \tag{1.27}$$

$$\frac{\partial \delta}{\partial t} + \frac{1}{a}\nabla\cdot(\delta+1)\mathbf{v} = 0 \tag{1.28}$$

The derivation of these expressions can be found more extensively at Peebles 1980 [123].

1.3.2 Linear Perturbation Theory

The exact solution to these set of equations is non-linear and, for this reason, it cannot be solved analytically. The easiest approach to obtain an analytical solution is to use perturbation theory at first order in δ, that is the limit in which the density and velocity perturbations are still very small ($\delta \ll 1$). This development is valid for large-scales.

In order to get a more accurate result (i.e. valid for a larger range of scales), one can use

perturbation theory at higher orders in δ. There are also approximations and models, such as the Zel'dovich approximation (Zel'dovich 1970), that are valid in the mildly non-linear regime, although their domain of validity is limited.

We apply now linear perturbation theory to the set of fluid equations we have obtained previously. Since δ and $\mathbf{v}$ are small perturbed quantities, at first order in perturbation theory we discard the higher order terms $\delta\mathbf{v}$, $(\mathbf{v}\cdot\nabla)\mathbf{v}$ and $\nabla P\delta$ in the equations (1.27) and (1.28):

$$\frac{\partial \mathbf{v}}{\partial t} + H\mathbf{v} = -\frac{1}{a\bar{\rho}}\nabla P - \frac{1}{a}\nabla\varphi \tag{1.29}$$

$$\frac{\partial \delta}{\partial t} + \frac{1}{a}\nabla\cdot\mathbf{v} = 0. \tag{1.30}$$

In the following section we will treat the evolution of matter inhomogeneities during the period in which the Universe was dominated by matter.

Matter Dominated Universe

From the linearized continuity equation (1.30) we find that $\nabla\cdot\mathbf{v} = -a\frac{\partial\delta}{\partial t}$. By taking the divergence of the linearized Euler equation (1.29) and combining it with this expression and the Poisson equation (1.23), we obtain a second order differential equation for the density contrast δ. It is convenient to switch to Fourier space because then we get rid of all the spatial derivatives (recall that the Fourier transform of the nabla operator ∇ is $i\mathbf{k}$, where $\mathbf{k}$ is the wavenumber). The subindex k denotes that it is the Fourier transform of the variable:

$$\frac{\partial^2\delta_k}{\partial t^2} + 2H\frac{\partial\delta_k}{\partial t} = 4\pi G\bar{\rho}\delta_k - \frac{k^2 P_k}{a^2\bar{\rho}}. \tag{1.31}$$

This equation is analogous to the damped harmonic oscillator. Thus, the factor $2H$ at the second term on the left-hand side, which is related to the expansion of the Universe, acts like a friction or resistance to the growth of δ.

On the right-hand side we have two opposing forces. On the one hand, there is gravity ($4\pi G\bar{\rho}\delta_k$), that enhances the growth of δ. On the other hand, pressure suppresses its growth, and this effect is magnified at high values of k or, equivalently, small scales.

Since most of the matter in the Universe appears to consist of cold dark matter (CDM) and it only interacts through gravity, from now on we will ignore the effects of pressure. So, in real

space:

$$\frac{\partial^2\delta}{\partial t^2} + 2H\frac{\partial\delta}{\partial t} = 4\pi G\bar{\rho}\delta \tag{1.32}$$

As nothing depends on $\mathbf{x}$ except δ, this equation admits factorisable solutions. Therefore, the general linear solution has the form:

$$\delta(\mathbf{x}, t) = D_1(t)A(\mathbf{x}) + D_2(t)B(\mathbf{x}). \tag{1.33}$$

The variables $D_1(t)$ and $D_2(t)$ are the density growth factors for the linear evolution of density perturbations, and $A(\mathbf{x})$ and $B(\mathbf{x})$ are given by the initial conditions. Consequently, the rate with which the primordial inhomogeneities are to grow in the linear regime solely depends on the growth factors $D_1(t)$ and $D_2(t)$.

One of these growth factors will decay faster than the other, so that its contribution can be neglected. Taking into account that $\bar{\rho} = \rho_c\Omega$ and the definition of ρ_c (1.8), we find that the time evolution of the leading growing factor $D(t)$ is determined by[1]:

$$\ddot{D} + 2H\dot{D} = \frac{3}{2}\Omega_m H^2 D = \frac{3}{2a^3}\Omega_{m,0}H_0^2 D \tag{1.34}$$

Matter and Dark Energy Dominated Universe

Currently, our Universe is dominated by matter and dark energy. For this reason, the growth of inhomogeneities in such a situation is of special interest. We are going to consider that the contribution of radiation to the total energy density is negligible ($\Omega_r \sim 0$). Combining the first and second derivatives of the Friedmann equation in (1.14), we find:

$$\ddot{H} + 2H\dot{H} = \frac{3}{2a^3}\Omega_{m,0}H_0^2 H \tag{1.35}$$

As a result, $H(t)$ evolves according to the same equation as the growth factor $D(t)$ in a Universe dominated by matter. These two equations can be combined by multiplying (1.35) by $D(t)$ and subtracting $H(t)$ times (1.34):

$$\ddot{H}D - \ddot{D}H + 2H(\dot{H}D - H\dot{D}) = 0 \tag{1.36}$$

[1] In a so-called Einstein-de Sitter (EdS) Universe, which is purely dominated by matter $\Omega = \Omega_m = 1$.

Rearranging this expression conveniently leads us to the following differential equation

$$\frac{d}{dt}\left[a^2H^2\frac{d}{dt}\left(\frac{D}{H}\right)\right] = 0 \tag{1.37}$$

whose solution is given by

$$D(z) = \frac{5\Omega_{m,0}H_0^2}{2}H(z)\int_z^\infty \frac{1+z'}{H^3(z')}dz'. \tag{1.38}$$

Here we have used the relation (1.4) between the redshift z and the scale factor a. The proportionality constant in front of the integral is obtained by requiring that for $a \ll 1$ the growth factor is the same as the one obtained for a matter dominated Universe (Einstein-de Sitter). In general, the equation (1.38) has an exact solution in terms of hyper-geometric functions (see [121]), but the following formula provides a sufficiently accurate approximation [24]:

$$(1+z)D(z) \approx \left(\frac{5}{2}\right)\frac{\Omega_m}{\Omega_m^{4/7} - \Omega_\Lambda + [1+\Omega_m/2][1+\Omega_\Lambda/70]} \tag{1.39}$$

where all the density parameters Ω_i are evaluated at redshift z:

$$\Omega_m(z) = \Omega_{m,0}(1+z)^3\frac{H_0^2}{H^2(z)} \tag{1.40}$$

$$\Omega_\Lambda(z) = \Omega_{\Lambda,0}\frac{H_0^2}{H^2(z)}. \tag{1.41}$$

The growth factor is usually normalized such that $D(z=0) = 1$, where $z = 0$ corresponds to t_0. With this normalization, and replacing cosmic time t with z, from (1.33) one can easily find the following relation in Fourier space:

$$\delta(\mathbf{k}, z) = D(z)\delta(\mathbf{k}, 0) \tag{1.42}$$

1.4 Redshift Space Distortions

Peculiar motions provoke perturbations in the observed redshift. A slightly overdense region which is just beginning to collapse appears squashed in redshift space, as is illustrated in Figure 1.2 below. In each case, a contour of constant density is distorted in redshift space. The arrows denote the direction and magnitude of the velocity.

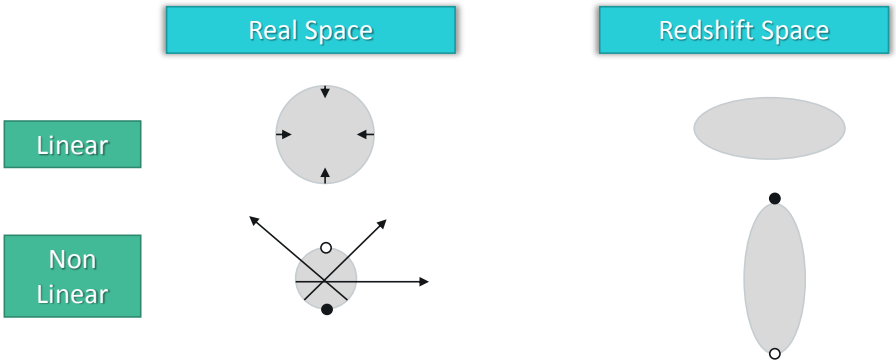

FIGURE 1.2: Illustration of the redshift space distortions.

For small (linear) overdensities, the peculiar velocities (v_p) are smaller than the velocities due to the expansion of the Universe (v_H): $v_p < v_H$. In Figure 1.2 we can see that, since the closest galaxies are moving away from us, they *appear* farther from us than they actually are. The opposite happens with the galaxies on the farthest side of the overdense region.

On the contrary, in the case of a higher overdense region, when non-linear effects come into play ($v_p > v_H$), it appears elongated along the line of sight. This is called the *fingers-of-God* effect: structures have a tendency to point towards the observer. Furthermore, the peculiar velocities are so large that the points on the bottom of the region (closest to us) appear at the opposite side in redshift space. The combined effect of redshift space distortions in large and small scales is an enhancement of the overdensity.

1.5 Angular Correlation Function

In order to characterize the evolution of large-scale structure in the Universe we need to use an statistical approach, as we do not have direct observational access to primordial fluctuations (the initial conditions for the evolution equations) and we cannot follow individual perturbations over cosmic time. In this way, we can think of the observable Universe as being the evolved image of a particular stochastic realization of a statistic ensemble of possibilities.

From now on, we consider the density field $\delta(\mathbf{x})$. Since at very large (linear) scales we observe that fluctuations are gaussian, we usually assume that primordial fluctuations are indeed gaussian, as generically predicted by inflation.

Then, according to the *Wick theorem*, we only need the two-point correlation function to characterize the density field (higher-order correlation functions vanish), which is defined as the ensemble average of the product of the density at two different locations

$$\xi(r) = \langle \delta(\mathbf{x})\delta(\mathbf{x}+\mathbf{r})\rangle \tag{1.43}$$

and it depends only on the norm of $\mathbf{r}$ due to the homogeneity and isotropy of the Universe. So, for very large scales (i.e. the linear regime), when we can assume that $\delta(\mathbf{x})$ is gaussian, we only need $\xi(r)$ to characterize the field.

The physical interpretation of the two-point correlation function is that it measures the excess over random probability that two particles at volume elements dV_1 and dV_2 are separated by a distance $x_{12} \equiv |\mathbf{x}_1 - \mathbf{x}_2|$,

$$\frac{dP_{12}}{dV_1 dV_2} = \bar{n}^2[1 + \xi(x_{12})] \tag{1.44}$$

where $\bar{n}$ is the mean density. It is convenient to work in Fourier space, as then it is easier to distinguish between small and large scales. The matter power spectrum is the Fourier transform of the two-point correlation function,

$$P(k) = \int d^3\mathbf{r}\xi(r)\exp(i\mathbf{k}\cdot\mathbf{r}). \tag{1.45}$$

Alternatively, we can express $P(k)$ in terms of the Fourier transform of $\delta(\mathbf{x})$ and the three-dimensional Dirac delta function $\delta_D^3(\mathbf{k}-\mathbf{k}')$:

$$\langle \delta(\mathbf{k})\delta(\mathbf{k}')\rangle = (2\pi)^3 P(k)\delta_D^3(\mathbf{k}-\mathbf{k}'). \tag{1.46}$$

In order to normalize the power spectrum it is common to use the σ_8 parameter (see Dodelson 2003 [60], page 286), which is defined as the variance of the mass density field filtered on a scale of 8 Mpc/h,

$$\sigma_8^2(z=0) = \frac{1}{2\pi^2}\int dk k^2 P(k, z=0)\tilde{W}_8^2(k), \tag{1.47}$$

where $\tilde{W}_8(k)$ is the Fourier transform of the top-hat filter function and is given by

$$\tilde{W}_8(k) = \frac{3j_1(8k)}{8k}, \tag{1.48}$$

with j_1 being a spherical Bessel function of the first kind. The σ_8 parameter is related to the observed abundance of massive clusters of galaxies. One of the more recent estimations of σ_8

(Dark Energy Survey Collaboration 2015 [165]) is $\sigma_8(\Omega_m/0.3)^{0.5} = 0.81 \pm 0.06$, where Ω_m is the matter density parameter today (1.9) and is estimated to have a value close to 0.3.

With the two-point correlation function or the power spectrum we can characterize the density field at very large scales in three dimensions. However, whenever there is an intrinsic uncertainty in the measure of radial distances to galaxies, e.g. for photometric surveys, it is more convenient to introduce the angular two-point correlation function, $\omega(\theta)$, that can be obtained from the projection of the spatial two-point correlation function onto the surface of a sphere centered at us. Since ξ is the ensemble average of the product of the density at two different points (1.43), in order to obtain its angular counterpart we will have to project radially ξ twice. That is,

$$\omega(\theta) = \int\int dz_1 dz_2 \phi(z_1)\phi(z_2)\xi(s) \tag{1.49}$$

where $s = \sqrt{r^2(z_1) + r^2(z_2) - 2r(z_1)r(z_2)\cos\theta}$ is the comoving separation between a pair of points and θ is the angular separation in the sky. Due to the uncertainty in the measured redshift, the surface of the sphere we are considering has a certain width Δz; the radial selection functions $\phi(z_1)$ and $\phi(z_2)$ are introduced in order to take into account this issue. In galaxy surveys, for example, $\phi(z)$ can be defined as the number of galaxies per unit redshift within a redshift bin (i.e. within the shell) and it is normalized to unity.

1.5.1 Galaxy Bias

Until now we have considered the matter density field, and hence equation (1.49) describes the angular distribution of the bulk of matter in the Universe. There is observational evidence that the spatial clustering of galaxies can be biased relative to the spatial clustering of matter (Kaiser 1984 [86], Bardeen et al. 1986 [17]). The *galaxy bias* is the relationship between these two distributions, that is between the spatial distribution of galaxies and the underlying matter density field (composed mainly of dark matter). It is the result of the various physics of galaxy formation which can cause the spatial distribution of baryons to differ from that of dark matter.

We define the linear galaxy bias as the ratio of the mean overdensity of galaxies δ_g to the mean overdensity of mass,

$$b \equiv \delta_g/\delta, \tag{1.50}$$

and can, in theory, depend on the scale and galaxy properties such as morphology, color, and redshift. Since the power spectrum is proportional to the square of the density field (equation

(1.46), in terms of the power spectrum, the linear bias can also be defined as:

$$b^2(k) \equiv P_g(k)/P(k). \tag{1.51}$$

Local Bias Model

The simplest possible model for the galaxy bias is the *local bias model* (see Fry & Gaztañaga 1993 [67]), in which the smoothed mean overdensity of galaxies is assumed to be a deterministic function of the (similarly smoothed) mass density field $\bar{\delta}_g(\mathbf{x}) = f(\bar{\delta}(\mathbf{x}))$, where the smoothed density field is

$$\bar{\delta}(\mathbf{x}) = \int d^3x' \delta(\mathbf{x}') W(\mathbf{x} - \mathbf{x}'), \tag{1.52}$$

and $W(\mathbf{x})$ is a normalized window function. For a top-hat window, $\bar{\delta}(\mathbf{x})$ is just the volume average of $\delta(\mathbf{x})$ over a sphere of radius R. On large scales, where $\delta << 1$, we can expand f as a Taylor series,

$$\bar{\delta}_g = f(\bar{\delta}) = \sum_{j=0}^{\infty} \frac{b_j}{j!} \bar{\delta}^j. \tag{1.53}$$

The linear term, b_1 corresponds to the so-called linear bias factor. We can use this model to obtain the power spectrum of galaxies from the matter power spectrum. Taking (1.53) at linear order, and using the definition of $P(k)$, eq. (1.46), we get

$$P_g(k) = b_1^2 P(k). \tag{1.54}$$

This expression is very useful in order to approximate the galaxy power spectrum at very large scales, i.e., in the linear regime.

1.5.2 The Kaiser Factor

We have already seen that redshift space distortions produce an enhancement of overdensities and hence they affect the power spectrum $P(k)$. In linear perturbation theory, the relation between the power spectrum in real and in redshift space is given by the so-called Kaiser factor.

According to Kaiser 1987 [87], the Fourier amplitude of fluctuations in redshift space $\delta^S_{\mathbf{k}}$ is amplified with respect to that of real space by a factor that depends on the angle between the

wavevector **k** and the line of sight **l**.

$$\delta^S_{\mathbf{k}} = \delta^R_{\mathbf{k}}(1 + \beta\mu^2_{\mathbf{kl}}) \tag{1.55}$$

Here $\mu_{\mathbf{kl}}$ is the cosine of the angle between **k** and **l** and $\beta \equiv f/b_1$, where f is the logarithmic derivative of the growth factor $D(z)$ and b_1 is the linear bias factor. From equation (1.55) we can obtain the relation between the two-dimensional power spectrum in redshift and in real space:

$$P^S(k, \mu_{\mathbf{kl}}) \equiv \langle \delta^S_{\mathbf{k}} \delta^{S*}_{\mathbf{k}} \rangle = P^R(k)(1 + \beta\mu^2_{\mathbf{kl}})^2. \tag{1.56}$$

It is convenient to characterize the two-dimensional redshift space power spectrum in terms of multipole moments, that define the decomposition of $P^S(k, \mu)$ into Legendre Polynomials,

$$P^S(k, \mu) = \sum_{l=0}^{\infty} P^S_l(k) L_l(\mu) \tag{1.57}$$

where $L_l(\mu)$ are the Legendre polynomials of l-th order. The multipole moments $P^S_l(k)$ can be computed by the inversion formula

$$P^S_l(k) \equiv \frac{2l+1}{2} \int_{-1}^{+1} d\mu P^S(k, \mu) L_l(\mu). \tag{1.58}$$

Recall that the first three even Legendre Polynomials are:

$$\begin{aligned} L_0(\mu) &= 1 \\ L_2(\mu) &= \frac{3\mu^2 - 1}{2} \\ L_4(\mu) &= \frac{35\mu^4 - 30\mu^2 + 3}{8}. \end{aligned} \tag{1.59}$$

With this, we can see in equation (1.56) that $P^S(k, \mu)$ contains no odd powers of μ and no powers higher than μ^4, and hence it is characterized completely by its monopole, quadrupole and hexadecapole moments ($l = 0, 2, 4$). As a consequence, all odd multipoles and also those with $l > 4$ must vanish according to (1.57). The non-vanishing multipole moments can be obtained by

direct integration:

$$P_0^S(k) = \left(1 + \frac{2}{3}\beta + \frac{1}{5}\beta^2\right) P^R(k)$$
$$P_2^S(k) = \left(\frac{4}{3}\beta + \frac{4}{7}\beta^2\right) P^R(k) \tag{1.60}$$
$$P_4^S(k) = \left(\frac{8}{35}\beta^2\right) P^R(k)$$
$$P_l^S(k) = 0 \text{ for } l \neq 0,\ 2,\ \text{or } 4. \tag{1.61}$$

1.5.3 Anisotropic Clustering

In order to introduce the effects of redshift space distortions in the shape of the angular correlation function $\omega(\theta)$ we need to replace the spatial correlation function in equation (1.49) with the anisotropic two-dimensional correlation function, as we can relate it with the two-dimensional power spectrum in redshift space of the previous section[2]: $P(k, \mu)$. That is,

$$\omega(\theta) = \int\int dz_1 dz_2 \phi(z_1)\phi(z_2)\xi(s, \mu_{\mathbf{sl}}) \tag{1.62}$$

where $\mu_{\mathbf{sl}}$ is the cosine of the angle between the separation vector $\mathbf{s}$ and the line of sight $\mathbf{l}$, and it takes the form:

$$\mu_{\mathbf{sl}} = \frac{r(z_2) - r(z_1)}{s} \cos\left(\frac{\theta}{2}\right). \tag{1.63}$$

Following the same procedure as in the previous section, it is convenient to expand the two-dimensional spatial correlation function $\xi(s, \mu_{\mathbf{sl}})$ as

$$\xi(s, \mu_{\mathbf{sl}}) = \sum_{l \text{ even}} \xi_l(s) L_l(\mu_{\mathbf{sl}}). \tag{1.64}$$

Even though in theory this is an expansion over infinite even multipoles, just a few of them have a non-negligible contribution at large scales (see e.g. Sánchez et al. 2013a [162]), meaning that, in practice, most of the information is enclosed in the monopole and the quadrupole, and the multipoles of order $l \geq 4$ can be safely neglected. Then,

$$\xi(s, \mu_{\mathbf{sl}}) = \xi_0(s) + L_2(\mu_{\mathbf{sl}})\xi_2(s), \tag{1.65}$$

[2]To simplify notation, from now on, we use $P(k, \mu)$ for $P^S(k, \mu)$. We also apply this notation to other parameters in redshift-space.

where $\xi_0(s)$ and $\xi_2(s)$ are, respectively, the monopole and the quadrupole and $L_0(\mu_{\mathbf{sl}})$ has been replaced by 1. In order to obtain a description of these multipoles $\xi_l(s)$ it is convenient to work with the two-dimensional redshift space power spectrum, $P(k, \mu_{\mathbf{kl}})$. As we have seen in the previous section, this quantity can be decomposed in terms of Legendre polynomials (1.57) and, from its multipoles $P_l(k)$, we can obtain the multipoles $\xi_l(s)$ through

$$\xi_l(s) = i^l \frac{1}{2\pi^2} \int_0^\infty dk k^2 P_l(k) j_l(ks) \tag{1.66}$$

where $\xi_l(s)$ is the l-th order harmonic coefficient of the redshift space two-dimensional correlation function and $j_l(ks)$ is the spherical Bessel function of order l. The derivation of this identity can be found in Cole et al. 1993 [49].

1.6 Weak Gravitational Lensing

One of the predictions of Einstein's General Relativity is that light is deflected when it propagates through an inhomogeneous gravitational field. Images of distant objects are distorted by the intervening foreground matter distribution, inducing changes in shapes, apparent positions and fluxes of the background population. This effect is called *gravitational lensing* and it is a powerful probe of cosmology because it provides an invaluable way of probing mass distributions directly. This way we can directly compare observations with theoretical predictions without the need of understanding galaxy bias.

One of the most spectacular manifestations of gravity bending light paths is the so-called strong gravitational lensing. This regime corresponds to strongly non-linear perturbations produced by highly non-linear massive objects (e.g. clusters of galaxies), and can lead to multiple images of distant objects. In this case, the analysis of the distortion of images of background sources can be used to extract information on the properties of the foreground lens, such as its mass. The first observation of a multiply imaged quasar was achieved in 1979 by Walsh, Carswell, and Weymann [170]. Since then, dozens of multiply imaged quasars have been observed.

Alternatively, in the weak gravitational lensing regime, the distortions are small (of the order of 1%) and are not associated with a particular intervening lens, but rather by the generic large-scale structure in the universe. Then, one does not use gravitational lensing to obtain the characteristics of a single massive object but tries to derive the statistical properties of the density field, such as the correlation function or the power spectrum (see §1.5). In the following we will thus focus on

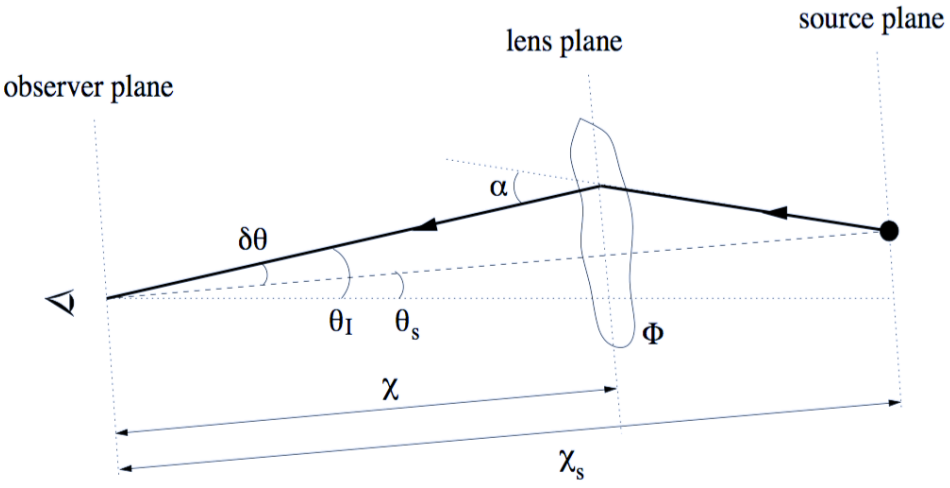

FIGURE 1.3: Sketch of the geometry of the gravitational lensing effect (from Munshi et al. 2008 [114]).

relating the distortion of galaxy images to the underlying mass power spectrum. For extensive reviews see [18, 82, 89, 114, 115, 140].

1.6.1 Deflection of Light Rays

A schematic picture of the light deflection due to gravitational lensing is shown in Fig. 1.3. As they travel from the source to the observer, photons get deflected an angle α by a gravitational potential fluctuation Φ. This changes the observed position of the source by the angle $\delta\theta$, from the intrinsic source direction θ_S to the image direction θ_I on the sky. The deflection angle, α is given by the line integral of the gravitational acceleration perpendicular to the path:

$$\alpha = -\frac{2}{c^2}\int \nabla_\perp \Phi(r')\,\mathrm{d}r'. \tag{1.67}$$

For small deflection angles, the phenomenon can be approximated to a single thin lens problem, and then from Fig. 1.3 we can see that $\delta\theta$ and α are related by the lens equation

$$\delta\boldsymbol{\theta} = -\frac{r_s - r}{r_s}\boldsymbol{\alpha}, \tag{1.68}$$

where $\delta\boldsymbol{\theta}$ and $\boldsymbol{\alpha}$ are vectors in the plane perpendicular to the unperturbed light ray, and r_s and r are the comoving radial distances to the source and the lens, respectively. Combining equations (1.67) and (1.68) we then have

$$\delta\boldsymbol{\theta} = \boldsymbol{\theta_I} - \boldsymbol{\theta_s} = \frac{2}{c^2}\int_0^{r_s} \mathrm{d}r \frac{r_s - r}{r_s}\nabla_\perp \Phi(r), \tag{1.69}$$

where $\boldsymbol{\theta_S}$ is the intrinsic position of the source on the sky and $\boldsymbol{\theta_I}$ is the observed position. It is useful to define the effective lensing potential as the projected Newtonian potential of the lenses

$$\Psi(\boldsymbol{\theta}, r_s) = \frac{2}{c^2}\int_0^{r_s} \mathrm{d}r \frac{r_s - r}{r_s\, r}\Phi(r, r\boldsymbol{\theta}), \tag{1.70}$$

since then the deflection angle reads

$$\alpha(r_s) = \nabla_{\boldsymbol{\theta}}\Psi(\boldsymbol{\theta}, r_s). \tag{1.71}$$

Equation (1.70) is valid for an extended three-dimensional distribution of matter, that is, it accounts for the distortions induced by all the lenses at any distance between the source and the observer. However, it assumes the Born approximation, in which integrals along the line-of-sight are computed along the unperturbed path. This is accurate in most cosmological situations, since the deflection angle is small, and we shall assume it hereafter.

If a source is much smaller than the angular scale on which the lens properties change, the lens mapping can locally be linearized. The distortion of images is then described by the amplification matrix A_{ij}, which is given by the Jacobian matrix of the transformation

$$A_{ij} \equiv \frac{\delta\boldsymbol{\theta_S}}{\delta\boldsymbol{\theta_I}} = \delta_{ij} - \partial_i\partial_j\Psi \equiv \begin{pmatrix} 1-\kappa-\gamma_1 & -\gamma_2 \\ -\gamma_2 & 1-\kappa+\gamma_1 \end{pmatrix}, \tag{1.72}$$

which defines the *convergence* κ and the *complex shear* $\gamma = \gamma_1 + i\gamma_2$. We are interested in the weak lensing limit, where $|\kappa|, |\gamma| \ll 1$. At linear order the convergence gives the magnification of the source as $\mu \simeq 1 + 2\kappa$. The shear is the quantity that is most easily determined from observations, and it is directly related to the ellipticity of the observed galaxy. From Eq.(1.72) the convergence κ and the shear components γ_1, γ_2 can be written at linear order in terms of the

second derivatives of the effective lensing potential

$$\begin{aligned} \kappa &= \frac{1}{2}\left(\Psi_{,11} + \Psi_{,22}\right) \\ \gamma_1 &= \frac{1}{2}\left(\Psi_{,11} - \Psi_{,22}\right), \quad \gamma_2 = \Psi_{,12} \end{aligned} \tag{1.73}$$

where the commas denote derivatives with respect to directions perpendicular to the line of sight.

1.6.2 Convergence and Shear Power Spectra

The gravitational potential, Φ, is related to the fluctuations of the density contrast, δ, by Poisson's equation,

$$\nabla^2\Phi = \frac{3\Omega_m H_0^2}{2a}\delta. \tag{1.74}$$

On the other hand, thanks to the radial integration over r in Eq.(1.70), gradients of the gravitational potential along the radial direction give a negligible contribution as compared with transverse fluctuations [84, 88, 101] since positive and negative fluctuations cancel along the line of sight. Since the convergence κ is related to the effective lensing potential Ψ via a 2D Laplacian (1.73), it can be expressed in terms of the 3D Laplacian (1.74) at each point along the line of sight. This yields for the converge

$$\kappa(\boldsymbol{\theta}, r_s) = \frac{3H_0^2\Omega_m}{2c^2}\int_0^{r_s} \mathrm{d}r\, \frac{r_s - r}{r_s}\frac{r}{a(r)}\delta(r, r\boldsymbol{\theta}). \tag{1.75}$$

Thus, the convergence can be expressed very simply in terms of the density field; it is merely an average of the local density contrast along the line of sight. Therefore, weak lensing observations allow us to measure the projected density field κ on the sky. The mean convergence from a population of source galaxies is obtained by weighting the above expression with the galaxy probability distribution in comoving distance, $\phi(r)\mathrm{d}r$. Interchanging the integral order results in the following expression,

$$\kappa(\boldsymbol{\theta}) = \frac{3H_0^2\Omega_m}{2c^2}\int_0^{r_{\rm lim}} \mathrm{d}r\, \frac{r}{a(r)}q(r)\delta(r, r\boldsymbol{\theta}), \tag{1.76}$$

$$q(r) = \int_r^{r_{\rm lim}} \mathrm{d}r_s\, \phi(r_s)\frac{r_s - r}{r_s}, \tag{1.77}$$

where we define q as the lens efficiency and $r_{\rm lim}$ is the limiting comoving distance of the galaxy sample. By construction, the expectation value of convergence and shear are zero, since

$\langle\delta\rangle = 0$. The first non-trivial statistical measure of the distribution of κ and γ are second moments. Similarly to what is shown in §1.5 for the density contrast, in real space the second-order function of the convergence is the two-point correlation function (2PCF) $\langle\kappa(\boldsymbol{\vartheta})\kappa(\boldsymbol{\vartheta}+\boldsymbol{\theta})\rangle$. The brackets denote ensemble average, which can be replaced by a spatial average over angular positions $\boldsymbol{\vartheta}$. Expressed in Fourier space, the 2PCF defines the convergence power spectrum P_κ with

$$\langle\kappa(\boldsymbol{\ell})\kappa(\boldsymbol{\ell}')\rangle = (2\pi)^2\,\delta_{\rm D}(\boldsymbol{\ell}-\boldsymbol{\ell}')P_\kappa(\ell). \tag{1.78}$$

In this equation we used a flat-sky approximation, which is sufficient for most weak lensing purposes. For lensing on very large scales, and for 3D lensing, the curvature has to be accounted for by more accurate expressions [103], or by applying spherical harmonics instead of Fourier transforms. Taking the square of (1.75) in Fourier space, we obtain the 2D convergence power spectrum in terms of the 3D matter power spectrum $P(k,r)$ integrated along the line of sight,

$$P_\kappa(\ell) = \frac{9\Omega_m H_0^4}{4c^2}\int_0^{r_{\rm lim}} {\rm d}r\,\frac{q^2(r)}{a^2(r)}P\left(k=\frac{\ell}{r},r\right). \tag{1.79}$$

In addition to the small-angle approximation and the flat-sky limit, here we have used Limber's approximation, which only collects modes that lie in the plane of the sky, thereby neglecting correlations along the line of sight [88, 100].

We can obtain the power spectrum of the shear from the convergence one from the relations between κ, γ and the lensing potential (1.73). Writing Eq.(1.73) in Fourier space, and using complex notation for the shear, one finds

$$\gamma(\boldsymbol{\ell}) = \frac{(\ell_1+i\ell_2)^2}{\ell^2}\kappa(\boldsymbol{\ell}) = {\rm e}^{2i\beta}\kappa(\boldsymbol{\ell}), \tag{1.80}$$

with β being the polar angle of the wave-vector $\boldsymbol{\ell} = (\ell_1, \ell_2)$, written as complex quantity. Therefore we get that the power spectrum of the shear equals the one of the convergence, $P_\gamma = P_\kappa$. The shear power spectrum can in principle be obtained directly from observed ellipticities (see e.g. Hu & White 2001 [80]). However, the simplest way to estimate second-order shear correlations are in real space, which we will discuss in the following section.

1.6.3 Shear Correlation Function

The advantage of the shear two-point correlation function over its Fourier transform, shown in the previous section, is that it can be estimated by simply multiplying the ellipticities of galaxy

pairs and averaging. For weak gravitational lensing, these estimates are very noisy, since the galaxies as a population have intrinsic ellipticities with a dispersion of about 0.4, whereas the typical cosmic shear is around 0.01. Therefore, one needs a large number of galaxies to decrease the noise associated with this intrinsic ellipticities.

The shear of each galaxy can be decomposed into two components: the *tangential shear*, γ_t, and the cross-component, $\gamma_\times$. With respect to a given direction vector $\boldsymbol{\theta}$ whose polar angle is β, they are defined as

$$\gamma_t = -\,\mathrm{Re}\left(\gamma e^{-2i\beta}\right) \tag{1.81}$$

$$\gamma_\times = -\,\mathrm{Im}\left(\gamma e^{-2i\beta}\right). \tag{1.82}$$

The minus sign is a convention in order to have a positive value of γ_t for the tangential alignment around a mass overdensity. Radial alignment around underdensities have a negative γ_t. Three two-point correlators can be formed from the shear components: $\langle\gamma_t\gamma_t\rangle$, $\langle\gamma_\times\gamma_\times\rangle$, and $\langle\gamma_t\gamma_\times\rangle$. The latter vanishes in a parity-symmetric universe, and the other two are combined into the two components of the shear two-point correlation function [111],

$$\xi_+(\theta) = \langle\gamma\gamma^*\rangle(\theta) = \langle\gamma_t\gamma_t\rangle(\theta) + \langle\gamma_\times\gamma_\times\rangle(\theta) \tag{1.83}$$

$$\xi_-(\theta) = \mathrm{Re}\left[\langle\gamma\gamma\rangle(\theta)e^{-4i\beta}\right] = \langle\gamma_t\gamma_t\rangle(\theta) - \langle\gamma_\times\gamma_\times\rangle(\theta. \tag{1.84}$$

From the equality of the shear and convergence power spectrum it follows that ξ_+ is identical to the two-point correlation function of the convergence, κ. Using equations (1.78) and (1.80), we can write the shear 2PCF as Hankel transforms of the convergence power spectrum,

$$\xi_+(\theta) = \frac{1}{2\pi}\int \mathrm{d}\ell\,\ell\, j_0(\ell\theta)P_\kappa(\ell) \tag{1.85}$$

$$\xi_-(\theta) = \frac{1}{2\pi}\int \mathrm{d}\ell\,\ell\, j_4(\ell\theta)P_\kappa(\ell), \tag{1.86}$$

where $j_{0,4}$ are spherical Bessel functions of order 0 and 4, respectively.

1.7 Cosmic Microwave Background

1.7.1 Introduction

At early times photons and baryons were highly coupled by Thomson scattering. There were two opposing forces in action, gravity against pressure, as depicted in (1.31). Overdense regions tend to be compressed by gravity. However, the compression of the region caused its temperature to rise, and hence increase its pressure. Since dark matter is also affected by gravity, it fell onto the perturbation overdensities. The effect of these forces generated the so-called acoustic waves in the baryon-photon fluid. The Universe was effectively opaque, since the mean free path of photons was very short. Since the Universe at that time was already expanding, there was a moment in which it cooled down enough for the photons to decouple from matter; thus making the Universe transparent. The photons from the plasma were then free to propagate through the Universe, generating the radiation that we see now in all directions of the sky, and that we call the *cosmic microwave background* (CMB). In this manner, the photons of the CMB picture the photon-baryon fluid at the *last scattering surface*.

The CMB was first detected by Penzias and Wilson in 1965 [125], when they detected an excess of temperature of about 3.5 K after accounting for all possible noise contributions in their observations. But it was not until 1992 that an experiment on the COBE satellite [158] confirmed the black-body spectrum of the CMB and determined the (isotropic) temperature to be 2.725 K [108, 109]. Even if the agreement with a black-body spectrum is extremely high, the CMB is not isotropic. If we look at different points in the sky we observe anisotropies giving slightly different temperatures for the photons in those regions, at the order of 1 part in 10^5. These anisotropies were originated by the acoustic oscillations in the primordial baryon-photon fluid, which eventually generated the large-scale structure distribution we observe today. Therefore, there is a lot of cosmological information imprinted in them and, more importantly, from the observations of these anisotropies we can extract cosmological information from the early Universe, which is complementary to the information we can extract from low-redshift probes (such as galaxy clustering and cosmic shear, described in the previous sections).

While COBE first detected anisotropies on the largest scales, there are now convincing and very precise measurements from space (e.g. WMAP [22], Planck [131, 132, 134]) and ground-based telescopes (e.g. the Atacama Cosmology Telescope [ACT, 55], the South Pole Telescope [SPT, 161]), and many future observations are planned at even greater resolution and/or sensitivity, such as the Simons Observatory [SO, 8]. The standard approach used when analyzing these

anisotropies consists in decomposing them in spherical harmonics, $Y_{\ell m}(\theta, \phi)$,

$$\frac{\Delta T(\theta, \phi)}{T_0} = \sum_{\ell=0}^{\infty} \sum_{m=-\ell}^{m=\ell} a_{\ell m} Y_{\ell m}(\theta, \phi). \tag{1.87}$$

And then from these $a_{\ell m}$ coefficients we can obtain the temperature angular power spectrum,

$$C_\ell = \frac{1}{2\ell + 1} \sum_{m=-\ell}^{\ell} |a_{\ell m}|^2 , \tag{1.88}$$

which is the primary observable for the CMB anisotropies. This statistical treatment is very similar to that of density fluctuations.

1.7.2 CMB lensing

Besides the temperature power spectrum we can also obtain cosmological information from the CMB polarization power spectrum and the CMB lensing; that is, the weak gravitational lensing of the CMB photons by the inhomogeneous matter distribution between us and the last scattering surface [97]. In order to analyze the CMB lensing signal we use the convergence angular power spectrum defined in §1.6.2, which is given by Eq.(1.79). The difference with respect to the convergence power spectrum of background (source) galaxies is that here the source is located at the last scattering surface (at $z \simeq 1090$). For more extensive reviews see [45, 60, 78, 79, 99, 148].

The effect of lensing is to remap the CMB fluctuations, so that the observed anisotropy in the direction $\hat{\boldsymbol{n}}$ is in fact the unlensed "primordial" anisotropy in the direction $\hat{\boldsymbol{n}} + \nabla\phi(\hat{\boldsymbol{n}})$, where $\phi(\hat{\boldsymbol{n}})$ is the CMB lensing potential. The lens-induced remapping imprints distinctive statistical signatures onto the observed CMB fluctuations, which can be used to extract cosmological information in a process known as lens reconstruction [117].

Quadratic combinations of the CMB fields can be used to form estimators of the projected gravitational potential, and therefore of the projected mass [72, 175]. Neglecting the lensing of primordial B-modes there are five possible estimators, denoted by $\hat{\phi}^{TT}$, $\hat{\phi}^{TE}$, $\hat{\phi}^{EE}$, $\hat{\phi}^{EB}$, and $\hat{\phi}^{TB}$, which are based on various correlations of the CMB temperature (T) and polarization (E and B). In addition, we can form a minimum-variance estimator, $\hat{\phi}^{MV}$, that combines all five estimators. In Fig. 1.4 we show as an example the lens reconstruction noise levels for these estimators from Planck 2015 [132]. The most powerful estimator is TT, although TE and EE estimators are also useful on large angular scales.

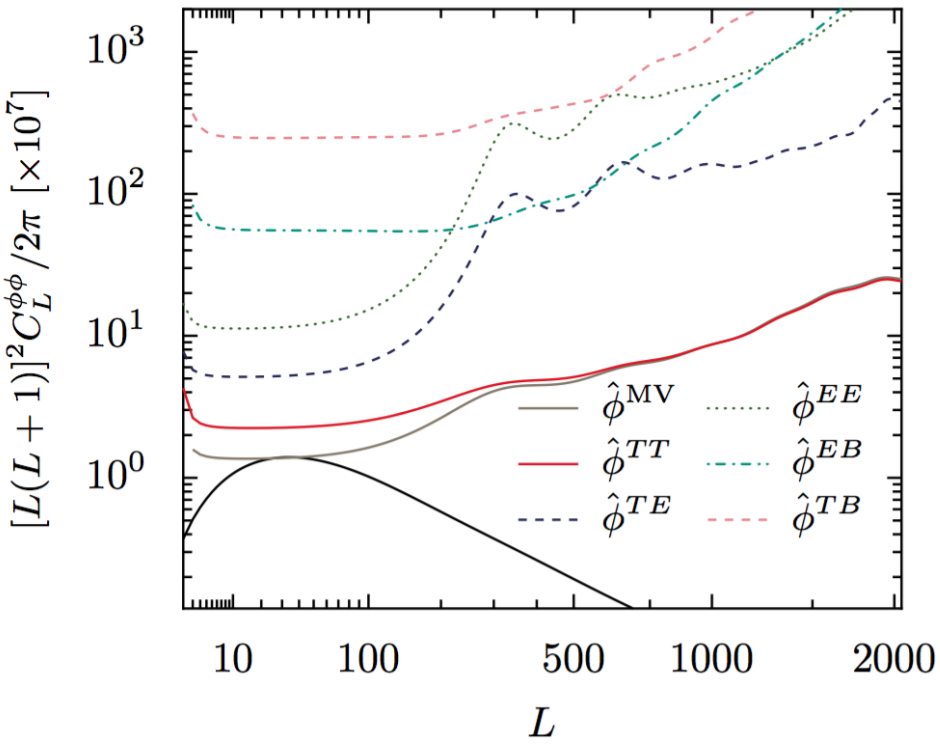

FIGURE 1.4: Lens reconstruction noise levels for the TT, TE, EE, EB, and TB estimators from Planck [132]. The noise level for their minimum-variance combination (MV) is shown in grey, while the fiducial theory CMB lensing power spectrum is shown in solid black.

The quadratic lensing estimators take inverse-variance filtered CMB multipoles as input, that are obtained using a filter that masks the Galaxy and point sources, including the brightest Sunyaev-Zel'dovich (SZ) clusters. After all the masks are applied, and the signal coming from systematics is corrected, we can estimate the power spectrum of the lensing potential using the auto- and cross-spectra of the quadratic lensing estimators. These spectra probe the 4-point function of the lensed CMB. Then, we can estimate the contribution to the 4-point function that is not sourced by lensing and subtract it, obtaining an estimate of the CMB lensing power spectrum.

Chapter 2

The Dark Energy Survey

As we have seen in Chapter 1, there is wealth of cosmological information that we can extract from galaxy clustering and cosmic shear and, in order to do so, we use 2-point statistics, either in real or Fourier space. Thus, we need large samples of galaxies in order to have precise measurements of the cosmological parameters. Over the past two decades, large galaxy surveys such as the Automatic Plate Measuring Survey [APM, 106], the 2dF Galaxy Redshift Survey [2dFGRS, 50], the Sloan Digital Sky Survey [SDSS, 172], the WiggleZ Dark Energy Survey [31] and the Baryon Oscillation Spectroscopic Survey [BOSS, 56] have enabled to study in detail the large-scale structure of the Universe, and galaxy clustering has become a powerful tool to study galaxy formation and evolution and to tighten constraints on cosmological parameters. In this chapter we focus our attention to describe the Dark Energy Survey [DES, 164], which is the main source of data used in this work.

2.1 Photometric Surveys

There are two ways of measuring redshifts: spectroscopy and photometry. The former consists in measuring the spectrum of light from the source and compare the observed wavelengths of spectral features to their respective rest frame values to obtain the redshift through its definition, $z \equiv (\lambda_{\rm obs} - \lambda_{\rm rest})/\lambda_{\rm rest}$. Some examples of spectral features commonly used are the H_α emission line at 6563 Å and the 4000 Å break, caused by a confluence of absorption lines. Unfortunately, even though the spectroscopic technique allows to measure redshifts with high accuracy, obtaining spectroscopic redshifts for all galaxies is typically impossible in wide-field imaging surveys due

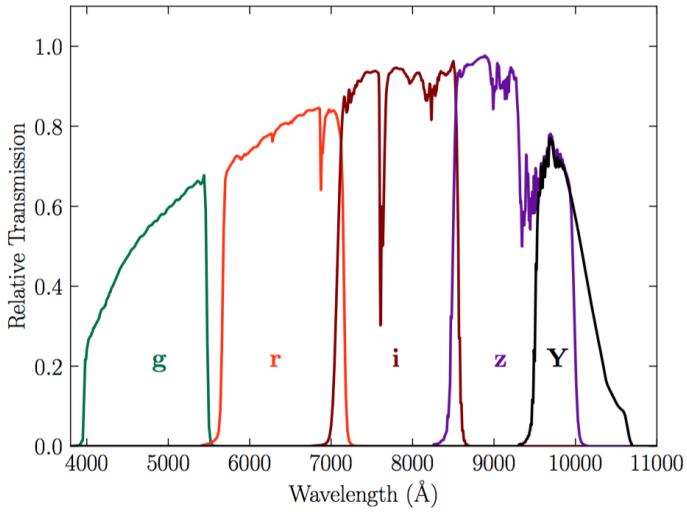

FIGURE 2.1: DES standard band-passes for the DECam *grizY* filters [4]. The band-passes represent the total system throughput, including atmospheric transmission and the average instrumental response across the science CCDs.

to the large number ($\sim 10^8 - 10^9$) of galaxies and the high cost of spectroscopy, especially for the high-redshift galaxies.

To circumvent this problem, the current approach in the community is to estimate redshifts using photometric measurements, i.e. fluxes from a few broad-band filters. Each of these filters has a transmission function $T_i(\lambda)$ associated to them, which determines the fraction of photons of a given wavelength that passes through the filter. By definition, $T_i(\lambda)$ always has values between 0 and 1, being 0 when the filter is opaque and 1 when the filter is transparent to that wavelength. Given an object with specific flux F_λ, and a filter with relative transmission $T_i(\lambda)$, the flux through that filter would be,

$$F_i = \int \mathrm{d}\lambda \, T_i(\lambda) F_\lambda. \tag{2.1}$$

In Fig. 2.1 we show as an example the relative transmission of the broad-band filters used in DES. Because of the low-resolution spectra measured with these broad-band filters, the photometric redshifts (hereafter photo-zs) cannot be inferred from a spectral feature, and are necessarily less accurate than spectroscopic redshifts. For this reason, the photo-z error distributions need to be quantified precisely in order to be able to use the photometric redshifts for the cosmological analysis. The standard approach to quantify, or calibrate, the photo-z error distributions is to use a small subsample of galaxies with accurately known redshifts. There are two main methods to

estimate the photometric redshifts: template-based and training-based.

The template-based technique uses a set of spectral energy distribution (SED) templates from real data or from theoretical models. Since the specific flux F_λ of these templates is known, we can then integrate them using the transmission functions of our filters (2.1) while redshifting the templates. This provides us with a set of fluxes for each band that depend on the redshift. We then compare our fluxes with the redshifted ones from the templates and look for the redshift that minimizes the differences.

In the other method, training-based, we start with a set of objects, a training sample, for which we have both photometry and spectroscopy. The technique consists in using this training sample to derive a relationship between redshift and fluxes, and then apply this function to all the objects for which we do not have spectroscopy. The standard approach to find this relationship is using machine-learning techniques, such as neural networks or random forests. See [73, 146] for several examples of template and training-based techniques.

2.2 Survey Specifications

2.2.1 Overview

DES is an imaging survey of 5000 deg^2 of the Southern sky, using a 570 megapixel camera on the Cerro Tololo Inter-American Observatory (CTIO) 4 m Blanco telescope in Chile. Photometric redshifts are obtained from the multi-band photometry to produce a quasi three-dimensional survey. The main goal of DES is to determine the dark energy equation of state parameter w (1.12) and other key cosmological parameters. DES will measure w using complementary techniques in a single survey: counts of galaxy clusters, weak gravitational lensing, galaxy clustering and Type Ia supernovae. DES is expected to catalog 300 million galaxies with photometric redshifts; 200 million of them will have shape measurements for weak lensing. It is expected that the uncertainty on w will be only a few percent for each probe. See [164] for detailed parameterizations and statistics.

DES is an international collaboration, with over 400 scientists from the US, the UK, Spain, Brazil, Germany, Switzerland and Australia. The DES Science is coordinated by a Science Committee comprised of thirteen Science Working Groups (SWGs). The first light of DES was obtained in September 2012, followed by commissioning of the Dark Energy Camera (DECam)

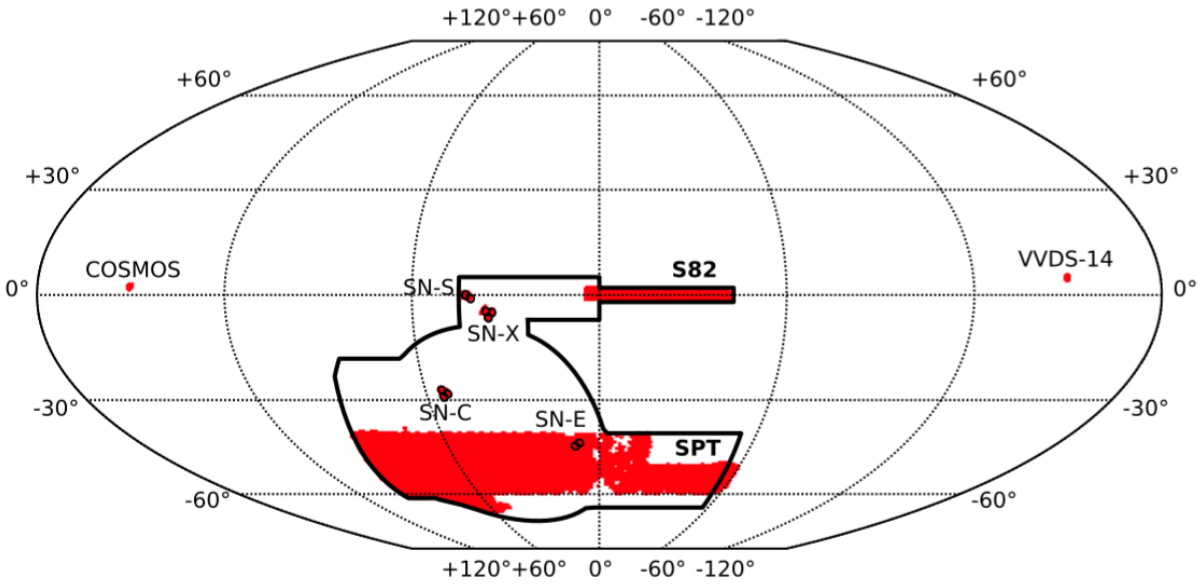

FIGURE 2.2: Image of the DES survey area in celestial coordinates, from [61]. The sky coverage in the first year of observations is shown in red. The ~ 5000 deg^2 wide-area survey footprint is outlined in black. The circles outlined in black represent the supernova fields, and the regions overlapping with Stripe 82 (S82) and SPT are also labeled.

[65]. Science verification (SV) observations took place from November 2012 to February 2013, and Year 1 observations were taken from August 2013 to February 2014. In this work we use data from the first year of observations (Y1) and from the first three years of observations (Y3 hereafter), which were taken from August 2013 to February 2016, see §2.3 for an overview of the characteristics of these datasets.

2.2.2 DECam and Observation Strategy

In this section we briefly describe the characteristics of the DECam instrument and the DES observation strategy. DECam is a wide-field-of-view (3 deg^2) mosaic camera containing 62 science CCDs [65]. The DES wide-area survey observes five broadband filters, *grizY*, which are very similar to their analogously named counterparts from other surveys. In Fig.2.1 we show the relative transmission functions of these filters. Additional details, including construction, installation, and a description of DECam subsystems and interfaces are provided in Flaugher et al. 2015 [65].

The DES footprint is shown in Fig.2.2. The wide-area footprint shape was selected to obtain a large overlap with the South Pole Telescope (SPT) survey [41] and Stripe 82 from SDSS [1], and includes a connection region to enhance overall calibration. Given the cosmological goals of the survey, DES avoids the Galactic plane to minimize stellar foregrounds and extinction from interstellar dust.

2.3 Data

In this section we briefly describe the two DES data sets considered in this work. Those are, the Y1 catalog, generated from the first year of observations, and the Y3 catalog, created from the first three years of observations.

2.3.1 Year 1

Here we describe the catalog used for the cosmological analysis of the first year of observations, the so-called Y1 'Gold' catalog, and the galaxy sample used for this work. The Y1 Gold data set is assembled from multiple epochs of DES imaging and it contains $\sim$ 137 million objects detected in coadded images covering 1800 deg^2 in the DES *grizY* filters. The sky coverage in Y1 is about 40% of the total DES footprint, averaging three to four visits per band. The Y1 footprint consists of two areas: one near the celestial equator including Stripe 82, and a much larger area that was also observed by SPT (see red region in Fig.2.2). After masking for bright stars and other poor-quality regions, including the Large Magellanic Cloud, the total area covered is reduced to $\sim$ 1500 deg^2. The limiting magnitude for galaxies at a signal-to-noise ratio of S/N= 10 is $g = 23.4$, $r = 23.2$, $i = 22.5$, $z = 21.8$, and $Y = 20.1$. See [61] for an extensive description of the Y1 Gold catalog.

In this work we use Y1 data for galaxy clustering measurements, i.e. for measuring the angular correlation function $\omega(\theta)$. The galaxy sample that we use here is the lens sample used for the joint analysis of galaxy clustering and cosmic shear in DES [2]. This sample consists of redMaGiC galaxies, which have the advantage of being easily identifiable, relatively strong clustered, and of having relatively small photo-z errors ($\sigma_z/(1+z) < 0.02$ over the redshift range of interest). They are selected using a simple algorithm described in [143] that consists in the following:

1. Fit *every* galaxy in the survey to a red-sequence template and compute the corresponding

Luminosity	Redshift range	$N_{\rm gal}$
$L > 0.5L_*$	0.15 – 0.30	63,719
$L > 0.5L_*$	0.30 – 0.45	163,446
$L > 0.5L_*$	0.45 – 0.60	240,727
$L > 1.0L_*$	0.60 – 0.75	143,524
$L > 1.5L_*$	0.75 – 0.90	42,275
Total	0.15 – 0.90	653,691

Table 2.1: Summary statistics of the DES red-sequence galaxy samples (redMaGiC) from Y1 data. The effective sky area covered by these samples is 1321 deg^2.

best-fit redshift $z_{\rm red}$.

2. Evaluate the goodness-of-fit χ^2 of the red-sequence template and the galaxy luminosity, using the assigned photometric redshift.

3. Include the galaxy in the redMaGiC catalog only if it is bright and the red-sequence template is a good fit; that is, if the luminosity of the galaxy is above a certain threshold ($L \geq L_{\rm min}$) and $\chi^2 \leq \chi^2_{\rm max}$.

The red-sequence template used in redMaGiC was generated by the training of the redMaPPer cluster finder [144, 145]. As described in [145], training of this red-sequence template requires overlapping spectroscopic, which in this work were obtained from SDSS in the Stripe 82 and the DES deep supernova fields [174]. In practice, we do not specify $\chi^2_{\rm max}$ but instead demand that the resulting galaxy sample has a constant comoving density as a function of redshift. Consequently, redMaGiC galaxy selection depends upon only two parameters: the luminosity threshold, $L_{\rm min}$, and the comoving density, $\bar{n}$, of the sample. Reference luminosities are defined as a function of L_*, computed using a Bruzual and Charlot [36] model for a single star-formation burst at $z = 3$, see §3.2 of [145]. Naturally, increasing the luminosity threshold provides a higher redshift sample as well as decreasing the comoving number density.

Three separate redMaGiC samples were generated from the Y1 data, referred to as the high-density, high-luminosity, and higher-luminosity samples. The corresponding luminosity thresholds and comoving densities for these samples are, respectively, $L_{\rm min} = 0.5L_*$, $1.0L_*$, and $1.5L_*$, and $\bar{n} = 10^{-3}, 4 \times 10^{-4}$, and 10^{-4} galaxies/$(h^{-1}\ {\rm Mpc})^3$, where h is the reduced Hubble constant. These galaxies are placed in five disjoint redshift bins of width $\Delta z = 0.15$ from $z = 0.15$ to $z = 0.9$. The lowest three bins are high-density, while the galaxies in the two highest redshift bins are high-luminosity and higher-luminosity, respectively.

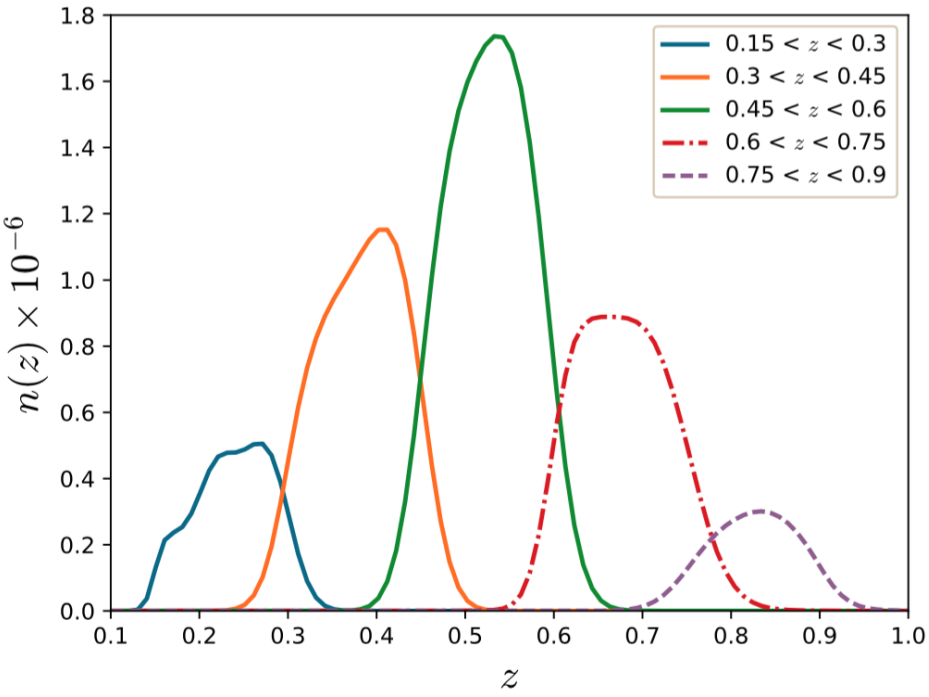

FIGURE 2.3: Redshift distribution of the combined REDMAGIC sample in 5 redshift bins, obtained from stacking Gaussian PDFs with mean and standard deviation given by the REDMAGIC algorithm [62].

The REDMAGIC algorithm produces a best-fit redshift $z_{\rm red}$ and an uncertainty σ_z. We assume that the redshift probability distribution function (PDF) for each galaxy is given by a Gaussian distribution with mean $z_{\rm red}$ and standard deviation σ_z. We then obtain an overall estimate of the redshift distributions of the samples by stacking these Gaussian PDFs. The details of these bins are given in Table 2.1 and their estimated redshift distributions are shown in Fig.2.3. The number of objects in each bin increases up to $z = 0.6$ due to the increase in volume, and decreases at higher redshift due to the increased luminosity threshold. The clustering properties of these galaxies are essential for the analysis of the galaxy clustering, that we use in this work. Thus, we need to ensure that the galaxy maps are not contaminated by systematic effects, as that could affect our clustering measurements. This requires the shallowest or otherwise irregular or patchy regions of the total $\sim 1800\,{\rm deg}^2$ Y1 area to be masked, leaving a contiguous $1321\,{\rm deg}^2$ as the area for the analysis. See [62] for a detailed description of the clustering properties of the sample and its calibration, masking and correction of systematic effects.

2.3.2 Year 3

Here we briefly describe the catalog that will be used for the cosmological analysis of the first three years of observations, the Y3 'Gold' catalog, and the galaxy samples used for this work. This catalog will be described more extensively in [150, in prep.] and it is largely based on the raw coadded catalog from the first three years of data (Y3) that was released publicly as the DES Data Release 1 (DR1)[1]. The DES DR1 is the first DES catalog that spans the whole footprint ($\sim$ 5000 deg^2, see Fig.2.2), and it is described in [4], alongside with the details of the Data Management pipeline in [112] and photometric calibrations in [37]. The Y3 Gold catalog contains $\sim$ 388 million objects detected in coadded images covering $\sim$ 5000 deg^2 in the DES *grizY* filters. The area has increased almost a factor 3 in *griz* with respect to the Y1 Gold catalog.

We will use two different lens samples for the Y3 joint analysis of galaxy clustering and galaxy-galaxy lensing. The first one is a sample generated using the REDMAGIC algorithm, which is designed to find red-sequence galaxies in photometric data. This is the method that was used for the Y1 analysis and has the advantage of producing galaxy samples with a small photometric uncertainty. The second one, the *magnitude limited sample*, is a sample defined with a magnitude cut in the *i* band depending linearly with the photometric redshift. In this way, this magnitude limited sample reaches higher number density and higher redshift than the REDMAGIC sample, with the caveat of slightly larger photometric uncertainties. Another advantage of the magnitude limited sample is that its selection is much simpler than with the REDMAGIC sample, hence we expect simpler modeling of nuisance parameters (e.g. galaxy bias) and covariance associated to the sample.

In the following, we will describe the characteristics of these samples. Note that the Y3 analysis is still ongoing, and the details of these samples may vary when the analysis is complete. Here we just present their approximate specifications, which will be the baseline of the forecasts presented in this work.

REDMAGIC sample

Similarly to Y1 (§2.3.1), three separate REDMAGIC samples are generated from Y3 data: high-density (HD), high-luminosity (HL) and higher-luminosity (HL+) samples. The corresponding thresholds and comoving densities are the same as in Y1. There are two differences in the Y3

[1] Available at https://des.ncsa.illinois.edu/releases/dr1

	redMaGiC		Magnitude limited	
Luminosity	Redshift range	$N_{\rm gal}$	Redshift range	$N_{\rm gal}$
$L > 0.5L_*$	0.15 – 0.35	341,602	0.20 – 0.35	1,680,160
$L > 0.5L_*$	0.35 – 0.50	589,562	0.35 – 0.50	1,678,655
$L > 0.5L_*$	0.50 – 0.65	877,267	0.50 – 0.65	1,460,354
$L > 1.0L_*$	0.65 – 0.85	679,291	0.65 – 0.80	1,975,242
$L > 1.0L_*$	0.85 – 0.95	418,986	0.80 – 0.95	2,374,205
			0.95 – 1.05	1,470,893
Total	0.15 – 0.95	2,906,708	0.20 – 1.05	10,639,509

Table 2.2: Summary statistics of the DES red-sequence redMaGiC galaxy sample (left) and the magnitude limited sample (right) from Y3 data. The effective sky area covered by these samples is 4182 deg^2.

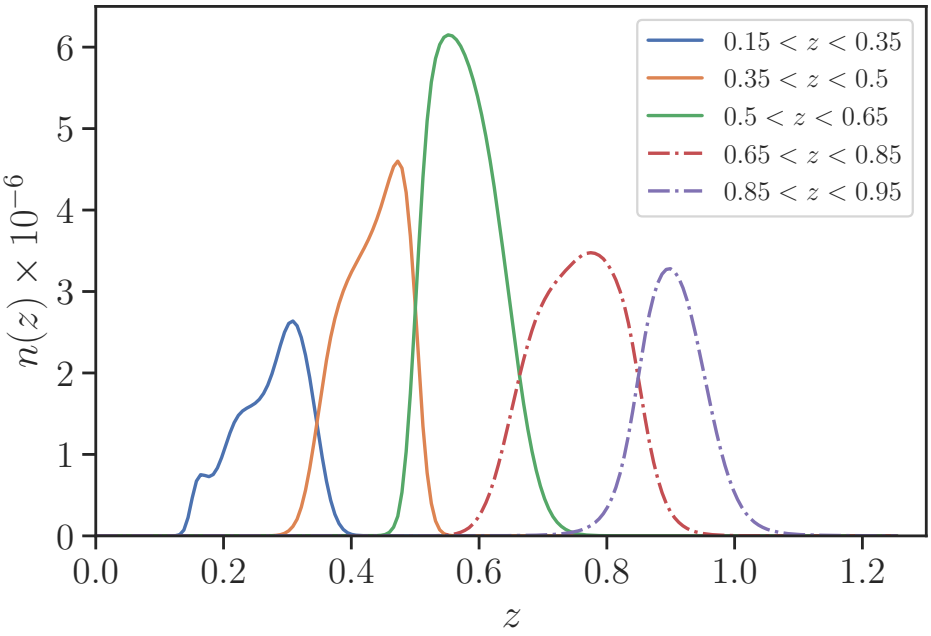

Figure 2.4: Redshift distribution of the combined Y3 redMaGiC sample in 5 redshift bins, obtained from stacking Gaussian PDFs with mean and standard deviation given by the redMaGiC algorithm.

data version of these samples. First, the HL and HL+ samples reach higher redshift than in Y1 ($z_{\rm max} = 0.95$ instead of $z_{\rm max} = 0.9$). Second, HL has a higher number of galaxies than HL+ across the whole redshift range. Thus, the combined Y3 redMaGiC is comprised by three HD redshift bins at low redshift, and two HL redshift bins at higher z. Therefore, we use HL for the last redshift bin instead of HL+, which was used for the Y1 analysis. The details of these are given in Table 2.2 (left), and their estimated redshift distributions are shown in Fig.2.4. The

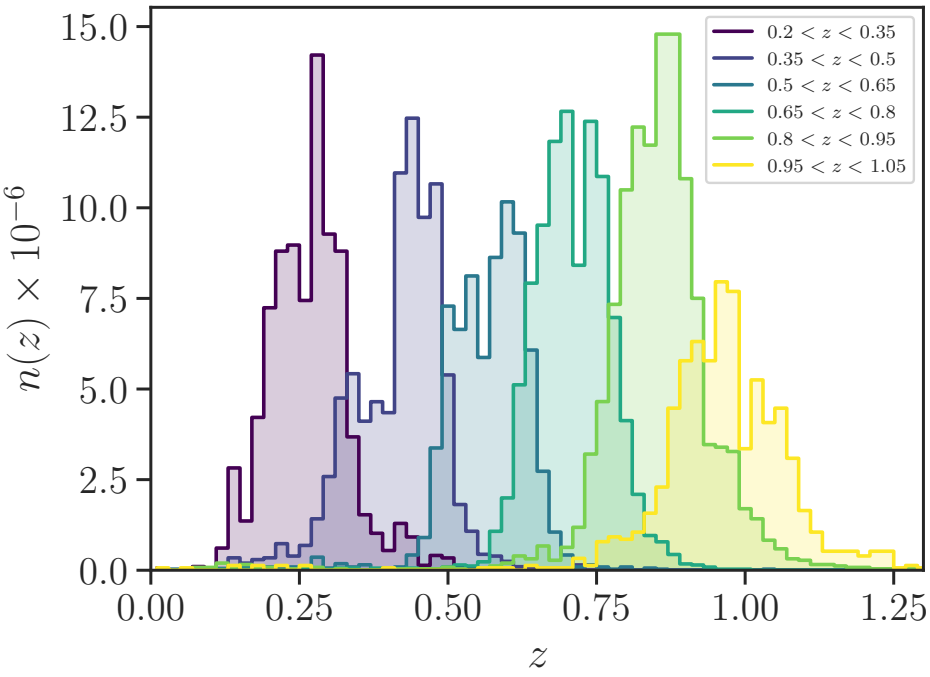

FIGURE 2.5: Redshift distributions of the DES Y3 magnitude limited sample in 6 redshift bins, obtained from the photo-z validation with VIPERS spectroscopic galaxies.

redshift distributions have been estimated by stacking Gaussian PDFs, similarly to Y1. After masking the shallowest or otherwise irregular or patchy regions of the total $\sim$ 5000 deg^2 Y3 area, a contiguous 4182 deg^2 area remains for the analysis. The correction of observational systematics and the galaxy clustering measurements for this and the magnitude limited sample will be presented in [141, in prep.].

Magnitude limited sample

This is a flux limited sample that has a magnitude cut on the i band depending linearly with the photometric redshift, and a lower cut to remove the most luminous objects. We select the galaxies applying these two cuts on the i band magnitude,

$$\begin{aligned} i &< 4z + 18, \\ i &> 17.5, \end{aligned} \tag{2.2}$$

and then we bin the sample in 6 tomographic z bins, from $z = 0.2$ to $z = 1.05$. The details of these are given in Table 2.2 (right), and their estimated redshift distributions are shown in Fig.2.5. The sample is complete in regions of the survey deeper than $i = 22.2$ magnitudes. Therefore, we will only consider such regions as our baseline footprint. Since we want to compare the cosmological constraints obtained from this sample with the REDMAGIC sample, we combine the masks of these two samples, resulting in a unique mask that is applied to both, with an effective area of 4182 deg^2.

The photometric redshifts used for redshift binning and galaxy selection (2.2) are derived using the Directional Neighborhood Fitting (DNF) algorithm [58], which is trained with public spectroscopic samples. We use the predicted value in the fitted hyper-plane from the DNF code as our point estimate for galaxy redshifts (photo-zs). As for the estimates of the redshift distribution of galaxies in each redshift bin (Fig.2.5), we use the stacking of counts of the nearest neighborhood redshifts from the VIPERS spectroscopic sample [147], which spans 24 deg^2 to $i < 22.5$. After correcting VIPERS for target, color, and spectroscopic incompleteness we select galaxies in a similar way as done with the data from the Gold catalog. We then use the VIPERS redshifts to estimate the true redshift distributions $n(z)$ of the magnitude limited sample.

Chapter 3

Joint Analysis of Galaxy Clustering and CMB lensing

As we have seen in §1.7, photons from the CMB are gravitationally deflected by the large-scale structure, and the distinct pattern of the lensed CMB can be used to probe lensing structures along the line of sight. By cross-correlating the CMB lensing signal with tracers of the matter distribution, such as galaxies, we can measure the growth of structure in the Universe across cosmic time. This is the motivation behind the work described in this chapter. We obtain constraints on the galaxy bias, the lensing amplitude (an overall multiplicative bias in the CMB lensing map), the growth function and the cosmological parameters from the joint analysis of galaxy clustering from DES Y1 data and CMB lensing from SPT and Planck.

3.1 CMB Data

3.1.1 SPT

The South Pole Telescope (SPT) [41] is a 10-meter telescope located at the National Science Foundation Amundsen-Scott South Pole Station in Antarctica. From 2008 to 2011, the telescope was used to conduct the SPT-SZ survey, a survey spanning a contiguous area of approximately 2500 deg^2 [161]. The survey footprint extends from 20^{h} to 7^{h} in right ascension (R.A.) and from -65° to -40° in declination. The total area was observed at three frequency bands centered at

roughly 95, 150, and 220 GHz. For this analysis, we will exclusively use the 150 GHz data, whose beam has a shape similar to a Gaussian with a full-width at half maximum (FWHM) of 1.2′. The typical noise level of SPT-SZ maps at 150 GHz is 18 μK-arcmin, with small variations across the footprint.

3.1.2 Planck

The Planck satellite, launched in 2009 by the European Space Agency [129], was used to observe the sky in nine frequency bands from 30 to 857 GHz. It achieved better resolution, higher sensitivity, and a wider range of frequencies than its predecessor, WMAP. In this work, we use the publicly available Planck 143 GHz map and beam provided in the 2015 data release [130], as the 143 GHz frequency band is closest to the SPT-SZ 150 GHz band. The 143 GHz beam can be approximated by a Gaussian beam with FWHM of $\sim$ 7 arcmin, and the instrument noise level is $\sim$ 30 μK-arcmin [130].

3.2 Context

The deflection of the paths of the CMB photons produced by gravitational lensing, on the order of a few arcminutes [48], alter the CMB primary anisotropies by redistributing power across different angular scales and producing a non-Gaussian component to the primordial distribution of temperature anisotropies. Measurement of this non-Gaussian structure can be used to infer the total amount of deflection that has occurred in a given direction [75, 117]. High signal-to-noise measurements of CMB lensing have been obtained by several collaborations, including the Atacama Cosmology Telescope [ACT, 55, 152], Planck [131, 132, 135], POLARBEAR [9], and the South Pole Telescope [SPT, 119, 160, 168].

The reconstructed CMB lensing signal is an integral of all deflections sourced by the large-scale structure between the last-scattering surface and us. Due to this projection, we cannot directly measure the evolution of structure along the line of sight by analyzing the lensing signal alone. However, the signal from CMB lensing can be cross-correlated with tracers of the matter distribution, such as galaxy catalogs with known redshifts. This allows us to measure the growth of structure in the Universe across cosmic time.

Galaxy density-CMB lensing cross-correlations have been detected by several groups, using a

variety of data sets. The first significant detection was reported by [156] correlating WMAP data with radio galaxies from NVSS[1] [51], which was later combined with other galaxy catalogs by [74]. After that, several galaxy-CMB lensing cross-correlation measurements with optical, infrared and radio galaxies have been carried out in the last few years [10, 13, 26, 27, 33, 59, 92, 120, 153, 154]. The first *tomographic* cross-correlation analysis using multiple redshift bins from a single galaxy survey was carried out by ([70] , hereafter G16) using CMB lensing data from SPT and Planck and the Dark Energy Survey (DES) Science Verification (SV) galaxies.

In this work, we update the results of G16 by measuring the cross-correlations between galaxy density from the DES Year-1 (Y1) data and a CMB lensing reconstruction using a combination of SPT and Planck data in the SPT-SZ survey area.[2] The total area used in this work is nearly a factor of 10 larger than in G16. We find a highly significant detection of the correlation between galaxy density and CMB lensing. We subject the correlation function measurements and corresponding covariance estimates to several tests for systematic effects, finding that biases due to these systematic effects are negligible over the range of angular scales used for the main analysis.

We use the measured galaxy-CMB lensing cross-correlations to extract cosmological information in several ways. First, assuming a fiducial cosmological model based on the results of [128], we measure the amplitude of our measurement relative to this model. The amplitude we obtain from this procedure can be directly compared with similar constraints obtained in previous studies. Second, we infer the linear growth function over the redshift ranges that DES is sensitive to, and compare that with the baseline ΛCDM model predictions derived from CMB observations. Two different approaches are used: (i) the $D_{\rm G}$ estimator introduced in G16, and (ii) a method that measures the growth and allows us to marginalize over galaxy bias parameters and parameters associated with systematic measurement errors. Finally, we fix the lensing amplitude and growth-rate parameters to their ΛCDM values and simultaneously estimate cosmological and systematics parameters. In some of these analyses, we perform joint fits to both the galaxy-CMB lensing cross-correlations and galaxy clustering measurements in order to break degeneracies with galaxy bias.

[1] The National Radio Astronomy Observatory (NRAO) Very Large Array (VLA) Sky Survey

[2] G16 cross-correlated galaxies with CMB lensing maps from SPT and Planck separately, whereas in this study, a lensing map derived from a combined temperature map presented in [47] is used.

3.3 Theory

From the CMB lensing convergence $\kappa_{\rm CMB}$ and galaxy overdensity $\delta_{\rm g}$ fields, one can construct the auto- and cross-angular power spectra, which can be written as a function of multipole ℓ using the Limber approximation[3] as:

$$C^{\delta^i_{\rm g}\delta^i_{\rm g}}(\ell) = \int d\chi \frac{q_{\delta^i_{\rm g}}\left(\frac{\ell+\frac{1}{2}}{\chi},\chi\right) q_{\delta^i_{\rm g}}\left(\frac{\ell+\frac{1}{2}}{\chi},\chi\right)}{\chi^2} P_{\rm NL}\left(\frac{\ell+\frac{1}{2}}{\chi}, z(\chi)\right) \tag{3.1}$$

$$C^{\delta^i_{\rm g}\kappa_{\rm CMB}}(\ell) = \int d\chi \frac{q_{\delta^i_{\rm g}}\left(\frac{\ell+\frac{1}{2}}{\chi},\chi\right) q_{\kappa_{\rm CMB}}(\chi)}{\chi^2} P_{\rm NL}\left(\frac{\ell+\frac{1}{2}}{\chi}, z(\chi)\right), \tag{3.2}$$

where χ is the comoving distance to redshift z, $P_{\rm NL}(k,z)$ is the non-linear matter power spectrum, and the galaxy and CMB lensing kernels are:

$$q_{\delta^i_{\rm g}}(k,\chi) = b^i_{\rm g}(k,z(\chi)) \frac{n^i_{\rm g}(z(\chi))}{\bar{n}^i_{\rm g}} \frac{dz}{d\chi}, \tag{3.3}$$

$$q_{\kappa_{\rm CMB}}(\chi) = \frac{3H_0^2\Omega_{\rm m}}{2c^2} \frac{\chi}{a(\chi)} \frac{\chi^* - \chi}{\chi^*}. \tag{3.4}$$

Here $b^i_{\rm g}(k,z)$ is the galaxy bias, $n^i_{\rm g}(z)$ is the redshift distribution of the i-th galaxy sample with total density $\bar{n}^i_{\rm g}$, a is the cosmological scale factor, and χ^* is the comoving distance to the horizon. We adopt a linear galaxy bias model (i.e. constant value for all values of k) with a single galaxy bias b^i parameter for each galaxy redshift bin. Following [91] and [20], we restrict the analysis to angular scales over which the linear bias approximation is accurate.

In order to be consistent with the filtering that has been applied to the CMB lensing maps (see §3.4), we multiply $C^{\delta_{\rm g}\kappa_{\rm CMB}}(\ell)$ by the filter function, $F(\ell)$, given by

$$F(\ell) = \begin{cases} \exp(-\ell(\ell+1)/\ell^2_{\rm beam}), & \text{for } 30 < \ell < 3000 \\ 0, & \text{otherwise,} \end{cases} \tag{3.5}$$

where $\ell_{\rm beam} \equiv \sqrt{16\ln 2}/\theta_{\rm FWHM}$, and $\theta_{\rm FWHM} = 5.4'$. The Gaussian filtering is equivalent to convolving the CMB lensing maps with a Gaussian beam of full width at half maximum $\theta_{\rm FWHM}$.

The harmonic-space expression above can be rewritten in position space by applying a Legendre

[3] See [91] for a discussion regarding the validity of the Limber approximation in the DES multi-probe framework.

transformation, yielding the two-point correlation functions between two fields a, b:

$$w^{ab}(\theta) = \sum_{\ell=0}^{\infty} \left(\frac{2\ell+1}{4\pi} \right) P_\ell(\cos\theta)\, C^{ab}(\ell) F(\ell)\,, \tag{3.6}$$

where $a, b \in \{\delta_{\rm g}^i, \kappa_{\rm CMB}\}$, P_ℓ are the Legendre polynomials, and the summation can be truncated to $\ell_{\rm max} \sim 10^4$ for the angular scales of interest.

Following [91] and [20], we model potential biases in the estimation of the galaxy redshift distributions using a single additive bias parameter for each galaxy redshift bin. The galaxy $n(z)$ is modified via

$$n^i_{\rm g,unbiased}(z) = n^i_{\rm g}(z - \Delta^i_{z,{\rm g}}), \tag{3.7}$$

where $\Delta^i_{z,{\rm g}}$ is the bias parameter. The biased $n^i_{\rm g}(z)$ is then propagated to the $C^{\delta_{\rm g}\kappa_{\rm CMB}}(\ell)$ as described above.

We calculate the power spectrum using the Boltzmann code CAMB[4] [76, 96] with the Halofit extension to nonlinear scales [157, 163] and the neutrino extension from [29].

3.4 Data

For the galaxy clustering measurements we use the DES Y1 lens galaxy sample, as described in §2.3.1. The only difference with respect to that sample is that here we also include the mask for the CMB lensing convergence measurements, giving as a result a combined mask with an effective area of 1289 deg^2.

For the CMB lensing convergence measurements, we use the CMB weak lensing map presented in [119], which we briefly describe here. This lensing map is derived from an inverse variance weighted combination of SPT 150 GHz (§3.1.1) and Planck 143 GHz (§3.1.2) temperature data over the SPT-SZ survey region ($20^{\rm h}$ to $7^{\rm h}$ in right ascension and from $-65°$ to $-40°$ in declination, see, e.g. [161]). The motivation for this is to obtain a temperature map that has broader multipole ℓ coverage and less noise than either individual map. Modes in this combined temperature map with $\ell < 100$ and $\ell > 3000$ are removed to avoid foreground contamination. The brightest point sources and clusters with a detection significance S/N> 6 (see [32]) are masked prior to the combining procedure to avoid contamination in the maps. Then, a quadratic estimator technique

[4] See `camb.info`.

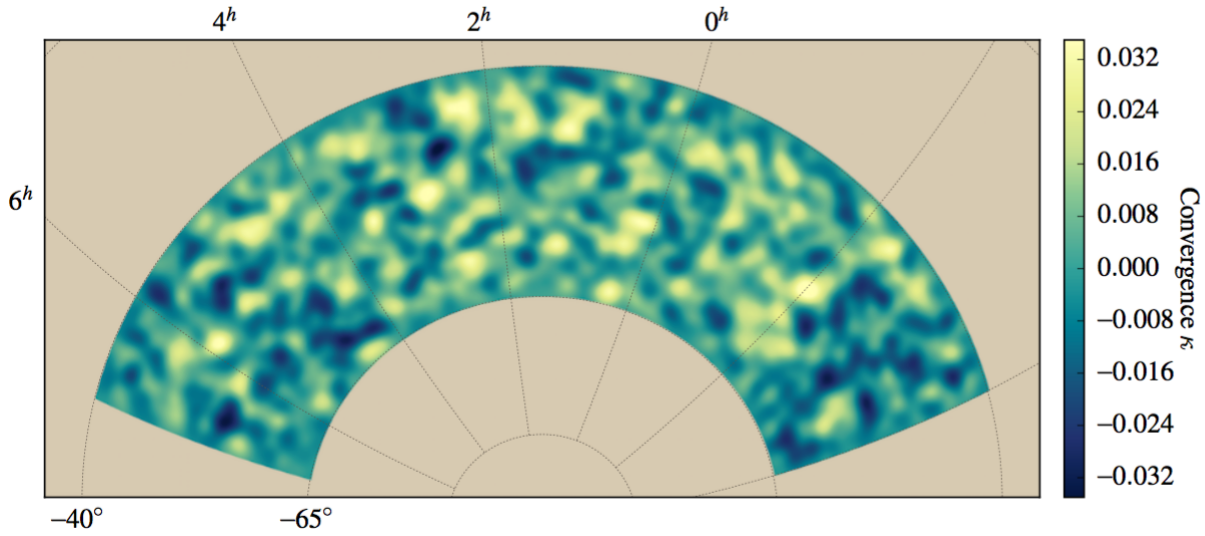

FIGURE 3.1: Reconstructed lensing map from the linear combination of SPT 150 GHz and Planck 143 GHz temperature maps, from [119].

[117] is applied to this combined temperature map to reconstruct a map of the gravitational lensing potential. Simulations are then used to debias and renormalise the amplitude of the lensing map, which is shown in Fig.3.1. In constructing the map, we use the lensing multipole range of $30 < \ell < 3000$ and apply a Gaussian smoothing of $\theta_{\rm FWHM} = 5.4'$ to the map. The low-pass filter (removing multipoles $\ell \leq 30$) is applied to suppress foreground contamination, while the high-pass filter (removing $\ell \geq 3000$) is applied to remove modes we measure poorly in the data. When calculating the correlation functions in this work, we apply an additional stricter mask that removes all the clusters with significance > 5 in [32] and DES and REDMAPPER clusters with high richness values ($\lambda > 80$). By masking massive clusters in the CMB lensing map, we remove regions of high contamination by the tSZ effect [42]. However, we also induce a secondary bias due to masking regions of high lensing convergence. It was shown in [20] that this secondary bias is small compared to other systematic effects such as tSZ.

3.5 Methodology

In this work, we measure the clustering of the galaxies and their correlations with the CMB lensing maps in position-space.

3.5.1 Correlation functions

We measure both the auto-correlation of the galaxy density field and the cross-correlation between galaxies and $\kappa_{\rm CMB}$. The former is calculated using the Landy-Szalay estimator [93]:

$$w^{\delta_{\rm g}\delta_{\rm g}}(\theta) = \frac{DD(\theta) - 2DR(\theta) + RR(\theta)}{RR(\theta)}, \tag{3.8}$$

with

$$DD(\theta) = \frac{1}{N_\theta^{DD}} \sum_{i=1}^{N_{\rm gal}} \sum_{j=1}^{N_{\rm gal}} \eta_i^D \eta_j^D \Theta_{i,j}, \tag{3.9}$$

$$DR(\theta) = \frac{1}{N_\theta^{DR}} \sum_{i=1}^{N_{\rm gal}} \sum_{j=1}^{N_{\rm rand}} \eta_i^D \eta_j^R \Theta_{i,j}, \tag{3.10}$$

$$RR(\theta) = \frac{1}{N_\theta^{RR}} \sum_{i=1}^{N_{\rm rand}} \sum_{j=1}^{N_{\rm rand}} \eta_i^R \eta_j^R \Theta_{i,j}, \tag{3.11}$$

where η^D are the weights for the individual galaxies determined from cross-correlation with systematic maps (see [62] for further details), N_θ are the total number of pairs of a given type [data-data (DD), data-random (DR), random-random (RR)] in a given angular bin θ, and $\Theta_{i,j}$ is 1 if a pair is separated by an angle θ within the bin size $\Delta\theta$ and 0 otherwise. Random galaxies are generated uniformly over the union of the galaxy and $\kappa_{\rm CMB}$ masks, and are included in the random catalog with probabilities matching the weight at the pixel which the random galaxies fall onto. Here, we only consider the weights coming from the *galaxy* mask, although both the galaxy and $\kappa_{\rm CMB}$ masks are used to determine the valid pixels.

For the correlation function between a galaxy catalog and a pixellated map such as the CMB lensing convergence map, the correlation function is calculated using:

$$w^{\delta_{\rm g}\kappa_{\rm CMB}}(\theta) = D\kappa_{\rm CMB}(\theta) - R\kappa_{\rm CMB}(\theta), \tag{3.12}$$

with

$$D\kappa_{\rm CMB}(\theta) = \frac{1}{N_\theta^{D\kappa_{\rm CMB}}} \sum_{i=1}^{N_{\rm gal}} \sum_{j=1}^{N_{\rm pix}} \eta_i^D \eta_j^{\kappa_{\rm CMB}} \kappa_{{\rm CMB},j} \Theta_{i,j}, \tag{3.13}$$

$$R\kappa_{\rm CMB}(\theta) = \frac{1}{N_\theta^{R\kappa_{\rm CMB}}} \sum_{i=1}^{N_{\rm rand}} \sum_{j=1}^{N_{\rm pix}} \eta_i^R \eta_j^{\kappa_{\rm CMB}} \kappa_{{\rm CMB},j} \Theta_{i,j}, \tag{3.14}$$

where $\eta_j^{\kappa_{\rm CMB}}$ is the value of the mask, and $\kappa_{{\rm CMB},j}$ is the value of convergence at the j-th pixel.[5] In measuring the auto-correlation of galaxy density, we use 20 bins equally spaced in logarithm between $2.5' < \theta < 250'$; these angular bins are consistent with those of [62]. For $w^{\delta_{\rm g}\kappa_{\rm CMB}}(\theta)$, we use 10 equally log-spaced angular bins over the same angular range due to the higher noise levels of this measurement. The measurements in both cases are carried out using the TreeCorr package[6] [85].

3.5.2 Angular scale cuts

Our model for the correlation functions ignores several potential complications, such as the effects of tSZ bias in the CMB lensing map, the effects of non-linear galaxy bias, and the effects of baryons on the matter power spectrum. In order to minimize biases to the inferred cosmological parameters in our analysis, we remove measurements at angular scales that we expect to be significantly impacted by these effects.

The choices of these angular scale cuts employed here were motivated for the analyses of $w^{\delta_{\rm g}\delta_{\rm g}}(\theta)$ and $w^{\delta_{\rm g}\kappa_{\rm CMB}}(\theta)$ in [91] and [20]. The scale cuts were determined by introducing unmodeled effects into simulated data vectors and performing simulated likelihood analyses to infer parameter biases. The scale cuts ultimately chosen in [91] and [20] were determined based on the joint analysis of two-point functions between the galaxy density, galaxy lensing and CMB lensing. Since the analysis of a single correlation function — such as $w^{\delta_{\rm g}\kappa_{\rm CMB}}(\theta)$ — will necessarily be less constraining, by adopting these scale cuts in this analysis we are being conservative. It was shown in [91] that with these scale cuts, the bias on the main cosmological parameters (Ω_m, $S_8 = \sigma_8 \sqrt{\Omega_m/0.3}$, and w) will be less than 0.4σ, where σ represents the statistical uncertainty on the parameters.

The scale cut choices motivated by [91] and [20] result in removing from the galaxy-CMB lensing cross-correlations angular scales that are smaller than

$$\theta_{\rm min}^{\delta_{\rm g}\kappa_{\rm CMB}} = [15', 25', 25', 15', 15'] \tag{3.15}$$

for the five redshift bins. The corresponding scale cuts for the galaxy auto-correlations are [62]

$$\theta_{\rm min}^{\delta_{\rm g}\delta_{\rm g}} = [45', 25', 25', 15', 15']\,. \tag{3.16}$$

[5] Here, we only consider the weights coming from the $\kappa_{\rm CMB}$ mask, although both the galaxy and $\kappa_{\rm CMB}$ masks are used to determine the valid pixels.

[6] https://github.com/rmjarvis/TreeCorr

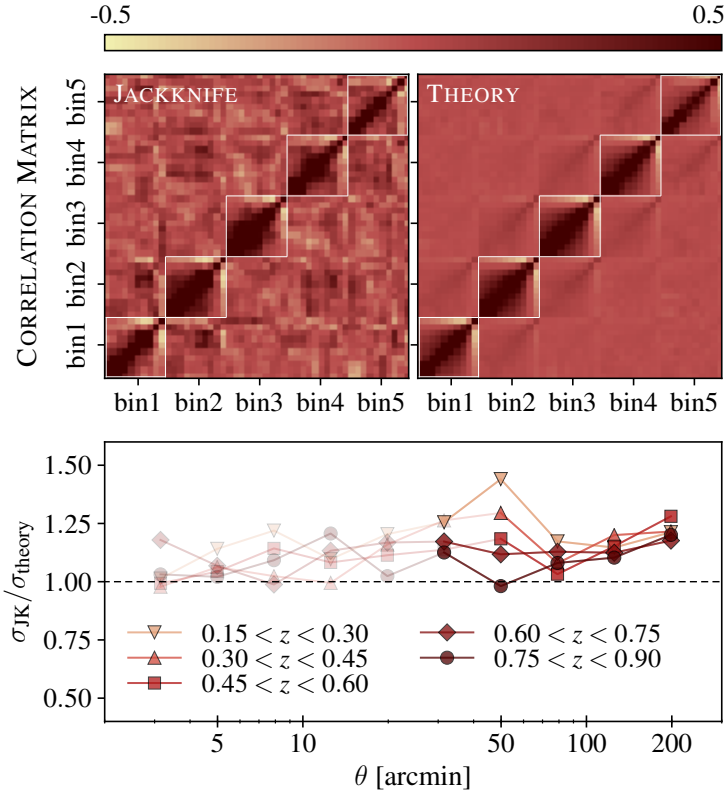

FIGURE 3.2: Covariance matrix for $w^{\delta_g \kappa_{\rm CMB}}(\theta)$ obtained using the jackknife method (upper left) and analytically (upper right). Each redshift bin includes 10 angular bins. The ratio of the diagonal elements are shown in the lower panel. The gray panel denotes ±30% margin compared to the analytical covariance.

3.5.3 Covariance matrix

It was shown by G16 that several covariance matrix estimators yield consistent results for the galaxy-CMB lensing correlation. Based on this comparison and the analysis of [91], we decided to use an analytic covariance estimate described in [91], but extended to include CMB lensing cross-correlations as described by [20]. Unlike G16, in which the analytic covariance only included Gaussian terms, we consider here a sum of Gaussian covariance and non-Gaussian terms based on a halo-model approach (which includes the trispectrum term and the super-sample covariance). We additionally modify the term of this covariance that involves correlations between $\kappa_{\rm CMB}$ noise and $\delta_{\rm g}$ noise, to take into account the survey geometry. This is done by replacing the analytic noise-noise covariance (which is calculated based on the galaxy number density and survey area only) with the covariance calculated from correlating Gaussian

realizations of the $\kappa_{\rm CMB}$ map and the galaxy random catalog using the survey mask. This correction increases the diagonal elements of the analytic covariance by $\sim 10\%$ for $w^{\delta_g\kappa_{\rm CMB}}(\theta)$.

We compare this theoretical covariance estimate to a data-based jackknife estimate of the covariance in Fig.3.2. From the data we compute the jackknife covariance as

$$C_{ij}^{\rm jk} = \frac{N_{\rm jk}-1}{N_{\rm jk}} \sum_{k}^{N_{\rm jk}} (\vec{d}^{k} - \bar{d})_i (\vec{d}^{k} - \bar{d})_j, \tag{3.17}$$

where $N_{\rm jk}$ is the number of jackknife patches used. We obtain diagonal covariance elements that are on average $\sim 17\%$ higher than the analytical covariance over the angular scales of interest. Based on the discussion in [116] and [66], we consider that these are in sufficient agreement given that the jackknife method is a noisy estimate of the underlying covariance.

3.5.4 Parameter inference

The cross-correlation between galaxy density and the CMB convergence map contains cosmological information. To extract this information, we assume that the likelihood of the measured data vector $\vec{d}$ given a model $\vec{m}$, is Gaussian:

$$\ln \mathcal{L}(\vec{d}|\vec{m}(\vec{p})) = -\frac{1}{2} \sum_{ij}^{N} \left(d_i - m_i(\vec{p})\right) \mathbf{C}_{ij}^{-1} \left(d_j - m_j(\vec{p})\right), \tag{3.18}$$

where N is the number of points in the data and model vectors. The posteriors on the model parameters are given by:

$$P(\vec{m}(\vec{p})|\vec{d}) \propto \mathcal{L}(\vec{d}|\vec{m}(\vec{p})) P_{\rm prior}(\vec{p}), \tag{3.19}$$

where $P_{\rm prior}(\vec{p})$ is the prior on the model parameters.

1. *Galaxy bias and lensing amplitude constraints*

   Assuming the cosmological model is tightly constrained, joint measurement of $w^{\delta_g\kappa_{\rm CMB}}(\theta)$ and $w^{\delta_g\delta_g}(\theta)$ allows us to simultaneously constrain galaxy bias, b, and an overall multiplicative bias in the $\kappa_{\rm CMB}$ map, which we call A_κ. This is possible because the amplitude of the galaxy-CMB lensing cross-correlation scales with bA_κ, while the amplitude of the galaxy clustering correlation function scales with b^2.

We consider two scenarios along these lines while fixing the cosmological model to the fiducial model introduced in § 3.2. In the first scenario we fix $A_\kappa = 1$ and constrain the galaxy bias in each redshift bin while marginalizing over the photo-z uncertainties. The second scenario is identical to the first, but we let A_κ be free. In both cases we adopt the priors on systematics parameters presented in Table 3.1.

2. *Growth function*

We use the measured correlation functions to constrain the cosmological growth function using two different methods. For both of these methods we assume $A_\kappa = 1$.

The first approach is the procedure introduced in G16 (also applied in [28]), which we compute here to compare with that analysis. For this method, we fix all the cosmological and nuisance parameters to the fiducial values listed in Table 3.1. We define the growth-removed auto- and cross-spectra, indicated with a slashed symbol, via:

$$\not{C}^{\delta_g\delta_g}(\ell) = \int d\chi \frac{q^i_{\delta_g}\left(\frac{\ell+\frac{1}{2}}{\chi},\chi\right) q^i_{\delta_g}\left(\frac{\ell+\frac{1}{2}}{\chi},\chi\right)}{\chi^2\, D^2[z(\chi)]} P_{\rm NL}\left(\frac{\ell+\frac{1}{2}}{\chi}, z(\chi)\right) \tag{3.20}$$

$$\not{C}^{\delta_g\kappa_{\rm CMB}}(\ell) = \int d\chi \frac{q^i_{\delta_g}\left(\frac{\ell+\frac{1}{2}}{\chi},\chi\right) q_{\kappa_{\rm CMB}}(\chi)}{\chi^2\, D^2[z(\chi)]} P_{\rm NL}\left(\frac{\ell+\frac{1}{2}}{\chi}, z(\chi)\right), \tag{3.21}$$

where $D(z)$ is the linear growth function. The angular power spectra are then transformed into $w(\theta)$ using Eq. 3.6, and our growth estimator is given by the ratio between[7] the observed and theoretical slashed correlation functions, averaged over a range of angular scales $[\theta^{\rm min}_{D_{\rm G}}, \theta^{\rm max}_{D_{\rm G}}]$:

$$D_{\rm G} = \left\langle \frac{w^{\delta_g\kappa_{\rm CMB}}_{\rm observed}(\theta)}{\not{w}^{\delta_g\kappa_{\rm CMB}}_{\rm theoretical}(\theta)} \sqrt{\frac{\not{w}^{\delta_g\delta_g}_{\rm theoretical}(\theta)}{w^{\delta_g\delta_g}_{\rm observed}(\theta)}} \right\rangle_{\theta^{\rm min}_{D_{\rm G}}<\theta<\theta^{\rm max}_{D_{\rm G}}}. \tag{3.22}$$

We measure this quantity for the five tomographic bins, which allows us to measure the evolution of the growth function in redshift bins (i.e. $D_{\rm G}(z_i)$). The advantage of this estimator is that the measured quantity is independent of galaxy bias since bias is canceled out by taking the ratio. Due to the filtering that removes $\ell < 30$ in the $\kappa_{\rm CMB}$ map, the fiducial model $w^{\delta_g\kappa_{\rm CMB}}_{\rm theoretical}(\theta)$ reaches zero near $\theta = 100'$, so we restrict our measurements to scales $\theta < \theta^{\rm max}_{D_{\rm G}} = 100'$. For $\theta^{\rm min}_{D_{\rm G}}$, we conservatively choose the larger scale between the auto- and cross-correlation scale cuts for each redshift bin.

[7] This ratio only works in the limit when the redshift slices are narrow.

Parameter	Fiducial	Prior
Cosmology		
$\Omega_{\rm m}$	0.309	[0.1, 0.9]
$A_{\rm s}/10^{-9}$	2.14	[0.5, 5.0]
$n_{\rm s}$	0.967	[0.87, 1.07]
w	-1.0	Fixed
$\Omega_{\rm b}$	0.0486	[0.03, 0.07]
h_0	0.677	[0.55, 0.91]
$\Omega_\nu h^2$	6.45×10^{-4}	[0.0006,0.01]
$\Omega_{\rm K}$	0	Fixed
τ	0.066	Fixed
Growth Amplitude		
$A_{\rm D}$	1.0	[0.1,4.0]
Lensing Amplitude		
A_κ	1.0	[0.1,4]
Galaxy bias		
b^i	1.45, 1.55, 1.65, 1.8, 2.0	[0.8,3.0]
Lens photo-z error		
$\Delta^1_{z,{\rm g}}$	0.010	(0.008,0.007)
$\Delta^2_{z,{\rm g}}$	-0.004	(-0.005,0.007)
$\Delta^3_{z,{\rm g}}$	0.009	(0.006,0.006)
$\Delta^4_{z,{\rm g}}$	0.001	(0.0,0.01)
$\Delta^5_{z,{\rm g}}$	0.0	(0.0,0.01)

Table 3.1: The fiducial parameter values and priors for cosmological and nuisance parameters used in this analysis. Square brackets denote a flat prior over the indicated range, while parentheses denote a Gaussian prior of the form $\mathcal{N}(\mu, \sigma)$. The Gaussian priors on photo-z errors are determined by [44]. The fiducial cosmological parameter values are taken from the [128], but here we assume 3 massive neutrinos to stay consistent with other DES-Y1 analyses. For the photo-z bias, peaks of the posterior distributions in the DES joint galaxy clustering and lensing analysis [2] are used as fiducial values.

In order to test for possible deviations from the baseline ΛCDM model across the five redshift bins, we assume the shape of the linear growth function $D(z)$ to be fixed by the fiducial cosmology, and we fit for a redshift-independent quantity $A_{\rm D}$ such that it minimizes:

$$\chi^2 = \sum_{ij}^{5} (D_{\rm obs}(z_i) - A_{\rm D} D_{\rm fid}(z_i)) \mathbf{C}_{ij}^{-1} (D_{\rm obs}(z_j) - A_{\rm D} D_{\rm fid}(z_j)), \tag{3.23}$$

with $D_{\rm obs}(z_i) \equiv D_{\rm G}$ for this method. We take 50,000 multivariate Gaussian draws from the analytical covariance matrix to produce simulated $w^{\delta_{\rm g}\delta_{\rm g}}(\theta)$ and $w^{\delta_{\rm g}\kappa_{\rm CMB}}(\theta)$ data vectors, calculate $D(z)$ for each draw, and compute the covariance matrix $\mathbf{C}_{ij}$ over the ensemble of realizations.

The second method for measuring the growth function consists of simultaneously fitting $A_{\rm D}$, galaxy bias, and photo-z bias to the observed auto- and cross-correlations using a Markov chain Monte Carlo (MCMC) approach. This method has an advantage of allowing us to vary over other systematic effects, such as photo-z errors. For this method, we fix the cosmological parameters to the fiducial values in Table 3.1 but vary the growth amplitude, galaxy biases and lens photo-z biases over the priors given in the same table.

3. *Cosmological parameter estimation*

Finally, we use the measurements of both $w^{\delta_{\rm g}\kappa_{\rm CMB}}$ and $w^{\delta_{\rm g}\delta_{\rm g}}$ presented in this work to constrain cosmological parameters. We generate posterior samples using the MULTINEST algorithm [64] as implemented in the COSMOSIS [176] package. We let the photo-z bias (i.e. lens $n(z)$ shift), galaxy bias and 6 cosmological parameters ($\Omega_{\rm m}$, $A_{\rm s}$, $n_{\rm s}$, $\Omega_{\rm b}$, h, Ω_ν) vary simultaneously, while we fix $A_\kappa = A_{\rm D} = 1$. Here, $A_{\rm s}$ is the amplitude of the matter power spectrum, $n_{\rm s}$ is the spectral index, $\Omega_{\rm b}$ is the baryon density, h is the reduced Hubble constant and Ω_ν is the neutrino density. Priors on these parameters are summarized in Table 3.1. In this study we will focus on the constraints on $\Omega_{\rm m}$ and $S_8 \equiv \sigma_8 \sqrt{\Omega_{\rm m}/0.3}$, where σ_8 is the RMS amplitude of mass fluctuations on $8h^{-1}$ Mpc scale. S_8 is defined to be approximately the most constrained cosmological parameter combination for galaxy weak lensing measurements.

3.5.5 Blinding

This analysis was blinded throughout the study using a combination of various blinding schemes. The analysis pipeline was first built using FLASK simulations as data vectors, and then we switched to using blinded data. In order to blind the data analysis, we multiplied the CMB lensing map by an unknown factor in the range between 0.8 and 1.2, shifted the cosmological parameter constraints that we obtained by an arbitrary number, and removed the axes when generating figures. After the data passed all systematic checks, the measurements were repeated using a CMB lensing map without the random factor applied (i.e. unblinded), and the cosmological parameter constraints were calculated without shifts.

3.6 Systematic Error Analysis

Systematic errors can impact the relationship between the measured and predicted correlation functions in three ways: (1) by affecting the observed density of galaxies on the sky, (2) by affecting the CMB lensing map, and (3) by affecting the inferred redshift distributions of the galaxies. Systematics affecting the observed density of DES REDMAGIC galaxies were explored by [62] as part of the [2] analysis. The main source of systematic error impacting the CMB lensing map is contamination by the tSZ effect which has been discussed and modeled in [20]. Systematic errors in the photometric redshift distributions of REDMAGIC galaxies were explored by [44], also as part of the [2] analysis. Below, we draw heavily from these companion papers to constrain the systematic contamination of the measured correlation functions.

3.6.1 Galaxy density and CMB lensing biases

We first consider systematics impacting galaxy density and the CMB lensing map. It is useful to divide these systematics into two categories: those that produce a bias due to galactic foregrounds, and those that produce a bias that is correlated with the large-scale structure (LSS). For the former, in order to generate a bias in $w^{\delta_g \kappa_{\rm CMB}}$, the systematic must contaminate *both* the galaxy density and $\kappa_{\rm CMB}$; if it only impacts one of these observables, its impact on the correlation function should average to zero. One of the strengths of cross-correlation measurements such as $w^{\delta_g \kappa_{\rm CMB}}$ is that there are not many systematics that could contaminate both of the observed fields. However, there are some potential sources of bias that could do this. One example is dust, which

is one of the foreground components of the CMB temperature measurements, and one can expect potential residuals in a single-frequency temperature map that can then propagate into the CMB lensing map. Dust also affects the photometry of the observed galaxies and is correlated with galactic latitude. This contamination can then induce density fluctuations through the change of mean density with latitude. Consequently, dust extinction may contaminate simultaneously galaxy density and CMB lensing, and could therefore contaminate measurement of $w^{\delta_g \kappa_{CMB}}$. In what follows we will consider dust extinction and stellar density maps as potential contaminants.

On the other hand, there are some sources of contamination which *are* correlated with the large-scale structure. In this case, the contaminant needs not affect both galaxy density and CMB lensing in order to bias $w^{\delta_g \kappa_{CMB}}(\theta)$. At $\sim$ 150 GHz (roughly the frequencies of the SPT and Planck maps used to generate the CMB lensing map), the tSZ effect results in a decrement in the observed CMB temperature around clusters. This non-Gaussian feature gets picked up as a false lensing signal by the quadratic estimator. Since hot gas is correlated with galaxies, we expect the tSZ effect to induce a bias in the measured correlation functions. The CIB, which is dominated by emission from dusty star forming galaxies, is another extragalactic foreground that injects non-Gaussian features in our temperature maps. While the CIB emission spectrum peaks at a higher frequency, minor correlations with 150 GHz observations are expected, which again lead to false lensing signal. Since both the CIB and tSZ originate from large-scale structure, we expect them to introduce biases in κ_{CMB} that are correlated with density fluctuations. Maps for both tSZ and CIB contamination are built and described in detail by [20]. That work also identified the tSZ effect as the dominant source of systematic affecting the cross-correlation measurement between κ_{CMB} and δ_g. While the angular scale cuts proposed by [20] and restated in §3.5.2 are chosen to mitigate these biases, they do not remove them entirely, and the residuals must be quantified.

Of all the systematic effects that could potentially be present in our maps and catalogs, only the ones which are correlated with *both* the observed CMB lensing map and the galaxy catalog affect our cross-correlation measurements. We can therefore measure the quantity:

$$\frac{w^{\kappa^{obs}_{CMB} \mathcal{S}}(\theta) w^{\delta^{obs}_g \mathcal{S}}(\theta)}{w^{\mathcal{S}\mathcal{S}}(\theta)} \tag{3.24}$$

to quantify the amplitude of the bias (to first order), which we expect to be zero for systematic maps that are not correlated with both the CMB lensing map and galaxy catalogs. However for astrophysical systematic effects such as tSZ and CIB which could potentially be contaminating the CMB temperature map, physical correlations with κ^{true}_{CMB} are expected, and therefore Equation 3.24 is not expected to equal 0. Therefore, for these systematic effects, we directly measure the

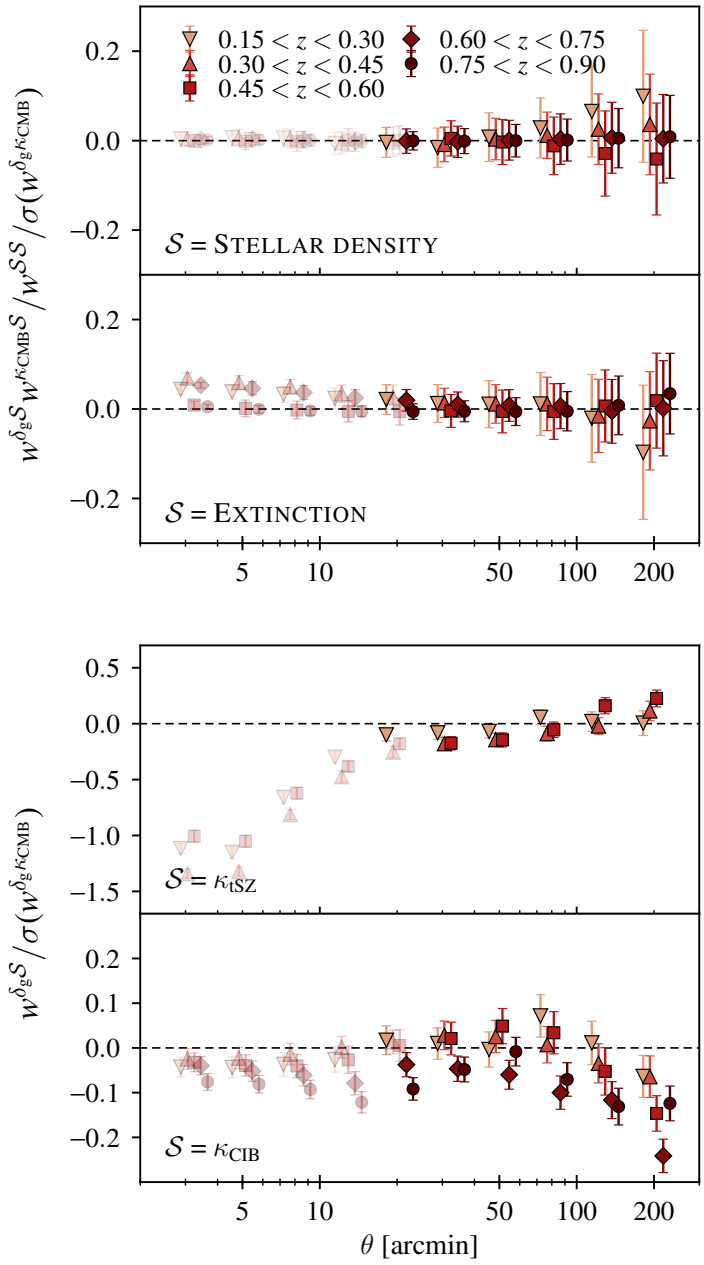

FIGURE 3.3: Top two panels: Contributions due to uncorrelated systematics to the galaxy-CMB lensing cross-correlations, as described by Eq. 3.24, in units of the statistical errors on the observed cross-correlation. Lower two panels: Contributions due to correlated systematics, given by the cross-correlations between the $\kappa_{\rm CMB}$ systematics ($\kappa_{\rm tSZ}$ and $\kappa_{\rm CIB}$) and $\delta_{\rm g}$, also in units of the statistical error. The faded points are removed from the analysis due to the imposed scale cuts. Note the different scales used for $\kappa_{\rm tSZ}$ and $\kappa_{\rm CIB}$.

correlations $w^{\delta_g \kappa_{tSZ}}(\theta)$ and $w^{\delta_g \kappa_{CIB}}(\theta)$ to quantify the bias. As described in more detail in [20], we estimate κ_{tSZ} by passing a template tSZ map through the lensing pipeline of [119]; similarly, κ_{CIB} is estimated by passing a 545 GHz CIB map [136] though the [119] lensing pipeline.

We first focus on those systematics that are uncorrelated with the true density. We show in the top half of Fig. 3.3 the ratio between $w^{\kappa_{CMB}S}(\theta)w^{\delta_g S}(\theta)/w^{SS}(\theta)$ measured for dust extinction and stellar contamination, and the uncertainty on the measured galaxy density-CMB lensing correlation and verify that this ratio is significantly smaller than 1 and consistent with 0 across all angular scales. We observe that within the angular scales we consider (note that the faded points are excluded from the analysis) the contributions to the measurements due to systematics are $< 1\sigma$ for all redshift bins and for all systematic maps.

Since the tSZ template is generated only using redMaPPer clusters up to $z = 0.6$, the correlations for the higher two redshift bins have been ignored (see [20]), as we apply our tSZ- induced bias measurements for the third-to-last redshift bin to the higher redshift bins. We expect this approximation to be conservative, since the tSZ bias apparently decreases as a function of redshift, as seen in [20]. We can see that the impact on the measurements is generally small compared with the statistical error bars, so that we can conclude there is no evidence for any of these contaminants making a significant impact on our results.

We then consider the correlated sources of systematics: tSZ and CIB, and we show their contributions to Eq. 3.24 in the bottom half of Fig. 3.3. Here we indeed see non-zero residuals coming from tSZ but most of this bias is removed by applying our default scale cuts, and the remaining bias is within 0.35σ, where σ is the statistical uncertainty.

We note that [62] investigated the impact of several observational systematics in addition to dust extinction and stellar density that could introduce spurious fluctuations in redMaGiC galaxy number density on large-scales. Using a set of 20 survey property maps,[8] in addition to stellar contamination and galactic extinction, they studied the dependence of number density as a function of these observational properties. The results of these tests indicated that redMaGiC galaxies were not largely impacted by these systematics. Furthermore, as mentioned above, since we do not expect the DES-specific survey systematics (exposure time, sky brightness, airmass, seeing, survey depth variations) to correlate with κ_{CMB}, we do not expect these to bias $w^{\delta_g \kappa_{CMB}}(\theta)$.

[8] These were exposure time, sky brightness, airmass, seeing and survey 10σ depth, in four different broad bands.

3.6.2 Photo-z systematics

Unlike biases in the galaxy density or CMB lensing maps, we explicitly model biases in the estimated redshift distributions of the galaxies as described in §3.3.

The analysis in [2] constrained biases in the inferred redshift distributions of the REDMAGIC galaxies using angular cross-correlations with spectroscopic data from the Sloan Digital Sky Survey (DR8), particularly BOSS luminous red galaxies. This analysis is presented in [44]. These resultant priors on the photo-z bias parameters $\Delta^i_{z,\mathrm{g}}$ for the five redshift bins are listed in Table 3.1. We let these values vary when calculating the growth amplitude and cosmological parameter constraints in §3.7.2.

3.7 Results

We show in Fig. 3.4 the measured auto-correlation functions of the REDMAGIC galaxy sample and its cross-correlation with the SPT+Planck CMB lensing map. The small-scale data points shown with faded symbols are the scales removed by the scale cuts as discussed in §3.5.2. The theoretical predictions assuming the fiducial cosmology listed in Table 3.1 are shown as the black lines. In the following sections we extract cosmological information using these measurements.

We note that we made few modifications in §3.7.1 after we unblinded the data. We first added constraints on the galaxy bias from $w^{\delta_\mathrm{g}\kappa_\mathrm{CMB}}(\theta)$ alone with the cosmology fixed to Planck best-fit values (instead of DES-Y1). The motivation for this was to allow us to directly compare the constraints on galaxy bias when varying over the cosmological parameters, but combining with the Planck baseline likelihood. Accordingly, we also changed the assumed cosmology when computing the best-fit biases from $w^{\delta_\mathrm{g}\delta_\mathrm{g}}(\theta) + w^{\delta_\mathrm{g}\kappa_\mathrm{CMB}}(\theta)$. Additionally, we recomputed the galaxy biases replacing $w^{\delta_\mathrm{g}\kappa_\mathrm{CMB}}(\theta)$ by $w^{\delta_\mathrm{g}\gamma_\mathrm{t}}(\theta)$ using the same data vectors as [138] but combined with Planck baseline likelihood.

3.7.1 Galaxy bias and lensing amplitude

We first fix the cosmological parameters to the fiducial values and vary the galaxy bias and lens photo-z error parameters simultaneously, imposing the priors shown in Table 3.1. We focus on constraining galaxy bias, assuming a fixed lensing amplitude of $A_\kappa = 1$.

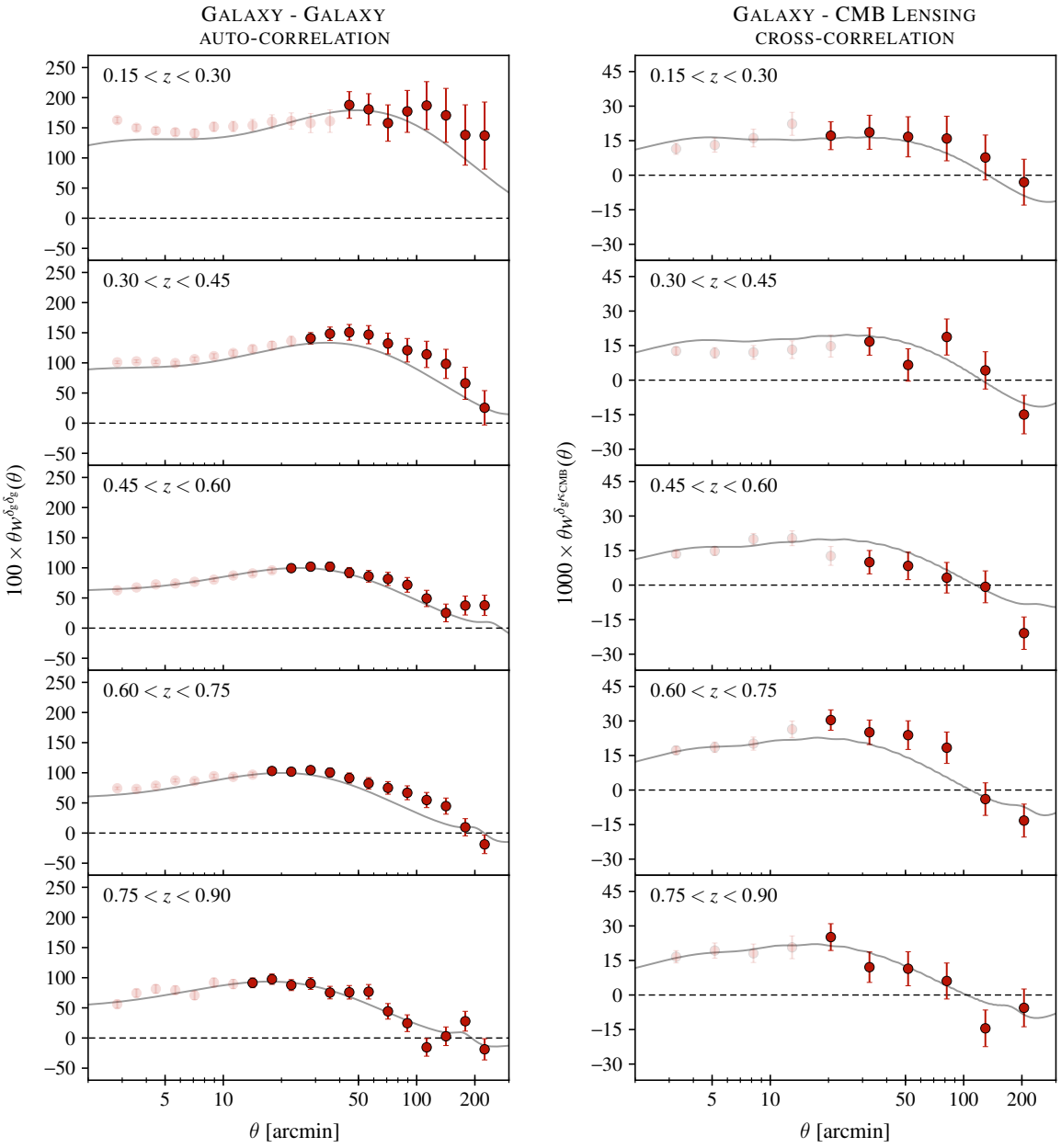

FIGURE 3.4: Measured auto- and cross-correlation functions between the REDMAGIC galaxy sample described in §3.4 and CMB lensing from [119]. The faded angular points have been excluded from the fits, consistently with [62] and with [20]. The theory modeling shown uses the mean bias and cross-correlations amplitudes found in §3.7 and Table 3.2, assuming the fiducial cosmology listed in Table 3.1. The error bars shown are the diagonal elements of the covariance matrix $\sqrt{\mathbf{C}_{ii}}$, and therefore, the correlations between the bins are ignored. In contrast, the best-fit amplitudes are calculated including the off-diagonal elements and therefore the best-fit lines and data points may not match visually in certain bins.

	$w^{\delta_g\delta_g}(\theta) + w^{\delta_g\kappa_{CMB}}(\theta)$		$w^{\delta_g\kappa_{CMB}}(\theta)$	
Sample	Bias ($A_\kappa = 1$)	Bias ($A_\kappa \neq 1$)	Fixed	+*Planck*
$0.15 < z < 0.30$	$1.47^{+0.08}_{-0.08}$	$1.46^{+0.09}_{-0.07}$	$1.54^{+0.44}_{-0.38}$	$1.47^{+0.51}_{-0.38}$
$0.30 < z < 0.45$	$1.67^{+0.06}_{-0.04}$	$1.68^{+0.06}_{-0.05}$	$1.45^{+0.33}_{-0.42}$	$1.30^{+0.46}_{-0.32}$
$0.45 < z < 0.60$	$1.68^{+0.04}_{-0.04}$	$1.68^{+0.04}_{-0.04}$	$1.10^{+0.36}_{-0.21}$	$1.06^{+0.34}_{-0.20}$
$0.60 < z < 0.75$	$2.03^{+0.04}_{-0.05}$	$2.02^{+0.05}_{-0.04}$	$2.69^{+0.23}_{-0.28}$	$2.78^{+0.17}_{-0.35}$
$0.75 < z < 0.90$	$2.14^{+0.05}_{-0.08}$	$2.12^{+0.08}_{-0.06}$	$2.17^{+0.45}_{-0.42}$	$2.31^{+0.35}_{-0.52}$
		$A_\kappa = 1.00^{+0.16}_{-0.09}$		

Table 3.2: Summary of the constraints on the galaxy bias parameters using $w^{\delta_g\delta_g}(\theta) + w^{\delta_g\kappa_{CMB}}(\theta)$ (left) and only $w^{\delta_g\kappa_{CMB}}(\theta)$ with the lensing amplitude fixed to 1 (right), assuming Planck best-fit ΛCDM cosmology. For the former, we consider two cases: fixing the lensing amplitude to 1 (2nd column in the table), and setting A_κ free (3rd column). For the latter, we first fix the cosmology (4th column) and then vary the cosmological parameters considering priors from Planck baseline likelihood (5th column).

The results are shown in Table 3.2 (second column). These correspond to $\chi^2 = 107.3$ for 82 data points. The high value of χ^2 is primarily driven by the galaxy clustering measurements (see [62]). The difference between the values reported here and in [62] is due to the cosmology assumed.

When we additionally treat the CMB lensing amplitude A_κ as a free parameter, we obtain the bias values shown in the third column of Table 3.2 . The recovered posterior on the lensing amplitude is $A_\kappa = 1.00^{+0.16}_{-0.09}$, with a total $\chi^2 = 107.2$. The similarity between the constraints on the galaxy bias values that we obtain with A_κ fixed to 1 and free suggests that the galaxy bias constraints in this analysis are dominated by $w^{\delta_g\delta_g}(\theta)$.

Next, we consider constraints on galaxy bias from $w^{\delta_g\kappa_{CMB}}(\theta)$ alone. We reject the hypothesis of no lensing with a significance[9] of 20σ when no scale cuts are imposed and 10σ after imposing scale cuts. We note that the significance prior to the conservative scale cuts, 20σ, is roughly what we would expect by the increase in area with respect to G16, which measured CMB lensing with a 6σ significance. The signal-to-noise is proportional to $\sqrt{f_{sky}}$, and we have ~ 10 times larger area, which translates into ~ 3 times higher S/N. The constraints on galaxy bias from this analysis are summarized in Table 3.2 (right). Not surprisingly, the constraints on galaxy bias from $w^{\delta_g\kappa_{CMB}}(\theta)$ alone are significantly weaker than in the case when the measurements are combined with $w^{\delta_g\delta_g}(\theta)$ (2nd column in the table). Similar constraints on galaxy biases are obtained when cosmological parameters are varied, but cosmological priors from *Planck* baseline

[9]The significance is calculated using $\sqrt{\chi^2_{null}}$, where χ^2_{null} is the value of χ^2 computed under the null model, i.e. with galaxy bias $b = 0$.

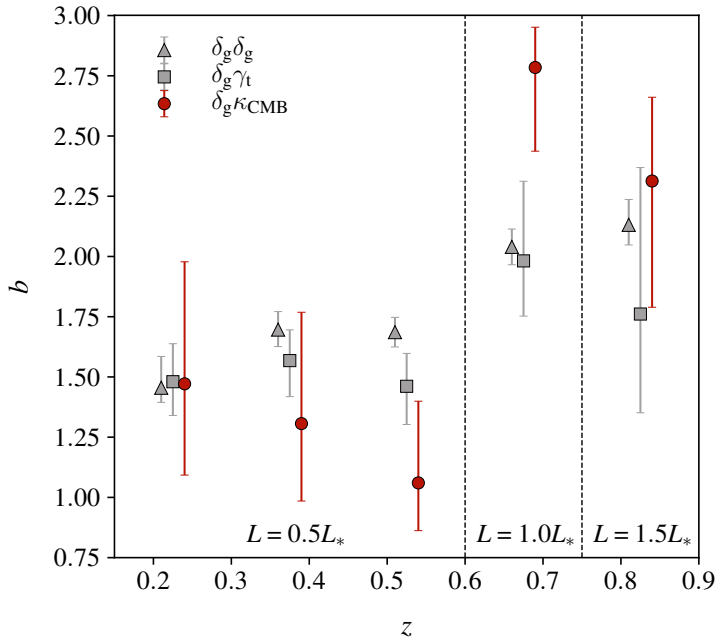

FIGURE 3.5: Galaxy bias estimation of REDMAGIC galaxies from different probes, as a function of redshift when combined with Planck baseline likelihood. The results from $w^{\delta_g\kappa_{CMB}}(\theta)$ assuming $A_\kappa = 1$ are shown in red. Additionally plotted are the measurements from galaxy clustering [62] (gray triangles) and galaxy-galaxy lensing [138] (gray squares).

likelihood are imposed (far right column of Table 3.2). In both cases photo-z biases are varied over with the priors from [2]. The χ^2 that we obtain are, respectively, 27.6 and 26.1 for 27 data points.

The bias constraints from $w^{\delta_g\kappa_{CMB}}(\theta)$, as well as those from the DES-Y1 galaxy clustering [62] and galaxy-galaxy lensing analyses [138] when combined with Planck baseline likelihood are shown in Fig. 3.5. We find that considerably tighter constraints can be obtained from $w^{\delta_g\delta_g}(\theta)$ relative to $w^{\delta_g\gamma_t}(\theta)$ and $w^{\delta_g\kappa_{CMB}}(\theta)$. The constraining power of $w^{\delta_g\kappa_{CMB}}(\theta)$ relative to $w^{\delta_g\gamma_t}(\theta)$ increases with higher redshift galaxy samples. This is because the number of available background galaxies decreases as we increase the redshift of the lens galaxy sample. In contrast, the signal improves for $w^{\delta_g\kappa_{CMB}}(\theta)$ due to the better overlap with the CMB lensing kernel.

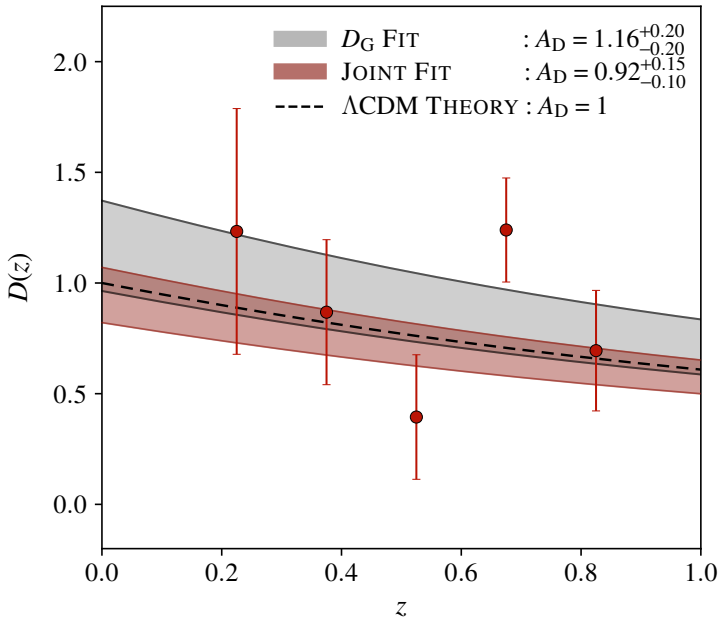

Figure 3.6: Growth function estimates from the combination of auto- and cross-correlation functions, at the fiducial cosmology. The red points show the measured value of D_G in each redshift bin, with error bars representing the diagonal elements of the covariance matrix described in §3.5.4. The grey band represents the 1σ confidence interval on the best-fit amplitude A_D, assuming the fiducial ΛCDM template shown in black (solid), and the red shaded regions describe the 1-σ uncertainties from the joint-fit analysis described in §3.7.2.

3.7.2 Growth constraints

Next, we study the broader cosmological implications of our measurement: we first assume cosmology to be fixed at high redshift, e.g. by the Planck CMB observations, and test whether the linear growth function inferred from our measurement at low redshift is consistent with the baseline ΛCDM model predictions. We test this using the two methods described in §3.5.4.

1. *The D_G estimator*

   We first measure the linear growth function $D(z)$ using the D_G estimator. We compute D_G for all five tomographic bins, applying the conservative angular scale cuts listed in §3.5.2, and additionally removing scales above 100′ (see §3.5.4 for details). The results are shown in Fig. 3.6. In addition, we also calculate the best-fit amplitude A_D by combining

all the bins, from which we obtain $A_{\rm D} = 1.16^{+0.20}_{-0.20}$, which agrees with the fiducial ΛCDM expectation of $A_{\rm D} = 1$.

2. *Joint growth fit results*

Here we keep the cosmological parameters fixed to the fiducial model, but marginalize over the five independent linear galaxy bias parameters (one for each redshift bin), the photo-z uncertainties and the linear growth parameter $A_{\rm D}$ using the priors presented in Table 3.1. We measure the linear galaxy bias to be $b^1 = 1.45^{+0.30}_{-0.15}$, $b^2 = 1.73^{+0.26}_{-0.22}$, $b^3 = 1.80^{+0.17}_{-0.29}$, $b^4 = 2.04^{+0.35}_{-0.21}$, $b^5 = 2.15^{+0.36}_{-0.24}$ and find a constraint of $A_{\rm D} = 0.92^{+0.15}_{-0.10}$ for the amplitude of the growth function. These measurements of the bias are in agreement with the results shown in Table 3.2. The recovered growth function agrees with the fiducial ΛCDM expectation, as the measurement of $A_{\rm D}$ is consistent with 1.0. We observe that the errors on the galaxy bias are larger compared to a direct best-fit estimation presented in §3.7.1. This is due to the fact that the bias and $A_{\rm D}$ parameters are correlated. In turn, the fact that the joint-fit method gets a different value of $A_{\rm D}$ with respect to the $D_{\rm G}$ method is because it explicitly takes into account the correlations between bias and growth.

3.7.3 Cosmological parameter estimation

Here we present the full cosmological analysis using the $w^{\delta_{\rm g}\delta_{\rm g}}(\theta)$+$w^{\delta_{\rm g}\kappa_{\rm CMB}}(\theta)$ data vectors and marginalizing over all the cosmological parameters and nuisance parameters (galaxy bias and photo-z bias, but we fix $A_{\rm D} = A_\kappa = 1$). The priors used in this analysis are summarized in Table 3.1, and are the same as used in [2] to maintain consistency between the analyses.

In Fig. 3.7 we show the constraints obtained on matter density $\Omega_{\rm m}$ and S_8 when all six cosmological parameters, photo-z errors and linear galaxy biases for the five redshift bins are marginalized over. This is then compared with the constraints from the combination of $w^{\delta_{\rm g}\delta_{\rm g}}(\theta) + w^{\delta_{\rm g}\gamma_{\rm t}}(\theta)$ as presented in [2]. We observe that these two measurements slice through the parameter space slightly differently. Using $w^{\delta_{\rm g}\delta_{\rm g}}(\theta) + w^{\delta_{\rm g}\kappa_{\rm CMB}}(\theta)$ we obtain $\Omega_{\rm m} = 0.276^{+0.029}_{-0.030}$ and $S_8 = 0.800^{+0.090}_{-0.094}$, whereas the combination of $w^{\delta_{\rm g}\delta_{\rm g}}(\theta) + w^{\delta_{\rm g}\gamma_{\rm t}}(\theta)$ gives us $\Omega_{\rm m} = 0.294^{+0.047}_{-0.029}$ and $S_8 = 0.759^{+0.037}_{-0.031}$. These two results can also be compared with the constraints from 3×2pt (the combination of $w^{\delta_{\rm g}\delta_{\rm g}}(\theta) + w^{\delta_{\rm g}\gamma_{\rm t}}(\theta) + \xi_{+/-}(\theta)$)[2], which gives $\Omega_{\rm m} = 0.267^{+0.030}_{-0.017}$, $S_8 = 0.773^{+0.026}_{-0.020}$. These results are highly consistent with each other as shown on Fig. 3.7. The measurements used in this analysis are combined in [3] with the $w^{\gamma_{\rm t}\kappa_{\rm CMB}}(\theta)$ presented in [118] and the results from [2], using the methodology outlined in [20].

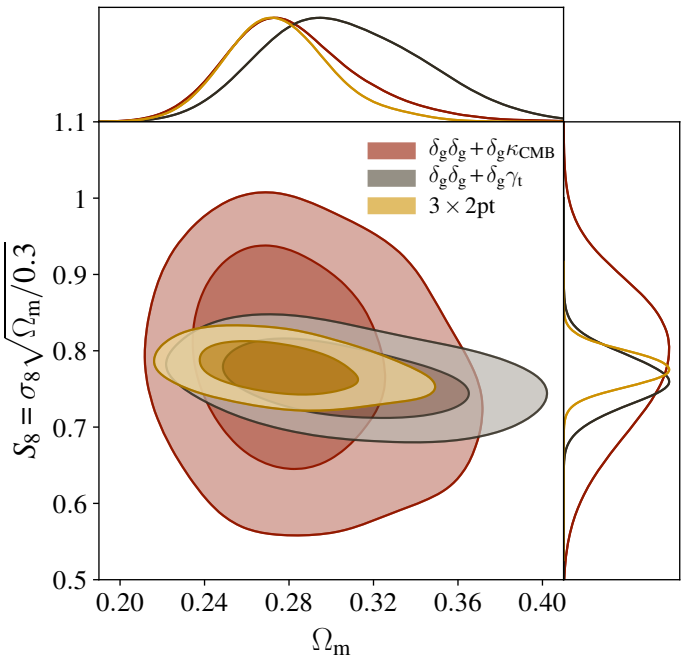

FIGURE 3.7: Constraints on Ω_m and S_8 from the measurements of this work and combinations of other two-point correlation functions. We show the constraints from $w^{\delta_g\delta_g}(\theta) + w^{\delta_g\kappa_{CMB}}(\theta)$ (red), $w^{\delta_g\delta_g}(\theta) + w^{\delta_g\gamma_t}(\theta)$ (gray) and 3×2pt (gold).

3.8 Prospects on neutrino mass constraints

Neutrinos have at least three individual mass states. However, direct experimental measurements of their absolute mass values have so far proved impossible because of their incredibly small values. A range of neutrino oscillation experiments have allowed measurements of the mass differences between the three species and the corresponding minimum total mass of 0.06 eV [40]. While particle physics experiments have provided the lower bound on the total neutrino mass, $\sum m_\nu$, the current tentative upper limit comes from cosmological studies. The Planck survey set a 95% upper limit of $\sum m_\nu < 0.12$ eV on the total neutrino mass using data from the CMB temperature and polarization anisotropies, lensing, and external large-scale structure probes (Baryon Acoustic Oscillations measurements) [133]. It is expected that next-generation CMB surveys will enhance this constraint further.

Meanwhile, galaxy surveys provide a strong complement to CMB information. The primary motivation for combining galaxy clustering with CMB lensing is that the latter also contains a relative suppression on small scales caused by the effects of neutrino free-steaming, analogous to

that in the matter power spectrum. While the galaxy power spectrum is a biased measurement of the matter power spectrum, CMB lensing probes it directly. Additionally, while the galaxy power spectrum contains contributions from the baryon and cold dark matter transfer functions only, the matter power spectrum probed by CMB lensing includes all matter, including massive neutrinos.

Additionally, forecasted constraints on $\sum m_\nu$ based on the full galaxy power spectrum will primarily be limited by weak constraints on the optical depth τ [13, 35], as these two parameters are both strongly correlated with A_s (or equivalently, σ_8). As shown by [34, 173], CMB lensing could help overcome this obstacle through its potential for constraining A_s.

In this section we explore the constraints on the sum of neutrino masses we obtain from the combination of galaxy clustering from DES Y1 and CMB lensing measurements from SPT + Planck, using the $w^{\delta_g\delta_g}(\theta)$+$w^{\delta_g\kappa_{\rm CMB}}(\theta)$ data vectors and marginalizing over all the cosmological and nuisance parameters using the priors from Table 3.1. We combine the result from $w^{\delta_g\delta_g}(\theta)$+$w^{\delta_g\kappa_{\rm CMB}}(\theta)$ with Planck temperature and polarization auto- and cross-spectra. For this purpose, we use the joint TT, EE, BB and TE likelihood for multipoles ℓ between 2 and 29 and the TT likelihood for ℓ between 30 and 2508 (commonly referred to as TT+lowP), provided by the Planck 2015 release. We obtain an upper bound at 95% confidence level (CL) of

$$\sum m_\nu < 0.81\,\mathrm{eV} \quad (95\%,\ w^{\delta_g\delta_g}(\theta) + w^{\delta_g\kappa_{\rm CMB}}(\theta) + \mathrm{Planck\,TT + lowP}), \tag{3.25}$$

while the constraints from Planck 2015 release [128] and its combination with DES Y1 3×2pt [2] are

$$\sum m_\nu < 0.72\,\mathrm{eV} \quad (95\%,\ \mathrm{Planck\,TT + lowP}) \tag{3.26}$$

$$\sum m_\nu < 0.47\,\mathrm{eV} \quad (95\%,\ 3\times2\mathrm{pt} + \mathrm{Planck\,TT + lowP}). \tag{3.27}$$

As mentioned before, the $w^{\delta_g\kappa_{\rm CMB}}(\theta)$ measurements in this work have limited constraining power due to the conservative scale cuts we have applied in this analysis. In addition, the clustering amplitude in DES Y1 is slightly lower than expected in ΛCDM informed by Planck. The three ways of reducing the clustering amplitude are to reduce Ω_m, reduce σ_8, or increase $\sum m_\nu$. The best fit cosmology in DES Y1 moves all three parameters slightly in the direction of less clustering in the present day. We expect to obtain better signal in the future as we use galaxy samples at higher redshifts and we improve our treatment of systematics and modeling to include smaller scales in our analysis.

3.9 Summary

We have presented measurements of the DES redMaGiC galaxy-CMB lensing cross-correlation as a function of redshift. Our measurement rejects the hypothesis of no-lensing at 19.9σ[10] significance prior to any scale cuts and 9.9σ using the conservative scale cuts from [20]. The conservative scale cuts reduce the signal to noise of the measurements in exchange for mitigation of systematic biases.

We test for the impact of possible systematics in the cross-correlations, considering contaminants to both the DES galaxy and the CMB lensing maps. We find that, on the scales we consider, all these contaminants have a small impact on our measurements compared with the statistical uncertainties. The largest effect comes from the tSZ contribution to the CMB lensing maps, which becomes large at smaller angular scales, and is the main limiting factor dictating our scale cuts [20]. Improving the modeling and subtraction of this contaminant will be the key to extracting the full statistical power of the temperature based CMB lensing maps in the future.

In obtaining the galaxy bias parameters, we find that galaxy-clustering measurements place significantly tighter constraints than galaxy-galaxy lensing or galaxy-CMB lensing correlations. However, the two cross-correlations are nonetheless important in breaking degeneracies in parameter space.

We use our measurements to infer cosmological information in a number of ways. We first constrain the linear growth function using the $D_{\rm G}$ estimator introduced by G16, finding a relative growth amplitude of $A_{\rm D} = 1.16^{+0.20}_{-0.20}$. This compiles measurements of growth in various tomographic bins, accounting for their covariance. We then extend this result and constrain the relative growth amplitude with a joint-fit method, marginalizing over galaxy biases and photo-z uncertainties, and considering the full covariance of the observables. In this case, we find $A_{\rm D} = 0.92^{+0.15}_{-0.10}$. Both of these results are consistent with the ΛCDM predictions of $A_{\rm D} = 1$.

Using these measurements, we finally run a full MCMC analysis over the ΛCDM cosmological parameters to also place marginalized constraints on the two parameters that are most directly related to the matter density field: $\Omega_{\rm m}$ and $S_8 \equiv \sigma_8 \sqrt{\Omega_{\rm m}/0.3}$. Using the combination of $w^{\delta_{\rm g}\delta_{\rm g}}(\theta)$ and $w^{\delta_{\rm g}\kappa_{\rm CMB}}(\theta)$ we obtain $\Omega_{\rm m} = 0.276^{+0.029}_{-0.030}$ and $S_8 = 0.800^{+0.090}_{-0.094}$. This can be compared with the results obtained using galaxy clustering and galaxy-galaxy lensing (i.e. $w^{\delta_{\rm g}\delta_{\rm g}}(\theta)$+$w^{\delta_{\rm g}\gamma_{\rm t}}(\theta)$), which

[10] We note that while certain systematics could add to the apparent signal and artificially inflate the significance, in this case the main contamination without scale cuts is tSZ, which artificially reduces $w^{\delta_{\rm g}\kappa_{\rm CMB}}$. In other words, in the absence of tSZ and scale cuts, the significance of this measurement would be higher than 19.9 σ.

gives $\Omega_{\rm m} = 0.294^{+0.047}_{-0.029}$ and $S_8 = 0.759^{+0.037}_{-0.031}$. We find that the constraining power is comparable despite the conservative scale cuts we have applied in this analysis, and we expect to obtain better signal in the future as we use galaxy samples at higher redshifts due to the better overlap with the CMB lensing kernel. We also combine $w^{\delta_{\rm g}\delta_{\rm g}}(\theta)$ and $w^{\delta_{\rm g}\kappa_{\rm CMB}}(\theta)$ with Planck TT+lowP likelihood obtaining an upper bound at 95% CL on the sum of neutrino masses of 0.81 eV, which slightly loosens the bound from Planck TT+lowP alone ($\sum m_\nu < 0.72$ eV at 95% CL).

The constraining power of DES measurements of galaxy-CMB lensing correlations has the potential to improve in future analyses. The DES-Y3 will cover the full 5000 deg^2 of the DES footprint at approximately the same depth as Y1. Since the extended area does not overlap with the SPT footprint, we expect the gain in the signal-to-noise to be small in terms of improvements in sky coverage. However, our analysis choice in this study is conservative; we have chosen the scale-cuts to minimize the biases in exchange for signal-to-noise ratio. To improve this measurement further, it will be essential to (1) characterize the bias to a higher accuracy, such that the signal loss is minimized, or (2) to improve the reconstruction of the CMB lensing map so that it is less prone to biases (see e.g. [107] for a discussion of modifications to temperature-based lensing reconstruction to minimize tSZ bias). Furthermore, newer data sets from SPT (SPTpol and SPT-3G [23]) have lower noise levels than SPT-SZ, and therefore, lensing maps generated from these data sets will have lower noise. Improvements along these lines will allow us to maximally extract the signal from this cross-correlation, and to reach the best possible accuracy on cosmology.

Chapter 4

Cosmological Constraints from Multiple Tracers

4.1 Context

Cosmic growth is parametrized by γ, which gives the growth rate as $f(z) = \Omega_m(z)^\gamma$. Modified gravity models can give different values of γ for the same expansion history, see e.g. [69, 83, 105]. On the other hand, non-gaussianity in the initial conditions of the universe is one of the most powerful mechanisms to discriminate among the competing theories of the early universe (see [19, 46] for reviews). Most of the models predict non-gaussianity of local type, i.e. a type of non-gaussianity that only depends on the local value of the potential. In this framework, the primordial gravitational potential can be parametrized as [68, 90]

$$\Phi = \phi + f_{\rm NL}(\phi^2 - \langle\phi^2\rangle) \tag{4.1}$$

where ϕ is a Gaussian field and $f_{\rm NL}$ describes the amplitude of the quadratic correction to the potential. In the simplest models of inflation primordial non-gaussianity (PNG) is predicted to be very small, $f_{\rm NL} \ll 1$ (see e.g. [7]), while many multi-field inflation models predict large non-gaussianity, $f_{\rm NL} \gg 1$ (see [38] for a review).

The random nature of fluctuations (sampling variance) limits the accuracy with which one can determine the matter power spectrum. McDonald & Seljak (2009) [110] proposed to use multiple tracers of the same underlying distribution to beat this limit and improve the constraints canceling

sampling variance with redshift space distortions (RSD), although this improvement can also be achieved with other observables, including $f_{\rm NL}$ [124, 149].

Bias-sensitive parameters, such as the redshift space distortions parameter, $\beta(z) = f(z)/b(z)$, and the amplitude of local non-Gaussianities, $f_{\rm NL}$, are related to the same realization of the density field. Therefore, comparing the clusterings between different types of tracers of large scale structure (LSS) enable us to measure these parameters with a precision that is not limited by cosmic variance. This technique has been explored in recent literature for spectroscopic and photometric galaxy surveys [5, 6, 14, 25, 71, 171].

At present, the best constraints on PNG come from Planck 2018 measurements of the three-point correlation function of the CMB temperature and polarization anisotropies [137], with $f_{\rm NL} = -0.9 \pm 5.1$ at 68% confidence level (CL), but large-scale structure is emerging as a promising complementary observable. The tightest constraints from large-scale structure are $-51 < f_{\rm NL} < 21$ at 95% CL from eBOSS Data Release 14 data [43]. It has been shown that non-gaussianity leads to a very unique dependence of the large scale bias, one that increases strongly towards large scales, and whose amplitude scales with the bias of the tracer relative to dark matter. Such large scales are affected strongly by cosmic variance. Thus, we can improve the expected constraints on $f_{\rm NL}$ by combining information from different LSS tracers (in a multi-tracer approach) to reduce the sample variance.

On the other hand, by combining two particular photometric galaxy samples there is a factor ~ 2.5 to be gained on the growth rate constraints compared to an analysis using just one sample [14]. In practice, the biases of the two samples may be correlated, which limits the potential gains of the multi-tracer approach.

In this work, we extend the idea of a multi-tracer analysis of RSD explored in [14] by including in addition the cross-correlations with CMB lensing in order to break possible degeneracies with the galaxy bias. We also explore the constraints that we could obtain with a multi-tracer analysis of local non-gaussianities, $f_{\rm NL}$, from photometric surveys. In addition, we forecast the constraints on RSD and $f_{\rm NL}$ considering the DES Y3 lens samples presented in §2.3.2: redMaGiC and magnitude limited.

4.2 Theory

We compute the anisotropic galaxy clustering using the equations from §1.5.3, and we include redshift space distortions through the Kaiser factors [87] (§1.5.2). In some parts of this work we include CMB lensing cross-correlations, which can be computed using (1.49) without the Kaiser factors and changing the radial selection functions, $\phi(z)$, by kernel functions,

$$\omega^{\delta_g \kappa_{\rm CMB}}(\theta) = \int\int dz_1 dz_2 W^{\delta_g}(z_1) W^{\kappa_{\rm CMB}}(z_2) \xi(s), \tag{4.2}$$

where $W^{\delta_g}(z)$ and $W^{\kappa_{\rm CMB}}(z)$ are the kernels related to the density contrast and CMB lensing convergence fields, respectively,

$$W^{\delta_g}(z) = b^i(z)\phi(z), \tag{4.3}$$

$$W^{\kappa_{\rm CMB}}(z) = \frac{3\Omega_m H_0^2}{2c} \frac{(1+z)}{H(z)} \chi(z) \frac{\chi_* - \chi}{\chi_*}(z), \tag{4.4}$$

and b^i is the linear galaxy bias of the tomographic bin i. This computation of the angular correlation function is exact, without assuming Limber approximation. We compute $\omega(\theta)$ using a code that we describe in §4.3. In order to obtain constraints on the growth index, γ, and on the amplitude of local primordial non-gaussianities, $f_{\rm NL}$, we modify the equations as described in the following sections §4.2.1 and §4.2.2. We calculate the power spectrum using the Boltzmann code CAMB [76, 96] with the Halofit extension to nonlinear scales [157, 163].

4.2.1 Growth history

The growth index can be conveniently defined as

$$f(z) \equiv \Omega_m^\gamma(z), \tag{4.5}$$

and $\gamma = 0.545$ for ΛCDM. Consistently with this, we obtain the growth history as,

$$D(z) \equiv \exp\left[-\int_0^z \frac{\Omega_m^\gamma(z)}{1+z} {\rm d}z\right], \tag{4.6}$$

where $D(z)$ is normalized to unity today ($z = 0$). It is shown in [102] that this is an accurate approximation for $D(z)$. The parameter γ is usually employed as an effective way of characterizing

modified gravity models that share the same cosmic history as General Relativity but different growth history [102].

4.2.2 Primordial non-gaussianities

In order to connect the density field δ to the gravitational potential Φ, we make use of the Poisson equation at late times (1.18)

$$\nabla^2\Phi = -\frac{3\Omega_m H_0^2}{2a}\delta. \tag{4.7}$$

At late times the gravitational potential Φ can be related to the primordial potential Φ_p by

$$\Phi(k,z) = \frac{T(k)D(z)}{a(z)}\frac{g(0)}{g(\infty)}\Phi_\mathrm{p}(k) \tag{4.8}$$

where $T(k)$ is the transfer function, and the factor $g(\infty)/g(0)$, with $g(z) = (1+z)D(z)$, arises due to our normalization of D(z) to unity at $z = 0$, and can be omitted if $D(z)$ is normalized to equal the scale factor, a, during the matter dominated era. From the Poisson equation (4.7), the primordial gravitational potential can be related to the density field via $\delta(k) = \alpha(k)\Phi_\mathrm{p}(k)$, with

$$\alpha(k) = \frac{2k^2T(k)D(z)}{3\Omega_m}\frac{c^2}{H_0^2}\frac{g(0)}{g(\infty)}, \tag{4.9}$$

Note that there are two conventions to define f_NL in (4.1): the LSS convention where Φ is normalized at $z = 0$, and the CMB convention where Φ is instead the primordial potential. Here we adopt the LSS convention. The relation between the two normalizations is $f_\mathrm{NL}^\mathrm{LSS} = g(\infty)/g(0)f_\mathrm{NL}^\mathrm{CMB} \approx 1.3 f_\mathrm{NL}^\mathrm{CMB}$.

In the presence of PNG, the local number of halos does not just depend on the large-scale matter perturbations, but it is also affected by the mode coupling between long and short wavelengths that acts like a local rescaling of the amplitude of (small-scale) matter fluctuations. The total bias, including local non-Gaussianity is then

$$b_\mathrm{tot} = b + \Delta b(k), \tag{4.10}$$

where b is the linear bias and $\Delta b(k)$ is the scale-dependent contribution due to PNG. In the local Ansatz this is given by [54, 155]

$$\Delta b(k) = 2(b-p)f_\mathrm{NL}\frac{\delta_\mathrm{crit}}{\alpha(k)}, \tag{4.11}$$

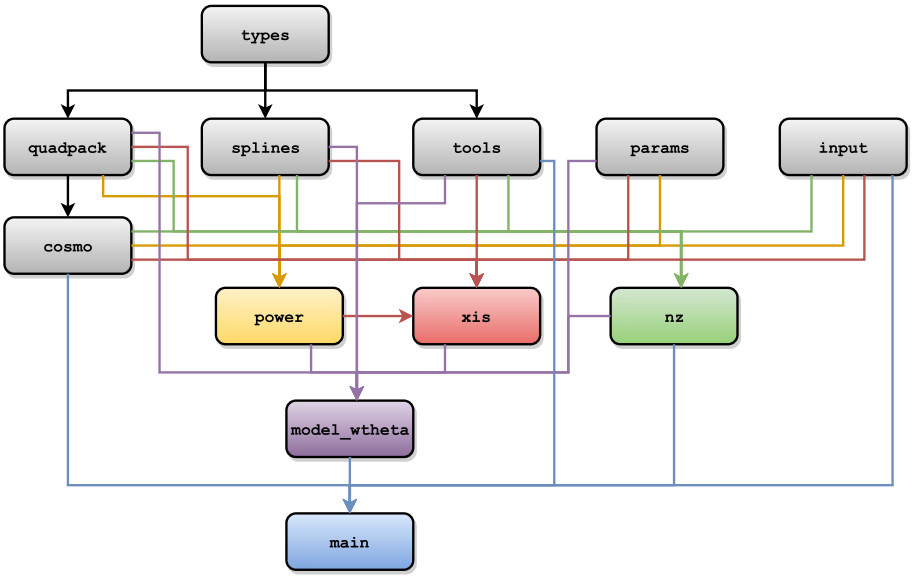

FIGURE 4.1: Dependency graph of the modules of the code.

where $\delta_{\rm crit} = 1.686$ and $1 < p < 1.6$ depending on the type of tracer. Here we follow [155] assuming $p = 1$ for galaxies. As seen in §1.5.2, in the limit of the plane parallel approximation, the linear matter power spectrum in redshift space is [87]

$$P(k,\mu) = (b_{\rm tot} + f\mu^2)^2 P_M(k), \tag{4.12}$$

where $P_M(k)$ is the linear matter power spectrum. The effect of PNG is included in the definition of the total bias.

4.3 Code implementation

We have developed a code that predicts the exact angular correlation function $\omega(\theta)$ (i.e. without assuming Limber approximation) given a matter power spectrum $P(k)$, a radial selection function $\phi(z)$ and a set of cosmological parameters. The $\omega(\theta)$ is then computed using the equations described in section 1.5.3 and in this chapter. In addition, we use the *local bias model* (see section 1.5.1) to estimate the galaxy angular correlation function.

The aim of this section is to describe the structure of the code developed in this work and its functionality. For this purpose, we briefly describe each one of the modules in the code. In

Figure 4.1, you can see a schema of its structure and the dependencies between modules.

Modules

`types` Includes definitions of different data types used in the code.

`params` Defines several parameters that are used in multiple modules across the code.

`input` Here we set the values of the cosmological parameters and the paths to the input files: mainly the power spectrum and the radial selection function.

`tools` Defines numerical constants used throughout the calculation, such as the number π, along with some utility tools, e.g. a subroutine that counts the number of lines in a file.

`splines` Includes two subroutines needed to obtain the cubic-spline interpolation of a set of data points. The first subroutine, `spline`, returns an array that contains the second derivatives of the interpolating function at the set of points given as input. Then, the second subroutine, `splint`, uses the set of points and the output from the previous `spline` subroutine to return a cubic-spline interpolated value. For further details, see [139].

`quadpack` Is a commonly used Fortran subroutine package for the numerical computation of definite one-dimensional integrals [127]. Aside from the quadpack subroutines, in this module we have also included the `gabq` subroutine for the computation of integrals using Gauss adaptive-bipartition quadrature, which is detailed in [63].

`cosmo` Computes several cosmological quantities, that are a function of the set of cosmological parameters from the `input` module. Some examples are the growth factor $D(z)$, the Hubble parameter $H(z)$ (1.14) and the radial comoving distance.

`nz` Reads the radial selection function $\phi(z_i)$ from the input file and then makes a change of units so that ϕ is a function of the radial comoving distance instead of the redshift z. It also normalizes the selection function to unity. It also includes the definition of the CMB lensing convergence kernel, $W^{\kappa_{\rm CMB}}$.

`power` Reads the matter power spectrum $P(k, z)$.

`xis` Computes the multipoles $\xi_0(s)$ and $\xi_2(s)$ using equation (1.66). If redshift space distortions are not considered, the parameter β is set to zero in equation (1.60).

`model_wtheta` Using the radial selection functions from `nz` and the multipoles $\xi_l(s)$ from `xis`, it computes the angular correlation function $\omega(\theta)$ using equation (1.62).

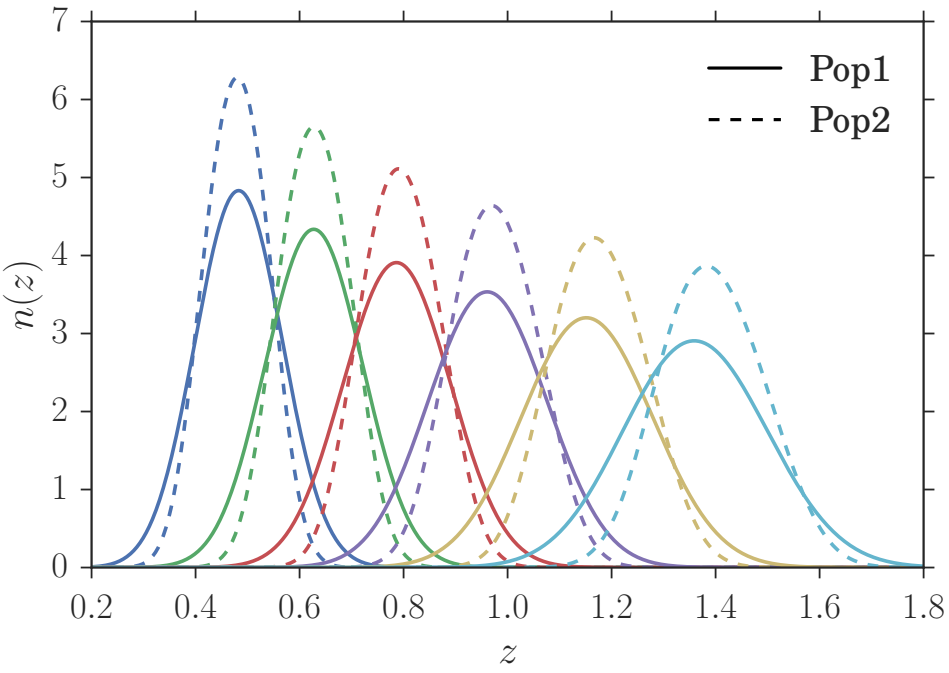

FIGURE 4.2: Normalized redshift distributions of the galaxy samples defined in A14.

main It calls the main subroutines of the code so that the computation of $\omega(\theta)$ is executed. Then, saves the result in an output file.

4.4 Data

In this work we reproduce the results in Asorey 2014 [14], hereafter A14, but in real space (instead of harmonic space) and we extend the analysis to include CMB lensing cross-correlations. Since the samples presented in A14 are optimistic, we then apply the method to the DES Y3 lens samples, which are more conservative and realistic. In this section we describe the fiducial galaxy samples we consider in our multi-tracer analysis.

In the first part of our analysis we use the same fiducial samples and photometric survey as described in A14. This corresponds to two galaxy sample populations: one with $b = 1$ constant across z, and photometric error $\sigma_z = 0.05(1 + z)$, and another with $b = 2$ and $\sigma_z = 0.03(1 + z)$. We refer to them as 'Pop1' and 'Pop2', respectively. These sample characteristics are based on the DES forecasts carried out in [16, 142], before DES observations started. We assume a total of 300 million galaxies observed in 1/8th of the sky ($f_{\rm sky} = 1/8$), which corresponds to ~ 5150

deg^2. We characterize the overall galaxy redshift distribution by

$$\frac{\mathrm{d}N}{\mathrm{d}z} = 4\pi f_{\rm sky} N_{\rm gal} \left(\frac{z}{0.5}\right)^2 \exp\left(-\frac{z}{0.5}\right)^{1.5}, \tag{4.13}$$

where $N_{\rm gal}$ is a normalization related to the total number of galaxies of the sample. We divide the sample in 6 z bins in the range $0.4 < z < 1.55$, assuming a z bin width of $\Delta z = 0.1(1+z)$. The redshift bin width evolves linearly with z to match the behavior of the photometric uncertainty σ_z.

The radial selection function in each redshift bin, $\phi(z)$, is the probability to include a galaxy in a given z bin. Thus, it is given by

$$\phi(z) = \frac{\mathrm{d}N}{\mathrm{d}z} W(z), \tag{4.14}$$

where $W(z)$ is the window function in each redshift bin. Since we are working with photometric redshifts, the window function can be obtained from,

$$W(z) = \int \mathrm{d}z_p P(z\,|z_p) W_{\rm ph}(z_p), \tag{4.15}$$

where z_p is the photometric redshift and $P(z\,|z_p)$ is the probability of the true redshift to be z if the photometric estimate is z_p. We assume that the individual redshift probability distribution for each galaxy, $P(z\,|z_p)$ is Gaussian with standard deviation given by the photometric uncertainty σ_z, and we bin in photometric z, which implies that $W_{\rm ph}(z_p)$ is a top-hat. This leads to

$$\phi(z) \propto \frac{\mathrm{d}N}{\mathrm{d}z} \left(\mathrm{erf}\left[\frac{z_{p,\rm max} - z}{\sqrt{2}\sigma_z}\right] - \mathrm{erf}\left[\frac{z_{p,\rm min} - z}{\sqrt{2}\sigma_z}\right]\right), \tag{4.16}$$

where $z_{p,\rm min}$ and $z_{p,\rm max}$ are the edges of each redshift bin. In Fig.4.2 we show the redshift distributions, $\phi(z)$, of the samples from A14 we consider in this work.

We then apply the multi-tracer approach to more realistic samples. For this purpose we consider the lens samples defined for the DES Y3 galaxy clustering analysis, that we present in §2.3.2. These consists of a redMaGiC sample and a magnitude limited sample. The fiducial galaxy bias values in each z bin that we assume for these samples are $b = 1.7, 1.7, 1.7, 2.0, 2.0$ for redMaGiC, and $b = 1.5, 1.8, 1.8, 1.9, 2.3, 2.3$ for the magnitude limited sample. These fiducial values for the galaxy bias are based on galaxy clustering measurements on a 10% subsample of the data, in consistency with the Y3 blinding scheme. We note that when we consider the DES Y3 samples we also assume the actual area covered in Y3, ~ 4182 deg^2.

4.5 Methodology

Our goal is to derive constraints on the growth of structure from redshift space distortions, and on the amplitude of primordial non-Gaussianities (PNG), $f_{\rm NL}$, using a multi-tracer approach to reduce sample variance. The multi-tracer approach consists in combining the two samples, that is, for each bin i we add the galaxy clustering cross-correlation of bin i between the two samples A, B, and we also include the corresponding correlations in the covariance matrix. We assume no overlap between galaxy samples A and B. We then compare the constraints coming from this combination, denoted by 'A x B', with the most constraining results coming from a single galaxy sample, either A or B. We analyze angular galaxy clustering using auto- and cross-correlations between different z bins. The latter allow us to include the radial modes that account for scales comparable to the bin separation. We also study the effect of including cross-correlations with CMB lensing in our analysis.

In the first part of our analysis, following A14, we obtain constraints on the growth index, γ, and $f\sigma_8$. Since $f\sigma_8$ depends on z, we associate one fitting parameter to each z bin, so that in practice we obtain constraints on $f\sigma_8$ evaluated at the mean z in each bin, which we assume to be the same for the bins of the two samples we consider. In the second part of our analysis we explore the constraints on $f_{\rm NL}$. In all cases we keep fixed all the cosmological parameters and only allow to vary the galaxy bias in each z bin, b^i, and the parameter of interest: either γ, $(f\sigma_8)^i$, or $f_{\rm NL}$. In the case of $(f\sigma_8)^i$ we actually allow to vary $(b\sigma_8)^i$ instead of b^i. In order to forecast the constraints on these parameters we use Fisher matrices. We assume a Gaussian likelihood,

$$\ln \mathcal{L}(\vec{d}|\vec{m}(\vec{p})) = -\frac{1}{2}\sum_{ij}^{N} \left(d_i - m_i(\vec{p})\right) \mathbf{C}_{ij}^{-1} \left(d_j - m_j(\vec{p})\right), \tag{4.17}$$

where N is the number of points in the data and model vectors. The Fisher matrix is then given by,

$$F_{ij} = \left\langle \frac{\partial^2 \left[-\ln \mathcal{L}(\vec{d}|\vec{m}(\vec{p}))\right]}{\partial p_i \partial p_j} \right\rangle, \tag{4.18}$$

whose inverse allows us to obtain an estimate of the error on the model parameters,

$$\Delta p_i \leq \sqrt{(F^{-1})_{ii}}. \tag{4.19}$$

The likelihood also depends upon the covariance matrix, $\mathbf{C}$, that describes how the points are correlated among them. This covariance also needs to take into account the correlation between the two galaxy samples, when we combine them, and with CMB lensing if included. Our method

to estimate the covariance matrix for our $\omega(\theta)$ predictions consists in an analytical prescription. We follow the approach of [52], which is based on the angular power spectrum C_l. For a full-sky survey, the covariance matrix in harmonic space is diagonal, with diagonal elements given by [see 60] $\sigma^2(C_l) = 2C_l^2/(2l+1)$. Given that the angular correlation function $\omega(\theta)$ is the Legendre transform of the angular power spectrum C_l,

$$\omega(\theta) = \sum_{l\geq 0}\left(\frac{2l+1}{4\pi}\right)P_l(\cos\theta)C_l, \tag{4.20}$$

and that the effect of observing only a fraction of the sky $f_{\rm sky}$ on the covariance, $\mathbf{C}$, between measurements is well approximated by $\mathbf{C} \sim f_{\rm sky}^{-1}\mathbf{C}^{\rm full\,sky}$ [see e.g. 39, 52, 142] one can arrive to,

$$\mathbf{C}^{XY}(\theta_i,\theta_j) = \sum_{l\geq 0}\frac{(2l+1)^2}{f_{\rm sky}(4\pi)^2}P_l(\cos\theta_i)P_l(\cos\theta_j)\sigma^2(C_l^{XY}), \tag{4.21}$$

where $\{X,\ Y\}$ denote fields $\{\kappa, g\}$, for CMB lensing and galaxy clustering, respectively. For galaxy clustering correlations $\sigma^2(C_l^{gg})$ is given by

$$\sigma^2(C_l^{gg}) = \frac{1}{2l+1}\left(C_l^{gg} + \frac{1}{\overline{n}}\right)^2, \tag{4.22}$$

where $1/\overline{n}$ is the number density of galaxies per steradian and accounts for the shot-noise of the galaxy counts, while the variance of galaxy-CMB lensing cross-correlations $\sigma^2(C_l^{g\kappa})$ is given by

$$\sigma^2(C_l^{g\kappa}) = \frac{1}{2l+1}\left[\left(C_l^{g\kappa}\right)^2 + \left(C_l^{gg} + \frac{1}{\overline{n}}\right)(C_l^{\kappa\kappa} + N^{\kappa\kappa})\right], \tag{4.23}$$

where $N^{\kappa\kappa}$ accounts for the primary CMB, instrumental and atmospheric noise for the CMB lensing maps. In this work we use $N^{\kappa\kappa}$ estimations from the combination of SPT and Planck data in the SPT-SZ survey area from [119] that was used in the DES Y1 analysis of cross-correlations with CMB lensing (see Chapter 3).

Throughout this work we assume a fiducial flat ΛCDM cosmology, with parameters: $\Omega_m = 0.25$, $\Omega_b = 0.045$, $h = 0.7$, $\tau = 0.08$, $n_s = 0.95$ and $\sigma_8 = 0.8$ at $z = 0$, where $h \equiv H_0/100\ \mathrm{kms}^{-1}$ We use the CosmoSIS pipeline to compute the theoretical predictions and the Fisher matrices, and we use the exact $\omega(\theta)$ computation described in §1.5.3 and §4.3, which we have implemented into the CosmoSIS pipeline.

4.6 Redshift Space Distortions

In this section we discuss the constraints on the growth index, γ, defined in (4.5), and on the more standard $f(z)\sigma_8(z)$ as a function of z. In both cases, we first compare our results with A14 using the same samples and survey specifications, and study the impact of including CMB lensing cross-correlations in the multi-tracer approach. We then explore the constraints we could obtain with the DES Y3 lens samples and survey area, and investigate ways of modifying these samples in order to optimize the constraints on γ and $f\sigma_8$.

4.6.1 Growth index

Let us first consider the constraints on the growth index, γ using the optimistic samples from A14. In Table 4.1 we show the 1σ expected constraints on γ considering the two samples separately and combined. The results we obtain are consistent with A14 and we find similar improvements when adding galaxy clustering cross-correlations between z bins and when combining the two galaxy samples. When including galaxy clustering cross-correlations, the constraints on γ improve almost a factor ~ 2 for Pop1 and a factor ~ 1.3 for Pop2. The reason behind the different improvement factors is due to the different photometric errors, σ_z. Pop2 has better photometric accuracy and, as seen in Fig. 4.2, consequently the overlap between different z bins (and the signal coming from z bin cross-correlations) is smaller. When combining the two samples we obtain almost a factor ~ 2 improvement on γ with respect to the most constraining galaxy sample (Pop1 in this case), which to a large extent is due to the sample variance cancellation.

We also study the effect of including galaxy clustering - CMB lensing cross-correlations in our analysis (denoted by '+ CMB') and see no impact in our constraints. Our interpretation is that the addition of CMB lensing correlations mainly improves the constraints on the galaxy bias, as possible degeneracies with the bias are broken by the different scaling of galaxy clustering ($\propto b^2$) and CMB lensing cross-correlations ($\propto b$). It is shown in A14 that fixing the galaxy bias only improves the RSD constraints slightly, which is consistent with the results we obtain when including CMB lensing cross-correlations. In our case, the improvement on the constraints is almost negligible because we are not fixing the bias, but only reducing the errors on this parameter. Hence in what follows, we concentrate in galaxy clustering only.

We then consider the DES Y3 lens samples, presented in §2.3.2, and the area they cover, which is a little less than considered in A14. The results for galaxy clustering auto- and cross-correlations

Sample(s)	gg auto	gg auto + cmb	gg cross	gg cross + cmb
Pop1	0.42	0.42	0.23	0.23
Pop2	0.46	0.46	0.37	0.37
Pop1 x Pop2	0.38	0.37	0.12	0.12

Table 4.1: Forecasted 68% CL constraints on γ using the samples from A14, considering galaxy auto-correlations ('gg auto'), galaxy auto and cross-correlations ('gg cross'), and these two with the addition of galaxy-CMB lensing cross-correlations ('CMB'). Pop1 x Pop2 includes the cross-correlation of the galaxy clustering from the two samples.

Sample(s)	gg auto	gg cross
redMaGiC	0.45	0.40
Mag lim	0.46	0.37
redMaGiC x Mag lim	0.37	0.28

Table 4.2: Forecasted 68% CL constraints on γ using the DES Y3 lens samples (§2.3.2), considering galaxy auto-correlations ('gg auto'), galaxy auto and cross-correlations ('gg cross'). 'redMaGiC x Mag lim' includes the cross-correlation of the galaxy clustering from the two samples.

are shown in Table 4.2. The constraints we obtain with galaxy auto-correlations are comparable to the previous results with the samples from A14. However, we find a smaller improvement when including galaxy cross-correlations between z bins, just a factor ~ 1.12 for redMaGiC and ~ 1.3 for the magnitude limited sample. This makes sense, as the redMaGiC galaxies have been selected to optimize photo-z accuracy, and hence the overlap between z bins is small, being negligible for non-adjacent z bins (see Fig. 2.4). The galaxy redshift distributions of the magnitude limited sample are slightly wider (Fig. 2.5), this is why in this case we gain more information when including cross-correlations.

When combining the redMaGiC and magnitude limited samples we only obtain a factor ~ 1.34 improvement on γ when considering a full tomographic analysis (including cross-correlations). We note that now the two samples have different tomographic binning and number of z bins. However, when we combine the two samples, we follow the same procedure: we include the galaxy cross-correlation between samples A and B of the same z bin, even if the z edges of the bin are different in each sample. We have repeated the analysis using the same tomographic binning and number of bins for both samples, finding similar results and somewhat worse constraints due to the fact that we lose information by removing the last z bin of the magnitude limited sample.

This gain when combining the two samples is smaller compared to the samples from A14. It has

Sample(s)	gg auto	gg cross
redMaGiC Low Bias (LB)	0.41	0.36
Mag lim High Bias (HB)	0.51	0.45
redMaGiC LB x Mag lim HB	0.29	0.26

Table 4.3: Forecasted 68% CL constraints on γ using the DES Y3 lens samples (§2.3.2), redMaGiC and magnitude limited, modified in order to have 20% lower and 20% higher values for the galaxy bias, respectively. The magnitude limited sample here has the same z binning as redMaGiC.

been shown in [12] that, in order to have sample variance cancellation, the bias values of the two samples need to be different; and the larger the bias difference, the greatest the improvement on the γ constraints with the multi-tracer approach. In addition, RSD become more important with lower bias values [12, 14, 142]. The DES Y3 lens samples we consider here have very similar bias values, around $b \sim 2$. For this reason we believe that we find a smaller improvement with the multi-tracer approach due to the samples not being optimal for this analysis, which it is understandable, as they have been optimized for the cosmological analysis of galaxy clustering in combination with cosmic shear.

In the following, we attempt to understand how we should modify the Y3 lens samples in order to have a larger gain from a multi-tracer approach. For this purpose, we consider both samples with the same tomographic binning and number of z bins. Thus, we remove the last z bin of the magnitude limited sample and we divide it in the same tomographic binning as redMaGiC. In Table 4.3 we compare the constraints on γ from the two samples and their combination, where we have modified their bias values to increase the bias difference between the two samples. We consider the redMaGiC sample with 20% lower bias, $b = 1.35, 1.35, 1.35, 1.6, 1.6$, and the magnitude limited sample with 20% higher bias, $b = 1.8, 2.2, 2.2, 2.3, 2.7$.

In Table 4.3 we see that by lowering the bias values we obtain tighter constraints on γ, in concordance with [12, 14, 142]. By combining the two modified samples in a full tomographic analysis we obtain a factor ~ 1.4 of improvement with respect to just one galaxy sample. Thus, the gain from the multi-tracer approach has improved with the bias difference, but it is still far from the factor ~ 2 from A14. It is rather likely that the samples are still not optimal for this analysis. Other possibilities to consider are increasing the number of galaxies (in order to reduce the shot-noise), increase the bias difference even more, and modify the width of the tomographic binning. We leave the study of these characteristics for future work.

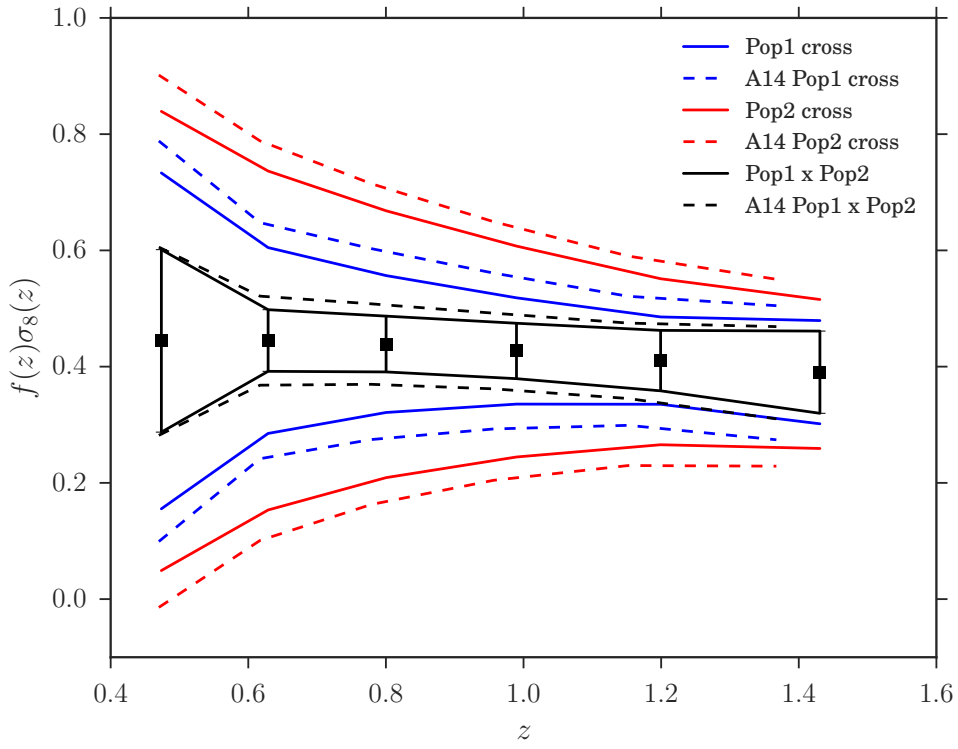

FIGURE 4.3: Constraints on $f(z)\sigma_8(z)$ derived at different redshift bins from a multi-tracer analysis (black) compared to a single tracer analysis (red and blue) from A14 (dashed lines) and this work (in solid).

4.6.2 Redshift evolution of the growth rate of structure

So far, we have used the combined analysis of all z bins to constrain one global parameter, the growth rate index γ. We now turn into constraining $f(z)\sigma_8(z)$ itself, as a function of redshift. In Fig. 4.3 we first compare our results with A14. While our constraints are consistent with A14 in that we find the same level of improvement when combining the two samples with respect to the constraints from a single tracer, on the other hand, we find systematically lower errors on $f(z)\sigma_8(z)$ for each one of the cases considered. We note that there are some differences between our analysis and A14. We perform the analysis in configuration space instead of harmonic space and we are not using exactly the same galaxy samples. Even though we have defined the samples based on the description in A14, there are some differences in the radial selection functions. In A14 it is shown that the RSD measurement is sensitive to the width of the tomographic binning. The fact that the z range in this work is slightly larger compared to A14[1] seems to indicate that, consequently, the width Δz is slightly different. This explains the offset with A14 constraints in

[1] In this work the range is $0.4 < z < 1.55$ while in A14 is $0.4 < z < 1.4$.

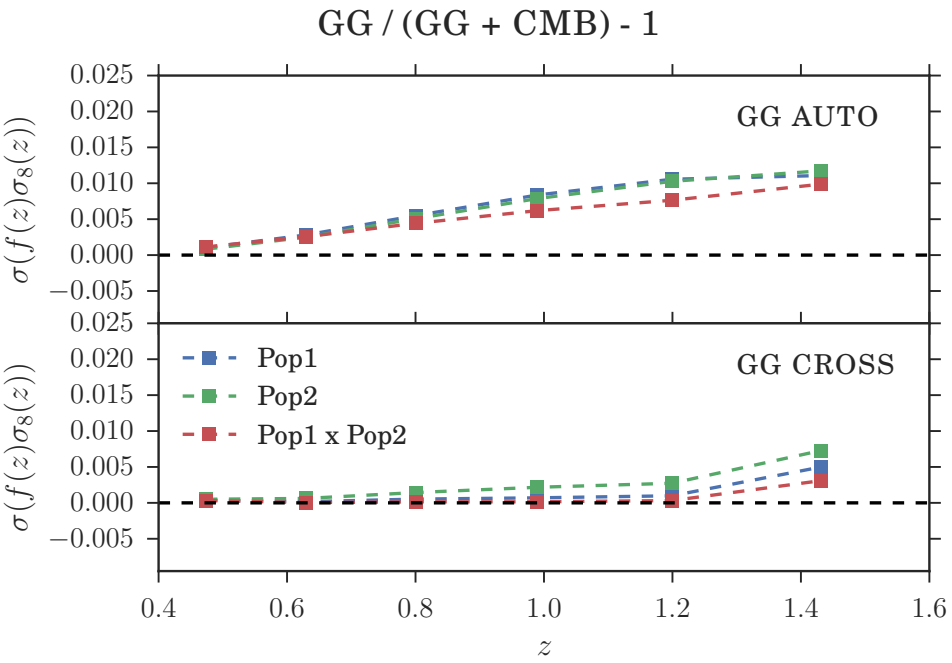

FIGURE 4.4: Comparison of constraints on $f(z)\sigma_8(z)$ from galaxy clustering auto- (top panel) and cross-correlations (bottom panel) with the addition of CMB lensing cross-correlations. We consider the samples from A14, namely Pop1 (blue), Pop2 (green) and their combination (red).

Fig. 4.3.

In the previous section we have explored the inclusion of galaxy clustering and CMB lensing cross-correlations in the analysis of the growth index. Similarly, in Fig. 4.4 we compare the constraints from galaxy clustering alone with those from galaxy clustering and CMB lensing correlations considering the samples from A14. We find that there is a slight improvement on the $f(z)\sigma_8(z)$ constraints when including CMB lensing cross-correlations. However, the improvement is negligible, $\sim 1\%$ or smaller. Thus, in the following we do not include CMB lensing cross-correlations.

We now consider the DES Y3 lens samples (§2.3.2), REDMAGIC and magnitude limited. Since we fit $f(z)\sigma_8(z)$ at the mean redshift of each bin, in order to combine the two samples in a multi-tracer approach, the two samples need to have similar tomographic binning. For this purpose, here we modify the magnitude limited sample to have the same tomographic binning as REDMAGIC. In Fig. 4.5 we compare the constraints on $f(z)\sigma_8(z)$ using REDMAGIC (red) and the magnitude limited sample (blue) with their combination (black). We consider two scenarios: using only galaxy clustering auto-correlations (left panel) and including cross-correlations between z bins

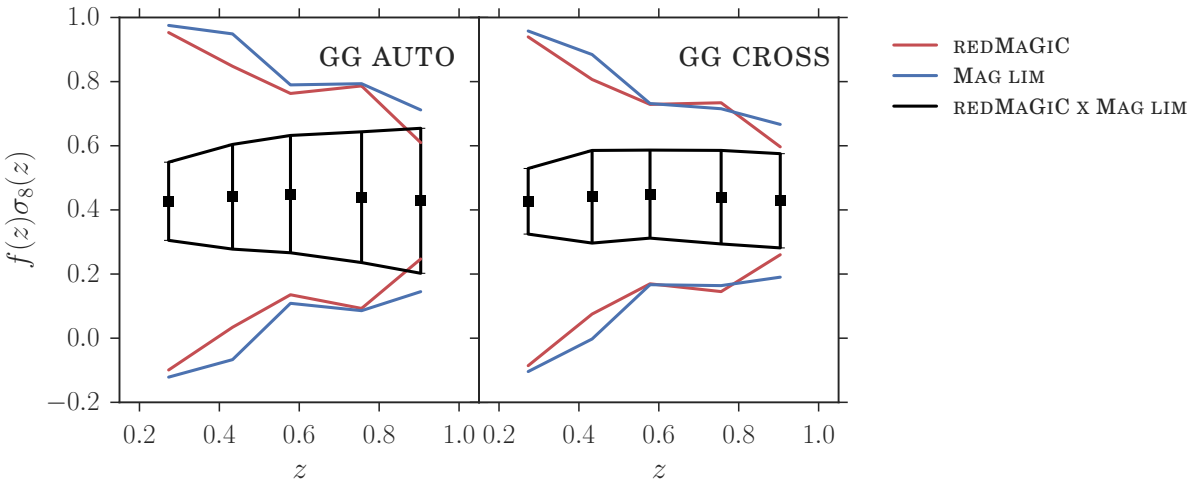

FIGURE 4.5: Constraints on $f(z)\sigma_8(z)$ from galaxy clustering auto- (left) and cross-correlations (right). We consider the DES Y3 lens samples (§2.3.2), reDMaGiC (red) and magnitude limited (blue), and their combination (black). The magnitude limited sample here has the same z binning as reDMaGiC.

(right panel).

We find that when considering a single tracer, both reDMaGiC and magnitude limited samples provide comparable constraints due to the relatively low bias difference between the samples. When including cross-correlations we do not find much improvement in the single tracer constraints, similarly to our results for the growth index γ. However, we do find a remarkable improvement with the multi-tracer approach, specially at low z, in consistency with A14. In addition, the multi-tracer approach benefits from the inclusion of cross-correlations between z bins. With a full tomographic analysis, the improvement is around a factor ~ 2, except for the first bin in which it is a factor ~ 5, and the last bin, in which the improvement is very small (~ 1.13).

If we compare our predictions to measurements from spectroscopic surveys like VIPERS [126] with constraints $f\sigma_8(z = 0.6) = 0.55 \pm 0.12$ or WiggleZ [30] where $f\sigma_8(z = 0.6) = 0.390 \pm 0.063$ and $f\sigma_8(z = 0.44) = 0.413 \pm 0.080$, we find that with a full tomographic multi-tracer analysis using the DES Y3 lens samples we can achieve a similar level of errors (e.g. $\sigma(f\sigma_8(z = 0.27)) = 0.10$, $\sigma(f\sigma_8(z = 0.58)) = 0.14$) in determining the growth of structure, specially at low z, where the gain from the multi-tracer approach is the largest.

We now explore the impact of modifying the relative bias between the samples on the $f(z)\sigma_8(z)$ constraints. In Fig. 4.6 we compare the 1σ errors from the two DES samples, modified in such

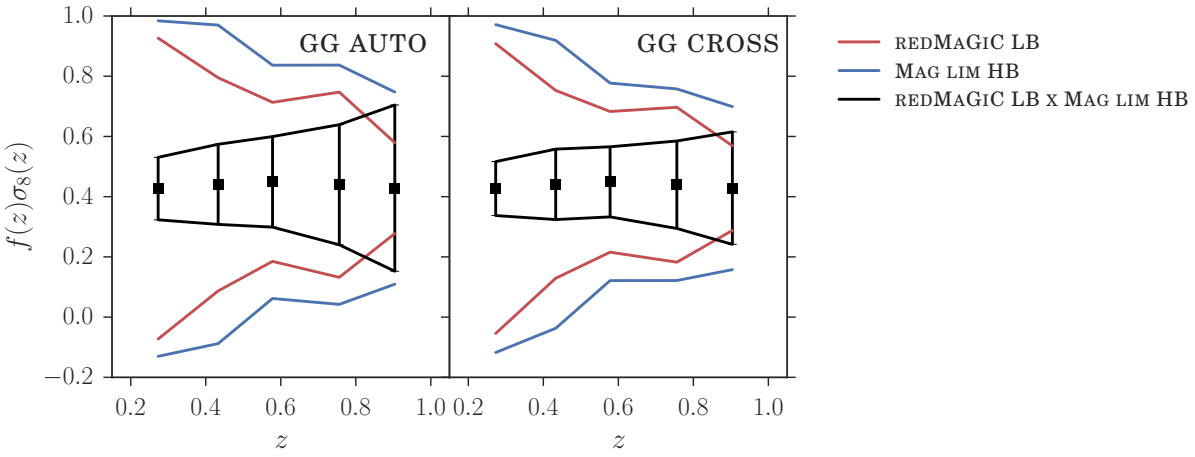

FIGURE 4.6: Constraints on $f(z)\sigma_8(z)$ from galaxy clustering auto- (left) and cross-correlations (right). We consider the DES Y3 lens samples (§2.3.2), REDMAGIC (red) and magnitude limited (blue), modified in order to have 20% lower and 20% higher values for the galaxy bias, respectively. The magnitude limited sample here has the same z binning as REDMAGIC.

a way that REDMAGIC has 20% lower bias and the magnitude limited sample 20% higher bias values. Since the RSD signal is boosted for lower bias values, now we see an improvement on the REDMAGIC constraints. The downside of having worse constraints coming from the magnitude limited sample (due to the increase on b) is that at high z the errors on $f(z)\sigma_8(z)$ degrade when combining the two samples with respect to REDMAGIC alone. A possible explanation for this is that, due to the difference in constraining power, at high z the gain we obtain by including the magnitude limited sample does not compensate the fact we are introducing 5 extra bias parameters in our analysis.

4.7 Local primordial non-gaussianities

In this section we discuss the constraints on the amplitude of local primordial non-Gaussianities, $f_{\rm NL}$, from a multi-tracer approach. In Table 4.4 we show the constraints from galaxy auto- (left) and cross-correlations (right) using the samples from A14, where we have modified the bias of Pop1 to $b = 1.2$ in order to have sensitivity to $f_{\rm NL}$. It can be seen from (4.11) that for $b = 1$ (and $p = 1$, which we are assuming) the contribution to the total bias coming from PNG vanishes. Table 4.4 shows that there is not much information on $f_{\rm NL}$ to be gained from the inclusion of cross-correlation between z bins. However, by combining the galaxy clustering from the two samples we can improve the constraints on $f_{\rm NL}$ by a factor ~ 2.3 from galaxy auto-correlations

Sample(s)	gg auto	gg cross
Pop1 ($b = 1.2$)	26.2	24.5
Pop2	8.3	8.2
Pop1 ($b = 1.2$) x Pop2	3.6	2.3

Table 4.4: Forecasted 68% CL constraints on $f_{\rm NL}$ using the samples from A14, considering galaxy auto-correlations ('gg auto'), galaxy auto and cross-correlations ('gg cross'), and these two with the addition of galaxy-CMB lensing cross-correlations ('CMB'). We have modified the bias of Pop1 to $b = 1.2$.

Sample(s)	gg auto	gg cross
redMaGiC	22	21.9
Mag lim	17.4	16.7
redMaGiC x Mag lim	15.3	15

Table 4.5: Forecasted 68% CL constraints on $f_{\rm NL}$ using the DES Y3 lens samples (§2.3.2), considering galaxy auto-correlations ('gg auto'), galaxy auto and cross-correlations ('gg cross'). 'redMaGiC x Mag lim' includes the cross-correlation of the galaxy clustering from the two samples.

alone, and a factor ~ 3.6 if we include cross-correlations between bins. Therefore, galaxy clustering measurements of $f_{\rm NL}$ can greatly benefit from a multi-tracer approach.

We now consider the DES Y3 samples, as described in §2.3.2, i.e. the magnitude limited sample has different tomographic binning compared to redMaGiC and an additional bin at higher z. In Table 4.5 we show the $f_{\rm NL}$ constraints from these two samples and their combination. Again, we find negligible gain from the inclusion of cross-correlations between bins. We see that the magnitude limited sample has more constraining power on $f_{\rm NL}$ than redMaGiC due to the fact that it is more biased, it has larger number density and it covers a greater z range. In fact, using the magnitude limited sample with just galaxy clustering auto-correlations, we could potentially obtain a 68% CL constraint on $f_{\rm NL}$ of 17.4, which is a great improvement compared to the tightest constraint from large-scale structure until now, $-51 < f_{\rm NL} < 21$ at 95% CL from eBOSS Data Release 14 data [43]. However, when combining the two samples we only find a factor ~ 1.15 of improvement compared to the most constraining single tracer. Again, this is probably due to these samples not being optimal for a multi-tracer analysis of $f_{\rm NL}$.

In an attempt to understand the effect of the bias difference between the two samples in the multi-tracer measurement of $f_{\rm NL}$, in Table 4.6 we compare the constraints from the two DES Y3 lens samples, where we have modified them in such a way that redMaGiC has 20% lower

Sample(s)	gg auto	gg cross
redMaGiC Low Bias (LB)	31.5	31.3
Mag lim High Bias (HB)	16.0	15.5
redMaGiC LB x Mag lim HB	14.6	13.2

Table 4.6: Forecasted 68% CL constraints on $f_{\rm NL}$ using the DES Y3 lens samples (§2.3.2), redMaGiC and magnitude limited, modified in order to have 20% lower and 20% higher values for the galaxy bias, respectively.

bias and the magnitude limited sample 20% higher bias values. In addition, now the magnitude limited sample has the same tomographic binning as redMaGiC. We find that the constraints on $f_{\rm NL}$ improve when considering a more biased tracer and degrade if we lower the galaxy bias, contrary to what happens when measuring RSD. However, we do not find much improvement from the multi-tracer approach, just a factor ~ 1.2 when including cross-correlations between bins. We may need to have an even larger bias difference between the two tracers in order to take full advantage of the multi-tracer approach. It is also possible that the lower number density of the redMaGiC sample holds down the possible gain from sample variance cancellation. We leave further studies on the optimization of these samples for future work.

4.8 Summary

In this chapter we have explored the constraints on RSD (for the growth index γ and $f(z)\sigma_8(z)$) and on PNG through the $f_{\rm NL}$ parameter using a multi-tracer approach. We have first reproduced the constraints on RSD from A14 in real space instead of harmonic space, and then we have studied the impact of including CMB lensing cross-correlations in our analysis. We have found that including CMB lensing cross-correlations has a negligible impact on the RSD constraints, at least in this case in which we leave the shape of the matter power spectrum $P(k,z)$ fixed (we only allow to vary the galaxy bias and the parameter of interest).

We have then measured RSD with the DES Y3 lens samples: redMaGiC and magnitude limited. In this case, we do not gain much if we include cross-correlations between z bins, due to the better photometric accuracy compared to the samples considered in A14. Our predictions from a full tomographic multi-tracer analysis are comparable to the latest measurements from spectroscopic surveys. While we find a great improvement of the $f(z)\sigma_8(z)$ constraints with a multi-tracer approach (specially at low z in which we can improve the constraints by a factor ~ 5), we only find a minor improvement on γ, a factor ~ 1.34. This may be due to a number of reasons, as

these samples have not been optimized for a multi-tracer measurement of RSD.

Since one of the characteristics that is important for sample variance cancellation is that the two tracers considered have large galaxy bias differences, we study the impact of the relative bias by lowering the bias of redMaGiC by 20% and increasing the bias of the magnitude limited sample by 20%. The RSD sensitivity is greater the lower the galaxy bias of the tracer. Therefore, the constraints from the magnitude limited sample degrade while the ones from redMaGiC improve. As a consequence, when combining the two samples we obtain somewhat less constraining measurements on $f(z)\sigma_8(z)$ at high z. This is probably due to the fact that the constraining power of the magnitude limited sample with such high bias values ($b = 2.7$ at the last bin) is not enough to compensate the fact that we are adding 5 more bias parameters allowed to vary. At low z we do find some improvement because the bias of both samples is lower. When measuring γ, however, we combine the information of all the z bins into one global parameter, and as a consequence the gain due to the increase in relative bias at low z is compensated by the poorer constraining power of the more biased sample at high z, and as a result we do not find much improvement in the constraints from the combination of the two samples, just a factor ~ 1.4.

We also explore the potential constraints on the amplitude of local PNG, $f_{\rm NL}$. We first consider the samples from A14, where we have increased the bias of Pop1 by a 20% in order to have a biased tracer. We find negligible improvement on the constraints with the inclusion of cross-correlations between z bins. However, by combining the two samples we can improve the constraints by a factor ~ 2.3 with galaxy auto-correlations only, and by a factor ~ 3.6 with a full tomographic analysis.

We then consider the DES Y3 lens samples, where we find that the magnitude limited sample is more constraining than redMaGiC due to the larger number density and higher bias. Our forecasts show that we could potentially obtain a 68% CL error on $f_{\rm NL}$ of 17.4 from the magnitude limited sample galaxy auto-correlations only, while the tightest constraints from large-scale sructure until now are $-51 < f_{\rm NL} < 21$ at 95% CL [43]. However, when combining the two samples we only find a factor ~ 1.15 of improvement.

We also explore the impact of increasing the relative bias between the two samples, by lowering the redMaGiC bias by 20% and increasing the magnitude limited sample bias by 20%. In the case of PNG measurements, we benefit from having more biased tracers. Thus, we find that the constraint coming from the magnitude limited sample increases, while the one from redMaGiC degrades. However, we do not find much improvement with a multi-tracer approach compared to the original DES Y3 samples. Similarly to what we have found with γ, this could be due to the

bias difference or the number density not being large enough (i.e. the samples not being optimal for constraining $f_{\rm NL}$ with a multi-tracer approach).

We leave to future work extending this analysis to allow to vary all cosmological parameters and other nuisance parameters, such as uncertainties in the photometric redshift estimations. We will also look further into how we should modify the DES Y3 lens samples in order to optimize them for the multi-tracer measurements of RSD an PNG. In addition, we plan on testing the impact of including CMB lensing cross-correlations in the multi-tracer measurement of $f_{\rm NL}$.

Chapter 5

Impact of Lens Sample on Cosmological Constraints from Multiple Probes

5.1 Context

As described in §2.3.2, in the DES Y3 analysis we will use two different lens samples to measure galaxy clustering and combine it with cosmic shear measurements. The first one consists of luminous red galaxies (LRG) that have been selected with the redMaGiC algorithm. This is the method that was used for the Y1 analysis and it has the advantage of selecting galaxies which have a small photometric uncertainty. The second one, the magnitude limited sample, is a flux limited sample that reaches higher number density and redshift than redMaGiC, with the caveat that it has slightly worse photometric accuracy.

In this chapter we describe and optimize the selection of the magnitude limited sample in terms of its cosmological constraints in σ_8, Ω_m and w, as these are the main parameters that are constrained in the joint analysis of galaxy clustering and weak lensing from DES data [2]. For this purpose we rely on Fisher forecasts, that we validate with some selected MCMC runs. We test how the forecasts on these cosmological parameters vary given the modifications obtained for the number density and estimated redshift uncertainty given by a set of magnitude cuts.

We also characterize the impact of redshift binning choices in our cosmological constraints for both samples and compare their final number densities and estimated redshift distributions. We finally forecast the cosmological constraints from the combination of galaxy clustering and

galaxy-galaxy lensing using redMaGiC and the magnitude limited sample, finding comparable constraints, and potentially 15% tighter 1σ errors with the magnitude limited sample.

5.2 Theory

Similarly to §3.3, under the Limber approximation [103] we can construct the galaxy clustering angular correlation function in the following way,

$$\omega^i(\theta) = \int \frac{\mathrm{d}\ell\,\ell}{2\pi} J_0(\ell\theta) \int d\chi \frac{q^i_{\delta_\mathrm{g}}\left(\frac{\ell+\frac{1}{2}}{\chi},\chi\right) q^i_{\delta_\mathrm{g}}\left(\frac{\ell+\frac{1}{2}}{\chi},\chi\right)}{\chi^2} P_\mathrm{NL}\left(\frac{\ell+\frac{1}{2}}{\chi}, z(\chi)\right), \tag{5.1}$$

where $P_\mathrm{NL}(k,z)$ is the non-linear matter power spectrum, J_0 is the first order Bessel funciton, and $q^i_{\delta_\mathrm{g}}$ is the density kernel,

$$q^i_{\delta_\mathrm{g}} = b^i(k,z(\chi)) \frac{n^i_\mathrm{g}(z(\chi))}{\bar{n}^i_\mathrm{g}} \frac{dz}{d\chi}. \tag{5.2}$$

Here $b^i(k,z)$ is the galaxy bias and $n^i_\mathrm{g}(z)$ is the redshift distribution of the i-th galaxy sample with total density $\bar{n}^i_\mathrm{g}$. For galaxy-galaxy lensing, we model the tangential shear, which consists of the correlation of lens galaxy positions in bin i with source galaxy shear in bin j. On large scales, it can be expressed as an integral over the power spectrum,

$$\gamma^{ij}_\mathrm{t}(\theta) = (1+m^j) \int \frac{\mathrm{d}\ell\,\ell}{2\pi} J_2(\ell\theta) \int d\chi \frac{q^i_{\delta_\mathrm{g}}\left(\frac{\ell+\frac{1}{2}}{\chi},\chi\right) q^j_\kappa(\chi)}{\chi^2} P_\mathrm{NL}\left(\frac{\ell+\frac{1}{2}}{\chi}, z(\chi)\right), \tag{5.3}$$

where m^j is the multiplicative shear bias in order to take into consideration potential biases in the inferred shears (see §5.3), J_2 is the second order Bessel function, and q_κ is the lensing efficiency (1.77),

$$q^i_\kappa(\chi) = \frac{3H_0^2\Omega_\mathrm{m}}{2c^2} \frac{\chi}{a(\chi)} \int_\chi^{\chi_\mathrm{lim}} \mathrm{d}\chi' \frac{n^i_\kappa(z(\chi'))\mathrm{d}z/\mathrm{d}\chi'}{\bar{n}^i_\kappa} \frac{\chi'-\chi}{\chi'}, \tag{5.4}$$

where χ_lim is the limiting comoving distance of the galaxy sample and $n^i_\kappa(z)$ is the redshift distribution of the i-th source galaxy sample with total density $\bar{n}^i_\kappa$. The cosmic shear signal is independent of galaxy bias but shares the same general form as the other sets of two-point functions. The theoretical predictions for these shear-shear two point functions are

$$\xi^{ij}_{+/-}(\theta) = (1+m^i)(1+m^j) \int \frac{\mathrm{d}\ell\,\ell}{2\pi} J_{0/4}(\ell\theta) \int d\chi \frac{q^i_\kappa(\chi)\, q^j_\kappa(\chi)}{\chi^2} P_\mathrm{NL}\left(\frac{\ell+\frac{1}{2}}{\chi}, z(\chi)\right), \tag{5.5}$$

where the efficiency functions are defined above, and J_0 and J_4 are the (0th and 4th order) Bessel functions for ξ_+ and ξ_-. We calculate the power spectrum using the Boltzmann code CAMB[1] [76, 96] with the Halofit extension to nonlinear scales [157, 163] and the neutrino extension from [29].

5.3 Data

All the likelihood analyses in this work use theory data vectors. However, the galaxy redshift distributions and galaxy number densities, that enter into the covariance and theory data vector computations, are taken from the data. For the galaxy clustering analysis we use two different galaxy samples, as described in §2.3.2. These are the so-called DES Y3 REDMAGIC and magnitude limited samples.

For the galaxy-galaxy lensing analysis we use these galaxy samples as lenses and the DES Y1 METACALIBRATION [81, 151] shear catalog as sources. METACALIBRATION uses the data itself to calibrate shear estimates by artificially shearing the galaxy images and re-measuring the shear to determine the response of the shape measurement to gravitational shear. METACALIBRATION also includes an algorithm for calibration of shear-dependent selection effects of galaxies, which could bias shear statistics at the few percent level otherwise. This calibration is carried out by measuring on both unsheared and sheared images all those galaxy properties that are used to select, bin, and weight galaxies in the catalog. Details of the practical application of these corrections are given in [138, 151, 166, 177]. Potential biases in the inferred shears are quantified by multiplicative shear-calibration parameters m^i in each source redshift bin i, such that the measured shear is related to the true shear in this way,

$$\gamma_{\rm meas} = (1 + m^i)\gamma_{\rm true}. \tag{5.6}$$

Conservative cuts on S/N and size have been applied to the shear catalog, which reduce the number of galaxies with shear estimates relative to the Y1 Gold input catalog significantly. After masking and binning the catalog, the final number of galaxy shapes in the METACALIBRATION sample is ~ 26 million down to an r-band magnitude of ≈ 23.

The METACALIBRATION sample is divided into 4 tomographic bins: $0.2 < z < 0.43$, $0.43 < z < 0.63$, $0.63 < z < 0.9$, and $0.9 < z < 1.3$, where here z is the mean of the redshift PDF for each galaxy

[1] See `camb.info`.

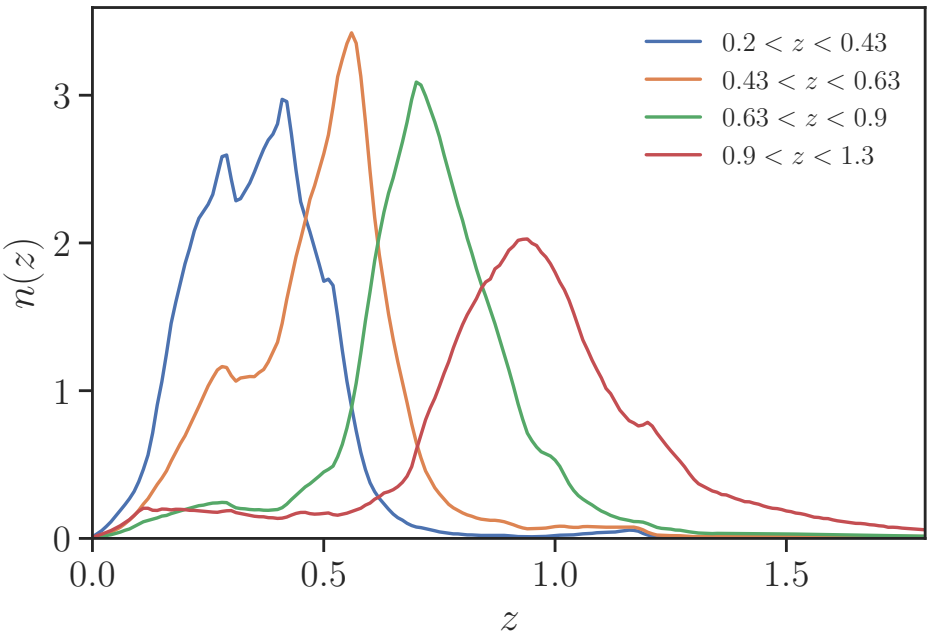

FIGURE 5.1: Normalized redshift distributions of the DES Y1 METACALIBRATION source galaxies.

as estimated from a modified version of the Bayesian Photometric Redshifts (BPZ) algorithm [21], detailed in [77]. These bin assignments are based upon photo-z estimates derived using photometric measurements made by the METACALIBRATION pipeline in order to allow for correction of selection effects. The resulting normalized redshift distributions are shown in Fig.5.1.

5.4 Methodology

In this work we run simulated likelihood analysis with both Fisher forecasts and Markov Chain Monte Carlo (MCMC) methods using noiseless theory data vectors (i.e. a theoretical prediction evaluated at the fiducial cosmology, that we maintain fixed in the likelihood sampling). For both approaches we need to sample the likelihood in the n-dimensional parameter space, where n is the number of parameters we vary in our analysis (see Table 5.4). We assume a Gaussian likelihood,

$$\ln \mathcal{L}(\vec{d}|\vec{m}(\vec{p})) = -\frac{1}{2}\sum_{ij}^{N} \left(d_i - m_i(\vec{p})\right) \mathbf{C}_{ij}^{-1} \left(d_j - m_j(\vec{p})\right), \tag{5.7}$$

where N is the number of points in the data and model vectors. The posteriors on the model parameters are given by:

$$P(\vec{m}(\vec{p})|\vec{d}) \propto \mathcal{L}(\vec{d}|\vec{m}(\vec{p}))P_{\rm prior}(\vec{p}), \tag{5.8}$$

where $P_{\rm prior}(\vec{p})$ is the prior on the model parameters. The Fisher matrix is then given by,

$$F_{ij} = \left\langle \frac{\partial^2 \left[-\ln P(\vec{m}(\vec{p})|\vec{d})\right]}{\partial p_i \partial p_j} \right\rangle, \tag{5.9}$$

whose inverse allows us to obtain an estimate of the error on the model parameters,

$$\Delta p_i \leq \sqrt{(F^{-1})_{ii}}. \tag{5.10}$$

The Fisher forecasts can provide inaccurate results for non-gaussian posterior distributions (e.g. when there are degeneracies between parameters), but they have the advantage that they are computationally much less expensive. For this reason, in this work we use Fisher forecasts when we want to compare the constraints of many different data vectors, and then we validate our conclusions with a full exploration of the likelihood using an MCMC method.

We use the CosmoSIS pipeline to compute the theoretical predictions, the Fisher matrices, and to generate the MCMC samples that map out the posterior space leading to parameter constraints. For the latter, we use the publicly available MultiNest sampler [64].

The likelihood also depends upon the covariance matrix, $\mathbf{C}$, that describes how the points are correlated among them. This covariance also needs to take into account the correlation between different probes, such as galaxy clustering and galaxy-galaxy lensing. We use analytical Gaussian covariance matrices generated using CosmoLike, which was validated against simulations in [91]. A Gaussian covariance matrix is sufficient for our efforts in this work because we are just interested in forecasting and comparing the cosmological constraints given by different sample definitions. In addition, we exclude small scales in our analysis (see §5.7.3), where the non-Gaussian terms of the covariance become dominant. In addition, we have checked that including non-Gaussian terms in our covariance matrix estimation does not impact our final results significantly.

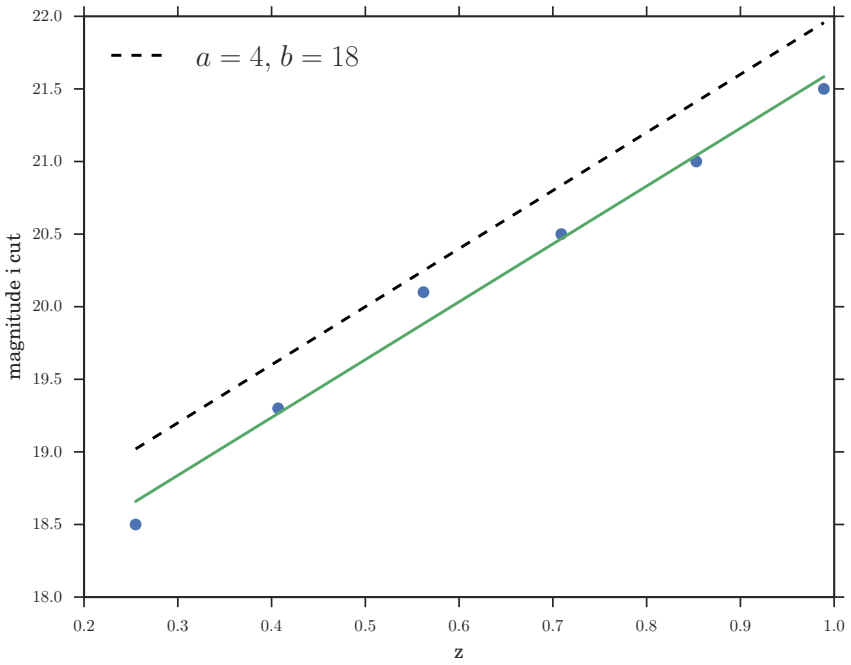

FIGURE 5.2: Different sample definitions considered. The first version (blue dots) applied a constant magnitude cut for each redshift bin, the second version (v2.0), in solid green, used a continuous magnitude cut evolving linearly with z, with slope and interception given by a fit to the blue points. In dashed black we show the final definition of the sample.

5.5 Sample Optimization

In this section we justify the magnitude limited sample selection used in this analysis and describe the optimization process we have carried out to reach the final definition of the sample. The first version of the sample just applied a constant magnitude cut in the i band to all the galaxies in the same redshift bin. This magnitude cut was different for each redshift bin, increasing with redshift.

In order to have a smoother bias evolution with redshift we henceforth apply the same continuous magnitude cut to all the galaxies of the sample, and, unless otherwise stated, we consider a cut evolving linearly with redshift, i.e. $i < az + b$. In order to get a first estimate for the slope and interception, we fit this function to the i and z values of the first version of the sample, obtaining $a = 4.0$ and $b = 17.64$. In Fig. 5.2 we show the i values used for the first version of the sample, the linear fit to these values, hereafter v2.0, and the cut corresponding to the final definition of

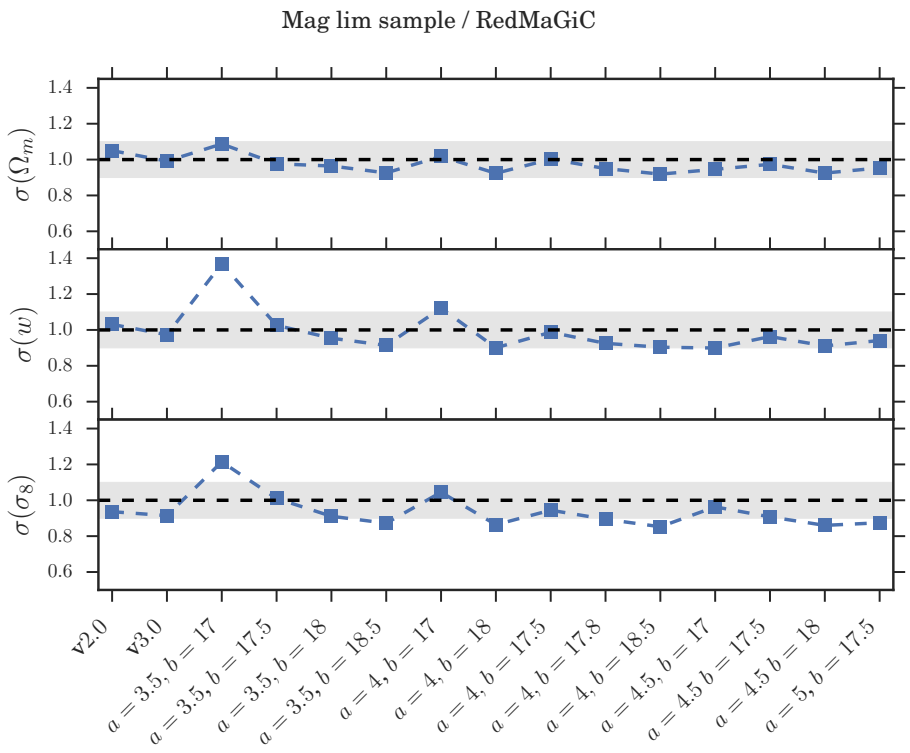

FIGURE 5.3: Standard deviations on Ω_m, w and σ_8 from different definitions of the magnitude limited sample normalized by estimates from the REDMAGICsample.

the sample, i.e. $i < 4z + 18$ (see §2.3.2).

We then find the optimal definition of this sample by running Fisher matrix forecasts on all the possible combinations of $(a,\ b)$ values in these ranges: $a = [3.5, 4, 4.5, 5]$, $b = [17, 17.5, 18, 18.5]$. These ranges of values are broad enough to cover a complete variety of possible sample definitions, as the minimum values for a and b (i.e. $i < 3.5z + 17$) result in a sample with very few galaxies, and the maximum values (i.e. $i < 5z + 18.5$) result in a sample with a very large limiting magnitude ($i < 23.75$), in such a way that we are practically selecting almost all the galaxies from the catalog. In addition, the sample is complete at full area (covering the whole ~ 5000 deg^2) for regions deeper than $i = 22$ magnitudes. If the limiting magnitude of the selection ($i_{\rm lim} = az_{\rm max} + b$) is larger than 22, we have to mask those regions of the footprint that are too shallow, thus reducing the effective sky area. With the final definition of the sample (§2.3.2) the limiting magnitude is $i = 22.2$, which implied masking of 1% the footprint. For some of these combinations of $(a,\ b)$ values, the limiting magnitude is 23, or larger. Given that with a limiting magnitude of 22.5 we already would have to mask about 5% of the footprint, we decide not to

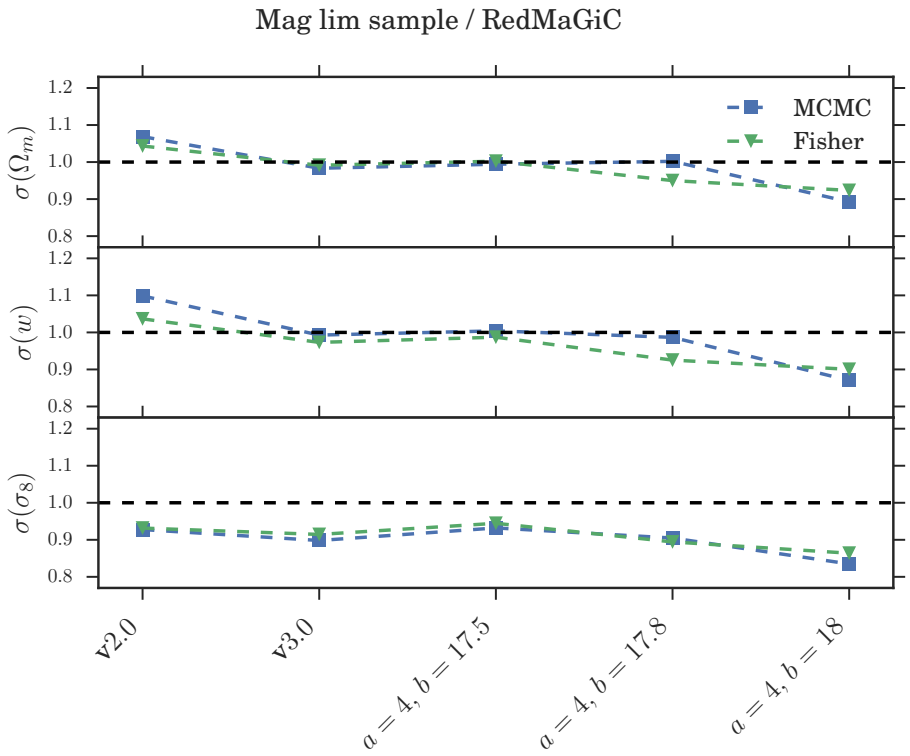

FIGURE 5.4: Standard deviations on Ω_m, w and σ_8 from different definitions of the magnitude limited sample normalized by estimates from the REDMAGICsample. We compare results obtained from Fisher matrix forecasts (green triangles) with those from MCMC (blue squares).

consider those selections that reach a limiting magnitude larger than 22.5.

We are interested in optimizing the sample in terms of its cosmological constraints. In this case, the parameters of interest are σ_8, Ω_m and w, as these are the main parameters that are constrained in the joint analysis of galaxy clustering and weak lensing from DES data [2]. For each one of these possible magnitude cuts, we compare the constraints on $\{\Omega_m, \sigma_8, w\}$ obtained from the joint analysis of galaxy clustering and galaxy-galaxy lensing using Fisher forecasts. In Fig.5.3 we show the standard deviations resulting from the forecasts, which are normalized by the constraints obtained from the Y3 REDMAGIC sample (see §2.3.2). Thus, the black dashed line represents constraints equal to those obtained from REDMAGIC, while points above or below that line correspond to samples giving worse or better constraints than REDMAGIC, respectively. The grey band delimits the region with 10% better or worse constraints compared to REDMAGIC. In Fig.5.3 we compare the relative gain on the constraints for most of the galaxy

REDSHIFT RANGE	$N_{\rm gal}$ REDMAGIC	$N_{\rm gal}$ MAG LIM
0.15 – 0.35	341,602	1,599,462
0.35 – 0.50	589,562	1,593,745
0.50 – 0.65	877,267	1,379,717
0.65 – 0.85	679,291	1,862,978
0.85 – 0.95	418,986	2,257,704
TOTAL	2,906,708	8,693,606

TABLE 5.1: Number of galaxies per redshift bin for REDMAGIC and magnitude limited samples assuming REDMAGIC redshift binning for both. The effective sky area covered by these samples is 4182 deg^2.

selections considered[2], and for the so-called v2.0 and v3.0 of the sample, which are the fits to the magnitude cuts considered in the first version of the sample (blue dots in Fig.5.2) assuming $i < az + b$ and $i < a\sqrt{z} + b$, respectively. Here we see that most of the samples considered yield constraints similar or slightly better than REDMAGIC. This is probably due to the fact that, even though the photo-z are less accurate, these samples have more galaxies and reach higher z than REDMAGIC. One of the samples provides significantly worse constraints ($i < 3.5z + 17$), but this is understandable, because it corresponds to the extreme case in which very few galaxies are selected from the Gold catalog. From all the samples considered we then choose as our fiducial magnitude limited sample for the Y3 cosmological analysis the one with the best constraints and with a limiting magnitude at $z_{\rm max}$ lower than 22.5. Since we bin in 6 z bins from $z = 0.2$ to $z = 1.05$, that sample corresponds to $i < 4z + 18$.

We compare the results obtained from the Fisher forecasts with full likelihood explorations using an MCMC method in Fig.5.4. Due to the fact that the MCMC method is much more computationally expensive than the Fisher forecasts, we only perform this comparison for some of the samples considered, including the result of the optimization ($i < 4z + 18$). We find that the constraints from both forecasting methods agree within few percent, thus we conclude that our choice of sample definition is robust and well justified.

5.6 Comparison with REDMAGIC

In this section we compare the characteristics of the magnitude limited and REDMAGIC samples. For this purpose, we consider here the same tomographic binning for the former as the one used

[2]In this comparison we have excluded those selections that reach too high limiting magnitudes, as that would imply masking more than 5% of the footprint.

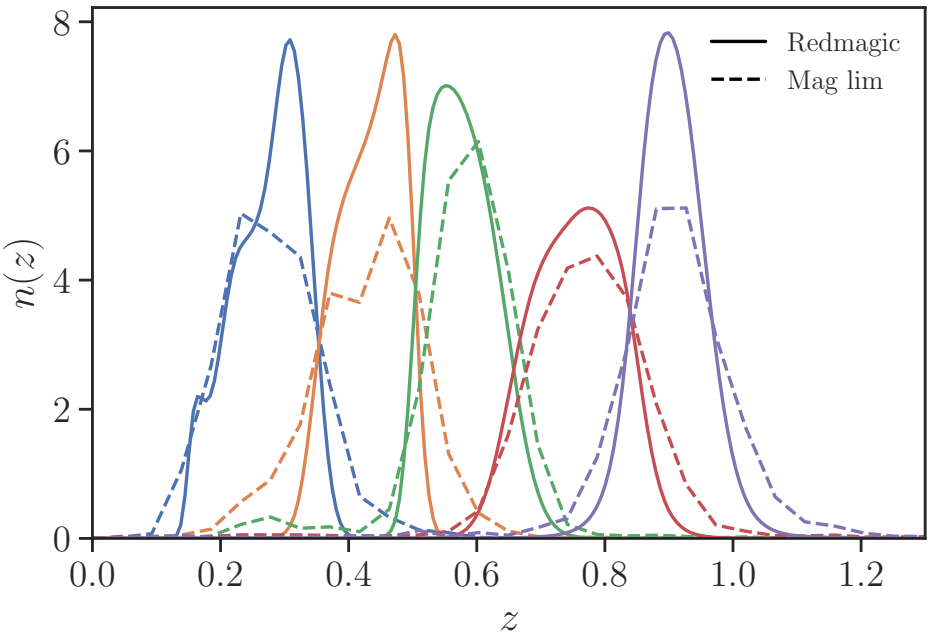

FIGURE 5.5: Normalized redshift distributions from magnitude limited (dashed lines) and REDMAGIC (solid lines) samples considering the same tomographic z binning as used for the REDMAGIC sample.

for the latter. This consists in five redshift bins ranging from $z = 0.15$ to $z = 0.95$. In Table 5.1 we show the details of this tomographic binning and the number of galaxies in each bin for both samples. The magnitude limited sample has on average between 2 and 3 times more galaxies than REDMAGIC. The difference in $N_{\rm gal}$ ranges from 60% more galaxies in the third bin to more than 4 times further galaxies in the last z bin.

In Fig.5.5 we compare the redshift distributions normalized such that $\int_{z_{\rm min}}^{z_{\rm max}} {\rm d}z\, n(z) = 1$ in each redshift bin. Here the $n(z)$ for REDMAGIC are the same as shown in Fig.2.4 but normalized to 1, while the distributions for the magnitude limited sample have been obtained by stacking of the nearest neighborhood redshifts from the DNF training sample (§2.3.2). Some parameters we can use to compare the accuracy of the photo-z are the width and height (or spread of the tails) of the normalized $n(z)$ distributions. For both samples we have binned the galaxies in photometric redshifts in the same way. Thus their distributions in true redshifts (normalized $n(z)$) will be broader and have larger tails (shorter peaks) if their error on the photo-z estimation σ_z is larger. In Fig.5.5 we see, as expected, that REDMAGIC has more accurate photo-z, which is given by their galaxies being selected with an algorithm optimized for photometric accuracy. However, the photo-zs of the magnitude limited sample are not very degraded compared to REDMAGIC, as

Fiducial		Same $N_{\rm gal}$		6 z-bins	
Luminosity	Redshift range	Luminosity	Redshift range	Luminosity	Redshift range
$L > 0.5L_*$	0.15 – 0.35	$L > 0.5L_*$	0.15 – 0.40	$L > 0.5L_*$	0.15 – 0.30
$L > 0.5L_*$	0.35 – 0.50	$L > 0.5L_*$	0.40 – 0.55	$L > 0.5L_*$	0.30 – 0.40
$L > 0.5L_*$	0.50 – 0.65	$L > 0.5L_*$	0.55 – 0.65	$L > 0.5L_*$	0.40 – 0.50
				$L > 0.5L_*$	0.50 – 0.65
$L > 1.0L_*$	0.65 – 0.85	$L > 1.0L_*$	0.65 – 0.80	$L > 1.0L_*$	0.65 – 0.85
$L > 1.0L_*$	0.85 – 0.95	$L > 1.0L_*$	0.80 – 0.95	$L > 1.0L_*$	0.85 – 0.95

Table 5.2: Different tomographic binning configurations for the redMaGiC sample.

the $n(z)$ distributions are not much broader. In particular the $n(z)$ for the third redshift bin looks quite similar in both samples. Thus, through the magnitude limited sample optimization carried out in §5.5, we have managed to generate a galaxy sample with 2–3 times more galaxies than redMaGiC and with slightly worse photo-z errors.

5.7 Analysis Choices

5.7.1 Tomographic Binning

Here we test the impact on the cosmological constraints of the number of tomographic bins and edges of the binning of the Y3 lens samples (redMaGiC and magnitude limited samples).

redMaGiC sample

As described in §2.3.2, the redMaGiC sample in Y3 consists of the combination of two redMaGiC samples selected with different luminosity thresholds: high-density ($L > 0.5L_*$) in the range $0.15 < z < 0.65$, and high-luminosity ($L > 1.0L_*$) in the range $0.65 < z < 0.95$. Taking this condition into account, here we explore different tomographic binnings for the redMaGiC sample. We consider two cases: first, we vary the edges of the z bins trying to have a more balanced $N_{\rm gal}$ across the redshift bins, we refer to this as the '*same* $N_{\rm gal}$' case; second, we divide the sample into 6 z bins instead of 5. In Table 5.2 we show the details of these tomographic binnings.

We test the impact of the tomographic binning of the redMaGiC sample in our cosmological

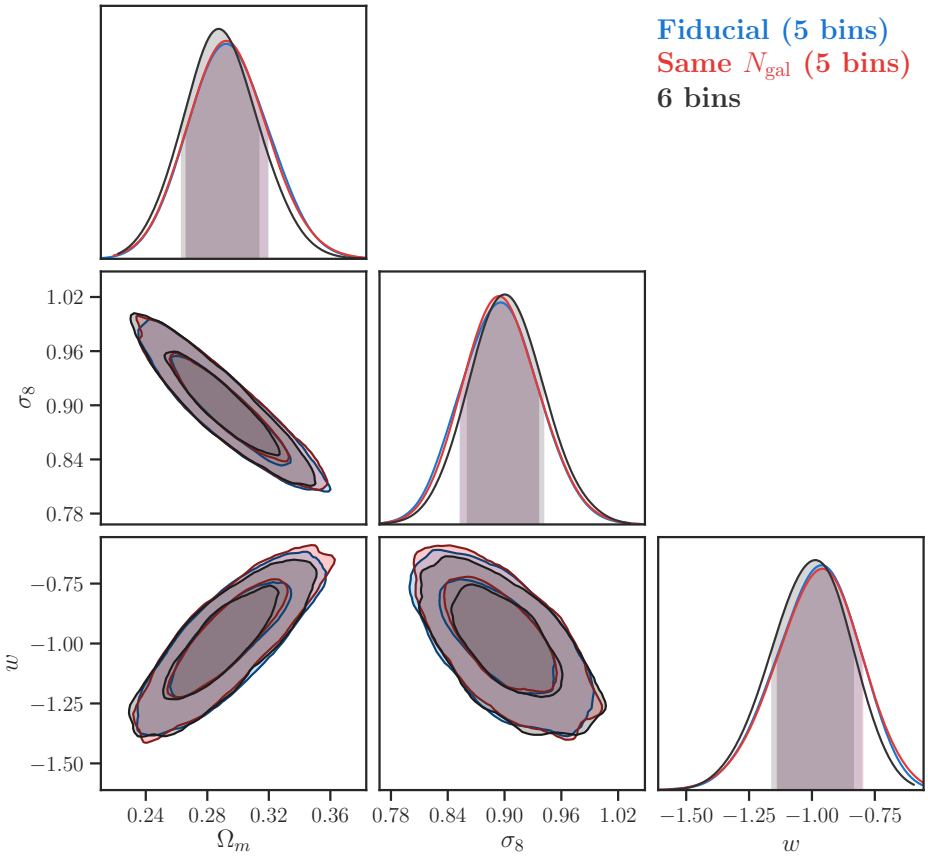

FIGURE 5.6: Constraints from the combination of galaxy clustering, galaxy-galaxy lensing and cosmic shear considering different tomographic binnings for the REDMAGIC sample, as specified in Table 5.2.

constraints by running MCMC simulated likelihood analyses from the combination of galaxy clustering, galaxy-galaxy lensing, and cosmic shear. In Fig.5.6 we compare the constraints of the fiducial REDMAGIC sample with the other binnings considered. We find that changing the edges of the tomographic binning –while keeping the same number of z bins– does not affect the posterior distributions. On the other hand, we find a slight improvement by dividing the sample in 6 z bins instead of 5. However, this is a considerably minor improvement, about 3-4%. Increasing the number of tomographic bins increases the total number of nuisance parameters to marginalize over and the size of the covariance matrix, which could lead to more degeneracies between nuisance and cosmological parameters. For this reason, we find that the fiducial definition with 5 z bins is preferable.

FIDUCIAL	SAME $N_{\rm gal}$	SAME $N_{\rm gal} \times b^i$
0.20 – 0.35	0.20 – 0.36	0.20 – 0.40
0.35 – 0.50	0.36 – 0.52	0.40 – 0.55
0.50 – 0.65	0.52 – 0.69	0.55 – 0.72
0.65 – 0.80	0.69 – 0.82	0.72 – 0.85
0.80 – 0.95	0.82 – 0.93	0.85 – 0.95
0.95 – 1.05	0.93 – 1.05	0.95 – 1.05

4 z-BINS	5 z-BINS	7 z-BINS
0.20 – 0.44	0.20 – 0.40	0.20 – 0.35
0.44 – 0.69	0.40 – 0.60	0.35 – 0.50
0.69 – 0.87	0.60 – 0.77	0.50 – 0.64
0.87 – 1.05	0.77 – 0.90	0.64 – 0.77
	0.90 – 1.05	0.77 – 0.86
		0.86 – 0.95
		0.95 – 1.05

TABLE 5.3: Different tomographic binning configurations for the magnitude limited sample, considering variations in the edges of the z bins (left) and the number of bins (right).

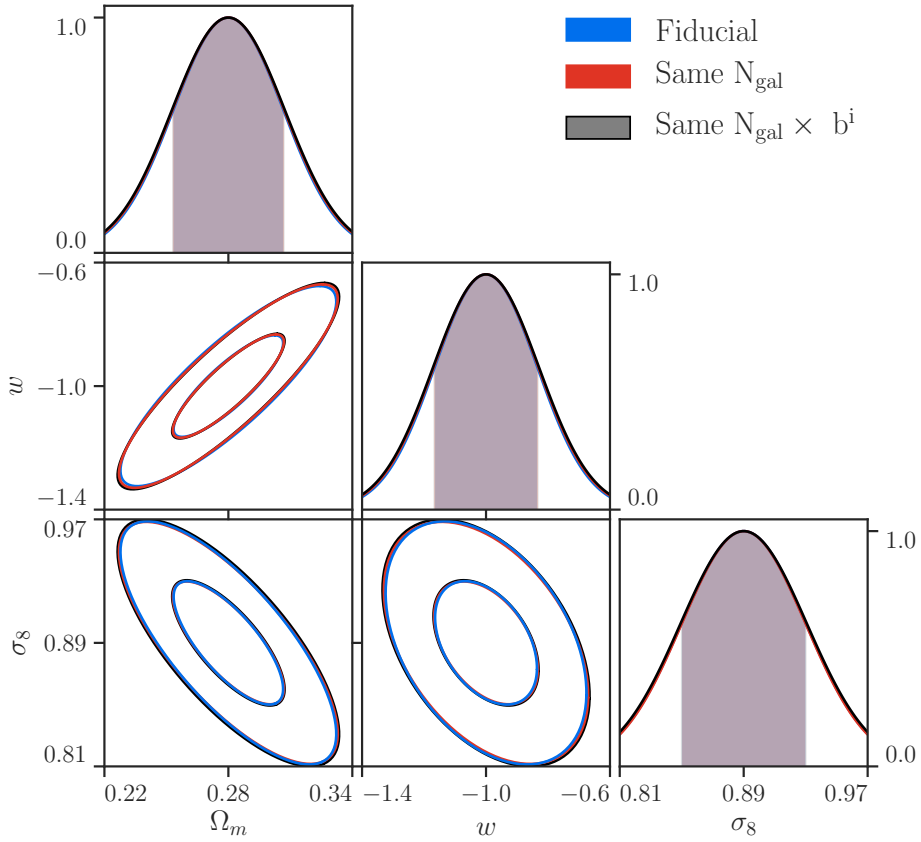

FIGURE 5.7: Comparison of Fisher constraints from the combination of galaxy clustering and galaxy-galaxy lensing considering different tomographic binnings for the magnitude limited sample, as described in Table 5.3 (left).

Magnitude limited sample

Similarly to what we have carried out for the REDMAGIC sample, here we test the impact of the choice of tomographic binning on the cosmological constraints from the combination of galaxy

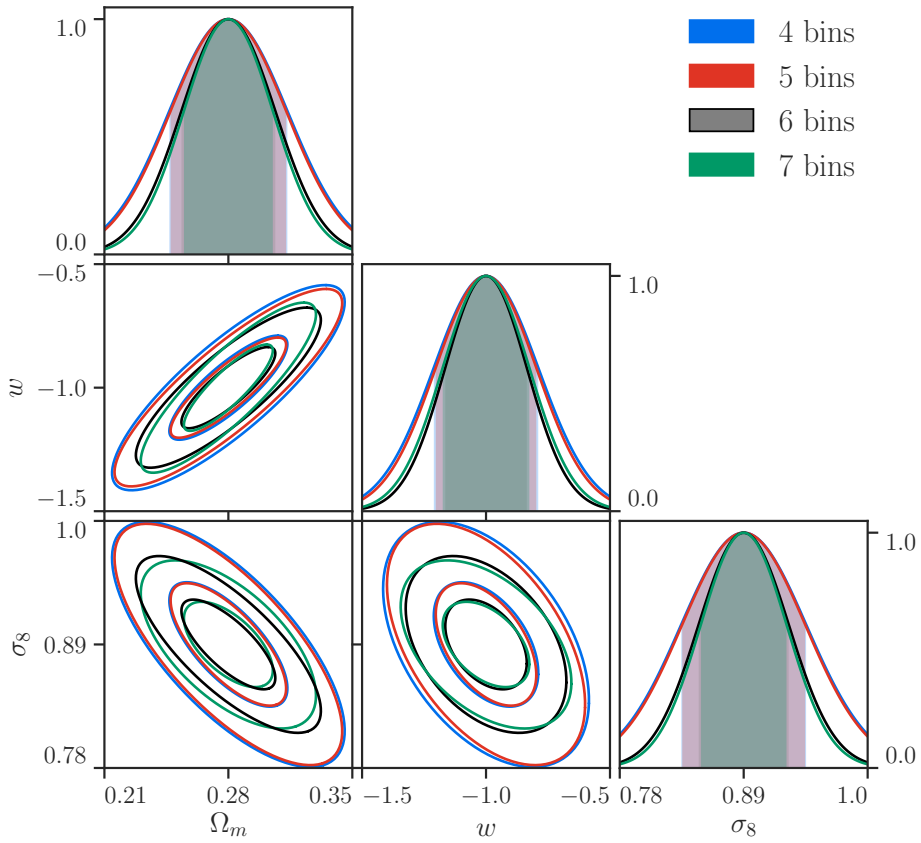

FIGURE 5.8: Comparison of Fisher constraints from the combination of galaxy clustering and galaxy-galaxy lensing considering different number of z bins for the magnitude limited sample, as described in Table 5.3 (right), where here the case with 6 bins corresponds to the fiducial magnitude limited sample.

clustering and galaxy-galaxy lensing. In all cases considered we maintain the same global z range as the fiducial sample, i.e. $0.2 < z < 1.05$. We first vary the edges of the tomographic binning, putting together two new configurations in which we balance the number of galaxies weighted by the galaxy bias in each redshift bin, '*same* $N_{\rm gal} \times b^i$', and unweighted, '*same* $N_{\rm gal}$'. The galaxy bias values we consider are listed in Table 5.4, and the definition of these z binnings is shown in Table 5.3 (left). The motivation for balancing the number of galaxies (weighted by the galaxy bias) is to have a more uniform signal-to-noise ratio across redshift. However, as we can see in Fig.5.7, where we compare the constraints coming from these different tomographic binnings, our choice of binning does not impact the cosmological constraints coming from the combination of galaxy clustering and galaxy-galaxy lensing, hereafter 2x2pt.

We then vary the number of tomographic bins in which we divide the sample in the range $0.2 < z < 1.05$. Our fiducial selection is divided in 6 z bins, and we consider additionally

sample selections with 4, 5 and 7 z bins. See Table 5.3 (right) for the details of the z binning for each one of these cases. In Fig.5.8 we compare the estimated Fisher 2x2pt constraints from each one of these sample selections with our fiducial choice with 6 z bins. We can extract two conclusions from these results. First, increasing the number of tomographic bins in which we divide the sample does not improve the cosmological constraints. Second, reducing the number of z bins degrades the cosmological constraints. This makes sense, as reducing the number of bins while keeping fixed the total z range to be covered effectively increases the width of the redshift distributions and, as shown in [15], there is a loss of information when projecting the 3D power spectrum into angular tomographic bins, with that loss being larger the wider the redshift bins. This is due to the fact that broad bins average down radial power on scales smaller than the bin width. Thus, we conclude that our choice of tomographic binning for the magnitude limited sample is robust and optimal for our cosmological analysis.

5.7.2 Parametrization and Priors

The cosmological model we consider in this work is spatially flat wCDM with fixed neutrino mass corresponding to the minimum allowed neutrino mass of 0.06 eV from oscillation experiments [122]. We split the neutrino mass equally among the three eigenstates, in consistency with [2]. The fiducial cosmological parameter values correspond to the best-fits of the posterior distributions from the DES Y1 3×2pt ΛCDM analysis in [2], that obtained cosmological constraints from the combination of galaxy clustering, galaxy-galaxy lensing, and cosmic shear.

In addition to the cosmological parameters, our model contains about 20 nuisance parameters. These are the galaxy bias parameters for the lens samples, b^i, the multiplicative shear biases, m^i, two parameters related to the intrinsic alignment model, $A_{\rm IA}$ and $\eta_{\rm IA}$, and the photo-z shift parameters for the lenses and the sources, Δz^i. These shift parameters are used in our analysis to quantify uncertainties in the redshift distribution. We assume that the true redshift distribution $n^i(z)$ in bin i is a shifted version of the photometrically derived distribution:

$$n^i(z) = n^i_{\rm PZ}(z - \Delta z^i). \tag{5.11}$$

The fiducial values and priors assumed for these parameters, shown in Table 5.4, are consistent with [2]. For the magnitude limited sample, we assume fiducial values for the galaxy bias based on galaxy clustering measurements on a 10% subsample of the data, in consistency with the Y3 blinding scheme. We have checked that our conclusions in this work are robust to changes in the magnitude limited sample galaxy bias values.

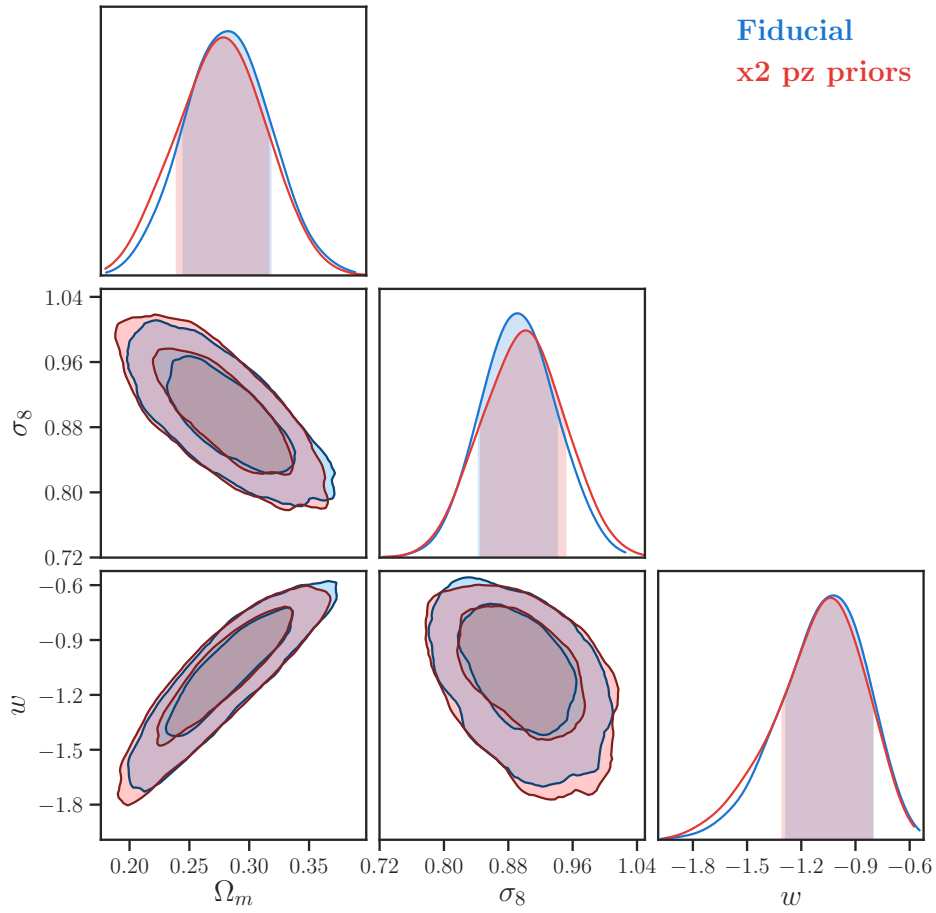

FIGURE 5.9: Comparison between parameter constraints obtained using the fiducial priors assumed for the magnitude limited sample Δz^i parameters in Table 5.4 (blue), and using priors twice as wide (red).

For the photo-z shift parameters we assume the same priors as in DES Y1, as we are using the same redshift distributions for the sources, and the photometric calibration for the Y3 REDMAGIC and magnitude limited samples is still ongoing. Note that throughout this analysis we assume the same priors on the shift parameters for the two lens samples, even though we have seen in Fig.5.5 that the magnitude limited sample has slightly worse photometric accuracy. We have tested the effect of this assumption by doubling the width of the priors on the magnitude limited sample Δz^i parameters, obtaining the constraints shown in Fig.5.9. The constraints degrade by less than a 10% when doubling the priors on Δz^i. Since the actual priors will be lower than this pessimistic scenario, we conclude that our analysis is robust to changes in the priors associated to the magnitude limited sample nuisance parameters.

Parameter	Fiducial	Prior
	Cosmology	
$\Omega_{\rm m}$	0.2837	[0.1, 0.9]
$A_{\rm s}/10^{-9}$	2.2606	[0.5, 5.0]
$n_{\rm s}$	0.9686	[0.87, 1.07]
w	-1.0	[-2, -0.33]
$\Omega_{\rm b}$	0.062	[0.03, 0.07]
h_0	0.8433	[0.55, 0.9]
$\Omega_\nu h^2$	6.155×10^{-4}	Fixed
$\Omega_{\rm K}$	0	Fixed
τ	0.08	Fixed
	Galaxy bias (redMaGiC)	
b^i	1.4, 1.6, 1.6, 1.93, 1.99	[0.8,3.0]
	Galaxy bias (Magnitude limited)	
b^i	1.49, 1.86, 1.81, 1.90, 2.26, 2.33	[0.8,3.0]
	Intrinsic alignment	
	$A_{\rm IA}(z) = A_{\rm IA}[(1+z)/1.62]^{\eta_{\rm IA}}$	
$A_{\rm IA}$	0.0	[-5.0,5.0]
$\eta_{\rm IA}$	0.0	[-5.0,5.0]
	Lens photo-z shift	
$\Delta^1_{z,{\rm l}}$	0.002	(0.0,0.007)
$\Delta^2_{z,{\rm l}}$	0.001	(0.0,0.007)
$\Delta^3_{z,{\rm l}}$	0.003	(0.0,0.006)
$\Delta^4_{z,{\rm l}}$	0.0	(0.0,0.01)
$\Delta^5_{z,{\rm l}}$	0.0	(0.0,0.01)
$\Delta^6_{z,{\rm l}}$	0.0	(0.0,0.01)
	Source photo-z shift	
$\Delta^1_{z,{\rm s}}$	0.002	(0.0,0.016)
$\Delta^2_{z,{\rm s}}$	-0.015	(0.0,0.013)
$\Delta^3_{z,{\rm s}}$	0.007	(0.0,0.011)
$\Delta^4_{z,{\rm s}}$	-0.018	(0.0,0.022)
	Shear calibration	
m^i $(i = 1, 4)$	0.012	(0.012, 0.023)

Table 5.4: The fiducial parameter values and priors for cosmological and nuisance parameters used in this analysis. Square brackets denote a flat prior over the indicated range, while parentheses denote a Gaussian prior of the form $\mathcal{N}(\mu, \sigma)$.

5.7.3 Scale Cuts

As seen in §1.3.2, in the linear regime perturbation theory can be used to calculate the matter power spectra. On smaller scales, N-body simulations are needed in order to capture the non-linear evolution of structure growth. For example, the HALOFIT method [157, 163], which we use in this work, employs a functional form of the matter power spectrum derived from halo models, which are in turn calibrated from N-body simulations. However, only gravitational physics are included in these dark matter only simulations,which neglects any modification of the matter distribution due to baryonic physics processes such as star formation, radiative cooling, and feedback [53, 113, 169]. At small scales, these processes can modify the matter power spectrum significantly [167].

In order to mitigate the impact of the uncertainty in how the baryonic physics modifies the matter power spectrum, we apply a set of scale cuts, as described in [2, 91], such that non-linear modeling limitations do not bias the cosmology results. We define scale cuts in terms of a specific comoving scale R, and calculate the angular scale cut $\theta^i_{\rm min}$ for bin i as

$$\theta^i_{\rm min} = \frac{R}{r\left(\langle z^i \rangle\right)}, \tag{5.12}$$

where $\left\langle z^i \right\rangle$ is the mean redshift of galaxies in the redshift bin i and r is the radial comoving distance at that z. In this work we use the same scale cuts as considered for the DES Y1 baseline analysis [2],

$$\begin{aligned} R_{\rm clustering} &= 8 \ \ {\rm Mpc}\, h^{-1}, \\ R_{\rm ggl} &= 12 \ \ {\rm Mpc}\, h^{-1}, \end{aligned} \tag{5.13}$$

where $R_{\rm clustering}$ denotes the scale cuts for the galaxy clustering data vector, and $R_{\rm clustering}$ for galaxy-galaxy lensing. See [91] for a detailed description of how these scale cuts were determined.

5.8 Cosmological Constraints

In this section we compare the cosmological constraints obtained from the two Y3 lens samples, REDMAGIC and magnitude limited sample, as defined in §2.3.2. We perform a full MCMC analysis of the combination of galaxy clustering and galaxy-galaxy lensing, assuming the fiducial values and priors listed in Table 5.4. The resulting constraints are shown in Fig.5.10. We find that the final definition of the magnitude limited sample, after the optimization process carried out in

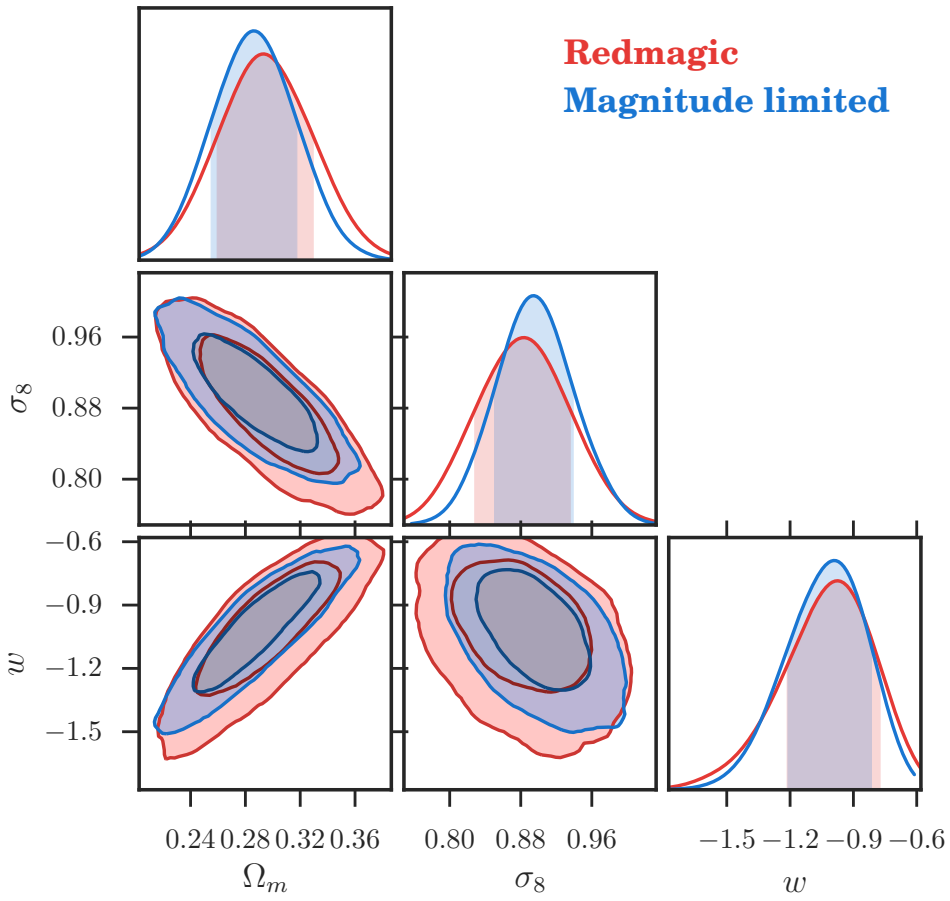

FIGURE 5.10: Comparison between parameter constraints obtained using the REDMAGIC (red) and magnitude limited (blue) samples from the combination of galaxy clustering and galaxy-galaxy lensing.

LENS SAMPLE	Ω_m	σ_8	w
REDMAGIC	0.295 ± 0.032	0.883 ± 0.049	-1.03 ± 0.21
MAGNITUDE LIMITED	0.287 ± 0.028	0.896 ± 0.041	-1.03 ± 0.18

TABLE 5.5: Comparison of 68% confidence level cosmological constraints in wCDM from the combination of galaxy clustering and galaxy-galaxy lensing, using REDMAGIC and magnitude limited samples as lenses.

§5.5, provides moderately better constraints than REDMAGIC for the cosmological parameters of interest, specially for Ω_m and σ_8, which are the parameters more constrained by the DES 3x2pt analysis [2]. In Table 5.5 we show the 68% confidence level constraints on these parameters. We obtain around 15% tighter constraints using the magnitude limited sample instead of REDMAGIC, which is probably due to the greater number of galaxies (2-3 times higher) and increased depth, reaching $z = 1.05$ instead of $z = 0.95$. This increase in depth will be particularly advantageous

when combining the 3x2pt analysis with CMB lensing [3], as the magnitude limited sample will have a greater overlap with the CMB lensing kernel, providing a higher signal-to-noise ratio of galaxy clustering and CMB lensing cross-correlations. We note that this is just a simulated likelihood analysis using a noiseless theory data vector, thus the relative constraining power will probably be slightly different with real data. However, this work indicates that the magnitude limited sample will give comparable and probably somewhat tighter cosmological constraints in the DES Y3 analysis with respect to redMaGiC. In addition, it will increase the robustness of our cosmological analysis with the use of another lens sample with galaxies selected in a completely different and simpler way, allowing us a smoother modeling of nuisance parameters, such as the galaxy bias.

5.9 Summary

In this chapter we have defined an alternative to redMaGiC for the DES Y3 galaxy clustering measurements. This is a magnitude limited sample defined with a magnitude cut in the i band with a linear dependency with the photometric redshift. We have optimized the definition of these samples in terms of its cosmological constraints on Ω_m, σ_8 and w, obtaining as a result a sample with 2-3 times more galaxies than redMaGiC with just slightly higher photometric redshift uncertainties. We have checked the robustness of our analysis by testing different tomographic binnings of the samples and extending the priors imposed on the photo-z nuisance parameters, finding no improvement on the cosmological constraints with alternative z binnings, and no significant alteration of the posterior distributions when widening the photo-z priors.

We finally run simulated likelihood analyses, obtaining as a result 15% tighter constraints compared to redMaGiC from the combination of galaxy clustering and galaxy-galaxy lensing. We plan to use this magnitude limited sample alongside redMaGiC for the galaxy clustering measurements in the DES Y3 analysis, as it can potentially provide tighter constraints and it will increase the robustness of our cosmological results. In addition, it will allow a higher signal-to-noise ratio of galaxy clustering and CMB lensing cross-correlations, due to its increased depth compared to redMaGiC.

Conclusions

This thesis is focused on the combination of multiple tracers of large-scale structure in order to obtain tighter cosmological constraints. In particular, we concentrate on the Dark Energy Survey and its combination with data from the South Pole Telescope (SPT) and Planck collaborations. After a theoretical introduction in Chapter 1, and an overview of the Dark Energy Survey (DES) in Chapter 2, in Chapter 3 we combine the galaxy clustering from DES Y1 data with Cosmic Microwave Background (CMB) lensing from SPT and Planck collaborations. Then, in Chapter 4, we combine the galaxy clustering of two different galaxy samples to constrain Redshift Space Distortions (RSD) and Primordial non-Gaussianities (PNG) in a multi-tracer approach. Here we also consider the inclusion of galaxy - CMB lensing cross-correlations. Last, in Chapter 5 we define and optimize a magnitude limited lens sample for the combined analysis of galaxy clustering and galaxy-galaxy lensing from DES Y3 data. In the following, we present the main conclusions from this thesis.

Joint analysis of galaxy clustering and CMB lensing

We measure the cross-correlation between DES Y1 REDMAGIC galaxies and CMB lensing from the optimal combination of SPT and Planck, rejecting the hypothesis of no-lensing at 20σ significance prior to any scale cuts and at 10σ using conservative scale cuts that mitigate systematic biases. We obtain constraints on the galaxy bias, the growth function and the cosmological parameters.

In obtaining the galaxy bias parameters, we find that galaxy clustering measurements place significantly tighter constraints than galaxy-galaxy lensing or galaxy-CMB lensing correlations. We measure the growth function with two different methods, assuming a fixed cosmology. First, using the D_G estimator introduced in the analysis of DES Science Verification data [70], finding

a relative growth amplitude of $A_{\rm D} = 1.16^{+0.20}_{-0.20}$. Second, from the joint fit of the galaxy bias, the growth function and systematic parameters associated to photo-z uncertainties using an MCMC approach. In this case, we find $A_{\rm D} = 0.92^{+0.15}_{-0.10}$. Both of these results are consistent with the ΛCDM predictions of $A_{\rm D} = 1$.

Last, we run a full MCMC analysis over the ΛCDM cosmological parameters. Combining galaxy clustering with galaxy - CMB lensing cross-correlations, we obtain $\Omega_{\rm m} = 0.276^{+0.029}_{-0.030}$ and $S_8 = 0.800^{+0.090}_{-0.094}$. We find that, despite the conservative scale cuts applied in this analysis, the constraining power is comparable to the combination of galaxy clustering with galaxy-galaxy lensing. We also combine galaxy clustering and galaxy - CMB lensing correlations with Planck TT+lowP obtaining an upper bound at 95% CL on the sum of neutrino masses of 0.81 eV, which slightly loosens the bound from Planck TT+lowP alone ($\sum m_\nu < 0.72$ eV at 95% CL).

Multi-tracer measurements of RSD and PNG

We explore the constraints on RSD –in particular, the growth index γ and $f(z)\sigma_8(z)$– and on PNG through the $f_{\rm NL}$ parameter using a multi-tracer approach. We reproduce the constraints on RSD from [14] (A14) in real space instead of harmonic space and we extend that analysis with the inclusion of galaxy - CMB lensing cross-correlations, finding they have a negligible impact on our results.

We then measure RSD with the DES Y3 lens samples (redMaGiC and magnitude limited), finding that our constraints have a limited improvement when including cross-correlations between redshift bins due to the better photometric accuracy compared to the samples in A14. We show that the constraints on $f(z)\sigma_8(z)$ can be improved by a factor five at low redshift with a multi-tracer approach, being comparable to the latest measurements from spectroscopic surveys such as VIPERS [126] and WiggleZ [30]. However, we only obtain a minor gain on γ, due to the samples not being optimal for this analysis. We test the impact of increasing the bias difference between the redMaGiC and magnitude limited samples finding no significant changes on γ, while the constraints on $f(z)\sigma_8(z)$ improve at low redshift and degrade at high redshift.

Regarding PNG, we first consider a pair of optimistic samples based on the ones from A14. We find that by combining the two samples we can improve the constraints more than a factor two with galaxy auto-correlations only, and more than a factor three with a full tomographic analysis. We then consider the DES Y3 lens samples and show that we could potentially obtain a

68% CL error on $f_{\rm NL}$ of 17.4 from the magnitude limited sample galaxy auto-correlations only, which is significantly smaller than the tightest constraints from large-scale structure until now, $-51 < f_{\rm NL} < 21$ at 95% CL [43]. However, we do not find much improvement when combining the two samples, even when increasing the bias difference.

Sample optimization for multi-probe cosmology

We define a DES Y3 lens sample alternative to redMaGiC, the so-called magnitude limited sample, which consists of a galaxy sample defined with a magnitude cut that evolves linearly with photometric redshift. We optimize the galaxy selection of this sample in terms of its cosmological constraints, obtaining as a result a sample with between two and three more galaxies than redMaGiC with just slightly larger photometric redshift uncertainties. For the sample optimization we rely on Fisher forecasts, and we test how these vary given the variations obtained for the number density and estimated redshift uncertainty given by a set of magnitude cuts.

We also characterize the impact of redshift binning choices in our cosmological constraints for both samples, concluding that our tomographic binning is robust. In addition, we extend the priors imposed on the nuisance parameters associated to photometric uncertainties, finding no significant alteration of the posterior distributions. Finally, we show that with the magnitude limited sample we can potentially obtain 15% tighter cosmological constraints than redMaGiC on Ω_m, σ_8, and w from the combined analysis of galaxy clustering and galaxy-galaxy lensing.

Future work

The joint analysis of galaxy clustering, galaxy-galaxy lensing and cosmic shear of DES Y1 data has produced cosmological constraints that are competitive with constraints derived from *Planck* observations of the CMB. The DES Y3 data includes data from the first three years of the survey and covers more than three times as much area to greater depth than Y1.

Most of the work in this thesis consists of forecasts considering the lens samples from DES Y3 data. We plan to use the magnitude limited sample presented here alongside the redMaGiC sample for the galaxy clustering measurements in the DES Y3 analysis that is still ongoing.

Then we will combine these galaxy clustering measurements with galaxy-galaxy lensing and cosmic shear (similarly to [2]), and with CMB lensing correlations (analogous to [3]). Using the magnitude limited sample alongside REDMAGIC can potentially provide tighter cosmological constraints and it will increase the robustness of our results. In addition, since the magnitude limited sample reaches higher redshift, it will allow a higher signal-to-noise ratio of galaxy clustering and CMB lensing cross-correlations.

From the CMB lensing side, we plan on reducing the systematic biases in order to apply less conservative scale cuts in the Y3 analysis. In order to improve the measurement of CMB lensing correlations, it will be essential to either characterize the systematic biases to a higher accuracy, or improve the reconstruction of the CMB lensing map so that it is less prone to biases. Furthermore, newer data sets from SPT (SPTpol and SPT-3G [23]) have lower noise levels, and thus lensing maps generated from these data sets will have lower noise.

On the other hand, we have seen that with the samples from A14 we can greatly improve the constraints on RSD and PNG with a multi-tracer approach. We intend to extend this analysis allowing all cosmological and nuisance parameters to vary, and testing the impact of including CMB lensing correlations in the multi-tracer measurement of $f_{\rm NL}$.

We also plan on exploring further how we should modify the DES Y3 lens samples in order to obtain a similar gain from their combination. Another possibility would be to define two new samples from DES Y3 data and optimize them for these analyses. This approach could also be taken with data from future surveys, such as the Dark Energy Spectroscopic Instrument (DESI), that will start observations at the end of 2019 or the beginning of 2020, and will cover much more area than DES, observing galaxies with a significantly greater precision.

Bibliography

[1] K. N. Abazajian, J. K. Adelman-McCarthy, M. A. Agüeros, S. S. Allam, C. Allende Prieto, D. An, K. S. J. Anderson, S. F. Anderson, J. Annis, N. A. Bahcall, and et al. The Seventh Data Release of the Sloan Digital Sky Survey. ApJS, 182(2):543–558, Jun 2009.

[2] T. M. C. Abbott, F. B. Abdalla, A. Alarcon, J. Aleksić, S. Allam, S. Allen, A. Amara, J. Annis, J. Asorey, S. Avila, and et al. Dark Energy Survey year 1 results: Cosmological constraints from galaxy clustering and weak lensing. Phys. Rev. D, 98(4):043526, Aug 2018.

[3] T. M. C. Abbott, F. B. Abdalla, A. Alarcon, S. Allam, J. Annis, S. Avila, K. Aylor, M. Banerji, N. Banik, E. J. Baxter, K. Bechtol, M. R. Becker, B. A. Benson, G. M. Bernstein, E. Bertin, F. Bianchini, J. Blazek, L. Bleem, L. E. Bleem, S. L. Bridle, D. Brooks, E. Buckley-Geer, D. L. Burke, J. E. Carlstrom, A. Carnero Rosell, M. Carrasco Kind, J. Carretero, F. J. Castander, R. Cawthon, C. Chang, C. L. Chang, H.-M. Cho, A. Choi, R. Chown, T. M. Crawford, A. T. Crites, M. Crocce, C. E. Cunha, C. B. D'Andrea, L. N. da Costa, C. Davis, T. de Haan, J. DeRose, S. Desai, J. De Vicente, H. T. Diehl, J. P. Dietrich, M. A. Dobbs, S. Dodelson, P. Doel, A. Drlica-Wagner, T. F. Eifler, J. Elvin-Poole, W. B. Everett, B. Flaugher, P. Fosalba, O. Friedrich, J. Frieman, J. García-Bellido, M. Gatti, E. Gaztanaga, E. M. George, D. W. Gerdes, T. Giannantonio, D. Gruen, R. A. Gruendl, J. Gschwend, G. Gutierrez, N. W. Halverson, N. L. Harrington, W. G. Hartley, G. P. Holder, D. L. Hollowood, W. L. Holzapfel, K. Honscheid, Z. Hou, B. Hoyle, J. D. Hrubes, D. Huterer, B. Jain, D. J. James, M. Jarvis, T. Jeltema, M. W. G. Johnson, M. D. Johnson, S. Kent, D. Kirk, L. Knox, N. Kokron, E. Krause, K. Kuehn, O. Lahav, A. T. Lee, E. M. Leitch, T. S. Li, M. Lima, H. Lin, D. Luong-Van, N. MacCrann, M. A. G. Maia, A. Manzotti, D. P. Marrone, J. L. Marshall, P. Martini, J. J. McMahon, F. Menanteau, S. S. Meyer, R. Miquel, L. M. Mocanu, J. J. Mohr, J. Muir, T. Natoli, A. Nicola, B. Nord, Y. Omori, S. Padin, S. Pandey, A. A. Plazas, A. Porredon, J. Prat, C. Pryke, M. M. Rau, C. L. Reichardt, R. P. Rollins, A. K. Romer, A. Roodman, A. J. Ross, E. Rozo, J. E. Ruhl, E. S. Rykoff, S. Samuroff, C. Sánchez, E. Sanchez, J. T. Sayre, V. Scarpine, K. K. Schaffer,

L. F. Secco, S. Serrano, I. Sevilla-Noarbe, E. Sheldon, E. Shirokoff, G. Simard, M. Smith, M. Soares-Santos, F. Sobreira, Z. Staniszewski, A. A. Stark, K. T. Story, E. Suchyta, M. E. C. Swanson, G. Tarle, D. Thomas, M. A. Troxel, D. L. Tucker, K. Vanderlinde, J. D. Vieira, P. Vielzeuf, V. Vikram, A. R. Walker, R. H. Wechsler, J. Weller, R. Williamson, W. L. K. Wu, B. Yanny, O. Zahn, Y. Zhang, and J. Zuntz. Dark Energy Survey Year 1 Results: Joint Analysis of Galaxy Clustering, Galaxy Lensing, and CMB Lensing Two-point Functions. *arXiv e-prints*, page arXiv:1810.02322, Oct 2018.

[4] T. M. C. Abbott, F. B. Abdalla, S. Allam, A. Amara, J. Annis, J. Asorey, S. Avila, O. Ballester, M. Banerji, W. Barkhouse, L. Baruah, M. Baumer, K. Bechtol, M. R. Becker, A. Benoit-Lévy, G. M. Bernstein, E. Bertin, J. Blazek, S. Bocquet, D. Brooks, D. Brout, E. Buckley-Geer, D. L. Burke, V. Busti, R. Campisano, L. Cardiel-Sas, A. C. Rosell, M. C. Kind, J. Carretero, F. J. Castander, R. Cawthon, C. Chang, X. Chen, C. Conselice, G. Costa, M. Crocce, C. E. Cunha, C. B. D'Andrea, L. N. da Costa, R. Das, G. Daues, T. M. Davis, C. Davis, J. D. Vicente, D. L. DePoy, J. DeRose, S. Desai, H. T. Diehl, J. P. Dietrich, S. Dodelson, P. Doel, A. Drlica-Wagner, T. F. Eifler, A. E. Elliott, A. E. Evrard, A. Farahi, A. F. Neto, E. Fernandez, D. A. Finley, B. Flaugher, R. J. Foley, P. Fosalba, D. N. Friedel, J. Frieman, J. García-Bellido, E. Gaztanaga, D. W. Gerdes, T. Giannantonio, M. S. S. Gill, K. Glazebrook, D. A. Goldstein, M. Gower, D. Gruen, R. A. Gruendl, J. Gschwend, R. R. Gupta, G. Gutierrez, S. Hamilton, W. G. Hartley, S. R. Hinton, J. M. Hislop, D. Hollowood, K. Honscheid, B. Hoyle, D. Huterer, B. Jain, D. J. James, T. Jeltema, M. W. G. Johnson, M. D. Johnson, T. Kacprzak, S. Kent, G. Khullar, M. Klein, A. Kovacs, A. M. G. Koziol, E. Krause, A. Kremin, R. Kron, K. Kuehn, S. Kuhlmann, N. Kuropatkin, O. Lahav, J. Lasker, T. S. Li, R. T. Li, A. R. Liddle, M. Lima, H. Lin, P. López-Reyes, N. MacCrann, M. A. G. Maia, J. D. Maloney, M. Manera, M. March, J. Marriner, J. L. Marshall, P. Martini, T. McClintock, T. McKay, R. G. McMahon, P. Melchior, F. Menanteau, C. J. Miller, R. Miquel, J. J. Mohr, E. Morganson, J. Mould, E. Neilsen, R. C. Nichol, F. Nogueira, B. Nord, P. Nugent, L. Nunes, R. L. C. Ogando, L. Old, A. B. Pace, A. Palmese, F. Paz-Chinchón, H. V. Peiris, W. J. Percival, D. Petravick, A. A. Plazas, J. Poh, C. Pond, A. Porredon, A. Pujol, A. Refregier, K. Reil, P. M. Ricker, R. P. Rollins, A. K. Romer, A. Roodman, P. Rooney, A. J. Ross, E. S. Rykoff, M. Sako, M. L. Sanchez, E. Sanchez, B. Santiago, A. Saro, V. Scarpine, D. Scolnic, S. Serrano, I. Sevilla-Noarbe, E. Sheldon, N. Shipp, M. L. Silveira, M. Smith, R. C. Smith, J. A. Smith, M. Soares-Santos, F. Sobreira, J. Song, A. Stebbins, E. Suchyta, M. Sullivan, M. E. C. Swanson, G. Tarle, J. Thaler, D. Thomas, R. C. Thomas, M. A. Troxel, D. L. Tucker, V. Vikram, A. K. Vivas, A. R. Walker, R. H. Wechsler, J. Weller, W. Wester, R. C. Wolf, H. Wu, B. Yanny, A. Zenteno, Y. Zhang, J. Zuntz, S. Juneau, M. Fitzpatrick,

R. Nikutta, D. Nidever, K. Olsen, A. Scott, and and. The dark energy survey: Data release 1. *The Astrophysical Journal Supplement Series*, 239(2):18, nov 2018.

[5] L. R. Abramo. The full Fisher matrix for galaxy surveys. MNRAS, 420(3):2042–2057, Mar 2012.

[6] L. R. Abramo, L. F. Secco, and A. Loureiro. Fourier analysis of multitracer cosmological surveys. MNRAS, 455(4):3871–3889, Feb 2016.

[7] V. Acquaviva, N. Bartolo, S. Matarrese, and A. Riotto. Gauge-invariant second-order perturbations and non-Gaussianity from inflation. *Nuclear Physics B*, 667(1-2):119–148, Sep 2003.

[8] P. Ade, J. Aguirre, Z. Ahmed, S. Aiola, A. Ali, D. Alonso, M. A. Alvarez, K. Arnold, P. Ashton, J. Austermann, and et al. The Simons Observatory: science goals and forecasts. J. Cosmology Astropart. Phys., 2019(2):056, Feb 2019.

[9] P. A. R. Ade, Y. Akiba, A. E. Anthony, K. Arnold, M. Atlas, D. Barron, D. Boettger, J. Borrill, S. Chapman, Y. Chinone, M. Dobbs, T. Elleflot, J. Errard, G. Fabbian, C. Feng, D. Flanigan, A. Gilbert, W. Grainger, N. W. Halverson, M. Hasegawa, K. Hattori, M. Hazumi, W. L. Holzapfel, Y. Hori, J. Howard, P. Hyland, Y. Inoue, G. C. Jaehnig, A. Jaffe, B. Keating, Z. Kermish, R. Keskitalo, T. Kisner, M. Le Jeune, A. T. Lee, E. Linder, E. M. Leitch, M. Lungu, F. Matsuda, T. Matsumura, X. Meng, N. J. Miller, H. Morii, S. Moyerman, M. J. Myers, M. Navaroli, H. Nishino, H. Paar, J. Peloton, E. Quealy, G. Rebeiz, C. L. Reichardt, P. L. Richards, C. Ross, I. Schanning, D. E. Schenck, B. Sherwin, A. Shimizu, C. Shimmin, M. Shimon, P. Siritanasak, G. Smecher, H. Spieler, N. Stebor, B. Steinbach, R. Stompor, A. Suzuki, S. Takakura, T. Tomaru, B. Wilson, A. Yadav, O. Zahn, and Polarbear Collaboration. Measurement of the Cosmic Microwave Background Polarization Lensing Power Spectrum with the POLARBEAR Experiment. Phys. Rev. Lett., 113(2):021301, Jul 2014.

[10] M. Aguilar Faundez, K. Arnold, C. Baccigalupi, D. Barron, D. Beck, F. Bianchini, D. Boettger, J. Borrill, J. Carron, K. Cheung, Y. Chinone, H. El Bouhargani, T. Elleflot, J. Errard, G. Fabbian, C. Feng, N. Galitzki, N. Goeckner-Wald, M. Hasegawa, M. Hazumi, L. Howe, D. Kaneko, N. Katayama, B. Keating, N. Krachmalnicoff, A. Kusaka, A. T. Lee, D. Leon, E. Linder, L. N. Lowry, F. Matsuda, Y. Minami, M. Navaroli, H. Nishino, A. T. P. Pham, D. Poletti, G. Puglisi, C. L. Reichardt, B. D. Sherwin, M. Silva-Feaver, R. Stompor, A. Suzuki, O. Tajima, S. Takakura, S. Takatori, G. P. Teply, C. Tsai, and C. Verges. Cross-correlation of POLARBEAR CMB Polarization Lensing with High-z Sub-mm Herschel-ATLAS galaxies. *arXiv e-prints*, page arXiv:1903.07046, Mar 2019.

[11] H. Aihara, N. Arimoto, R. Armstrong, S. Arnouts, N. A. Bahcall, S. Bickerton, J. Bosch, K. Bundy, P. L. Capak, J. H. H. Chan, M. Chiba, J. Coupon, E. Egami, M. Enoki, F. Finet, H. Fujimori, S. Fujimoto, H. Furusawa, J. Furusawa, T. Goto, A. Goulding, J. P. Greco, J. E. Greene, J. E. Gunn, T. Hamana, Y. Harikane, Y. Hashimoto, T. Hattori, M. Hayashi, Y. Hayashi, K. G. Hełminiak, R. Higuchi, C. Hikage, P. T. P. Ho, B.-C. Hsieh, K. Huang, S. Huang, H. Ikeda, M. Imanishi, A. K. Inoue, K. Iwasawa, I. Iwata, A. T. Jaelani, H.-Y. Jian, Y. Kamata, H. Karoji, N. Kashikawa, N. Katayama, S. Kawanomoto, I. Kayo, J. Koda, M. Koike, T. Kojima, Y. Komiyama, A. Konno, S. Koshida, Y. Koyama, H. Kusakabe, A. Leauthaud, C.-H. Lee, L. Lin, Y.-T. Lin, R. H. Lupton, R. Mand elbaum, Y. Matsuoka, E. Medezinski, S. Mineo, S. Miyama, H. Miyatake, S. Miyazaki, R. Momose, A. More, S. More, Y. Moritani, T. J. Moriya, T. Morokuma, S. Mukae, R. Murata, H. Murayama, T. Nagao, F. Nakata, M. Niida, H. Niikura, A. J. Nishizawa, Y. Obuchi, M. Oguri, Y. Oishi, N. Okabe, S. Okamoto, Y. Okura, Y. Ono, M. Onodera, M. Onoue, K. Osato, M. Ouchi, P. A. Price, T.-S. Pyo, M. Sako, M. Sawicki, T. Shibuya, K. Shimasaku, A. Shimono, M. Shirasaki, J. D. Silverman, M. Simet, J. Speagle, D. N. Spergel, M. A. Strauss, Y. Sugahara, N. Sugiyama, Y. Suto, S. H. Suyu, N. Suzuki, P. J. Tait, M. Takada, T. Takata, N. Tamura, M. M. Tanaka, M. Tanaka, M. Tanaka, Y. Tanaka, T. Terai, Y. Terashima, Y. Toba, N. Tominaga, J. Toshikawa, E. L. Turner, T. Uchida, H. Uchiyama, K. Umetsu, F. Uraguchi, Y. Urata, T. Usuda, Y. Utsumi, S.-Y. Wang, W.-H. Wang, K. C. Wong, K. Yabe, Y. Yamada, H. Yamanoi, N. Yasuda, S. Yeh, A. Yonehara, and S. Yuma. The Hyper Suprime-Cam SSP Survey: Overview and survey design. PASJ, 70:S4, Jan 2018.

[12] A. Alarcon, M. Eriksen, and E. Gaztanaga. Cosmological constraints from multiple tracers in spectroscopic surveys. MNRAS, 473(2):1444–1460, Jan 2018.

[13] R. Allison, P. Caucal, E. Calabrese, J. Dunkley, and T. Louis. Towards a cosmological neutrino mass detection. Phys. Rev. D, 92(12):123535, Dec 2015.

[14] J. Asorey, M. Crocce, and E. Gaztañaga. Redshift-space distortions from the cross-correlation of photometric populations. MNRAS, 445(3):2825–2835, Dec 2014.

[15] J. Asorey, M. Crocce, E. Gaztañaga, and A. Lewis. Recovering 3D clustering information with angular correlations. MNRAS, 427(3):1891–1902, Dec 2012.

[16] M. Banerji, F. B. Abdalla, O. Lahav, and H. Lin. Photometric redshifts for the Dark Energy Survey and VISTA and implications for large-scale structure. MNRAS, 386(3):1219–1233, May 2008.

[17] J. M. Bardeen, J. R. Bond, N. Kaiser, and A. S. Szalay. The statistics of peaks of Gaussian random fields. *The Astrophysical Journal*, 304:15–61, May 1986.

[18] M. Bartelmann and P. Schneider. Weak gravitational lensing. *Physics Reports*, 340:291–472, Jan. 2001.

[19] N. Bartolo, E. Komatsu, S. Matarrese, and A. Riotto. Non-Gaussianity from inflation: theory and observations. Phys. Rep., 402(3-4):103–266, Nov 2004.

[20] E. J. Baxter, Y. Omori, C. Chang, T. Giannantonio, D. Kirk, E. Krause, J. Blazek, L. Bleem, A. Choi, T. M. Crawford, S. Dodelson, T. F. Eifler, O. Friedrich, D. Gruen, G. P. Holder, B. Jain, M. Jarvis, N. MacCrann, A. Nicola, S. Pandey, J. Prat, C. L. Reichardt, S. Samuroff, C. Sánchez, L. F. Secco, E. Sheldon, M. A. Troxel, J. Zuntz, T. M. C. Abbott, F. B. Abdalla, J. Annis, S. Avila, K. Bechtol, B. A. Benson, E. Bertin, D. Brooks, E. Buckley-Geer, D. L. Burke, A. Carnero Rosell, M. Carrasco Kind, J. Carretero, F. J. Castander, R. Cawthon, C. E. Cunha, C. B. D'Andrea, L. N. da Costa, C. Davis, J. De Vicente, D. L. DePoy, H. T. Diehl, P. Doel, J. Estrada, A. E. Evrard, B. Flaugher, P. Fosalba, J. Frieman, J. García-Bellido, E. Gaztanaga, D. W. Gerdes, R. A. Gruendl, J. Gschwend, G. Gutierrez, W. G. Hartley, D. Hollowood, B. Hoyle, D. J. James, S. Kent, K. Kuehn, N. Kuropatkin, O. Lahav, M. Lima, M. A. G. Maia, M. March, J. L. Marshall, P. Melchior, F. Menanteau, R. Miquel, A. A. Plazas, A. Roodman, E. S. Rykoff, E. Sanchez, R. Schindler, M. Schubnell, I. Sevilla-Noarbe, M. Smith, R. C. Smith, M. Soares-Santos, F. Sobreira, E. Suchyta, M. E. C. Swanson, G. Tarle, A. R. Walker, W. L. K. Wu, J. Weller, DES, and SPT Collaborations. Dark Energy Survey Year 1 results: Methodology and projections for joint analysis of galaxy clustering, galaxy lensing, and CMB lensing two-point functions. Phys. Rev. D, 99(2):023508, Jan 2019.

[21] N. Benítez. Bayesian Photometric Redshift Estimation. ApJ, 536(2):571–583, Jun 2000.

[22] C. L. Bennett, D. Larson, J. L. Weiland, N. Jarosik, G. Hinshaw, N. Odegard, K. M. Smith, R. S. Hill, B. Gold, M. Halpern, E. Komatsu, M. R. Nolta, L. Page, D. N. Spergel, E. Wollack, J. Dunkley, A. Kogut, M. Limon, S. S. Meyer, G. S. Tucker, and E. L. Wright. Nine-year Wilkinson Microwave Anisotropy Probe (WMAP) Observations: Final Maps and Results. ApJS, 208(2):20, Oct 2013.

[23] B. A. Benson, P. A. R. Ade, Z. Ahmed, S. W. Allen, K. Arnold, J. E. Austermann, A. N. Bender, L. E. Bleem, J. E. Carlstrom, C. L. Chang, H. M. Cho, J. F. Cliche, T. M. Crawford, A. Cukierman, T. de Haan, M. A. Dobbs, D. Dutcher, W. Everett, A. Gilbert, N. W. Halverson, D. Hanson, N. L. Harrington, K. Hattori, J. W. Henning, G. C. Hilton, G. P. Holder, W. L. Holzapfel, K. D. Irwin, R. Keisler, L. Knox, D. Kubik, C. L. Kuo, A. T. Lee, E. M. Leitch, D. Li, M. McDonald, S. S. Meyer, J. Montgomery, M. Myers, T. Natoli, H. Nguyen, V. Novosad, S. Padin, Z. Pan, J. Pearson, C. Reichardt, J. E. Ruhl,

B. R. Saliwanchik, G. Simard, G. Smecher, J. T. Sayre, E. Shirokoff, A. A. Stark, K. Story, A. Suzuki, K. L. Thompson, C. Tucker, K. Vanderlinde, J. D. Vieira, A. Vikhlinin, G. Wang, V. Yefremenko, and K. W. Yoon. SPT-3G: a next-generation cosmic microwave background polarization experiment on the South Pole telescope. In Proc. SPIE, volume 9153 of *Society of Photo-Optical Instrumentation Engineers (SPIE) Conference Series*, page 91531P, Jul 2014.

[24] F. Bernardeau, S. Colombi, E. Gaztañaga, et al. Large-scale structure of the Universe and cosmological perturbation theory. *Physics Reports*, 367(1-3):1–248, Sept. 2002.

[25] G. M. Bernstein and Y.-C. Cai. Cosmology without cosmic variance. MNRAS, 416(4):3009–3016, Oct 2011.

[26] F. Bianchini, P. Bielewicz, A. Lapi, J. Gonzalez-Nuevo, C. Baccigalupi, G. de Zotti, L. Danese, N. Bourne, A. Cooray, L. Dunne, S. Dye, S. Eales, R. Ivison, S. Maddox, M. Negrello, D. Scott, M. W. L. Smith, and E. Valiante. Cross-correlation between the CMB Lensing Potential Measured by Planck and High-z Submillimeter Galaxies Detected by the Herschel-Atlas Survey. ApJ, 802(1):64, Mar 2015.

[27] F. Bianchini, A. Lapi, M. Calabrese, P. Bielewicz, J. Gonzalez-Nuevo, C. Baccigalupi, L. Danese, G. de Zotti, N. Bourne, A. Cooray, L. Dunne, S. Eales, and E. Valiante. Toward a Tomographic Analysis of the Cross-Correlation between Planck CMB Lensing and H-ATLAS Galaxies. ApJ, 825(1):24, Jul 2016.

[28] F. Bianchini and C. L. Reichardt. Constraining Gravity at Large Scales with the 2MASS Photometric Redshift Catalog and Planck Lensing. ApJ, 862(1):81, Jul 2018.

[29] S. Bird, M. Viel, and M. G. Haehnelt. Massive neutrinos and the non-linear matter power spectrum. MNRAS, 420(3):2551–2561, Mar 2012.

[30] C. Blake, S. Brough, M. Colless, C. Contreras, W. Couch, S. Croom, D. Croton, T. M. Davis, M. J. Drinkwater, K. Forster, D. Gilbank, M. Gladders, K. Glazebrook, B. Jelliffe, R. J. Jurek, I. h. Li, B. Madore, D. C. Martin, K. Pimbblet, G. B. Poole, M. Pracy, R. Sharp, E. Wisnioski, D. Woods, T. K. Wyder, and H. K. C. Yee. The WiggleZ Dark Energy Survey: joint measurements of the expansion and growth history at z < 1. MNRAS, 425(1):405–414, Sep 2012.

[31] C. Blake, E. A. Kazin, F. Beutler, T. M. Davis, D. Parkinson, S. Brough, M. Colless, C. Contreras, W. Couch, S. Croom, D. Croton, M. J. Drinkwater, K. Forster, D. Gilbank, M. Gladders, K. Glazebrook, B. Jelliffe, R. J. Jurek, I. H. Li, B. Madore, D. C. Martin,

K. Pimbblet, G. B. Poole, M. Pracy, R. Sharp, E. Wisnioski, D. Woods, T. K. Wyder, and H. K. C. Yee. The WiggleZ Dark Energy Survey: mapping the distance-redshift relation with baryon acoustic oscillations. MNRAS, 418(3):1707–1724, Dec 2011.

[32] L. E. Bleem, B. Stalder, T. de Haan, K. A. Aird, S. W. Allen, D. E. Applegate, M. L. N. Ashby, M. Bautz, M. Bayliss, B. A. Benson, S. Bocquet, M. Brodwin, J. E. Carlstrom, C. L. Chang, I. Chiu, H. M. Cho, A. Clocchiatti, T. M. Crawford, A. T. Crites, S. Desai, J. P. Dietrich, M. A. Dobbs, R. J. Foley, W. R. Forman, E. M. George, M. D. Gladders, A. H. Gonzalez, N. W. Halverson, C. Hennig, H. Hoekstra, G. P. Holder, W. L. Holzapfel, J. D. Hrubes, C. Jones, R. Keisler, L. Knox, A. T. Lee, E. M. Leitch, J. Liu, M. Lueker, D. Luong-Van, A. Mantz, D. P. Marrone, M. McDonald, J. J. McMahon, S. S. Meyer, L. Mocanu, J. J. Mohr, S. S. Murray, S. Padin, C. Pryke, C. L. Reichardt, A. Rest, J. Ruel, J. E. Ruhl, B. R. Saliwanchik, A. Saro, J. T. Sayre, K. K. Schaffer, T. Schrabback, E. Shirokoff, J. Song, H. G. Spieler, S. A. Stanford, Z. Staniszewski, A. A. Stark, K. T. Story, C. W. Stubbs, K. Vanderlinde, J. D. Vieira, A. Vikhlinin, R. Williamson, O. Zahn, and A. Zenteno. Galaxy Clusters Discovered via the Sunyaev-Zel'dovich Effect in the 2500-Square-Degree SPT-SZ Survey. ApJS, 216:27, Feb. 2015.

[33] L. E. Bleem, A. van Engelen, G. P. Holder, K. A. Aird, R. Armstrong, M. L. N. Ashby, M. R. Becker, B. A. Benson, T. Biesiadzinski, M. Brodwin, M. T. Busha, J. E. Carlstrom, C. L. Chang, H. M. Cho, T. M. Crawford, A. T. Crites, T. de Haan, S. Desai, M. A. Dobbs, O. Doré, J. Dudley, J. E. Geach, E. M. George, M. D. Gladders, A. H. Gonzalez, N. W. Halverson, N. Harrington, F. W. High, B. P. Holden, W. L. Holzapfel, S. Hoover, J. D. Hrubes, M. Joy, R. Keisler, L. Knox, A. T. Lee, E. M. Leitch, M. Lueker, D. Luong-Van, D. P. Marrone, J. Martinez-Manso, J. J. McMahon, J. Mehl, S. S. Meyer, J. J. Mohr, T. E. Montroy, T. Natoli, S. Padin, T. Plagge, C. Pryke, C. L. Reichardt, A. Rest, J. E. Ruhl, B. R. Saliwanchik, J. T. Sayre, K. K. Schaffer, L. Shaw, E. Shirokoff, H. G. Spieler, B. Stalder, S. A. Stanford, Z. Staniszewski, A. A. Stark, D. Stern, K. Story, A. Vallinotto, K. Vanderlinde, J. D. Vieira, R. H. Wechsler, R. Williamson, and O. Zahn. A Measurement of the Correlation of Galaxy Surveys with CMB Lensing Convergence Maps from the South Pole Telescope. ApJ, 753(1):L9, Jul 2012.

[34] A. Boyle. Understanding the neutrino mass constraints achievable by combining CMB lensing and spectroscopic galaxy surveys. J. Cosmology Astropart. Phys., 2019(4):038, Apr 2019.

[35] A. Boyle and E. Komatsu. Deconstructing the neutrino mass constraint from galaxy redshift surveys. J. Cosmology Astropart. Phys., 2018(3):035, Mar 2018.

[36] G. Bruzual and S. Charlot. Stellar population synthesis at the resolution of 2003. MNRAS, 344(4):1000–1028, Oct 2003.

[37] D. L. Burke, E. S. Rykoff, S. Allam, J. Annis, K. Bechtol, G. M. Bernstein, A. Drlica-Wagner, D. A. Finley, R. A. Gruendl, D. J. James, S. Kent, R. Kessler, S. Kuhlmann, J. Lasker, T. S. Li, D. Scolnic, J. Smith, D. L. Tucker, W. Wester, B. Yanny, T. M. C. Abbott, F. B. Abdalla, A. Benoit-Lévy, E. Bertin, A. Carnero Rosell, M. Carrasco Kind, J. Carretero, C. E. Cunha, C. B. D'Andrea, L. N. da Costa, S. Desai, H. T. Diehl, P. Doel, J. Estrada, J. García-Bellido, D. Gruen, G. Gutierrez, K. Honscheid, K. Kuehn, N. Kuropatkin, M. A. G. Maia, M. March, J. L. Marshall, P. Melchior, F. Menanteau, R. Miquel, A. A. Plazas, M. Sako, E. Sanchez, V. Scarpine, R. Schindler, I. Sevilla-Noarbe, M. Smith, R. C. Smith, M. Soares-Santos, F. Sobreira, E. Suchyta, G. Tarle, A. R. Walker, and DES Collaboration. Forward Global Photometric Calibration of the Dark Energy Survey. AJ, 155:41, Jan. 2018.

[38] C. T. Byrnes and K.-Y. Choi. Review of Local Non-Gaussianity from Multifield Inflation. *Advances in Astronomy*, 2010:724525, Jan 2010.

[39] A. Cabré, P. Fosalba, E. Gaztañaga, and M. Manera. Error analysis in cross-correlation of sky maps: application to the Integrated Sachs-Wolfe detection. MNRAS, 381:1347–1368, Nov. 2007.

[40] F. Capozzi, E. Lisi, A. Marrone, D. Montanino, and A. Palazzo. Neutrino masses and mixings: Status of known and unknown 3ν parameters. *Nuclear Physics B*, 908:218–234, Jul 2016.

[41] J. E. Carlstrom, P. A. R. Ade, K. A. Aird, B. A. Benson, L. E. Bleem, S. Busetti, C. L. Chang, E. Chauvin, H. M. Cho, T. M. Crawford, A. T. Crites, M. A. Dobbs, N. W. Halverson, S. Heimsath, W. L. Holzapfel, J. D. Hrubes, M. Joy, R. Keisler, T. M. Lanting, A. T. Lee, E. M. Leitch, J. Leong, W. Lu, M. Lueker, D. Luong-Van, J. J. McMahon, J. Mehl, S. S. Meyer, J. J. Mohr, T. E. Montroy, S. Padin, T. Plagge, C. Pryke, J. E. Ruhl, K. K. Schaffer, D. Schwan, E. Shirokoff, H. G. Spieler, Z. Staniszewski, A. A. Stark, C. Tucker, K. Vand erlinde, J. D. Vieira, and R. Williamson. The 10 Meter South Pole Telescope. PASP, 123(903):568, May 2011.

[42] J. E. Carlstrom, G. P. Holder, and E. D. Reese. Cosmology with the Sunyaev-Zel'dovich Effect. ARA&A, 40:643–680, Jan 2002.

[43] E. Castorina, N. Hand, U. Seljak, F. Beutler, C.-H. Chuang, C. Zhao, H. Gil-Marín, W. J. Percival, A. J. Ross, P. D. Choi, K. Dawson, A. de la Macorra, G. Rossi, R. Rug-

geri, D. Schneider, and G.-B. Zhao. Redshift-weighted constraints on primordial non-Gaussianity from the clustering of the eBOSS DR14 quasars in Fourier space. *arXiv e-prints*, page arXiv:1904.08859, Apr 2019.

[44] R. Cawthon, C. Davis, M. Gatti, P. Vielzeuf, J. Elvin-Poole, E. Rozo, J. Frieman, E. S. Rykoff, A. Alarcon, G. M. Bernstein, C. Bonnett, A. Carnero Rosell, F. J. Castander, C. Chang, L. N. da Costa, J. De Vicente, J. DeRose, A. Drlica-Wagner, E. Gaztanaga, T. Giannantonio, D. Gruen, J. Gschwend, W. G. Hartley, B. Hoyle, H. Lin, M. A. G. Maia, R. Miquel, R. L. C. Ogando, M. M. Rau, A. Roodman, A. J. Ross, I. Sevilla-Noarbe, M. A. Troxel, R. H. Wechsler, T. M. C. Abbott, F. B. Abdalla, S. Allam, J. Annis, S. Avila, M. Banerji, K. Bechtol, R. A. Bernstein, E. Bertin, D. Brooks, D. L. Burke, M. Carrasco Kind, J. Carretero, C. E. Cunha, C. B. D'Andrea, D. L. DePoy, S. Desai, H. T. Diehl, P. Doel, T. F. Eifler, A. E. Evrard, B. Flaugher, P. Fosalba, J. García-Bellido, D. W. Gerdes, R. A. Gruendl, G. Gutierrez, D. Hollowood, K. Honscheid, D. J. James, T. Jeltema, E. Krause, K. Kuehn, S. Kuhlmann, N. Kuropatkin, O. Lahav, M. Lima, J. L. Marshall, P. Martini, F. Menanteau, C. J. Miller, A. A. Plazas, E. Sanchez, V. Scarpine, R. Schindler, M. Schubnell, E. Sheldon, M. Smith, R. C. Smith, M. Soares-Santos, F. Sobreira, E. Suchyta, M. E. C. Swanson, G. Tarle, D. Thomas, D. L. Tucker, A. R. Walker, and DES Collaboration. Dark Energy Survey Year 1 Results: calibration of redMaGiC redshift distributions in DES and SDSS from cross-correlations. MNRAS, 481(2):2427–2443, Dec 2018.

[45] A. Challinor. Anisotropies in the Cosmic Microwave Background. *arXiv e-prints*, pages astro–ph/0403344, Mar 2004.

[46] X. Chen. Primordial Non-Gaussianities from Inflation Models. *Advances in Astronomy*, 2010:638979, Jan 2010.

[47] R. Chown, Y. Omori, K. Aylor, B. A. Benson, L. E. Bleem, J. E. Carlstrom, C. L. Chang, H. M. Cho, T. M. Crawford, A. T. Crites, T. de Haan, M. A. Dobbs, W. B. Everett, E. M. George, J. W. Henning, N. W. Halverson, N. L. Harrington, G. Holder, W. L. Holzapfel, Z. Hou, J. D. Hrubes, L. Knox, A. T. Lee, D. Luong-Van, D. P. Marrone, J. J. McMahon, S. S. Meyer, M. Millea, L. M. Mocanu, J. J. Mohr, T. Natoli, S. Padin, C. Pryke, C. L. Reichardt, J. E. Ruhl, J. T. Sayre, K. K. Schaffer, E. Shirokoff, G. Simard, Z. Staniszewski, A. A. Stark, K. T. Story, K. Vanderlinde, J. D. Vieira, R. Williamson, W. L. K. Wu, and South Pole Telescope Collaboration. Maps of the Southern Millimeter-wave Sky from Combined 2500 deg^2 SPT-SZ and Planck Temperature Data. ApJS, 239(1):10, Nov 2018.

[48] S. Cole and G. Efstathiou. Gravitational lensing of fluctuations in the microwave background radiation. MNRAS, 239:195–200, Jul 1989.

[49] S. Cole, K. B. Fisher, and D. H. Weinberg. Fourier analysis of redshift-space distortions and the determination of . *Monthly Notices of the Royal Astronomical Society*, 267(3):785–799, Apr. 1994.

[50] M. Colless, G. Dalton, S. Maddox, W. Sutherland , P. Norberg, S. Cole, J. Bland - Hawthorn, T. Bridges, R. Cannon, C. Collins, W. Couch, N. Cross, K. Deeley, R. De Propris, S. P. Driver, G. Efstathiou, R. S. Ellis, C. S. Frenk, K. Glazebrook, C. Jackson, O. Lahav, I. Lewis, S. Lumsden, D. Madgwick, J. A. Peacock, B. A. Peterson, I. Price, M. Seaborne, and K. Taylor. The 2dF Galaxy Redshift Survey: spectra and redshifts. MNRAS, 328(4):1039–1063, Dec 2001.

[51] J. J. Condon, W. D. Cotton, E. W. Greisen, Q. F. Yin, R. A. Perley, G. B. Taylor, and J. J. Broderick. The NRAO VLA Sky Survey. AJ, 115(5):1693–1716, May 1998.

[52] M. Crocce, A. Cabré, and E. Gaztañaga. Modelling the angular correlation function and its full covariance in photometric galaxy surveys. MNRAS, 414(1):329–349, jun 2011.

[53] W. Cui, S. Borgani, and G. Murante. The effect of active galactic nuclei feedback on the halo mass function. MNRAS, 441(2):1769–1782, Jun 2014.

[54] N. Dalal, O. Doré, D. Huterer, and A. Shirokov. Imprints of primordial non-Gaussianities on large-scale structure: Scale-dependent bias and abundance of virialized objects. Phys. Rev. D, 77(12):123514, Jun 2008.

[55] S. Das, T. Louis, M. R. Nolta, G. E. Addison, E. S. Battistelli, J. R. Bond, E. Calabrese, D. Crichton, M. J. Devlin, S. Dicker, J. Dunkley, R. Dünner, J. W. Fowler, M. Gralla, A. Hajian, M. Halpern, M. Hasselfield, M. Hilton, A. D. Hincks, R. Hlozek, K. M. Huffenberger, J. P. Hughes, K. D. Irwin, A. Kosowsky, R. H. Lupton, T. A. Marriage, D. Marsden, F. Menanteau, K. Moodley, M. D. Niemack, L. A. Page, B. Partridge, E. D. Reese, B. L. Schmitt, N. Sehgal, B. D. Sherwin, J. L. Sievers, D. N. Spergel, S. T. Staggs, D. S. Swetz, E. R. Switzer, R. Thornton, H. Trac, and E. Wollack. The Atacama Cosmology Telescope: temperature and gravitational lensing power spectrum measurements from three seasons of data. J. Cosmology Astropart. Phys., 2014(4):014, Apr 2014.

[56] K. S. Dawson, D. J. Schlegel, C. P. Ahn, S. F. Anderson, É. Aubourg, S. Bailey, R. H. Barkhouser, J. E. Bautista, A. r. Beifiori, A. A. Berlind, V. Bhardwaj, D. Bizyaev, C. H.

Blake, M. R. Blanton, M. Blomqvist, A. S. Bolton, A. Borde, J. Bovy, W. N. Brandt, H. Brewington, J. Brinkmann, P. J. Brown, J. R. Brownstein, K. Bundy, N. G. Busca, W. Carithers, A. R. Carnero, M. A. Carr, Y. Chen, J. Comparat, N. Connolly, F. Cope, R. A. C. Croft, A. J. Cuesta, L. N. da Costa, J. R. A. Davenport, T. Delubac, R. de Putter, S. Dhital, A. Ealet, G. L. Ebelke, D. J. Eisenstein, S. Escoffier, X. Fan, N. Filiz Ak, H. Finley, A. Font-Ribera, R. Génova-Santos, J. E. Gunn, H. Guo, D. Haggard, P. B. Hall, J.-C. Hamilton, B. Harris, D. W. Harris, S. Ho, D. W. Hogg, D. Holder, K. Honscheid, J. Huehnerhoff, B. Jordan, W. P. Jordan, G. Kauffmann, E. A. Kazin, D. Kirkby, M. A. Klaene, J.-P. Kneib, J.-M. Le Goff, K.-G. Lee, D. C. Long, C. P. Loomis, B. Lundgren, R. H. Lupton, M. A. G. Maia, M. Makler, E. Malanushenko, V. Malanushenko, R. Mandelbaum, M. Manera, C. Maraston, D. Margala, K. L. Masters, C. K. McBride, P. McDonald, I. D. McGreer, R. G. McMahon, O. Mena, J. Miralda-Escudé, A. D. Montero-Dorta, F. Montesano, D. Muna, A. D. Myers, T. Naugle, R. C. Nichol, P. Noterdaeme, S. E. Nuza, M. D. Olmstead, A. Oravetz, D. J. Oravetz, R. Owen, N. Padmanabhan, N. Palanque-Delabrouille, K. Pan, J. K. Parejko, I. Pâris, W. J. Percival, I. Pérez-Fournon, I. Pérez-Ràfols, P. Petitjean, R. Pfaffenberger, J. Pforr, M. M. Pieri, F. Prada, A. M. Price-Whelan, M. J. Raddick, R. Rebolo, J. Rich, G. T. Richards, C. M. Rockosi, N. A. Roe, A. J. Ross, N. P. Ross, G. Rossi, J. A. Rubiño-Martin, L. Samushia, A. G. Sánchez, C. Sayres, S. J. Schmidt, D. P. Schneider, C. G. Scóccola, H.-J. Seo, A. Shelden, E. Sheldon, Y. Shen, Y. Shu, A. Slosar, S. A. Smee, S. A. Snedden, F. Stauffer, O. Steele, M. A. Strauss, A. Streblyanska, N. Suzuki, M. E. C. Swanson, T. Tal, M. Tanaka, D. Thomas, J. L. Tinker, R. Tojeiro, C. A. Tremonti, M. Vargas Magaña, L. Verde, M. Viel, D. A. Wake, M. Watson, B. A. Weaver, D. H. Weinberg, B. J. Weiner, A. A. West, M. White, W. M. Wood-Vasey, C. Yeche, I. Zehavi, G.-B. Zhao, and Z. Zheng. The Baryon Oscillation Spectroscopic Survey of SDSS-III. AJ, 145(1):10, Jan 2013.

[57] J. T. A. de Jong, G. A. Verdoes Kleijn, K. H. Kuijken, and E. A. Valentijn. The Kilo-Degree Survey. *Experimental Astronomy*, 35(1-2):25–44, Jan 2013.

[58] J. De Vicente, E. Sánchez, and I. Sevilla-Noarbe. DNF - Galaxy photometric redshift by Directional Neighbourhood Fitting. MNRAS, 459(3):3078–3088, Jul 2016.

[59] C. Devereux, J. E. Geach, and M. J. Hardcastle. The linear bias of radio galaxies at z ≈ 0.3 via cosmic microwave background lensing. MNRAS, 485(1):L1–L5, May 2019.

[60] S. Dodelson. *Modern Cosmology*. 2003.

[61] A. Drlica-Wagner, I. Sevilla-Noarbe, E. S. Rykoff, R. A. Gruendl, B. Yanny, D. L. Tucker, B. Hoyle, A. Carnero Rosell, G. M. Bernstein, K. Bechtol, M. R. Becker, A. Benoit-Lévy,

E. Bertin, M. Carrasco Kind, C. Davis, J. de Vicente, H. T. Diehl, D. Gruen, W. G. Hartley, B. Leistedt, T. S. Li, J. L. Marshall, E. Neilsen, M. M. Rau, E. Sheldon, J. Smith, M. A. Troxel, S. Wyatt, Y. Zhang, T. M. C. Abbott, F. B. Abdalla, S. Allam, M. Banerji, D. Brooks, E. Buckley-Geer, D. L. Burke, D. Capozzi, J. Carretero, C. E. Cunha, C. B. D'Andrea, L. N. da Costa, D. L. DePoy, S. Desai, J. P. Dietrich, P. Doel, A. E. Evrard, A. Fausti Neto, B. Flaugher, P. Fosalba, J. Frieman, J. García-Bellido, D. W. Gerdes, T. Giannantonio, J. Gschwend, G. Gutierrez, K. Honscheid, D. J. James, T. Jeltema, K. Kuehn, S. Kuhlmann, N. Kuropatkin, O. Lahav, M. Lima, H. Lin, M. A. G. Maia, P. Martini, R. G. McMahon, P. Melchior, F. Menanteau, R. Miquel, R. C. Nichol, R. L. C. Ogand o, A. A. Plazas, A. K. Romer, A. Roodman, E. Sanchez, V. Scarpine, R. Schindler, M. Schubnell, M. Smith, R. C. Smith, M. Soares-Santos, F. Sobreira, E. Suchyta, G. Tarle, V. Vikram, A. R. Walker, R. H. Wechsler, J. Zuntz, and DES Collaboration. Dark Energy Survey Year 1 Results: The Photometric Data Set for Cosmology. ApJS, 235(2):33, Apr 2018.

[62] J. Elvin-Poole, M. Crocce, A. J. Ross, T. Giannantonio, E. Rozo, E. S. Rykoff, S. Avila, N. Banik, J. Blazek, S. L. Bridle, R. Cawthon, A. Drlica-Wagner, O. Friedrich, N. Kokron, E. Krause, N. MacCrann, J. Prat, C. Sánchez, L. F. Secco, I. Sevilla-Noarbe, M. A. Troxel, T. M. C. Abbott, F. B. Abdalla, S. Allam, J. Annis, J. Asorey, K. Bechtol, M. R. Becker, A. Benoit-Lévy, G. M. Bernstein, E. Bertin, D. Brooks, E. Buckley-Geer, D. L. Burke, A. Carnero Rosell, D. Carollo, M. Carrasco Kind, J. Carretero, F. J. Castander, C. E. Cunha, C. B. D'Andrea, L. N. da Costa, T. M. Davis, C. Davis, S. Desai, H. T. Diehl, J. P. Dietrich, S. Dodelson, P. Doel, T. F. Eifler, A. E. Evrard, E. Fernandez, B. Flaugher, P. Fosalba, J. Frieman, J. García-Bellido, E. Gaztanaga, D. W. Gerdes, K. Glazebrook, D. Gruen, R. A. Gruendl, J. Gschwend, G. Gutierrez, W. G. Hartley, S. R. Hinton, K. Honscheid, J. K. Hoormann, B. Jain, D. J. James, M. Jarvis, T. Jeltema, M. W. G. Johnson, M. D. Johnson, A. King, K. Kuehn, S. Kuhlmann, N. Kuropatkin, O. Lahav, G. Lewis, T. S. Li, C. Lidman, M. Lima, H. Lin, E. Macaulay, M. March, J. L. Marshall, P. Martini, P. Melchior, F. Menanteau, R. Miquel, J. J. Mohr, A. Möller, R. C. Nichol, B. Nord, C. R. O'Neill, W. J. Percival, D. Petravick, A. A. Plazas, A. K. Romer, M. Sako, E. Sanchez, V. Scarpine, R. Schindler, M. Schubnell, E. Sheldon, M. Smith, R. C. Smith, M. Soares-Santos, F. Sobreira, N. E. Sommer, E. Suchyta, M. E. C. Swanson, G. Tarle, D. Thomas, B. E. Tucker, D. L. Tucker, S. A. Uddin, V. Vikram, A. R. Walker, R. H. Wechsler, J. Weller, W. Wester, R. C. Wolf, F. Yuan, B. Zhang, J. Zuntz, and DES Collaboration. Dark Energy Survey year 1 results: Galaxy clustering for combined probes. Phys. Rev. D, 98(4):042006, Aug 2018.

[63] J. Fernández-Varea, D. Liljequist, R. Mayol, and F. Salvat. *Calculation of inelastic*

mean free path and stopping power for electrons in solids from an optical-data model. Stockholm University, 1992.

[64] F. Feroz, M. P. Hobson, and M. Bridges. MULTINEST: an efficient and robust Bayesian inference tool for cosmology and particle physics. MNRAS, 398(4):1601–1614, Oct 2009.

[65] B. Flaugher, H. T. Diehl, K. Honscheid, T. M. C. Abbott, O. Alvarez, R. Angstadt, J. T. Annis, M. Antonik, O. Ballester, L. Beaufore, G. M. Bernstein, R. A. Bernstein, B. Bigelow, M. Bonati, D. Boprie, D. Brooks, E. J. Buckley-Geer, J. Campa, L. Cardiel-Sas, F. J. Castand er, J. Castilla, H. Cease, J. M. Cela-Ruiz, S. Chappa, E. Chi, C. Cooper, L. N. da Costa, E. Dede, G. Derylo, D. L. DePoy, J. de Vicente, P. Doel, A. Drlica-Wagner, J. Eiting, A. E. Elliott, J. Emes, J. Estrada, A. Fausti Neto, D. A. Finley, R. Flores, J. Frieman, D. Gerdes, M. D. Gladders, B. Gregory, G. R. Gutierrez, J. Hao, S. E. Holland, S. Holm, D. Huffman, C. Jackson, D. J. James, M. Jonas, A. Karcher, I. Karliner, S. Kent, R. Kessler, M. Kozlovsky, R. G. Kron, D. Kubik, K. Kuehn, S. Kuhlmann, K. Kuk, O. Lahav, A. Lathrop, J. Lee, M. E. Levi, P. Lewis, T. S. Li, I. Mand richenko, J. L. Marshall, G. Martinez, K. W. Merritt, R. Miquel, F. Muñoz, E. H. Neilsen, R. C. Nichol, B. Nord, R. Ogando, J. Olsen, N. Palaio, K. Patton, J. Peoples, A. A. Plazas, J. Rauch, K. Reil, J. P. Rheault, N. A. Roe, H. Rogers, A. Roodman, E. Sanchez, V. Scarpine, R. H. Schindler, R. Schmidt, R. Schmitt, M. Schubnell, K. Schultz, P. Schurter, L. Scott, S. Serrano, T. M. Shaw, R. C. Smith, M. Soares-Santos, A. Stefanik, W. Stuermer, E. Suchyta, A. Sypniewski, G. Tarle, J. Thaler, R. Tighe, C. Tran, D. Tucker, A. R. Walker, G. Wang, M. Watson, C. Weaverdyck, W. Wester, R. Woods, B. Yanny, and DES Collaboration. The Dark Energy Camera. AJ, 150(5):150, Nov 2015.

[66] O. Friedrich, S. Seitz, T. F. Eifler, and D. Gruen. Performance of internal covariance estimators for cosmic shear correlation functions. MNRAS, 456(3):2662–2680, Mar 2016.

[67] J. N. Fry and E. Gaztanaga. Biasing and hierarchical statistics in large-scale structure. *The Astrophysical Journal*, 413:447–452, Aug. 1993.

[68] A. Gangui, F. Lucchin, S. Matarrese, and S. Mollerach. The Three-Point Correlation Function of the Cosmic Microwave Background in Inflationary Models. ApJ, 430:447, Aug 1994.

[69] E. Gaztañaga and J. A. Lobo. Nonlinear Gravitational Growth of Large-Scale Structures Inside and Outside Standard Cosmology. ApJ, 548(1):47–59, Feb 2001.

[70] T. Giannantonio, P. Fosalba, et al. CMB lensing tomography with the DES Science Verification galaxies. MNRAS, 456:3213–3244, Mar. 2016.

[71] H. Gil-Marín, C. Wagner, L. Verde, R. Jimenez, and A. F. Heavens. Reducing sample variance: halo biasing, non-linearity and stochasticity. MNRAS, 407(2):772–790, Sep 2010.

[72] J. Guzik, U. Seljak, and M. Zaldarriaga. Lensing effect on polarization in the microwave background: Extracting the convergence power spectrum. Phys. Rev. D, 62(4):043517, Aug 2000.

[73] H. Hildebrandt, S. Arnouts, P. Capak, L. A. Moustakas, C. Wolf, F. B. Abdalla, R. J. Assef, M. Banerji, N. Benítez, G. B. Brammer, T. Budavári, S. Carliles, D. Coe, T. Dahlen, R. Feldmann, D. Gerdes, B. Gillis, O. Ilbert, R. Kotulla, O. Lahav, I. H. Li, J. M. Miralles, N. Purger, S. Schmidt, and J. Singal. PHAT: PHoto-z Accuracy Testing. A&A, 523:A31, Nov 2010.

[74] C. M. Hirata, S. Ho, N. Padmanabhan, U. Seljak, and N. A. Bahcall. Correlation of CMB with large-scale structure. II. Weak lensing. Phys. Rev. D, 78(4):043520, Aug 2008.

[75] C. M. Hirata and U. Seljak. Reconstruction of lensing from the cosmic microwave background polarization. Phys. Rev. D, 68(8):083002, Oct 2003.

[76] C. Howlett, A. Lewis, A. Hall, and A. Challinor. CMB power spectrum parameter degeneracies in the era of precision cosmology. *Journal of Cosmology and Astroparticle Physics*, 2012(04):027–027, Apr. 2012.

[77] B. Hoyle, D. Gruen, G. M. Bernstein, M. M. Rau, J. De Vicente, W. G. Hartley, E. Gaztanaga, J. DeRose, M. A. Troxel, C. Davis, A. Alarcon, N. MacCrann, J. Prat, C. Sánchez, E. Sheldon, R. H. Wechsler, J. Asorey, M. R. Becker, C. Bonnett, A. Carnero Rosell, D. Carollo, M. Carrasco Kind, F. J. Castander, R. Cawthon, C. Chang, M. Childress, T. M. Davis, A. Drlica-Wagner, M. Gatti, K. Glazebrook, J. Gschwend, S. R. Hinton, J. K. Hoormann, A. G. Kim, A. King, K. Kuehn, G. Lewis, C. Lidman, H. Lin, E. Macaulay, M. A. G. Maia, P. Martini, D. Mudd, A. Möller, R. C. Nichol, R. L. C. Ogando, R. P. Rollins, A. Roodman, A. J. Ross, E. Rozo, E. S. Rykoff, S. Samuroff, I. Sevilla-Noarbe, R. Sharp, N. E. Sommer, B. E. Tucker, S. A. Uddin, T. N. Varga, P. Vielzeuf, F. Yuan, B. Zhang, T. M. C. Abbott, F. B. Abdalla, S. Allam, J. Annis, K. Bechtol, A. Benoit-Lévy, E. Bertin, D. Brooks, E. Buckley-Geer, D. L. Burke, M. T. Busha, D. Capozzi, J. Carretero, M. Crocce, C. B. D'Andrea, L. N. da Costa, D. L. DePoy, S. Desai, H. T.

Diehl, P. Doel, T. F. Eifler, J. Estrada, A. E. Evrard, E. Fernandez, B. Flaugher, P. Fosalba, J. Frieman, J. García-Bellido, D. W. Gerdes, T. Giannantonio, D. A. Goldstein, R. A. Gruendl, G. Gutierrez, K. Honscheid, D. J. James, M. Jarvis, T. Jeltema, M. W. G. Johnson, M. D. Johnson, D. Kirk, E. Krause, S. Kuhlmann, N. Kuropatkin, O. Lahav, T. S. Li, M. Lima, M. March, J. L. Marshall, P. Melchior, F. Menanteau, R. Miquel, B. Nord, C. R. O'Neill, A. A. Plazas, A. K. Romer, M. Sako, E. Sanchez, B. Santiago, V. Scarpine, R. Schindler, M. Schubnell, M. Smith, R. C. Smith, M. Soares-Santos, F. Sobreira, E. Suchyta, M. E. C. Swanson, G. Tarle, D. Thomas, D. L. Tucker, V. Vikram, A. R. Walker, J. Weller, W. Wester, R. C. Wolf, B. Yanny, J. Zuntz, and DES Collaboration. Dark Energy Survey Year 1 Results: redshift distributions of the weak-lensing source galaxies. MNRAS, 478(1):592–610, Jul 2018.

[78] W. Hu. CMB temperature and polarization anisotropy fundamentals. *Annals of Physics*, 303(1):203–225, Jan 2003.

[79] W. Hu and S. Dodelson. Cosmic Microwave Background Anisotropies. ARA&A, 40:171–216, Jan 2002.

[80] W. Hu and M. White. Power Spectra Estimation for Weak Lensing. ApJ, 554(1):67–73, Jun 2001.

[81] E. Huff and R. Mandelbaum. Metacalibration: Direct Self-Calibration of Biases in Shear Measurement. *arXiv e-prints*, page arXiv:1702.02600, Feb 2017.

[82] D. Huterer. Weak lensing, dark matter and dark energy. *General Relativity and Gravitation*, 42(9):2177–2195, Sep 2010.

[83] D. Huterer, D. Kirkby, R. Bean, A. Connolly, K. Dawson, S. Dodelson, A. Evrard, B. Jain, M. Jarvis, E. Linder, R. Mandelbaum, M. May, A. Raccanelli, B. Reid, E. Rozo, F. Schmidt, N. Sehgal, A. Slosar, A. van Engelen, H.-Y. Wu, and G. Zhao. Growth of cosmic structure: Probing dark energy beyond expansion. *Astroparticle Physics*, 63:23–41, Mar 2015.

[84] B. Jain, U. Seljak, and S. White. Ray-tracing Simulations of Weak Lensing by Large-Scale Structure. *Astrophysical Journal*, 530(2):547–577, Feb 2000.

[85] M. Jarvis, G. Bernstein, and B. Jain. The skewness of the aperture mass statistic. MNRAS, 352(1):338–352, Jul 2004.

[86] N. Kaiser. On the spatial correlations of Abell clusters. *The Astrophysical Journal*, 284:L9–L12, Sept. 1984.

[87] N. Kaiser. Clustering in real space and in redshift space. *Monthly Notices of the Royal Astronomical Society*, 227:1–21, July 1987.

[88] N. Kaiser. Weak Gravitational Lensing of Distant Galaxies. *Astrophysical Journal*, 388:272, Apr 1992.

[89] M. Kilbinger. Cosmology with cosmic shear observations: a review. *Reports on Progress in Physics*, 78(8):086901, Jul 2015.

[90] E. Komatsu and D. N. Spergel. Acoustic signatures in the primary microwave background bispectrum. Phys. Rev. D, 63(6):063002, Mar 2001.

[91] E. Krause, T. F. Eifler, J. Zuntz, O. Friedrich, M. A. Troxel, S. Dodelson, J. Blazek, L. F. Secco, N. MacCrann, E. Baxter, C. Chang, N. Chen, M. Crocce, J. DeRose, A. Ferte, N. Kokron, F. Lacasa, V. Miranda, Y. Omori, A. Porredon, R. Rosenfeld, S. Samuroff, M. Wang, R. H. Wechsler, T. M. C. Abbott, F. B. Abdalla, S. Allam, J. Annis, K. Bechtol, A. Benoit-Levy, G. M. Bernstein, D. Brooks, D. L. Burke, D. Capozzi, M. Carrasco Kind, J. Carretero, C. B. D'Andrea, L. N. da Costa, C. Davis, D. L. DePoy, S. Desai, H. T. Diehl, J. P. Dietrich, A. E. Evrard, B. Flaugher, P. Fosalba, J. Frieman, J. Garcia-Bellido, E. Gaztanaga, T. Giannantonio, D. Gruen, R. A. Gruendl, J. Gschwend, G. Gutierrez, K. Honscheid, D. J. James, T. Jeltema, K. Kuehn, S. Kuhlmann, O. Lahav, M. Lima, M. A. G. Maia, M. March, J. L. Marshall, P. Martini, F. Menanteau, R. Miquel, R. C. Nichol, A. A. Plazas, A. K. Romer, E. S. Rykoff, E. Sanchez, V. Scarpine, R. Schindler, M. Schubnell, I. Sevilla-Noarbe, M. Smith, M. Soares-Santos, F. Sobreira, E. Suchyta, M. E. C. Swanson, G. Tarle, D. L. Tucker, V. Vikram, A. R. Walker, and J. Weller. Dark Energy Survey Year 1 Results: Multi-Probe Methodology and Simulated Likelihood Analyses. *arXiv e-prints*, page arXiv:1706.09359, Jun 2017.

[92] A. Kuntz. Cross-correlation of CFHTLenS galaxy catalogue and Planck CMB lensing using the halo model prescription. A&A, 584:A53, Dec 2015.

[93] S. D. Landy and A. S. Szalay. Bias and Variance of Angular Correlation Functions. ApJ, 412:64, Jul 1993.

[94] R. Laureijs, J. Amiaux, S. Arduini, J. L. Augueres, J. Brinchmann, R. Cole, M. Cropper, C. Dabin, L. Duvet, A. Ealet, B. Garilli, P. Gondoin, L. Guzzo, J. Hoar, H. Hoekstra, R. Holmes, T. Kitching, T. Maciaszek, Y. Mellier, F. Pasian, W. Percival, J. Rhodes, G. Saavedra Criado, M. Sauvage, R. Scaramella, L. Valenziano, S. Warren, R. Bender, F. Castander, A. Cimatti, O. Le Fèvre, H. Kurki-Suonio, M. Levi, P. Lilje, G. Meylan, R. Nichol, K. Pedersen, V. Popa, R. Rebolo Lopez, H. W. Rix, H. Rottgering,

W. Zeilinger, F. Grupp, P. Hudelot, R. Massey, M. Meneghetti, L. Miller, S. Paltani, S. Paulin-Henriksson, S. Pires, C. Saxton, T. Schrabback, G. Seidel, J. Walsh, N. Aghanim, L. Amendola, J. Bartlett, C. Baccigalupi, J. P. Beaulieu, K. Benabed, J. G. Cuby, D. Elbaz, P. Fosalba, G. Gavazzi, A. Helmi, I. Hook, M. Irwin, J. P. Kneib, M. Kunz, F. Mannucci, L. Moscardini, C. Tao, R. Teyssier, J. Weller, G. Zamorani, M. R. Zapatero Osorio, O. Boulade, J. J. Foumond, A. Di Giorgio, P. Guttridge, A. James, M. Kemp, J. Martignac, A. Spencer, D. Walton, T. Blümchen, C. Bonoli, F. Bortoletto, C. Cerna, L. Corcione, C. Fabron, K. Jahnke, S. Ligori, F. Madrid, L. Martin, G. Morgante, T. Pamplona, E. Prieto, M. Riva, R. Toledo, M. Trifoglio, F. Zerbi, F. Abdalla, M. Douspis, C. Grenet, S. Borgani, R. Bouwens, F. Courbin, J. M. Delouis, P. Dubath, A. Fontana, M. Frailis, A. Grazian, J. Koppenhöfer, O. Mansutti, M. Melchior, M. Mignoli, J. Mohr, C. Neissner, K. Noddle, M. Poncet, M. Scodeggio, S. Serrano, N. Shane, J. L. Starck, C. Surace, A. Taylor, G. Verdoes-Kleijn, C. Vuerli, O. R. Williams, A. Zacchei, B. Altieri, I. Escudero Sanz, R. Kohley, T. Oosterbroek, P. Astier, D. Bacon, S. Bardelli, C. Baugh, F. Bellagamba, C. Benoist, D. Bianchi, A. Biviano, E. Branchini, C. Carbone, V. Cardone, D. Clements, S. Colombi, C. Conselice, G. Cresci, N. Deacon, J. Dunlop, C. Fedeli, F. Fontanot, P. Franzetti, C. Giocoli, J. Garcia-Bellido, J. Gow, A. Heavens, P. Hewett, C. Heymans, A. Holland, Z. Huang, O. Ilbert, B. Joachimi, E. Jennins, E. Kerins, A. Kiessling, D. Kirk, R. Kotak, O. Krause, O. Lahav, F. van Leeuwen, J. Lesgourgues, M. Lombardi, M. Magliocchetti, K. Maguire, E. Majerotto, R. Maoli, F. Marulli, S. Maurogordato, H. McCracken, R. McLure, A. Melchiorri, A. Merson, M. Moresco, M. Nonino, P. Norberg, J. Peacock, R. Pello, M. Penny, V. Pettorino, C. Di Porto, L. Pozzetti, C. Quercellini, M. Radovich, A. Rassat, N. Roche, S. Ronayette, E. Rossetti, B. Sartoris, P. Schneider, E. Semboloni, S. Serjeant, F. Simpson, C. Skordis, G. Smadja, S. Smartt, P. Spano, S. Spiro, M. Sullivan, A. Tilquin, R. Trotta, L. Verde, Y. Wang, G. Williger, G. Zhao, J. Zoubian, and E. Zucca. Euclid Definition Study Report. *arXiv e-prints*, page arXiv:1110.3193, Oct 2011.

[95] M. Levi, C. Bebek, T. Beers, R. Blum, R. Cahn, D. Eisenstein, B. Flaugher, K. Honscheid, R. Kron, O. Lahav, P. McDonald, N. Roe, D. Schlegel, and representing the DESI collaboration. The DESI Experiment, a whitepaper for Snowmass 2013. *arXiv e-prints*, page arXiv:1308.0847, Aug 2013.

[96] A. Lewis, Anthony, and A. Lasenby. Efficient computation of cosmic microwave background anisotropies in closed friedmann-robertson-walker models. *The Astrophysical Journal*, 538(2):473, 2000.

[97] A. Lewis and A. Challinor. Weak gravitational lensing of the {CMB}. *Physics Reports*, 429(1):1 – 65, 2006.

[98] A. R. Liddle. An introduction to cosmological inflation. 1999.

[99] A. R. Liddle and D. H. Lyth. *Cosmological Inflation and Large-Scale Structure*. 2000.

[100] D. N. Limber. The Analysis of Counts of the Extragalactic Nebulae in Terms of a Fluctuating Density Field. ApJ, 117:134, Jan 1953.

[101] D. N. Limber. The Analysis of Counts of the Extragalactic Nebulae in Terms of a Fluctuating Density Field. II. *Astrophysical Journal*, 119:655, May 1954.

[102] E. V. Linder. Cosmic growth history and expansion history. Phys. Rev. D, 72(4):043529, Aug 2005.

[103] M. Loverde and N. Afshordi. Extended Limber approximation. *Physical Review D*, 78(12):123506, Dec 2008.

[104] LSST Science Collaboration, P. A. Abell, J. Allison, S. F. Anderson, J. R. Andrew, J. R. P. Angel, L. Armus, D. Arnett, S. J. Asztalos, T. S. Axelrod, S. Bailey, D. R. Ballantyne, J. R. Bankert, W. A. Barkhouse, J. D. Barr, L. F. Barrientos, A. J. Barth, J. G. Bartlett, A. C. Becker, J. Becla, T. C. Beers, J. P. Bernstein, R. Biswas, M. R. Blanton, J. S. Bloom, J. J. Bochanski, P. Boeshaar, K. D. Borne, M. Bradac, W. N. Brandt, C. R. Bridge, M. E. Brown, R. J. Brunner, J. S. Bullock, A. J. Burgasser, J. H. Burge, D. L. Burke, P. A. Cargile, S. Chand rasekharan, G. Chartas, S. R. Chesley, Y.-H. Chu, D. Cinabro, M. W. Claire, C. F. Claver, D. Clowe, A. J. Connolly, K. H. Cook, J. Cooke, A. Cooray, K. R. Covey, C. S. Culliton, R. de Jong, W. H. de Vries, V. P. Debattista, F. Delgado, I. P. Dell'Antonio, S. Dhital, R. Di Stefano, M. Dickinson, B. Dilday, S. G. Djorgovski, G. Dobler, C. Donalek, G. Dubois-Felsmann, J. Durech, A. Eliasdottir, M. Eracleous, L. Eyer, E. E. Falco, X. Fan, C. D. Fassnacht, H. C. Ferguson, Y. R. Fernandez, B. D. Fields, D. Finkbeiner, E. E. Figueroa, D. B. Fox, H. Francke, J. S. Frank, J. Frieman, S. Fromenteau, M. Furqan, G. Galaz, A. Gal-Yam, P. Garnavich, E. Gawiser, J. Geary, P. Gee, R. R. Gibson, K. Gilmore, E. A. Grace, R. F. Green, W. J. Gressler, C. J. Grillmair, S. Habib, J. S. Haggerty, M. Hamuy, A. W. Harris, S. L. Hawley, A. F. Heavens, L. Hebb, T. J. Henry, E. Hileman, E. J. Hilton, K. Hoadley, J. B. Holberg, M. J. Holman, S. B. Howell, L. Infante, Z. Ivezic, S. H. Jacoby, B. Jain, R, Jedicke, M. J. Jee, J. Garrett Jernigan, S. W. Jha, K. V. Johnston, R. L. Jones, M. Juric, M. Kaasalainen, Styliani, Kafka, S. M. Kahn, N. A. Kaib, J. Kalirai, J. Kantor, M. M. Kasliwal, C. R. Keeton, R. Kessler, Z. Knezevic, A. Kowalski, V. L. Krabbendam, K. S. Krughoff, S. Kulkarni, S. Kuhlman,

M. Lacy, S. Lepine, M. Liang, A. Lien, P. Lira, K. S. Long, S. Lorenz, J. M. Lotz, R. H. Lupton, J. Lutz, L. M. Macri, A. A. Mahabal, R. Mandelbaum, P. Marshall, M. May, P. M. McGehee, B. T. Meadows, A. Meert, A. Milani, C. J. Miller, M. Miller, D. Mills, D. Minniti, D. Monet, A. S. Mukadam, E. Nakar, D. R. Neill, J. A. Newman, S. Nikolaev, M. Nordby, P. O'Connor, M. Oguri, J. Oliver, S. S. Olivier, J. K. Olsen, K. Olsen, E. W. Olszewski, H. Oluseyi, N. D. Padilla, A. Parker, J. Pepper, J. R. Peterson, C. Petry, P. A. Pinto, J. L. Pizagno, B. Popescu, A. Prsa, V. Radcka, M. J. Raddick, A. Rasmussen, A. Rau, J. Rho, J. E. Rhoads, G. T. Richards, S. T. Ridgway, B. E. Robertson, R. Roskar, A. Saha, A. Sarajedini, E. Scannapieco, T. Schalk, R. Schindler, S. Schmidt, S. Schmidt, D. P. Schneider, G. Schumacher, R. Scranton, J. Sebag, L. G. Seppala, O. Shemmer, J. D. Simon, M. Sivertz, H. A. Smith, J. Allyn Smith, N. Smith, A. H. Spitz, A. Stanford, K. G. Stassun, J. Strader, M. A. Strauss, C. W. Stubbs, D. W. Sweeney, A. Szalay, P. Szkody, M. Takada, P. Thorman, D. E. Trilling, V. Trimble, A. Tyson, R. Van Berg, D. Vand en Berk, J. VanderPlas, L. Verde, B. Vrsnak, L. M. Walkowicz, B. D. Wand elt, S. Wang, Y. Wang, M. Warner, R. H. Wechsler, A. A. West, O. Wiecha, B. F. Williams, B. Willman, D. Wittman, S. C. Wolff, W. M. Wood-Vasey, P. Wozniak, P. Young, A. Zentner, and H. Zhan. LSST Science Book, Version 2.0. *arXiv e-prints*, page arXiv:0912.0201, Dec 2009.

[105] A. Lue, R. Scoccimarro, and G. Starkman. Differentiating between modified gravity and dark energy. Phys. Rev. D, 69(4):044005, Feb 2004.

[106] S. J. Maddox, W. J. Sutherland, G. Efstathiou, and J. Loveday. The APM galaxy survey - I. APM measurements and star-galaxy separation. MNRAS, 243:692–712, Apr 1990.

[107] M. S. Madhavacheril and J. C. Hill. Mitigating Foreground Biases in CMB Lensing Reconstruction Using Cleaned Gradients. *arXiv e-prints*, page arXiv:1802.08230, Feb 2018.

[108] J. C. Mather, E. S. Cheng, D. A. Cottingham, J. Eplee, R. E., D. J. Fixsen, T. Hewagama, R. B. Isaacman, K. A. Jensen, S. S. Meyer, P. D. Noerdlinger, S. M. Read, L. P. Rosen, R. A. Shafer, E. L. Wright, C. L. Bennett, N. W. Boggess, M. G. Hauser, T. Kelsall, J. Moseley, S. H., R. F. Silverberg, G. F. Smoot, R. Weiss, and D. T. Wilkinson. Measurement of the Cosmic Microwave Background Spectrum by the COBE FIRAS Instrument. ApJ, 420:439, Jan 1994.

[109] J. C. Mather, D. J. Fixsen, R. A. Shafer, C. Mosier, and D. T. Wilkinson. Calibrator Design for the COBE Far-Infrared Absolute Spectrophotometer (FIRAS). ApJ, 512(2):511–520, Feb 1999.

[110] P. McDonald and U. Seljak. How to evade the sample variance limit on measurements of redshift-space distortions. J. Cosmology Astropart. Phys., 2009(10):007, Oct 2009.

[111] J. Miralda-Escude. The Correlation Function of Galaxy Ellipticities Produced by Gravitational Lensing. ApJ, 380:1, Oct 1991.

[112] E. Morganson, R. A. Gruendl, F. Menanteau, M. Carrasco Kind, Y.-C. Chen, G. Daues, A. Drlica-Wagner, D. N. Friedel, M. Gower, M. W. G. Johnson, M. D. Johnson, R. Kessler, F. Paz-Chinchón, D. Petravick, C. Pond, B. Yanny, S. Allam, R. Armstrong, W. Barkhouse, K. Bechtol, A. Benoit-Lévy, G. M. Bernstein, E. Bertin, E. Buckley-Geer, R. Covarrubias, S. Desai, H. T. Diehl, D. A. Goldstein, D. Gruen, T. S. Li, H. Lin, J. Marriner, J. J. Mohr, E. Neilsen, C.-C. Ngeow, K. Paech, E. S. Rykoff, M. Sako, I. Sevilla-Noarbe, E. Sheldon, F. Sobreira, D. L. Tucker, W. Wester, and DES Collaboration. The Dark Energy Survey Image Processing Pipeline. PASP, 130(7):074501, July 2018.

[113] B. O. Mummery, I. G. McCarthy, S. Bird, and J. Schaye. The separate and combined effects of baryon physics and neutrino free streaming on large-scale structure. MNRAS, 471(1):227–242, Oct 2017.

[114] D. Munshi, P. Valageas, L. van Waerbeke, and A. Heavens. Cosmology with weak lensing surveys. *Physics Reports*, 462(3):67–121, Jun 2008.

[115] R. Narayan and M. Bartelmann. Lectures on Gravitational Lensing. *arXiv e-prints*, pages astro–ph/9606001, Jun 1996.

[116] P. Norberg, C. M. Baugh, E. Gaztañaga, and D. J. Croton. Statistical analysis of galaxy surveys - I. Robust error estimation for two-point clustering statistics. MNRAS, 396(1):19–38, Jun 2009.

[117] T. Okamoto and W. Hu. Cosmic microwave background lensing reconstruction on the full sky. Phys. Rev. D, 67(8):083002, Apr 2003.

[118] Y. Omori, E. Baxter, C. Chang, D. Kirk, A. Alarcon, G. M. Bernstein, L. E. Bleem, R. Cawthon, A. Choi, R. Chown, T. M. Crawford, C. Davis, J. De Vicente, J. DeRose, S. Dodelson, T. F. Eifler, P. Fosalba, O. Friedrich, M. Gatti, E. Gaztanaga, T. Giannantonio, D. Gruen, W. G. Hartley, G. P. Holder, B. Hoyle, D. Huterer, B. Jain, M. Jarvis, E. Krause, N. MacCrann, R. Miquel, J. Prat, M. M. Rau, C. L. Reichardt, E. Rozo, S. Samuroff, C. Sánchez, L. F. Secco, E. Sheldon, G. Simard, M. A. Troxel, P. Vielzeuf, R. H. Wechsler, J. Zuntz, T. M. C. Abbott, F. B. Abdalla, S. Allam, J. Annis, S. Avila, K. Aylor, B. A. Benson, E. Bertin, S. L. Bridle, D. Brooks, D. L. Burke, J. E. Carlstrom, A. Carnero Rosell,

M. Carrasco Kind, J. Carretero, F. J. Castander, C. L. Chang, H.-M. Cho, A. T. Crites, M. Crocce, C. E. Cunha, L. N. da Costa, T. de Haan, S. Desai, H. T. Diehl, J. P. Dietrich, M. A. Dobbs, W. B. Everett, E. Fernand ez, B. Flaugher, J. Frieman, J. García-Bellido, E. M. George, R. A. Gruendl, G. Gutierrez, N. W. Halverson, N. L. Harrington, D. L. Hollowood, K. Honscheid, W. L. Holzapfel, Z. Hou, J. D. Hrubes, D. J. James, T. Jeltema, K. Kuehn, N. Kuropatkin, M. Lima, H. Lin, A. T. Lee, E. M. Leitch, D. Luong-Van, M. A. G. Maia, A. Manzotti, D. P. Marrone, J. L. Marshall, P. Martini, J. J. McMahon, P. Melchior, F. Menanteau, S. S. Meyer, L. M. Mocanu, J. J. Mohr, T. Natoli, R. L. C. Ogand o, S. Padin, A. A. Plazas, C. Pryke, A. K. Romer, A. Roodman, J. E. Ruhl, E. S. Rykoff, E. Sanchez, V. Scarpine, K. K. Schaffer, R. Schindler, I. Sevilla-Noarbe, E. Shirokoff, M. Smith, R. C. Smith, M. Soares-Santos, F. Sobreira, Z. Staniszewski, A. A. Stark, K. T. Story, E. Suchyta, M. E. C. Swanson, G. Tarle, D. Thomas, K. Vanderlinde, J. D. Vieira, V. Vikram, A. R. Walker, J. Weller, R. Williamson, W. L. K. Wu, and O. Zahn. Dark Energy Survey Year 1 Results: Cross-correlation between DES Y1 galaxy weak lensing and SPT+Planck CMB weak lensing. *arXiv e-prints*, page arXiv:1810.02441, Oct 2018.

[119] Y. Omori, R. Chown, G. Simard, K. T. Story, K. Aylor, E. J. Baxter, B. A. Benson, L. E. Bleem, J. E. Carlstrom, C. L. Chang, H. M. Cho, T. M. Crawford, A. T. Crites, T. de Haan, M. A. Dobbs, W. B. Everett, E. M. George, N. W. Halverson, N. L. Harrington, G. P. Holder, Z. Hou, W. L. Holzapfel, J. D. Hrubes, L. Knox, A. T. Lee, E. M. Leitch, D. Luong-Van, A. Manzotti, D. P. Marrone, J. J. McMahon, S. S. Meyer, L. M. Mocanu, J. J. Mohr, T. Natoli, S. Padin, C. Pryke, C. L. Reichardt, J. E. Ruhl, J. T. Sayre, K. K. Schaffer, E. Shirokoff, Z. Staniszewski, A. A. Stark, K. Vanderlinde, J. D. Vieira, R. Williamson, and O. Zahn. A 2500 deg^2 CMB Lensing Map from Combined South Pole Telescope and Planck Data. ApJ, 849(2):124, Nov 2017.

[120] Y. Omori and G. Holder. Cross-Correlation of CFHTLenS Galaxy Number Density and Planck CMB Lensing. *arXiv e-prints*, page arXiv:1502.03405, Feb 2015.

[121] T. Padmanabhan. Cosmological constant-the weight of the vacuum. Phys. Rep., 380(5-6):235–320, Jul 2003.

[122] C. Patrignani, Particle Data Group, K. Agashe, G. Aielli, C. Amsler, M. Antonelli, D. M. Asner, H. Baer, S. Banerjee, R. M. Barnett, T. Basaglia, C. W. Bauer, J. J. Beatty, V. I. Belousov, J. Beringer, S. Bethke, H. Bichsel, O. Biebel, E. Blucher, G. Brooijmans, O. Buchmueller, V. Burkert, M. A. Bychkov, R. N. Cahn, M. Carena, A. Ceccucci, A. Cerri, D. Chakraborty, M. C. Chen, R. S. Chivukula, K. Copic, G. Cowan, O. Dahl, G. D'Ambrosio, T. Damour, D. de Florian, A. de Gouvea, T. DeGrand, P. de Jong,

G. Dissertori, B. A. Dobrescu, M. D'Onofrio, M. Doser, M. Drees, H. K. Dreiner, D. A. Dwyer, P. Eerola, S. Eidelman, J. Ellis, J. Erler, V. V. Ezhela, W. Fetscher, B. D. Fields, B. Foster, A. Freitas, H. Gallagher, L. Garren, H. J. Gerber, G. Gerbier, T. Gershon, T. Gherghetta, A. A. Godizov, M. Goodman, C. Grab, A. V. Gritsan, C. Grojean, D. E. Groom, M. Grünewald, A. Gurtu, T. Gutsche, H. E. Haber, K. Hagiwara, C. Hanhart, S. Hashimoto, Y. Hayato, K. G. Hayes, A. Hebecker, B. Heltsley, J. J. Hernández-Rey, K. Hikasa, J. Hisano, A. Höcker, J. Holder, A. Holtkamp, J. Huston, T. Hyodo, K. Irwin, J. D. Jackson, K. F. Johnson, M. Kado, M. Karliner, U. F. Katz, S. R. Klein, E. Klempt, R. V. Kowalewski, F. Krauss, M. Kreps, B. Krusche, Y. V. Kuyanov, Y. Kwon, O. Lahav, J. Laiho, P. Langacker, A. Liddle, Z. Ligeti, C. J. Lin, C. Lippmann, T. M. Liss, L. Littenberg, K. S. Lugovsky, S. B. Lugovsky, A. Lusiani, Y. Makida, F. Maltoni, T. Mannel, A. V. Manohar, W. J. Marciano, A. D. Martin, A. Masoni, J. Matthews, U. G. Meißner, D. Milstead, R. E. Mitchell, P. Molaro, K. Mönig, F. Moortgat, M. J. Mortonson, H. Murayama, K. Nakamura, M. Narain, P. Nason, S. Navas, M. Neubert, P. Nevski, Y. Nir, K. A. Olive, S. Pagan Griso, J. Parsons, J. A. Peacock, M. Pennington, S. T. Petcov, V. A. Petrov, A. Piepke, A. Pomarol, A. Quadt, S. Raby, J. Rademacker, G. Raffelt, B. N. Ratcliff, P. Richardson, A. Ringwald, S. Roesler, S. Rolli, A. Romaniouk, L. J. Rosenberg, J. L. Rosner, G. Rybka, R. A. Ryutin, C. T. Sachrajda, Y. Sakai, G. P. Salam, S. Sarkar, F. Sauli, O. Schneider, K. Scholberg, A. J. Schwartz, D. Scott, V. Sharma, S. R. Sharpe, T. Shutt, M. Silari, T. Sjöstrand , P. Skands, T. Skwarnicki, J. G. Smith, G. F. Smoot, S. Spanier, H. Spieler, C. Spiering, A. Stahl, S. L. Stone, Y. Sumino, T. Sumiyoshi, M. J. Syphers, F. Takahashi, M. Tanabashi, K. Terashi, J. Terning, R. S. Thorne, L. Tiator, M. Titov, N. P. Tkachenko, N. A. Törnqvist, D. Tovey, G. Valencia, R. van de Water, N. Varelas, G. Venanzoni, M. G. Vincter, P. Vogel, A. Vogt, S. P. Wakely, W. Walkowiak, C. W. Walter, D. Wands, D. R. Ward, M. O. Wascko, G. Weiglein, D. H. Weinberg, E. J. Weinberg, M. White, L. R. Wiencke, S. Willocq, C. G. Wohl, L. Wolfenstein, J. Womersley, C. L. Woody, R. L. Workman, W. M. Yao, G. P. Zeller, O. V. Zenin, R. Y. Zhu, F. Zimmermann, and P. A. Zyla. Review of Particle Physics. *Chinese Physics C*, 40(10):100001, Oct 2016.

[123] P. J. E. Peebles. *The Large-scale Structure of the Universe*. 1980.

[124] U.-L. Pen. Beating lensing cosmic variance with galaxy tomography. MNRAS, 350(4):1445–1448, Jun 2004.

[125] A. A. Penzias and R. W. Wilson. A Measurement of Excess Antenna Temperature at 4080 Mc/s. ApJ, 142:419–421, Jul 1965.

[126] A. Pezzotta, S. de la Torre, J. Bel, B. R. Granett, L. Guzzo, J. A. Peacock, B. Garilli,

M. Scodeggio, M. Bolzonella, U. Abbas, C. Adami, D. Bottini, A. Cappi, O. Cucciati, I. Davidzon, P. Franzetti, A. Fritz, A. Iovino, J. Krywult, V. Le Brun, O. Le Fèvre, D. Maccagni, K. Małek, F. Marulli, M. Polletta, A. Pollo, L. A. M. Tasca, R. Tojeiro, D. Vergani, A. Zanichelli, S. Arnouts, E. Branchini, J. Coupon, G. De Lucia, J. Koda, O. Ilbert, F. Mohammad, T. Moutard, and L. Moscardini. The VIMOS Public Extragalactic Redshift Survey (VIPERS). The growth of structure at 0.5 < z < 1.2 from redshift-space distortions in the clustering of the PDR-2 final sample. A&A, 604:A33, Jul 2017.

[127] R. Piessens, E. de Doncker-Kapenga, C. W. Überhuber, and D. K. Kahaner. *Quadpack*, volume 1 of *Springer Series in Computational Mathematics*. Springer, Jan. 1983.

[128] Planck Collaboration. Planck 2015 results. XIII. Cosmological parameters. Feb. 2015.

[129] Planck Collaboration, R. Adam, P. A. R. Ade, N. Aghanim, Y. Akrami, M. I. R. Alves, F. Argüeso, M. Arnaud, F. Arroja, M. Ashdown, and et al. Planck 2015 results. I. Overview of products and scientific results. A&A, 594:A1, Sep 2016.

[130] Planck Collaboration, R. Adam, P. A. R. Ade, N. Aghanim, M. Arnaud, M. Ashdown, J. Aumont, C. Baccigalupi, A. J. Banday, R. B. Barreiro, and et al. Planck 2015 results. VIII. High Frequency Instrument data processing: Calibration and maps. A&A, 594:A8, Sep 2016.

[131] Planck Collaboration, P. A. R. Ade, N. Aghanim, C. Armitage-Caplan, M. Arnaud, M. Ashdown, F. Atrio-Barand ela, J. Aumont, C. Baccigalupi, A. J. Banday, and et al. Planck 2013 results. XVII. Gravitational lensing by large-scale structure. A&A, 571:A17, Nov 2014.

[132] Planck Collaboration, P. A. R. Ade, N. Aghanim, M. Arnaud, M. Ashdown, J. Aumont, C. Baccigalupi, A. J. Banday, R. B. Barreiro, J. G. Bartlett, and et al. Planck 2015 results. XV. Gravitational lensing. A&A, 594:A15, Sep 2016.

[133] Planck Collaboration, N. Aghanim, Y. Akrami, M. Ashdown, J. Aumont, C. Baccigalupi, M. Ballardini, A. J. Banday, R. B. Barreiro, N. Bartolo, S. Basak, R. Battye, K. Benabed, J. P. Bernard, M. Bersanelli, P. Bielewicz, J. J. Bock, J. R. Bond, J. Borrill, F. R. Bouchet, F. Boulanger, M. Bucher, C. Burigana, R. C. Butler, E. Calabrese, J. F. Cardoso, J. Carron, A. Challinor, H. C. Chiang, J. Chluba, L. P. L. Colombo, C. Combet, D. Contreras, B. P. Crill, F. Cuttaia, P. de Bernardis, G. de Zotti, J. Delabrouille, J. M. Delouis, E. Di Valentino, J. M. Diego, O. Doré, M. Douspis, A. Ducout, X. Dupac, S. Dusini, G. Efstathiou, F. Elsner, T. A. Enßlin, H. K. Eriksen, Y. Fantaye, M. Farhang, J. Fergusson, R. Fernandez-Cobos, F. Finelli, F. Forastieri, M. Frailis, E. Franceschi, A. Frolov, S. Galeotta, S. Galli,

K. Ganga, R. T. Génova-Santos, M. Gerbino, T. Ghosh, J. González-Nuevo, K. M. Górski, S. Gratton, A. Gruppuso, J. E. Gudmundsson, J. Hamann, W. Hand ley, D. Herranz, E. Hivon, Z. Huang, A. H. Jaffe, W. C. Jones, A. Karakci, E. Keihänen, R. Keskitalo, K. Kiiveri, J. Kim, T. S. Kisner, L. Knox, N. Krachmalnicoff, M. Kunz, H. Kurki-Suonio, G. Lagache, J. M. Lamarre, A. Lasenby, M. Lattanzi, C. R. Lawrence, M. Le Jeune, P. Lemos, J. Lesgourgues, F. Levrier, A. Lewis, M. Liguori, P. B. Lilje, M. Lilley, V. Lindholm, M. López-Caniego, P. M. Lubin, Y. Z. Ma, J. F. Macías-Pérez, G. Maggio, D. Maino, N. Mandolesi, A. Mangilli, A. Marcos-Caballero, M. Maris, P. G. Martin, M. Martinelli, E. Martínez-González, S. Matarrese, N. Mauri, J. D. McEwen, P. R. Meinhold, A. Melchiorri, A. Mennella, M. Migliaccio, M. Millea, S. Mitra, M. A. Miville-Deschênes, D. Molinari, L. Montier, G. Morgante, A. Moss, P. Natoli, H. U. Nørgaard-Nielsen, L. Pagano, D. Paoletti, B. Partridge, G. Patanchon, H. V. Peiris, F. Perrotta, V. Pettorino, F. Piacentini, L. Polastri, G. Polenta, J. L. Puget, J. P. Rachen, M. Reinecke, M. Remazeilles, A. Renzi, G. Rocha, C. Rosset, G. Roudier, J. A. Rubiño-Martín, B. Ruiz-Granados, L. Salvati, M. Sandri, M. Savelainen, D. Scott, E. P. S. Shellard, C. Sirignano, G. Sirri, L. D. Spencer, R. Sunyaev, A. S. Suur-Uski, J. A. Tauber, D. Tavagnacco, M. Tenti, L. Toffolatti, M. Tomasi, T. Trombetti, L. Valenziano, J. Valiviita, B. Van Tent, L. Vibert, P. Vielva, F. Villa, N. Vittorio, B. D. Wand elt, I. K. Wehus, M. White, S. D. M. White, A. Zacchei, and A. Zonca. Planck 2018 results. VI. Cosmological parameters. *arXiv e-prints*, page arXiv:1807.06209, Jul 2018.

[134] Planck Collaboration, N. Aghanim, Y. Akrami, M. Ashdown, J. Aumont, C. Baccigalupi, M. Ballardini, A. J. Banday, R. B. Barreiro, N. Bartolo, S. Basak, K. Benabed, J. P. Bernard, M. Bersanelli, P. Bielewicz, J. J. Bock, J. R. Bond, J. Borrill, F. R. Bouchet, F. Boulanger, M. Bucher, C. Burigana, E. Calabrese, J. F. Cardoso, J. Carron, A. Challinor, H. C. Chiang, L. P. L. Colombo, C. Combet, B. P. Crill, F. Cuttaia, P. de Bernardis, G. de Zotti, J. Delabrouille, E. Di Valentino, J. M. Diego, O. Doré, M. Douspis, A. Ducout, X. Dupac, G. Efstathiou, F. Elsner, T. A. Enßlin, H. K. Eriksen, Y. Fantaye, R. Fernandez-Cobos, F. Forastieri, M. Frailis, A. A. Fraisse, E. Franceschi, A. Frolov, S. Galeotta, S. Galli, K. Ganga, R. T. Génova-Santos, M. Gerbino, T. Ghosh, J. González-Nuevo, K. M. Górski, S. Gratton, A. Gruppuso, J. E. Gudmundsson, J. Hamann, W. Hand ley, F. K. Hansen, D. Herranz, E. Hivon, Z. Huang, A. H. Jaffe, W. C. Jones, A. Karakci, E. Keihänen, R. Keskitalo, K. Kiiveri, J. Kim, L. Knox, N. Krachmalnicoff, M. Kunz, H. Kurki-Suonio, G. Lagache, J. M. Lamarre, A. Lasenby, M. Lattanzi, C. R. Lawrence, M. Le Jeune, F. Levrier, A. Lewis, M. Liguori, P. B. Lilje, V. Lindholm, M. López-Caniego, P. M. Lubin, Y. Z. Ma, J. F. Macías-Pérez, G. Maggio, D. Maino, N. Mandolesi, A. Mangilli, A. Marcos-Caballero, M. Maris, P. G. Martin, E. Martínez-González, S. Matarrese, N. Mauri, J. D.

McEwen, A. Melchiorri, A. Mennella, M. Migliaccio, M. A. Miville-Deschênes, D. Molinari, A. Moneti, L. Montier, G. Morgante, A. Moss, P. Natoli, L. Pagano, D. Paoletti, B. Partridge, G. Patanchon, F. Perrotta, V. Pettorino, F. Piacentini, L. Polastri, G. Polenta, J. L. Puget, J. P. Rachen, M. Reinecke, M. Remazeilles, A. Renzi, G. Rocha, C. Rosset, G. Roudier, J. A. Rubiño-Martín, B. Ruiz-Granados, L. Salvati, M. Sandri, M. Savelainen, D. Scott, C. Sirignano, R. Sunyaev, A. S. Suur-Uski, J. A. Tauber, D. Tavagnacco, M. Tenti, L. Toffolatti, M. Tomasi, T. Trombetti, J. Valiviita, B. Van Tent, P. Vielva, F. Villa, N. Vittorio, B. D. Wandelt, I. K. Wehus, M. White, S. D. M. White, A. Zacchei, and A. Zonca. Planck 2018 results. VIII. Gravitational lensing. *arXiv e-prints*, page arXiv:1807.06210, Jul 2018.

[135] Planck Collaboration, N. Aghanim, Y. Akrami, M. Ashdown, J. Aumont, C. Baccigalupi, M. Ballardini, A. J. Banday, R. B. Barreiro, N. Bartolo, S. Basak, K. Benabed, J. P. Bernard, M. Bersanelli, P. Bielewicz, J. J. Bock, J. R. Bond, J. Borrill, F. R. Bouchet, F. Boulanger, M. Bucher, C. Burigana, E. Calabrese, J. F. Cardoso, J. Carron, A. Challinor, H. C. Chiang, L. P. L. Colombo, C. Combet, B. P. Crill, F. Cuttaia, P. de Bernardis, G. de Zotti, J. Delabrouille, E. Di Valentino, J. M. Diego, O. Doré, M. Douspis, A. Ducout, X. Dupac, G. Efstathiou, F. Elsner, T. A. Enßlin, H. K. Eriksen, Y. Fantaye, R. Fernandez-Cobos, F. Forastieri, M. Frailis, A. A. Fraisse, E. Franceschi, A. Frolov, S. Galeotta, S. Galli, K. Ganga, R. T. Génova-Santos, M. Gerbino, T. Ghosh, J. González-Nuevo, K. M. Górski, S. Gratton, A. Gruppuso, J. E. Gudmundsson, J. Hamann, W. Hand ley, F. K. Hansen, D. Herranz, E. Hivon, Z. Huang, A. H. Jaffe, W. C. Jones, A. Karakci, E. Keihänen, R. Keskitalo, K. Kiiveri, J. Kim, L. Knox, N. Krachmalnicoff, M. Kunz, H. Kurki-Suonio, G. Lagache, J. M. Lamarre, A. Lasenby, M. Lattanzi, C. R. Lawrence, M. Le Jeune, F. Levrier, A. Lewis, M. Liguori, P. B. Lilje, V. Lindholm, M. López-Caniego, P. M. Lubin, Y. Z. Ma, J. F. Macías-Pérez, G. Maggio, D. Maino, N. Mandolesi, A. Mangilli, A. Marcos-Caballero, M. Maris, P. G. Martin, E. Martínez-González, S. Matarrese, N. Mauri, J. D. McEwen, A. Melchiorri, A. Mennella, M. Migliaccio, M. A. Miville-Deschênes, D. Molinari, A. Moneti, L. Montier, G. Morgante, A. Moss, P. Natoli, L. Pagano, D. Paoletti, B. Partridge, G. Patanchon, F. Perrotta, V. Pettorino, F. Piacentini, L. Polastri, G. Polenta, J. L. Puget, J. P. Rachen, M. Reinecke, M. Remazeilles, A. Renzi, G. Rocha, C. Rosset, G. Roudier, J. A. Rubiño-Martín, B. Ruiz-Granados, L. Salvati, M. Sandri, M. Savelainen, D. Scott, C. Sirignano, R. Sunyaev, A. S. Suur-Uski, J. A. Tauber, D. Tavagnacco, M. Tenti, L. Toffolatti, M. Tomasi, T. Trombetti, J. Valiviita, B. Van Tent, P. Vielva, F. Villa, N. Vittorio, B. D. Wandelt, I. K. Wehus, M. White, S. D. M. White, A. Zacchei, and A. Zonca. Planck 2018 results. VIII. Gravitational lensing. *arXiv e-prints*, page arXiv:1807.06210, Jul 2018.

[136] Planck Collaboration, N. Aghanim, M. Ashdown, J. Aumont, C. Baccigalupi, M. Ballardini, A. J. Band ay, R. B. Barreiro, N. Bartolo, S. Basak, K. Benabed, J. P. Bernard, M. Bersanelli, P. Bielewicz, L. Bonavera, J. R. Bond, J. Borrill, F. R. Bouchet, F. Boulanger, C. Burigana, E. Calabrese, J. F. Cardoso, J. Carron, H. C. Chiang, L. P. L. Colombo, B. Comis, F. Couchot, A. Coulais, B. P. Crill, A. Curto, F. Cuttaia, P. de Bernardis, G. de Zotti, J. Delabrouille, E. Di Valentino, C. Dickinson, J. M. Diego, O. Doré, M. Douspis, A. Ducout, X. Dupac, S. Dusini, F. Elsner, T. A. Enßlin, H. K. Eriksen, E. Falgarone, Y. Fantaye, F. Finelli, F. Forastieri, M. Frailis, A. A. Fraisse, E. Franceschi, A. Frolov, S. Galeotta, S. Galli, K. Ganga, R. T. Génova-Santos, M. Gerbino, T. Ghosh, Y. Giraud-Héraud, J. González-Nuevo, K. M. Górski, A. Gruppuso, J. E. Gudmundsson, F. K. Hansen, G. Helou, S. Henrot-Versillé, D. Herranz, E. Hivon, Z. Huang, A. H. Jaffe, W. C. Jones, E. Keihänen, R. Keskitalo, K. Kiiveri, T. S. Kisner, N. Krachmalnicoff, M. Kunz, H. Kurki-Suonio, J. M. Lamarre, M. Langer, A. Lasenby, M. Lattanzi, C. R. Lawrence, M. Le Jeune, F. Levrier, P. B. Lilje, M. Lilley, V. Lindholm, M. López-Caniego, Y. Z. Ma, J. F. Macías-Pérez, G. Maggio, D. Maino, N. Mand olesi, A. Mangilli, M. Maris, P. G. Martin, E. Martínez-González, S. Matarrese, N. Mauri, J. D. McEwen, A. Melchiorri, A. Mennella, M. Migliaccio, M. A. Miville-Deschênes, D. Molinari, A. Moneti, L. Montier, G. Morgante, A. Moss, P. Natoli, C. A. Oxborrow, L. Pagano, D. Paoletti, G. Patanchon, O. Perdereau, L. Perotto, V. Pettorino, F. Piacentini, S. Plaszczynski, L. Polastri, G. Polenta, J. L. Puget, J. P. Rachen, B. Racine, M. Reinecke, M. Remazeilles, A. Renzi, G. Rocha, C. Rosset, M. Rossetti, G. Roudier, J. A. Rubiño-Martín, B. Ruiz-Granados, L. Salvati, M. Sandri, M. Savelainen, D. Scott, C. Sirignano, G. Sirri, J. D. Soler, L. D. Spencer, A. S. Suur-Uski, J. A. Tauber, D. Tavagnacco, M. Tenti, L. Toffolatti, M. Tomasi, M. Tristram, T. Trombetti, J. Valiviita, F. Van Tent, P. Vielva, F. Villa, N. Vittorio, B. D. Wandelt, I. K. Wehus, A. Zacchei, and A. Zonca. Planck intermediate results. XLVIII. Disentangling Galactic dust emission and cosmic infrared background anisotropies. A&A, 596:A109, Dec 2016.

[137] Planck Collaboration, Y. Akrami, F. Arroja, M. Ashdown, J. Aumont, C. Baccigalupi, M. Ballardini, A. J. Banday, R. B. Barreiro, N. Bartolo, S. Basak, K. Benabed, J. P. Bernard, M. Bersanelli, P. Bielewicz, J. R. Bond, J. Borrill, F. R. Bouchet, M. Bucher, C. Burigana, R. C. Butler, E. Calabrese, J. F. Cardoso, B. Casaponsa, A. Challinor, H. C. Chiang, L. P. L. Colombo, C. Combet, B. P. Crill, F. Cuttaia, P. de Bernardis, A. de Rosa, G. de Zotti, J. Delabrouille, J. M. Delouis, E. Di Valentino, J. M. Diego, O. Doré, M. Douspis, A. Ducout, X. Dupac, S. Dusini, G. Efstathiou, F. Elsner, T. A. Enßlin, H. K. Eriksen, Y. Fantaye, J. Fergusson, R. Fernand ez-Cobos, F. Finelli, M. Frailis, A. A. Fraisse, E. Franceschi, A. Frolov, S. Galeotta, K. Ganga, R. T. Génova-Santos,

M. Gerbino, J. González-Nuevo, K. M. Górski, S. Gratton, A. Gruppuso, J. E. Gudmundsson, J. Hamann, W. Hand ley, F. K. Hansen, D. Herranz, E. Hivon, Z. Huang, A. H. Jaffe, W. C. Jones, G. Jung, E. Keihänen, R. Keskitalo, K. Kiiveri, J. Kim, N. Krachmalnicoff, M. Kunz, H. Kurki-Suonio, J. M. Lamarre, A. Lasenby, M. Lattanzi, C. R. Lawrence, M. Le Jeune, F. Levrier, A. Lewis, M. Liguori, P. B. Lilje, V. Lindholm, M. López-Caniego, Y. Z. Ma, J. F. Macías-Pérez, G. Maggio, D. Maino, N. Mand olesi, A. Marcos-Caballero, M. Maris, P. G. Martin, E. Martínez-González, S. Matarrese, N. Mauri, J. D. McEwen, P. D. Meerburg, P. R. Meinhold, A. Melchiorri, A. Mennella, M. Migliaccio, M. A. Miville-Deschênes, D. Molinari, A. Moneti, L. Montier, G. Morgante, A. Moss, M. Münchmeyer, P. Natoli, F. Oppizzi, L. Pagano, D. Paoletti, B. Partridge, G. Patanchon, F. Perrotta, V. Pettorino, F. Piacentini, G. Polenta, J. L. Puget, J. P. Rachen, B. Racine, M. Reinecke, M. Remazeilles, A. Renzi, G. Rocha, J. A. Rubiño-Martín, B. Ruiz-Granados, L. Salvati, M. Savelainen, D. Scott, E. P. S. Shellard, M. Shiraishi, C. Sirignano, G. Sirri, K. Smith, L. D. Spencer, L. Stanco, R. Sunyaev, A. S. Suur-Uski, J. A. Tauber, D. Tavagnacco, M. Tenti, L. Toffolatti, M. Tomasi, T. Trombetti, J. Valiviita, B. Van Tent, P. Vielva, F. Villa, N. Vittorio, B. D. Wandelt, I. K. Wehus, A. Zacchei, and A. Zonca. Planck 2018 results. IX. Constraints on primordial non-Gaussianity. *arXiv e-prints*, page arXiv:1905.05697, May 2019.

[138] J. Prat, C. Sánchez, Y. Fang, D. Gruen, J. Elvin-Poole, N. Kokron, L. F. Secco, B. Jain, R. Miquel, N. MacCrann, M. A. Troxel, A. Alarcon, D. Bacon, G. M. Bernstein, J. Blazek, R. Cawthon, C. Chang, M. Crocce, C. Davis, J. De Vicente, J. P. Dietrich, A. Drlica-Wagner, O. Friedrich, M. Gatti, W. G. Hartley, B. Hoyle, E. M. Huff, M. Jarvis, M. M. Rau, R. P. Rollins, A. J. Ross, E. Rozo, E. S. Rykoff, S. Samuroff, E. Sheldon, T. N. Varga, P. Vielzeuf, J. Zuntz, T. M. C. Abbott, F. B. Abdalla, S. Allam, J. Annis, K. Bechtol, A. Benoit-Lévy, E. Bertin, D. Brooks, E. Buckley-Geer, D. L. Burke, A. Carnero Rosell, M. Carrasco Kind, J. Carretero, F. J. Castander, C. E. Cunha, C. B. D'Andrea, L. N. da Costa, S. Desai, H. T. Diehl, S. Dodelson, T. F. Eifler, E. Fernand ez, B. Flaugher, P. Fosalba, J. Frieman, J. García-Bellido, E. Gaztanaga, D. W. Gerdes, T. Giannantonio, D. A. Goldstein, R. A. Gruendl, J. Gschwend, G. Gutierrez, K. Honscheid, D. J. James, T. Jeltema, M. W. G. Johnson, M. D. Johnson, D. Kirk, E. Krause, K. Kuehn, S. Kuhlmann, O. Lahav, T. S. Li, M. Lima, M. A. G. Maia, M. March, J. L. Marshall, P. Martini, P. Melchior, F. Menanteau, J. J. Mohr, R. C. Nichol, B. Nord, A. A. Plazas, A. K. Romer, A. Roodman, M. Sako, E. Sanchez, V. Scarpine, R. Schindler, M. Schubnell, I. Sevilla-Noarbe, M. Smith, R. C. Smith, M. Soares-Santos, F. Sobreira, E. Suchyta, M. E. C. Swanson, G. Tarle, D. Thomas, D. L. Tucker, V. Vikram, A. R. Walker, R. H. Wechsler, B. Yanny, Y. Zhang, and DES Collaboration. Dark Energy Survey year 1 results:

Galaxy-galaxy lensing. Phys. Rev. D, 98(4):042005, Aug 2018.

[139] W. H. Press. *Numerical Recipes in Fortran 90: The Art of Parallel Scientific Computing, Volume 2*. 1996.

[140] A. Refregier. Weak Gravitational Lensing by Large-Scale Structure. *Annual Review of Astron and Astrophysics*, 41:645–668, Jan 2003.

[141] M. Rodriguez-Monroy et al. Dark Energy Survey year 3 results: Galaxy clustering for combined probes. in prep.

[142] A. J. Ross, W. J. Percival, M. Crocce, A. Cabré, and E. Gaztañaga. Measuring redshift-space distortions using photometric surveys. MNRAS, 415:2193–2204, Aug. 2011.

[143] E. Rozo, E. S. Rykoff, A. Abate, C. Bonnett, M. Crocce, C. Davis, B. Hoyle, B. Leistedt, H. V. Peiris, R. H. Wechsler, T. Abbott, F. B. Abdalla, M. Banerji, A. H. Bauer, A. Benoit-Lévy, G. M. Bernstein, E. Bertin, D. Brooks, E. Buckley-Geer, D. L. Burke, D. Capozzi, A. C. Rosell, D. Carollo, M. C. Kind, J. Carretero, F. J. Castander, M. J. Childress, C. E. Cunha, C. B. D'Andrea, T. Davis, D. L. DePoy, S. Desai, H. T. Diehl, J. P. Dietrich, P. Doel, T. F. Eifler, A. E. Evrard, A. F. Neto, B. Flaugher, P. Fosalba, J. Frieman, E. Gaztanaga, D. W. Gerdes, K. Glazebrook, D. Gruen, R. A. Gruendl, K. Honscheid, D. J. James, M. Jarvis, A. G. Kim, K. Kuehn, N. Kuropatkin, O. Lahav, C. Lidman, M. Lima, M. A. G. Maia, M. March, P. Martini, P. Melchior, C. J. Miller, R. Miquel, J. J. Mohr, R. C. Nichol, B. Nord, C. R. O'Neill, R. Ogando, A. A. Plazas, A. K. Romer, A. Roodman, M. Sako, E. Sanchez, B. Santiago, M. Schubnell, I. Sevilla-Noarbe, R. C. Smith, M. Soares-Santos, F. Sobreira, E. Suchyta, M. E. C. Swanson, J. Thaler, D. Thomas, S. Uddin, V. Vikram, A. R. Walker, W. Wester, Y. Zhang, and L. N. da Costa. redMaGiC: selecting luminous red galaxies from the DES Science Verification data. MNRAS, 461(2):1431–1450, Sep 2016.

[144] E. S. Rykoff, E. Rozo, M. T. Busha, C. E. Cunha, A. Finoguenov, A. Evrard, J. Hao, B. P. Koester, A. Leauthaud, B. Nord, M. Pierre, R. Reddick, T. Sadibekova, E. S. Sheldon, and R. H. Wechsler. redMaPPer. I. Algorithm and SDSS DR8 Catalog. ApJ, 785(2):104, Apr 2014.

[145] E. S. Rykoff, E. Rozo, D. Hollowood, A. Bermeo-Hernand ez, T. Jeltema, J. Mayers, A. K. Romer, P. Rooney, A. Saro, C. Vergara Cervantes, R. H. Wechsler, H. Wilcox, T. M. C. Abbott, F. B. Abdalla, S. Allam, J. Annis, A. Benoit-Lévy, G. M. Bernstein, E. Bertin, D. Brooks, D. L. Burke, D. Capozzi, A. Carnero Rosell, M. Carrasco Kind, F. J. Castander, M. Childress, C. A. Collins, C. E. Cunha, C. B. D'Andrea, L. N. da

Costa, T. M. Davis, S. Desai, H. T. Diehl, J. P. Dietrich, P. Doel, A. E. Evrard, D. A. Finley, B. Flaugher, P. Fosalba, J. Frieman, K. Glazebrook, D. A. Goldstein, D. Gruen, R. A. Gruendl, G. Gutierrez, M. Hilton, K. Honscheid, B. Hoyle, D. J. James, S. T. Kay, K. Kuehn, N. Kuropatkin, O. Lahav, G. F. Lewis, C. Lidman, M. Lima, M. A. G. Maia, R. G. Mann, J. L. Marshall, P. Martini, P. Melchior, C. J. Miller, R. Miquel, J. J. Mohr, R. C. Nichol, B. Nord, R. Ogando, A. A. Plazas, K. Reil, M. Sahlén, E. Sanchez, B. Santiago, V. Scarpine, M. Schubnell, I. Sevilla-Noarbe, R. C. Smith, M. Soares-Santos, F. Sobreira, J. P. Stott, E. Suchyta, M. E. C. Swanson, G. Tarle, D. Thomas, D. Tucker, S. Uddin, P. T. P. Viana, V. Vikram, A. R. Walker, Y. Zhang, and DES Collaboration. The RedMaPPer Galaxy Cluster Catalog From DES Science Verification Data. ApJS, 224(1):1, May 2016.

[146] C. Sánchez, M. Carrasco Kind, H. Lin, R. Miquel, F. B. Abdalla, A. Amara, M. Banerji, C. Bonnett, R. Brunner, D. Capozzi, A. Carnero, F. J. Castander, L. A. N. da Costa, C. Cunha, A. Fausti, D. Gerdes, N. Greisel, J. Gschwend, W. Hartley, S. Jouvel, O. Lahav, M. Lima, M. A. G. Maia, P. Martí, R. L. C. Ogando, F. Ostrovski, P. Pellegrini, M. M. Rau, I. Sadeh, S. Seitz, I. Sevilla-Noarbe, A. Sypniewski, J. de Vicente, T. Abbot, S. S. Allam, D. Atlee, G. Bernstein, J. P. Bernstein, E. Buckley-Geer, D. Burke, M. J. Childress, T. Davis, D. L. DePoy, A. Dey, S. Desai, H. T. Diehl, P. Doel, J. Estrada, A. Evrard, E. Fernández, D. Finley, B. Flaugher, J. Frieman, E. Gaztanaga, K. Glazebrook, K. Honscheid, A. Kim, K. Kuehn, N. Kuropatkin, C. Lidman, M. Makler, J. L. Marshall, R. C. Nichol, A. Roodman, E. Sánchez, B. X. Santiago, M. Sako, R. Scalzo, R. C. Smith, M. E. C. Swanson, G. Tarle, D. Thomas, D. L. Tucker, S. A. Uddin, F. Valdés, A. Walker, F. Yuan, and J. Zuntz. Photometric redshift analysis in the Dark Energy Survey Science Verification data. MNRAS, 445(2):1482–1506, Dec 2014.

[147] M. Scodeggio, L. Guzzo, B. Garilli, B. R. Granett, M. Bolzonella, S. de la Torre, U. Abbas, C. Adami, S. Arnouts, D. Bottini, A. Cappi, J. Coupon, O. Cucciati, I. Davidzon, P. Franzetti, A. Fritz, A. Iovino, J. Krywult, V. Le Brun, O. Le Fèvre, D. Maccagni, K. Małek, A. Marchetti, F. Marulli, M. Polletta, A. Pollo, L. A. M. Tasca, R. Tojeiro, D. Vergani, A. Zanichelli, J. Bel, E. Branchini, G. De Lucia, O. Ilbert, H. J. McCracken, T. Moutard, J. A. Peacock, G. Zamorani, A. Burden, M. Fumana, E. Jullo, C. Marinoni, Y. Mellier, L. Moscardini, and W. J. Percival. The VIMOS Public Extragalactic Redshift Survey (VIPERS). Full spectroscopic data and auxiliary information release (PDR-2). A&A, 609:A84, Jan 2018.

[148] D. Scott and G. Smoot. Cosmic Microwave Background Mini-Review. *arXiv e-prints*, pages astro–ph/0601307, Jan 2006.

[149] U. Seljak. Extracting Primordial Non-Gaussianity without Cosmic Variance. Phys. Rev. Lett., 102(2):021302, Jan 2009.

[150] I. Sevilla-Noarbe, K. Bechtol, M. Carrasco Kind, et al. The Dark Energy Survey Year 3 Results: Photometric Data Set for Cosmology. *To be submitted to ApJS*, in prep.

[151] E. S. Sheldon and E. M. Huff. Practical Weak-lensing Shear Measurement with Metacalibration. ApJ, 841(1):24, May 2017.

[152] B. D. Sherwin, A. van Engelen, N. Sehgal, M. Madhavacheril, G. E. Addison, S. Aiola, R. Allison, N. Battaglia, D. T. Becker, J. A. Beall, J. R. Bond, E. Calabrese, R. Datta, M. J. Devlin, R. Dünner, J. Dunkley, A. E. Fox, P. Gallardo, M. Halpern, M. Hasselfield, S. Henderson, J. C. Hill, G. C. Hilton, J. Hubmayr, J. P. Hughes, A. D. Hincks, R. Hlozek, K. M. Huffenberger, B. Koopman, A. Kosowsky, T. Louis, L. Maurin, J. McMahon, K. Moodley, S. Naess, F. Nati, L. Newburgh, M. D. Niemack, L. A. Page, J. Sievers, D. N. Spergel, S. T. Staggs, R. J. Thornton, J. Van Lanen, E. Vavagiakis, and E. J. Wollack. Two-season Atacama Cosmology Telescope polarimeter lensing power spectrum. Phys. Rev. D, 95(12):123529, Jun 2017.

[153] S. Singh, S. Alam, R. Mandelbaum, U. Seljak, S. Rodriguez-Torres, and S. Ho. Probing gravity with a joint analysis of galaxy and CMB lensing and SDSS spectroscopy. MNRAS, 482(1):785–806, Jan 2019.

[154] S. Singh, R. Mandelbaum, and J. R. Brownstein. Cross-correlating Planck CMB lensing with SDSS: lensing-lensing and galaxy-lensing cross-correlations. MNRAS, 464(2):2120–2138, Jan 2017.

[155] A. Slosar, C. Hirata, U. Seljak, S. Ho, and N. Padmanabhan. Constraints on local primordial non-Gaussianity from large scale structure. J. Cosmology Astropart. Phys., 2008(8):031, Aug 2008.

[156] K. M. Smith, O. Zahn, and O. Doré. Detection of gravitational lensing in the cosmic microwave background. Phys. Rev. D, 76(4):043510, Aug 2007.

[157] R. E. Smith, J. A. Peacock, A. Jenkins, S. D. M. White, C. S. Frenk, F. R. Pearce, P. A. Thomas, G. Efstathiou, and H. M. P. Couchman. Stable clustering, the halo model and non-linear cosmological power spectra. MNRAS, 341:1311–1332, June 2003.

[158] G. F. Smoot, C. L. Bennett, A. Kogut, E. L. Wright, J. Aymon, N. W. Boggess, E. S. Cheng, G. de Amici, S. Gulkis, M. G. Hauser, G. Hinshaw, P. D. Jackson, M. Janssen, E. Kaita, T. Kelsall, P. Keegstra, C. Lineweaver, K. Loewenstein, P. Lubin, J. Mather, S. S.

Meyer, S. H. Moseley, T. Murdock, L. Rokke, R. F. Silverberg, L. Tenorio, R. Weiss, and D. T. Wilkinson. Structure in the COBE Differential Microwave Radiometer First-Year Maps. ApJ, 396:L1, Sep 1992.

[159] D. Spergel, N. Gehrels, C. Baltay, D. Bennett, J. Breckinridge, M. Donahue, A. Dressler, B. S. Gaudi, T. Greene, O. Guyon, C. Hirata, J. Kalirai, N. J. Kasdin, B. Macintosh, W. Moos, S. Perlmutter, M. Postman, B. Rauscher, J. Rhodes, Y. Wang, D. Weinberg, D. Benford, M. Hudson, W. S. Jeong, Y. Mellier, W. Traub, T. Yamada, P. Capak, J. Colbert, D. Masters, M. Penny, D. Savransky, D. Stern, N. Zimmerman, R. Barry, L. Bartusek, K. Carpenter, E. Cheng, D. Content, F. Dekens, R. Demers, K. Grady, C. Jackson, G. Kuan, J. Kruk, M. Melton, B. Nemati, B. Parvin, I. Poberezhskiy, C. Peddie, J. Ruffa, J. K. Wallace, A. Whipple, E. Wollack, and F. Zhao. Wide-Field InfrarRed Survey Telescope-Astrophysics Focused Telescope Assets WFIRST-AFTA 2015 Report. *arXiv e-prints*, page arXiv:1503.03757, Mar 2015.

[160] K. T. Story, D. Hanson, P. A. R. Ade, K. A. Aird, J. E. Austermann, J. A. Beall, A. N. Bender, B. A. Benson, L. E. Bleem, J. E. Carlstrom, C. L. Chang, H. C. Chiang, H. M. Cho, R. Citron, T. M. Crawford, A. T. Crites, T. de Haan, M. A. Dobbs, W. Everett, J. Gallicchio, J. Gao, E. M. George, A. Gilbert, N. W. Halverson, N. Harrington, J. W. Henning, G. C. Hilton, G. P. Holder, W. L. Holzapfel, S. Hoover, Z. Hou, J. D. Hrubes, N. Huang, J. Hubmayr, K. D. Irwin, R. Keisler, L. Knox, A. T. Lee, E. M. Leitch, D. Li, C. Liang, D. Luong-Van, J. J. McMahon, J. Mehl, S. S. Meyer, L. Mocanu, T. E. Montroy, T. Natoli, J. P. Nibarger, V. Novosad, S. Padin, C. Pryke, C. L. Reichardt, J. E. Ruhl, B. R. Saliwanchik, J. T. Sayre, K. K. Schaffer, G. Smecher, A. A. Stark, C. Tucker, K. Vand erlinde, J. D. Vieira, G. Wang, N. Whitehorn, V. Yefremenko, and O. Zahn. A Measurement of the Cosmic Microwave Background Gravitational Lensing Potential from 100 Square Degrees of SPTpol Data. ApJ, 810(1):50, Sep 2015.

[161] K. T. Story, C. L. Reichardt, Z. Hou, R. Keisler, K. A. Aird, B. A. Benson, L. E. Bleem, J. E. Carlstrom, C. L. Chang, H. M. Cho, T. M. Crawford, A. T. Crites, T. de Haan, M. A. Dobbs, J. Dudley, B. Follin, E. M. George, N. W. Halverson, G. P. Holder, W. L. Holzapfel, S. Hoover, J. D. Hrubes, M. Joy, L. Knox, A. T. Lee, E. M. Leitch, M. Lueker, D. Luong-Van, J. J. McMahon, J. Mehl, S. S. Meyer, M. Millea, J. J. Mohr, T. E. Montroy, S. Padin, T. Plagge, C. Pryke, J. E. Ruhl, J. T. Sayre, K. K. Schaffer, L. Shaw, E. Shirokoff, H. G. Spieler, Z. Staniszewski, A. A. Stark, A. van Engelen, K. Vand erlinde, J. D. Vieira, R. Williamson, and O. Zahn. A Measurement of the Cosmic Microwave Background Damping Tail from the 2500-Square-Degree SPT-SZ Survey. ApJ, 779(1):86, Dec 2013.

[162] A. Sánchez, E. Kazin, et al. Stable clustering, the halo model and nonlinear cosmological

power spectra. *Monthly Notices of the Royal Astronomical Society*, 433(2):1202–1222, 2013.

[163] R. Takahashi, M. Sato, T. Nishimichi, A. Taruya, and M. Oguri. Revising the Halofit Model for the Nonlinear Matter Power Spectrum. ApJ, 761:152, Dec. 2012.

[164] The Dark Energy Survey Collaboration. The Dark Energy Survey. *arXiv e-prints*, pages astro–ph/0510346, Oct 2005.

[165] The Dark Energy Survey Collaboration et al. Cosmology from Cosmic Shear with DES Science Verification Data. July 2015.

[166] M. A. Troxel, N. MacCrann, J. Zuntz, T. F. Eifler, E. Krause, S. Dodelson, D. Gruen, J. Blazek, O. Friedrich, S. Samuroff, J. Prat, L. F. Secco, C. Davis, A. Ferté, J. DeRose, A. Alarcon, A. Amara, E. Baxter, M. R. Becker, G. M. Bernstein, S. L. Bridle, R. Cawthon, C. Chang, A. Choi, J. De Vicente, A. Drlica-Wagner, J. Elvin-Poole, J. Frieman, M. Gatti, W. G. Hartley, K. Honscheid, B. Hoyle, E. M. Huff, D. Huterer, B. Jain, M. Jarvis, T. Kacprzak, D. Kirk, N. Kokron, C. Krawiec, O. Lahav, A. R. Liddle, J. Peacock, M. M. Rau, A. Refregier, R. P. Rollins, E. Rozo, E. S. Rykoff, C. Sánchez, I. Sevilla-Noarbe, E. Sheldon, A. Stebbins, T. N. Varga, P. Vielzeuf, M. Wang, R. H. Wechsler, B. Yanny, T. M. C. Abbott, F. B. Abdalla, S. Allam, J. Annis, K. Bechtol, A. Benoit-Lévy, E. Bertin, D. Brooks, E. Buckley-Geer, D. L. Burke, A. Carnero Rosell, M. Carrasco Kind, J. Carretero, F. J. Castander, M. Crocce, C. E. Cunha, C. B. D'Andrea, L. N. da Costa, D. L. DePoy, S. Desai, H. T. Diehl, J. P. Dietrich, P. Doel, E. Fernandez, B. Flaugher, P. Fosalba, J. García-Bellido, E. Gaztanaga, D. W. Gerdes, T. Giannantonio, D. A. Goldstein, R. A. Gruendl, J. Gschwend, G. Gutierrez, D. J. James, T. Jeltema, M. W. G. Johnson, M. D. Johnson, S. Kent, K. Kuehn, S. Kuhlmann, N. Kuropatkin, T. S. Li, M. Lima, H. Lin, M. A. G. Maia, M. March, J. L. Marshall, P. Martini, P. Melchior, F. Menanteau, R. Miquel, J. J. Mohr, E. Neilsen, R. C. Nichol, B. Nord, D. Petravick, A. A. Plazas, A. K. Romer, A. Roodman, M. Sako, E. Sanchez, V. Scarpine, R. Schindler, M. Schubnell, M. Smith, R. C. Smith, M. Soares-Santos, F. Sobreira, E. Suchyta, M. E. C. Swanson, G. Tarle, D. Thomas, D. L. Tucker, V. Vikram, A. R. Walker, J. Weller, Y. Zhang, and DES Collaboration. Dark Energy Survey Year 1 results: Cosmological constraints from cosmic shear. Phys. Rev. D, 98(4):043528, Aug 2018.

[167] M. P. van Daalen, J. Schaye, C. M. Booth, and C. Dalla Vecchia. The effects of galaxy formation on the matter power spectrum: a challenge for precision cosmology. MNRAS, 415(4):3649–3665, Aug 2011.

[168] A. van Engelen, R. Keisler, O. Zahn, K. A. Aird, B. A. Benson, L. E. Bleem, J. E. Carlstrom, C. L. Chang, H. M. Cho, T. M. Crawford, A. T. Crites, T. de Haan, M. A. Dobbs, J. Dudley, E. M. George, N. W. Halverson, G. P. Holder, W. L. Holzapfel, S. Hoover, Z. Hou, J. D. Hrubes, M. Joy, L. Knox, A. T. Lee, E. M. Leitch, M. Lueker, D. Luong-Van, J. J. McMahon, J. Mehl, S. S. Meyer, M. Millea, J. J. Mohr, T. E. Montroy, T. Natoli, S. Padin, T. Plagge, C. Pryke, C. L. Reichardt, J. E. Ruhl, J. T. Sayre, K. K. Schaffer, L. Shaw, E. Shirokoff, H. G. Spieler, Z. Staniszewski, A. A. Stark, K. Story, K. Vanderlinde, J. D. Vieira, and R. Williamson. A Measurement of Gravitational Lensing of the Microwave Background Using South Pole Telescope Data. ApJ, 756:142, Sept. 2012.

[169] M. Velliscig, M. P. van Daalen, J. Schaye, I. G. McCarthy, M. Cacciato, A. i. M. C. Le Brun, and C. Dalla Vecchia. The impact of galaxy formation on the total mass, mass profile and abundance of haloes. MNRAS, 442(3):2641–2658, Aug 2014.

[170] D. Walsh, R. F. Carswell, and R. J. Weymann. 0957+561 A, B: twin quasistellar objects or gravitational lens? *Nature*, 279:381–384, May 1979.

[171] M. White, Y.-S. Song, and W. J. Percival. Forecasting cosmological constraints from redshift surveys. MNRAS, 397(3):1348–1354, Aug 2009.

[172] D. G. York, J. Adelman, J. Anderson, John E., S. F. Anderson, J. Annis, N. A. Bahcall, J. A. Bakken, R. Barkhouser, S. Bastian, E. Berman, W. N. Boroski, S. Bracker, C. Briegel, J. W. Briggs, J. Brinkmann, R. Brunner, S. Burles, L. Carey, M. A. Carr, F. J. Castander, B. Chen, P. L. Colestock, A. J. Connolly, J. H. Crocker, I. Csabai, P. C. Czarapata, J. E. Davis, M. Doi, T. Dombeck, D. Eisenstein, N. Ellman, B. R. Elms, M. L. Evans, X. Fan, G. R. Federwitz, L. Fiscelli, S. Friedman, J. A. Frieman, M. Fukugita, B. Gillespie, J. E. Gunn, V. K. Gurbani, E. de Haas, M. Haldeman, F. H. Harris, J. Hayes, T. M. Heckman, G. S. Hennessy, R. B. Hindsley, S. Holm, D. J. Holmgren, C.-h. Huang, C. Hull, D. Husby, S.-I. Ichikawa, T. Ichikawa, Ž. Ivezić, S. Kent, R. S. J. Kim, E. Kinney, M. Klaene, A. N. Kleinman, S. Kleinman, G. R. Knapp, J. Korienek, R. G. Kron, P. Z. Kunszt, D. Q. Lamb, B. Lee, R. F. Leger, S. Limmongkol, C. Lindenmeyer, D. C. Long, C. Loomis, J. Loveday, R. Lucinio, R. H. Lupton, B. MacKinnon, E. J. Mannery, P. M. Mantsch, B. Margon, P. McGehee, T. A. McKay, A. Meiksin, A. Merelli, D. G. Monet, J. A. Munn, V. K. Narayanan, T. Nash, E. Neilsen, R. Neswold, H. J. Newberg, R. C. Nichol, T. Nicinski, M. Nonino, N. Okada, S. Okamura, J. P. Ostriker, R. Owen, A. G. Pauls, J. Peoples, R. L. Peterson, D. Petravick, J. R. Pier, A. Pope, R. Pordes, A. Prosapio, R. Rechenmacher, T. R. Quinn, G. T. Richards, M. W. Richmond, C. H. Rivetta, C. M. Rockosi, K. Ruthmansdorfer, D. Sand ford, D. J. Schlegel, D. P. Schneider, M. Sekiguchi,

G. Sergey, K. Shimasaku, W. A. Siegmund, S. Smee, J. A. Smith, S. Snedden, R. Stone, C. Stoughton, M. A. Strauss, C. Stubbs, M. SubbaRao, A. S. Szalay, I. Szapudi, G. P. Szokoly, A. R. Thakar, C. Tremonti, D. L. Tucker, A. Uomoto, D. Vanden Berk, M. S. Vogeley, P. Waddell, S.-i. Wang, M. Watanabe, D. H. Weinberg, B. Yanny, N. Yasuda, and SDSS Collaboration. The Sloan Digital Sky Survey: Technical Summary. AJ, 120(3):1579–1587, Sep 2000.

[173] B. Yu, R. Z. Knight, B. D. Sherwin, S. Ferraro, L. Knox, and M. Schmittfull. Towards Neutrino Mass from Cosmology without Optical Depth Information. *arXiv e-prints*, page arXiv:1809.02120, Sep 2018.

[174] F. Yuan, C. Lidman, T. M. Davis, M. Childress, F. B. Abdalla, M. Banerji, E. Buckley-Geer, A. Carnero Rosell, D. Carollo, F. J. Castander, C. B. D'Andrea, H. T. Diehl, C. E. Cunha, R. J. Foley, J. Frieman, K. Glazebrook, J. Gschwend, S. Hinton, S. Jouvel, R. Kessler, A. G. Kim, A. L. King, K. Kuehn, S. Kuhlmann, G. F. Lewis, H. Lin, P. Martini, R. G. McMahon, J. Mould, R. C. Nichol, R. P. Norris, C. R. O'Neill, F. Ostrovski, A. Papadopoulos, D. Parkinson, S. Reed, A. K. Romer, P. J. Rooney, E. Rozo, E. S. Rykoff, M. Sako, R. Scalzo, B. P. Schmidt, D. Scolnic, N. Seymour, R. Sharp, F. Sobreira, M. Sullivan, R. C. Thomas, D. Tucker, S. A. Uddin, R. H. Wechsler, W. Wester, H. Wilcox, B. Zhang, T. Abbott, S. Allam, A. H. Bauer, A. Benoit-Lévy, E. Bertin, D. Brooks, D. L. Burke, M. Carrasco Kind, R. Covarrubias, M. Crocce, L. N. da Costa, D. L. DePoy, S. Desai, P. Doel, T. F. Eifler, A. E. Evrard, A. Fausti Neto, B. Flaugher, P. Fosalba, E. Gaztanaga, D. Gerdes, D. Gruen, R. A. Gruendl, K. Honscheid, D. James, N. Kuropatkin, O. Lahav, T. S. Li, M. A. G. Maia, M. Makler, J. Marshall, C. J. Miller, R. Miquel, R. Ogando, A. A. Plazas, A. Roodman, E. Sanchez, V. Scarpine, M. Schubnell, I. Sevilla-Noarbe, R. C. Smith, M. Soares-Santos, E. Suchyta, M. E. C. Swanson, G. Tarle, J. Thaler, and A. R. Walker. OzDES multifibre spectroscopy for the Dark Energy Survey: first-year operation and results. MNRAS, 452(3):3047–3063, Sep 2015.

[175] M. Zaldarriaga and U. Seljak. Reconstructing projected matter density power spectrum from cosmic microwave background. Phys. Rev. D, 59(12):123507, Jun 1999.

[176] J. Zuntz, M. Paterno, E. Jennings, D. Rudd, A. Manzotti, S. Dodelson, S. Bridle, S. Sehrish, and J. Kowalkowski. CosmoSIS: Modular cosmological parameter estimation. *Astronomy and Computing*, 12:45–59, Sept. 2015.

[177] J. Zuntz, E. Sheldon, S. Samuroff, M. A. Troxel, M. Jarvis, N. MacCrann, D. Gruen, J. Prat, C. Sánchez, A. Choi, S. L. Bridle, G. M. Bernstein, S. Dodelson, A. Drlica-Wagner, Y. Fang, R. A. Gruendl, B. Hoyle, E. M. Huff, B. Jain, D. Kirk, T. Kacprzak,

C. Krawiec, A. A. Plazas, R. P. Rollins, E. S. Rykoff, I. Sevilla-Noarbe, B. Soergel, T. N. Varga, T. M. C. Abbott, F. B. Abdalla, S. Allam, J. Annis, K. Bechtol, A. Benoit-Lévy, E. Bertin, E. Buckley-Geer, D. L. Burke, A. Carnero Rosell, M. Carrasco Kind, J. Carretero, F. J. Castander, M. Crocce, C. E. Cunha, C. B. D'Andrea, L. N. da Costa, C. Davis, S. Desai, H. T. Diehl, J. P. Dietrich, P. Doel, T. F. Eifler, J. Estrada, A. E. Evrard, A. Fausti Neto, E. Fernandez, B. Flaugher, P. Fosalba, J. Frieman, J. García-Bellido, E. Gaztanaga, D. W. Gerdes, T. Giannantonio, J. Gschwend, G. Gutierrez, W. G. Hartley, K. Honscheid, D. J. James, T. Jeltema, M. W. G. Johnson, M. D. Johnson, K. Kuehn, S. Kuhlmann, N. Kuropatkin, O. Lahav, T. S. Li, M. Lima, M. A. G. Maia, M. March, P. Martini, P. Melchior, F. Menanteau, C. J. Miller, R. Miquel, J. J. Mohr, E. Neilsen, R. C. Nichol, R. L. C. Ogando, N. Roe, A. K. Romer, A. Roodman, E. Sanchez, V. Scarpine, R. Schindler, M. Schubnell, M. Smith, R. C. Smith, M. Soares-Santos, F. Sobreira, E. Suchyta, M. E. C. Swanson, G. Tarle, D. Thomas, D. L. Tucker, V. Vikram, A. R. Walker, R. H. Wechsler, Y. Zhang, and DES Collaboration. Dark Energy Survey Year 1 results: weak lensing shape catalogues. MNRAS, 481(1):1149–1182, Nov 2018.